This is to certify that the

dissertation entitled

A PENALTY-BASED INTERFACE TECHNOLOGY FOR CONNECTING INDEPENDENTLY MODELED SUBSTRUCTURES AND FOR SIMULATING GROWTH OF DELAMINATION IN COMPOSITE STRUCTURES

presented by

Antonio Pantano

has been accepted towards fulfillment
of the requirements for

PhD degree in Mechanics

Ronald C. Averill
Major professor

Date JUNE 17, 2002

A PENALTY-BASED INTERFACE TECHNOLOGY FOR CONNECTING INDEPENDENTLY MODELED SUBSTRUCTURES AND FOR SIMULATING GROWTH OF DELAMINATION IN COMPOSITE STRUCTURES

By

Antonio Pantano

A DISSERTATION

Submitted to
Michigan State University
in partial fulfillment of the requirements
for the degree of

DOCTOR OF PHILOSOPHY

Department of Mechanical Engineering

2002

ABSTRACT

A PENALTY-BASED INTERFACE TECHNOLOGY FOR CONNECTING INDEPENDENTLY MODELED SUBSTRUCTURES AND FOR SIMULATING GROWTH OF DELAMINATION IN COMPOSITE STRUCTURES

By

Antonio Pantano

An effective and robust interface element technology able to connect independently modeled finite element subdomains is presented. This method has been developed using penalty constraints and allows coupling of finite element models whose nodes do not coincide along their common interface. Additionally, the present formulation leads to a computational approach that is very efficient and completely compatible with existing commercial software. A significant effort has been directed toward identifying those model characteristics (element geometric properties, material properties and loads) that most strongly affect the required penalty parameter, and subsequently to developing simple "formulae" for automatically calculating the proper penalty parameter for each interface constraint. This task is especially critical in composite materials and structures, where adjacent sub-regions may be composed of significantly different materials or laminates. The present interface element has been implemented in the commercial finite element code ABAQUS as a User Element Subroutine (UEL), making it easy to test the approach for a wide range of problems.

Once the reliability and the effectiveness of the interface element were established, new capabilities were implemented in the FE code in order to simulate delamination growth in composite laminates. Thanks to its special features, the interface element approach has several advantages over the conventional FE ones. An analysis of the literature on delamination techniques shows that generally delamination growth is simulated in a discretized form by releasing nodes of the FEM. The presented interface element allows this limitation to be overcome. It is possible to release portions of the interface surface whose length is smaller than that of the finite elements. In addition, for each portion the value of the penalty parameter can be changed at will, allowing the damage model to be applied to a desired fraction of the interface between the two meshes. The approach implemented in the interface element is one of the most commonly adopted. It mixes features of the strength of materials approach and fracture mechanics. The strength-based part predicts the onset of damage when the interfacial stress reaches the interlaminar tensile strength. Meanwhile, the relation between the work of separation and the critical value of the energy release rate provides a reliable softening model, required to describe how the stiffness is gradually reduced to zero after the onset of damage. Results for double cantilever beam DCB, end-loaded split (ELS) and Fixed-Ratio Mixed Mode (FRMM) specimens are presented. These results are compared to measured data to assess the ability of the present damage model to simulate delamination growth for Mode I, Mode II and Mixed Mode I+II.

To my Mother and Father

ACKNOWLEDGMENTS

I will always be grateful to my beloved parents for years of unconditional support. I hope they will be proud of me, now and in the future.

I would like to reserve a special gratitude to my sweet wife Giulia. Without her love this result would have been harder to achieve.

I definitely recognize the immense fortune I had to meet a person like my research advisor Prof. Ronald Averill. His uncommon humanity equals only his exceptional academic knowledge.

I also greatly appreciate Prof. Gary J. Burgess, Dahsin Liu and Hungyu Tsai for making efforts to serve my thesis committee.

This work was sponsored by NASA Langley Research Center under grant NAG-1-2213. The authors are grateful for the helpful comments of Dr. Jonathan Ransom, the grant technical monitor. Partial support was also provided by the State of Michigan Research Excellence Fund.

Antonio Pantano

June 2002

East Lansing, Michigan

LIST O

LIST O

CHAP

CHA

CH

TABLE OF CONTENTS

CHAP

CHA

LIST OF TABLES

LIST OF FIGURES

Figure 20.

Figure 21.

Figure 22

Figure 23

Figure 24

Figure 25

Figure 26

Figure 27

Figure

Figure

Figure

Figure

Figur

Figur

Figur

Figur

Fig

Fig

Figure 110.

Figure 111.

Figure 112.

Figure 113

Figure 114

Figure 115

Figure 116

Figure 11

Figure 11

Figure 11

Figure 12

Figure 12

Figure 1

Figure 1

Figure 1

Figure 1

Figure 1

Figure

Figure

Figure

Figure

Figure

Figure

CHAPTER 1 INTRODUCTION TO THE INTERFACE ELEMENT

1.1 Introduction and Literature Review

The ways in which analysis and design are performed have changed extensively during the past decade. Automated design algorithms are now plentiful and increasingly robust, and no longer are individual components of a structure designed in a vacuum. Facilitated in part by product data management (PDM) and product lifecycle management (PLM) software and internet-based data sharing, integrated design activities are now possible. Further, the speed and economy of modern computers have enabled engineers to perform many large scale analyses that were unheard of a decade ago. It is now common to analyze and simulate the response of entire aircraft, spacecraft, automobiles, ships, and other structural assemblies to a variety of complex and combined types of loading. The CPU time required to perform such analyses is very small compared to the time required for engineers to create the mathematical and computer models, and the latter effort is usually the most expensive component of a large scale analysis or simulation.

With model sharing and large scale analysis activities on the rise, it is becoming

evident that improved technology for building computer models is needed. One issue that arises often is the need to perform a unified analysis of a structural assembly using sub-structural models created independently. These sub-structural models are frequently created by different engineers using different software and in different geographical locations, with little or no communication between the teams of engineers creating the models. As a result, these models are likely to be incompatible at their interfaces, making it very difficult to combine them for a unified analysis of the entire assembly.

Finite element interface technology has been developed during the past decade to facilitate the joining of independently modeled substructures. Unconventional approaches have been employed to connect special elements based on analytical solutions to finite element models [1-2]. In [1] a near-field solution for a dynamically propagating crack at the interface of two dissimilar anisotropic elastic materials was successfully implemented into a hybrid-displacement finite element formulation. In [2] Lagrange multiplier terms are used to couple a special element, based on a stress analytical solution, to standard finite elements.

In order to take advantage of parallel computing, Farhat and colleagues [3-4] developed a domain decomposition approach for partitioning the spatial domain into a set of disconnected subdomains, each assigned to an individual processor. Lagrange multipliers were introduced to enforce compatibility at the interface nodes. In [5] non-conforming "mortar" elements are employed to connect incompatible subdomains using a conjugate gradient iterative technique in a domain decomposition scheme designed for parallel computers.

The finite element interface technology developed at NASA LaRC [6-10] and

elsewhere [11] allows the connection of independently modeled substructures with incompatible discretization along the common boundary. This approach has matured to a point that it is now very effective. However, because the interface technology utilizes Lagrange multipliers to enforce the interface constraint conditions, the resulting system of equations is not positive-definite. Hence, state-of-the-art sparse solver technology cannot be utilized with the interface technology.

Recently, an alternative formulation for the finite element interface technology based on Lagrange multipliers has been developed [12]. The alternative approach recasts the interface element constraint equations in the form of multi-point constraints. This change allows an easier implementation of the formulation in a standard finite element code and alleviates the issues related to the resulting non-positive definite system of equations. The method seems to provide reliable results, but the formulation of the interface method is still quite complicated.

A possible remedy for these shortcomings is to modify the current hybrid variational formulation of the interface element by enforcing the interface constraints via a penalty method as opposed to the current Lagrange multiplier approach. The primary consequences of this modification will be (i) a simple formulation that is easily implemented in commercial finite elements codes, (ii) a positive-definite and banded stiffness matrix and (iii) a reduced number of DOFs, since the Lagrange multiplier degrees of freedom (DOFs) will not be present. Thus, the proposed approach should greatly enhance the computational efficiency of the interface element technology.

From an accuracy point of view, the penalty method enforces the constraints only approximately, depending on the value of the penalty parameter chosen, while the

Lagrange multiplier approach enforces the constraints exactly. The penalty method interface approach was recently attempted using a single global value of the penalty parameter to enforce all constraints [13]. This study demonstrated the validity and the effectiveness of the penalty approach in an interface element. However, there is need for specific guidelines regarding the selection of an appropriate value of the penalty parameter, especially when the substructures to be connected have different material and/or section stiffnesses.

There is a large body of literature related to the determination of an optimal value of the penalty parameter (see, e.g. [14-26]). However, there is no existing criterion for choosing the penalty parameter in the framework of the interface element under investigation. The determination of such a criterion is one of the goals of the effort presented herein.

An effective and robust interface element technology has been developed using the penalty method. A significant part of the work has been directed toward identifying those model characteristics that most strongly affect the required penalty parameter, and subsequently to developing simple "formulae" for automatically calculating the proper penalty parameter for each interface constraint. The new approach has been validated through a wide variety of one, two-dimensional and three-dimensional problems that have been investigated extensively from both an analytical and a computational point of view. Finally, the penalty based interface element technology has been implemented into an existing commercial code.

1.2 Org

A g

Applicati

Chapter 3

develope

meshes o

Ch

for moda

capabili

composi

presente

1.2 Organization of the Thesis

A general description of the interface element is presented in Chapter 2. Applications of the hybrid and penalty interface methods to 1D beams are provided in Chapter 3. A version of the interface element for 2D plane elasticity and plate elements is developed in Chapter 4 and Chapter 5, respectively. The interface element for connecting meshes of 3D solid 8-node brick elements is described in Chapter 6.

Chapter 7 introduces to the development of the novel interface element technology for modeling crack growth, by reviewing the literature on the subject. The additional capabilities implemented in the interface element in order to simulate delamination in composite laminates and the numerical tests performed to validate the approach are presented in Chapter 8.

CHAPTER 2 GENERAL DESCRIPTION OF THE INTERFACE ELEMENT

Consider two independently modeled subdomains Ω_1 and Ω_2 as shown in Figure 1(a) and 1(b), respectively, for a 2D and for a 3D geometry. The two substructures are connected to each other using an interface element acting like "glue" at the common interface. The interface element is discretized with a set of nodes that are independent of the nodes at the interface in subdomains Ω_1 and Ω_2. Both in the hybrid interface method and in the penalty method, the coupling terms associated to the interface element are arranged in the form of a "stiffness" matrix and assembled with the other finite element stiffness matrices as usual.

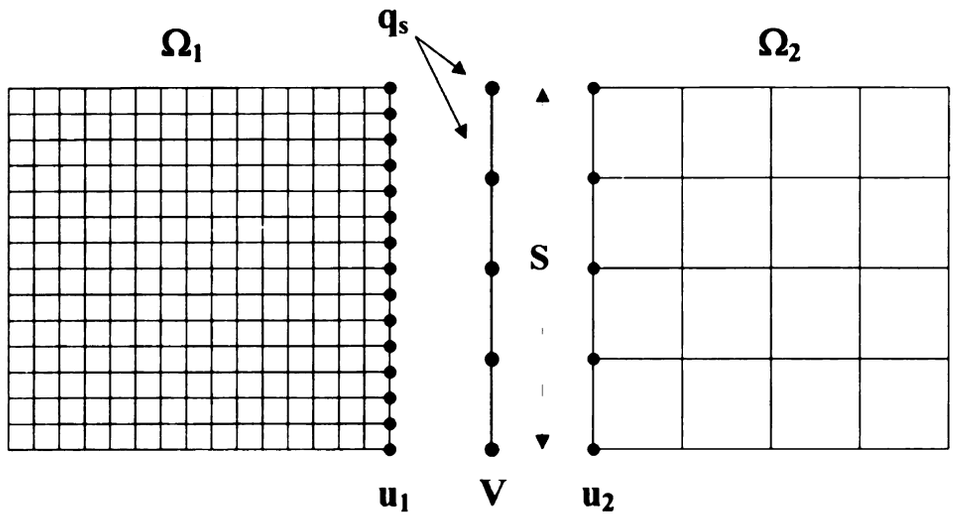

(a)

Figur

2.1

multipl

displac

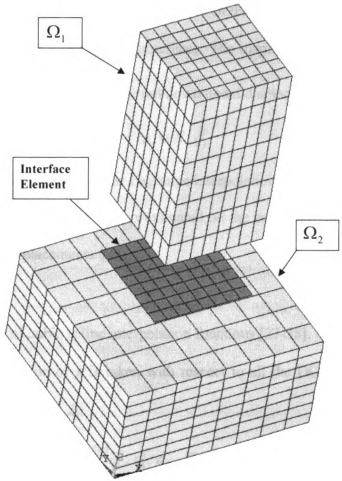

(b)

Figure 1. ***2D (a) and 3D (b) Interface element configurations.***

2.1 Hybrid Interface Method

The hybrid interface method [6-12] introduces two vectors of Lagrange multipliers λ_1 and λ_2 in the total potential energy (TPE) of the system to satisfy the displacement continuity conditions. Thus the TPE of the system assumes the form:

$$\pi = \pi_{\Omega_1} + \pi_{\Omega_2} + \int_S \lambda_1 (V - u_1) ds + \int_S \lambda_2 (V - u_2) ds \tag{1}$$

The nodal displacements of the sub-domain Ω_j are identified by q_j^o and q_j^i. The

superscript o identifies the degrees of freedom (DOFs) that are not on the interfaces, while i denotes DOFs that are on the interfaces. The displacement field u_j of the sub-domain Ω_j is expressed in terms of the unknown nodal displacements q_j^i as:

$$u_j = N_j q_j^i \tag{2}$$

where N_j can be the matrices of linear Lagrange interpolation functions.

The displacement field V is approximated on the entire interface surface in terms of unknown nodal displacements q_s as:

$$V = T q_s \tag{3}$$

where T is a matrix of cubic spline interpolation functions [27-38].

The first variation of π is taken with respect to all the DOFs and the vectors of Lagrange multipliers λ_1 and λ_2:

$$\delta\pi\big|_{q_1^o,\, q_1^i,\, q_S,\, q_2^o,\, q_2^i, \lambda_1, \lambda_2} = 0 \tag{4}$$

On the interface part of the subdomains the following equations result:

$$u_j = V, \quad \lambda_j = t_j, \quad \lambda_1 + \lambda_2 = 0 \qquad \text{for } j = 1, 2 \tag{5}$$

where t_j is the traction on the interface. These equations show that:

- Displacement continuity is enforced,
- λ_j are interface tractions,
- the total traction is zero on the interface.

The first variation of π yields the system of equations:

$$\begin{bmatrix} K_1^{ii} & K_1^{io} & 0 & 0 & 0 & M_1 & 0 \\ K_1^{oi} & K_1^{oo} & 0 & 0 & 0 & 0 & 0 \\ 0 & 0 & K_2^{ii} & K_2^{io} & 0 & 0 & M_2 \\ 0 & 0 & K_2^{oi} & K_2^{oo} & 0 & 0 & 0 \\ 0 & 0 & 0 & 0 & 0 & G_1 & G_2 \\ M_1^T & 0 & 0 & 0 & G_1^I & 0 & 0 \\ 0 & 0 & M_2^I & 0 & G_2^I & 0 & 0 \end{bmatrix} \begin{Bmatrix} q_1^i \\ q_1^o \\ q_2^i \\ q_2^o \\ q_s \\ \lambda_1 \\ \lambda_2 \end{Bmatrix} = \begin{Bmatrix} f_1^i \\ f_1^o \\ f_2^i \\ f_2^o \\ 0 \\ 0 \\ 0 \end{Bmatrix} \tag{6}$$

It can be seen that the resulting global stiffness matrix is sparse, symmetric, not banded and not positive definite. Inside [K] the interface element is represented by the coupling terms M_j and G_j which augment the stiffness matrix of the subdomains.

A "stiffness" matrix and generalized vector of unknown displacements can be associated with the interface element, so that:

$$\begin{bmatrix} 0 & 0 & 0 & M_1 & 0 \\ 0 & 0 & 0 & 0 & M_2 \\ 0 & 0 & 0 & G_1 & G_2 \\ M_1^I & 0 & G_1^I & 0 & 0 \\ 0 & M_2^I & G_2^I & 0 & 0 \end{bmatrix} \begin{Bmatrix} q_1^i \\ q_2^i \\ q_s \\ \lambda_1 \\ \lambda_2 \end{Bmatrix} \tag{7}$$

2.2 Penalty Hybrid Interface Method

In the penalty hybrid interface method the displacement continuity constraint is imposed in a least squares sense through two vectors of penalty parameters γ_1 and γ_2. Thus the TPE of the system assumes the form:

$$\pi = \pi_{\Omega_1} + \pi_{\Omega_2} + \frac{1}{2}\gamma_1 \int_S (V - u_1)^2 \, ds + \frac{1}{2}\gamma_2 \int_S (V - u_2)^2 \, ds \tag{8}$$

The displacement fields u_j and V are approximated in a similar way as in the original hybrid interface method.

The first variation of π is taken with respect to all the DOFs, but not the vectors of penalty parameters γ_1 and γ_2, which are predetermined constants.

$$\delta\pi\big|_{q_1^o,\, q_1^i,\, q_S,\, q_2^o,\, q_2^i} = 0 \tag{9}$$

We now define:

$$G_J^{ii} = \gamma_J \int_S \left(N_J^T N_J \right) ds \tag{10}$$

$$G_J^{is} = \gamma_J \int_S \left(N_J^T T_J \right) ds \tag{11}$$

$$G_J^{si} = \left[G_J^{is} \right]^T \tag{12}$$

$$G_J^{ss} = \gamma_J \int_S \left(T_J^T T_J \right) ds \tag{13}$$

So the global system of equations of the penalty hybrid interface method assumes the following form:

$$\begin{bmatrix} K_1^{oo} & K_1^{oi} & 0 & 0 & 0 \\ K_1^{io} & K_1^{ii} + G_1^{ii} & -G_1^{is} & 0 & 0 \\ 0 & -G_1^{si} & G_1^{ss} + G_2^{ss} & -G_2^{si} & 0 \\ 0 & 0 & -G_2^{is} & K_2^{ii} + G_2^{ii} & K_2^{io} \\ 0 & 0 & 0 & K_2^{oi} & K_2^{oo} \end{bmatrix} \begin{Bmatrix} q_1^o \\ q_1^i \\ q_s \\ q_2^i \\ q_2^o \end{Bmatrix} = \begin{Bmatrix} f_1^o \\ f_1^i \\ 0 \\ f_2^i \\ f_2^o \end{Bmatrix} \tag{14}$$

This is a symmetric, banded and positive definite (after boundary conditions are imposed) global stiffness matrix. The "stiffness" matrix and generalized vector of unknown displacements associated with the interface element can be defined such that:

$$\begin{bmatrix} G_1^{ii} & -G_1^{is} & 0 \\ -G_1^{si} & G_1^{ss} + G_2^{ss} & -G_2^{si} \\ 0 & -G_2^{is} & G_2^{ii} \end{bmatrix} \begin{Bmatrix} q_1^i \\ q_s \\ q_2^i \end{Bmatrix} = \begin{Bmatrix} 0 \\ 0 \\ 0 \end{Bmatrix} \tag{15}$$

2.3

2.3 *Determination of the Penalty Parameters*

In the penalty method, the displacement continuity constraint is imposed through penalty parameters, a set of predetermined constants. The FE solution obtained using this method is approximate, with its accuracy depending on the value of the adopted penalty parameters. It is known that the penalty parameter should depend on the material and/or geometric properties of the two sub-regions being joined. Further, there is a relationship between the penalty parameter and the Lagrange multiplier that enforces a given constraint.

The Lagrange multiplier method imposes the continuity constraint exactly. Thus, the Lagrange multiplier method defines the upper limit to the accuracy of the penalty method. Knowledge of the correct solution facilitates relating the value of the penalty parameter to the geometrical and material properties of the model under consideration. In our pursuit of the proper penalty parameter values, a variety of one and two-dimensional problems have been studied with both the Lagrange multiplier method and the penalty method.

The types of finite elements that have been investigated are: conventionally formulated and reduced integrated Timoshenko beam elements, plane stress quadrilateral elements and plate elements based on the first order shear deformation theory (FSDT), or Mindlin plate theory. For each finite element formulation, different penalty parameters are associated to the various nodal DOFs. For example, the Timoshenko beam element has three independent nodal DOFs: the axial displacement u, the transverse displacement w and the rotation ψ. Thus, three different penalty parameters γ_u, γ_w and γ_ψ are

employed to enforce the interface continuity constraints on the DOFs u, w and ψ. An independent choice of the penalty parameters is of fundamental importance since each degree of freedom can be related differently to the material and geometric properties of the finite element model.

The methodology adopted in finding the relations will now be described. First the most common load cases for the FE type under consideration are applied separately to a simple model of one or two elements. For example, for the Timoshenko beam element the following load cases are considered: axial load, transversely distributed load, concentrated transverse load and concentrated moment applied at the tip. These loads are applied to two different models: a single beam element connected to a fixed point by one interface element, and two linear beam elements connected using an interface element and clamped at the tip.

The formulations and solutions are obtained using both the Lagrange multiplier method and the penalty method. The displacement solutions from the two methods are compared individually for each degree of freedom. The ratio between the two solutions is expressed in the form:

$$\frac{u^{penalty}}{u^{Lagrange}} = 1 + \frac{f}{\gamma} \tag{16}$$

where $f = f$(element geometric properties, material properties, and loads)

Once this simple expression has been identified, the penalty parameter γ is set equal to:

$$\gamma = \beta f \tag{17}$$

Then, the ratio between the solutions becomes independent of material and geometrical properties of the element:

$$\frac{u^{penalty}}{u^{Lagrange}} = 1 + \frac{1}{\beta} \tag{18}$$

The accuracy of the solution depends directly on the value assigned to the parameter β. For example, if β is equal to 1000, the penalty solution differs from that obtained by use of the Lagrange multipliers by 0.1%. The degree of precision of the solution cannot be indefinitely increased, since round off amplification error would rise. However, once a reasonable compromise between constraint representation error and the round off error has been evaluated, a value of β can be identified that is able to produce the same level of accuracy for every combination of material and geometrical properties.

In some cases, however, the displacement solution related to a particular DOF depends on the penalty parameter used to enforce a different DOF. An example of this situation is represented by the following relations:

$$\frac{u_1^{penalty}}{u_1^{Lagrange}} = 1 + \frac{f_1}{\gamma_1} + \frac{f_2}{\gamma_2} \tag{19}$$

$$\frac{u_2^{penalty}}{u_2^{Lagrange}} = 1 + \frac{f_3}{\gamma_2} \tag{20}$$

where u_1 and u_2 are displacement solutions computed at the same node for two different DOFs, while f_1, f_2 and f_3 are independent functions of the model properties and the loads.

Two possible options are available in this situation. The first option is to choose $\gamma_1 = 2\beta f_1$ and $\gamma_2 = 2\beta f_2$ in order to obtain the desired simple relation between the solution ratio and β only for the DOF 1.

$$\frac{u_1^{penalty}}{u_1^{Lagrange}} = 1 + \frac{1}{2\beta} + \frac{1}{2\beta} = 1 + \frac{1}{\beta} \qquad \frac{u_2^{penalty}}{u_2^{Lagrange}} = 1 + \frac{f_3}{2\beta f_2} \tag{21}$$

The other option is to set $\gamma_1 = 2\beta f_1$ and $\gamma_2 = \beta f_3$, favoring a simple relation for the DOF 2.

$$\frac{u_1^{penalty}}{u_1^{Lagrange}} = 1 + \frac{1}{2\beta} + \frac{f_2}{\beta f_3} \qquad \frac{u_2^{penalty}}{u_2^{Lagrange}} = 1 + \frac{1}{\beta} \tag{22}$$

Clearly a conflict arises about the value of the penalty parameter γ_2. A reasonable way to address this issue is to compare the two possible values for γ_2 and to choose the greater. Thus, the accuracy for one DOF is directly proportional to β as desired, and the precision of the other one should be slightly higher.

As discussed previously, one of the objectives of this study is to establish an automatic choice of the optimal penalty parameter. The investigations of the ratio between the solutions based on Lagrange multipliers and the penalty method constitute the basis for pursuing this goal. Nevertheless, it should be underlined that an exact value of the penalty parameter is not required. Rather, a value that is of the right order of magnitude is sufficient. In fact, even in the most complex FE analysis, there exists a range of values for this parameter for which the numerical outcomes change very little. This range can equal as much as 12 orders of magnitude for simple analyses, but usually is not less than two orders of magnitude in most situations.

2.4 Automatic Round-Off Error Control

Several terms describe the magnitude of rounding error, due to the machine-dependent precision of the floating-point arithmetic. A floating-point approximation to a real constant or to a computed result may err by as much as 1/2 unit in the last place, the b_{P-1} bit, where P is the mantissa bit. The abbreviation *ULP* represents the measure "unit

in the last place." Another measure of the rounding error uses the relative error, which is the difference between the exact number and its approximation divided by the exact number. The relative error that corresponds to 1/2 *ULP* is bounded by:

$$\frac{1}{2}\cdot 2^{-P} \le \frac{1}{2}\cdot ULP \le 2^{-P} \tag{23}$$

The upper bound $ESP = 2^{-P}$, the machine epsilon, is commonly used in discussions of rounding errors because it expresses the smallest floating-point number that you can add to 1.0 with a result that does not round to 1.0.

Additional guard bits are included in floating-point hardware to allow rounding on the order of *EPS*. The result of any one floating-point operation is therefore tolerably imprecise, but the total error that results from many such operations on propagated numbers accumulates unavoidably.

Due to finite precision in floating-point arithmetic used when the interface element stiffness matrix is numerically integrated, the stiffness coefficients are always approximated. However, in order to be imposed correctly (and to contribute no energy to the system), the displacement continuity constraint $(V-u)$ requires the sum of the terms in every row of its stiffness matrix (15) to be zero. This condition usually cannot be achieved, due to the round-off error, and the resulting inaccuracy grows with the value of the penalty parameter. Precisely, the important measure is the ratio between the order of magnitude of the interface element stiffness matrix rows' imbalance and the element stiffness. If K_n is the stiffness associated to the *n*-th nodal DOF, it is sufficient to consider the ratio:

$$Q_n = \frac{ER_n}{K_n} \tag{24}$$

where EI

DOF n.

W

appreciabl

parameter.

Acc

steps can b

- Stiffnes

  known

- For each

  c

  c

  c

- The hig

  $1 \cdot 10^{-}$

- If $Q >$

- The in

  Th

solution.

where ER_n is the unbalance in the interface element stiffness matrix row related to the DOF *n*.

$$ER_n = \sum_j K_{nj} \tag{25}$$

When the value of Q_n exceeds about $1 \cdot 10^{-4}$, errors in the solution may become appreciable. The discussed row imbalance is proportional to the value of the penalty parameter, $ER_n \propto \gamma$. It is also approximately true that:

$$ER_n \propto \gamma \propto \beta \cdot K_n \quad \Rightarrow \quad Q_n \propto \beta \tag{26}$$

Accordingly, an algorithm has been developed to control the round-off error. Its steps can be summarized as follows:

- Stiffness terms for every nodal DOF in the interface element are computed from known geometrical and material properties.
- For each row in the stiffness matrix:
    - The highest stiffness term is selected and assigned to a variable K
    - The row imbalance of the stiffness matrix is stored in a variable ER
    - $Q = \frac{ER}{K}$ is evaluated
- The highest Q found is compared to a given constant value C. Typically $C = 1 \cdot 10^{-7}$ is used.
- If $Q > C$, the parameter β is reduced according to: $\beta^{new} = \frac{C}{Q} \cdot \beta$
- The interface element stiffness matrix is recalculated using the new value $\beta = \beta^{new}$.

This approach reduces the risk that round-off errors could adversely affect the solution. Thus, the initial value of β can be increased, in order to get a higher degree of

accuracy, knowing that it will be automatically reduced if rounding errors don't allow that precision to be realized.

2.5 Implementation as Abaqus User Element Subroutine

To test the behavior of the penalty method based "interface" element and the accuracy of the obtained relations for an automatic choice of the penalty parameters, the element has been implemented in the commercial finite element code ABAQUS as a User Element Subroutine (UEL) [39].

The UEL subroutine receives all the necessary information about geometry and material properties of the two connected meshes of finite elements from the input file. Then, the stiffness matrix of the interface element is built as previously defined:

$$\begin{bmatrix} G_1^{tt} & -G_1^{ts} & 0 \\ -G_1^{st} & G_1^{ss}+G_2^{ss} & -G_2^{st} \\ 0 & -G_2^{ts} & G_2^{tt} \end{bmatrix} \tag{27}$$

The appropriate values of penalty parameters for each constraint are assigned automatically inside the subroutine.

CHAPTER 3 TIMOSHENKO BEAM

In this chapter the Hybrid Interface Method and the Penalty Frame Method are applied to connect Timoshenko beam elements. The first goal is to define the stiffness matrix that could be associated with an interface element able to accomplish the link. The Hybrid Interface Method defines the upper limit to the accuracy of the Penalty Frame Method and lets us explore the relation between the Lagrange multiplier and the penalty parameter for the Timoshenko beam elements.

Very simple problems are studied in order to pursue our objectives. FE analyses involving axial and bending loads are considered separately. Problems related to flexural DOFs are modeled both with conventionally formulated FEM of the Timoshenko beam and with a Reduced Integrated Element.

3.1 Extensional Load – One Element

The first problem to be studied is one of the simplest available: the extension of a beam under a uniform load P applied at the tip. This case is analyzed using a single linear beam element connected to one fixed point V by a displacement continuity constraint, which is imposed through a Lagrange multiplier or a Penalty parameter. The configuration of the geometry and the mesh is plotted in Figure 2.

Fig

3.1

pote

Thu

whe

disp

where

forces

If the

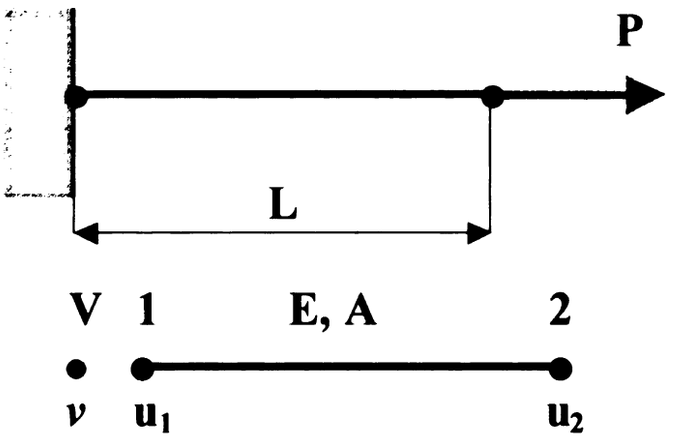

Figure 2. ***Beam under an axial load applied at the tip – One Element***

3.1.1 Lagrange Multiplier Method

The hybrid interface method introduces a Lagrange multiplier λ_1 in the total potential energy (TPE) of the system to satisfy the displacement continuity condition. Thus the TPE of the system in this study assumes the following form.

$$\pi = \pi_1 + \lambda_1 \cdot (v - u_1) - r_1 \cdot v \tag{28}$$

where π_1 is the TPE of the bar; r_1 and v are, respectively, the reaction force and the displacement at point V. Expanding and simplifying:

$$\pi = \int_V \frac{1}{2}(\sigma_x \cdot \varepsilon_x) dV - \sum_{i=1}^{2} f_i \cdot u_i + \lambda_1 \cdot (v - u_1) - r_1 \cdot v \tag{29}$$

$$\pi = \frac{1}{2} \cdot \int_0^L EA\left(\frac{du}{dx}\right)^2 dx - \sum_{i=1}^{2} f_i \cdot u_i + \lambda_1 \cdot (v - u_1) - r_1 \cdot v \tag{30}$$

where E is the Young's modulus, A is the cross sectional area and f_i are the applied nodal forces.

If the displacements are approximated linearly by:

π takes the

Setting to z

following e

Thus, the re

Since V is

$$u = \sum_{J=1}^{2} u_J N_J = u_1\left(1 - \frac{x}{L}\right) + u_2\left(\frac{x}{L}\right) \tag{31}$$

π takes the following form.

$$\pi = \frac{EA}{2} \cdot \int_0^L \left(\sum_I u_I \frac{dN_I}{dx}\right)\left(\sum_J u_J \frac{dN_J}{dx}\right) dx - P \cdot u_2 + \lambda_1 \cdot (v - u_1) - r_1 \cdot v \tag{32}$$

Setting to zero the first variation of π, taken with respect all the DOFs, produces the following equations.

$$\frac{\partial \pi}{\partial u_1} = EA \cdot \int_0^L \left(\frac{dN_1}{dx}\right)\left(\sum_J u_J \frac{dN_J}{dx}\right) dx - \lambda_1 = 0 \tag{33}$$

$$\frac{\partial \pi}{\partial u_2} = EA \cdot \int_0^L \left(\frac{dN_2}{dx}\right)\left(\sum_J u_J \frac{dN_J}{dx}\right) dx - P = 0 \tag{34}$$

$$\frac{\partial \pi}{\partial v} = \lambda_1 - r_1 = 0 \tag{35}$$

$$\frac{\partial \pi}{\partial \lambda_1} = v - u_1 = 0 \tag{36}$$

Thus, the resulting FE model is:

$$\begin{bmatrix} \frac{EA}{L} & -\frac{EA}{L} & 0 & -1 \\ -\frac{EA}{L} & \frac{EA}{L} & 0 & 0 \\ 0 & 0 & 0 & 1 \\ -1 & 0 & 1 & 0 \end{bmatrix} \begin{Bmatrix} u_1 \\ u_2 \\ v \\ \lambda_1 \end{Bmatrix} = \begin{Bmatrix} 0 \\ P \\ r_1 \\ 0 \end{Bmatrix} \tag{37}$$

Since V is fixed, $v = 0$, and the solution is found to be:

$$r_1 = \lambda_1 = -P \tag{38}$$

$$u_1 = v = 0 \tag{39}$$

$$u_2 = \frac{PL}{EA} \tag{40}$$

The solut

one.

3.1.2 P

In

penalty pa

Approxima

$$\pi = \frac{F}{}$$

The first va

parameter.

The resul

The solution provided by the hybrid interface method coincides with the exact theoretical one.

3.1.2 Penalty Method

In the penalty method the displacement continuity constraint is imposed through a penalty parameter γ_1. Therefore the TPE of the system takes the form:

$$\pi = \pi_1 + \frac{1}{2}\gamma_1 \cdot (v - u_1)^2 - r_1 \cdot v \tag{41}$$

$$\pi = \int_V \frac{1}{2}(\sigma_x \cdot \varepsilon_x)\, dV - \sum_{i=1}^{2} f_i \cdot u_i + \frac{1}{2}\gamma_1 \cdot (v - u_1)^2 - r_1 \cdot v \tag{42}$$

$$\pi = \frac{1}{2} \cdot \int_0^L EA\left(\frac{du}{dx}\right)^2 dx - \sum_{i=1}^{2} f_i \cdot u_i + \frac{1}{2}\gamma_1 \cdot (v - u_1)^2 - r_1 \cdot v \tag{43}$$

Approximating the displacements linearly:

$$\pi = \frac{EA}{2} \cdot \int_0^L \left(\sum_i u_i \frac{dN_i}{dx}\right)\left(\sum_j u_j \frac{dN_j}{dx}\right) dx - P \cdot u_2 + \frac{1}{2}\gamma_1 \cdot (v - u_1)^2 - r_1 \cdot v \tag{44}$$

The first variation of π in this case is taken with respect all the DOFs, but not the penalty parameter.

$$\frac{\partial \pi}{\partial u_1} = EA \cdot \int_0^L \left(\frac{dN_1}{dx}\right)\left(\sum_j u_j \frac{dN_j}{dx}\right) dx - \gamma_1 \cdot (v - u_1) = 0 \tag{45}$$

$$\frac{\partial \pi}{\partial u_2} = EA \cdot \int_0^L \left(\frac{dN_2}{dx}\right)\left(\sum_j u_j \frac{dN_j}{dx}\right) dx - P = 0 \tag{46}$$

$$\frac{\partial \pi}{\partial v} = \gamma_1 \cdot (v - u) - r_1 = 0 \tag{47}$$

The resulting FE model is:

Solv

3.1.3

tends

Moreo

If we

Possibl

penalty

$$\begin{bmatrix} \frac{EA}{L}+\gamma_1 & -\frac{EA}{L} & -\gamma_1 \\ -\frac{EA}{L} & \frac{EA}{L} & 0 \\ -\gamma_1 & 0 & \gamma_1 \end{bmatrix} \begin{Bmatrix} u_1 \\ u_2 \\ v \end{Bmatrix} = \begin{Bmatrix} 0 \\ P \\ r_1 \end{Bmatrix} \tag{48}$$

Solving the system of equations:

$$r_1 = -P \tag{49}$$

$$u_1 = \frac{P}{\gamma_1} \tag{50}$$

$$u_2 = \left(\frac{1}{\gamma_1}+\frac{L}{EA}\right)P \tag{51}$$

3.1.3 Comparison between the Two Methods

When the penalty parameter approaches infinity, the penalty method solution tends to the one obtained using the Lagrange multiplier method.

$$\underset{\gamma_1\to\infty}{Limit}\, u_1 = \underset{\gamma_1\to\infty}{Limit}\frac{P}{\gamma_1} = 0 \tag{52}$$

$$\underset{\gamma_1\to\infty}{Limit}\, u_2 = \underset{\gamma_1\to\infty}{Limit}\left(\frac{1}{\gamma_1}+\frac{L}{EA}\right)P = \left(\frac{L}{EA}\right)P \tag{53}$$

Moreover, the constraint that has been enforced is:

$$C_1(u_1,u_2,v) = (v-u_1) \tag{54}$$

If we define $u_{1\gamma}, u_{2\gamma}, v_\gamma$ as the solutions derived from the penalty formulation, it is possible to verify the well-known relation between the Lagrange multiplier and the penalty parameter.

$$\lambda_1 = \gamma_1 \cdot C_1\left(u_{1\gamma}, u_{2\gamma}, v_\gamma\right) = \gamma_1 \cdot \left(v_\gamma - u_{1\gamma}\right) = \gamma_1 \cdot \left[0 - \frac{P}{\gamma_1}\right] = -P \tag{55}$$

3.1.4 Relation between Penalty Parameter and Beam Properties

In this section the obtained solutions are investigated in order to find a relation between material and geometrical properties of the beam and the penalty parameter.

As underlined previously, the exact displacement of the tip of the beam matches that from the Lagrange multiplier finite element formulation.

$$u_2^{exact} = \frac{L}{EA} P \tag{56}$$

The Penalty parameter solution $u_2^{penalty}$ differs from the exact one by the presence of an additional term $\left(P/\gamma_1\right)$:

$$u_2^{penalty} = \left(\frac{1}{\gamma_1} + \frac{L}{EA}\right) P \tag{57}$$

The ratio $u_2^{penalty} / u_2^{exact}$ is evaluated in order to identify the relationship between the two solutions:

$$\frac{u_2^{penalty}}{u_2^{exact}} = \frac{\left(\frac{1}{\gamma_1} + \frac{L}{EA}\right) P}{\left(\frac{L}{EA}\right) P} = 1 + \frac{\left(\frac{EA}{L}\right)}{\gamma_1} \tag{58}$$

The penalty parameter γ_1 is now substituted by:

$$\gamma_1 = \beta \cdot \left(\frac{EA}{L}\right) \tag{59}$$

It follows that the ratio between the solutions becomes independent of material and geometrical properties of the beam.

$$\frac{u_2^{penalty}}{u_2^{exact}} = 1 + \frac{1}{\beta} \tag{60}$$

As underlined in the previous chapter, the accuracy of the solution comes to depend directly on the value assigned to the parameter β. For example if β is equal to 1000 the Penalty solution will differ from that obtained by use of the Lagrange multipliers by 0.1%. The degree of precision of the solution cannot be indefinitely increased, since round off amplification error would rise.

3.2 Extensional Load – Two Elements

The previous analysis has been modified in order to analyze the imposition of a continuity constraint between two beams elements.

Two linear beams elements are connected using a Lagrange multiplier or a Penalty parameter continuity constraint. The configuration of the geometry and the mesh is depicted in Figure 3.

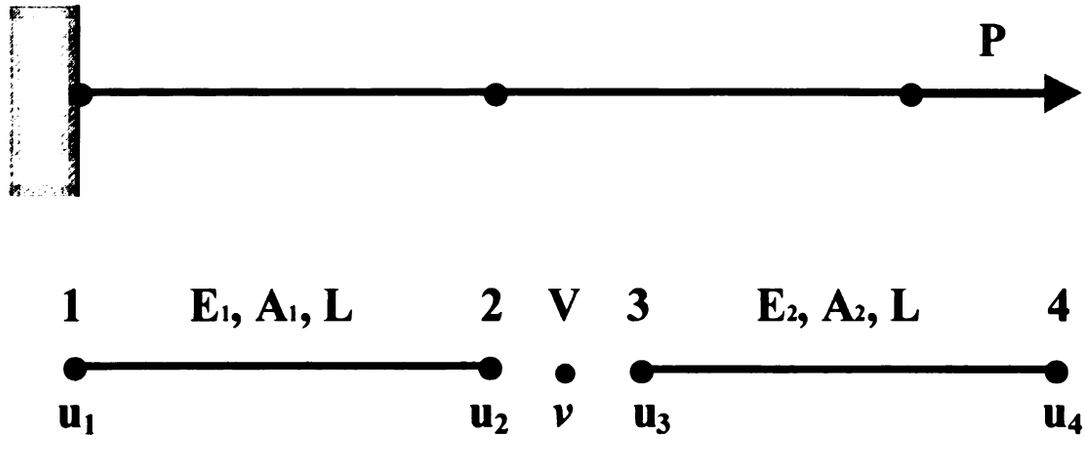

Figure 3. ***Beam under an axial load applied at the tip – Two Elements***

3.2.1

The tot

Where

$$\pi$$

$$\pi = \frac{1}{2}$$

$$\pi = \frac{1}{2}$$

Displace

Substitut

$$\pi = \frac{E}{}$$

Setting th

3.2.1 Lagrange Multiplier Method

The total potential energy of the system π is:

$$\pi = \pi_1 + \pi_2 + \lambda_1 \cdot (v - u_2) + \lambda_2 \cdot (v - u_3) \tag{61}$$

Where π_1, π_2 are, respectively, the TPE of the first and of the second bar.

$$\pi = \int_{V_1} \frac{1}{2}(\sigma_x \cdot \varepsilon_x)\, dV + \int_{V_2} \frac{1}{2}(\sigma_x \cdot \varepsilon_x)\, dV - \sum_{i=1}^{4} f_i \cdot u_i + \lambda_1 \cdot (v - u_2) + \lambda_2 \cdot (v - u_3) \tag{62}$$

$$\pi = \frac{1}{2} \cdot \int_0^{L} E_1 A_1 \left(\frac{du}{dx}\right)^2 dx + \frac{1}{2} \cdot \int_{L}^{2L} E_2 A_2 \left(\frac{du}{dx}\right)^2 dx - \sum_{i=1}^{4} f_i \cdot u_i + \lambda_1 \cdot (v - u_2) + \lambda_2 \cdot (v - u_3) \tag{63}$$

$$\pi = \frac{1}{2} \cdot \int_0^{L} E_1 A_1 \left(\frac{du}{dx}\right)^2 dx + \frac{1}{2} \cdot \int_{L}^{2L} E_2 A_2 \left(\frac{du}{dx}\right)^2 dx - \sum_{i=1}^{4} f_i \cdot u_i + \lambda_1 \cdot (v - u_2) + \lambda_2 \cdot (v - u_3) \tag{64}$$

Displacements are approximated linearly.

$$u = \sum_{j=1}^{2} u_j N_j = u_1 \left(1 - \frac{x}{L}\right) + u_2 \left(\frac{x}{L}\right) \tag{65}$$

Substituting:

$$\pi = \frac{E_1 A_1}{2} \cdot \int_0^{L} \left(\sum_i u_i \frac{dN_i}{dx}\right)\left(\sum_j u_j \frac{dN_j}{dx}\right) dx + \frac{E_2 A_2}{2} \cdot \int_{L}^{2L} \left(\sum_i u_i \frac{dN_i}{dx}\right)\left(\sum_j u_j \frac{dN_j}{dx}\right) dx - \\ - P \cdot u_4 + \lambda_1 \cdot (v - u_2) + \lambda_2 \cdot (v - u_3) \tag{66}$$

Setting the first variation with respect all the DOF to zero we get:

$$\frac{\partial \pi}{\partial u_1} = E_1 A_1 \cdot \int_0^{L} \left(\frac{dN_1}{dx}\right)\left(\sum_j u_j \frac{dN_j}{dx}\right) dx = 0 \tag{67}$$

$$\frac{\partial \pi}{\partial u_2} = E_1 A_1 \cdot \int_0^{L} \left(\frac{dN_2}{dx}\right)\left(\sum_j u_j \frac{dN_j}{dx}\right) dx - \lambda_1 = 0 \tag{68}$$

$$\frac{\partial \pi}{\partial u_3} = E_2 A_2 \cdot \int_0^{L} \left(\frac{dN_1}{dx}\right)\left(\sum_j u_j \frac{dN_j}{dx}\right) dx - \lambda_2 = 0 \tag{69}$$

$$\frac{\partial \pi}{\partial u_4} = E_2 A_2 \cdot \int_0^{l_2} \left(\frac{dN_2}{dx} \right) \left(\sum_j u_j \frac{dN_j}{dx} \right) dx - P = 0 \tag{70}$$

$$\frac{\partial \pi}{\partial v} = \lambda_1 + \lambda_2 = 0 \tag{71}$$

$$\frac{\partial \pi}{\partial \lambda_1} = v - u_2 = 0, \quad \frac{\partial \pi}{\partial \lambda_2} = v - u_3 = 0 \tag{72}$$

The resulting FE model is:

$$\begin{bmatrix} \frac{E_1 A_1}{L} & -\frac{E_1 A_1}{L} & 0 & 0 & 0 & 0 & 0 \\ -\frac{E_1 A_1}{L} & \frac{E_1 A_1}{L} & 0 & 0 & 0 & -1 & 0 \\ 0 & 0 & \frac{E_2 A_2}{L} & -\frac{E_2 A_2}{L} & 0 & 0 & -1 \\ 0 & 0 & -\frac{E_2 A_2}{L} & \frac{E_2 A_2}{L} & 0 & 0 & 0 \\ 0 & 0 & 0 & 0 & 0 & 1 & 1 \\ 0 & -1 & 0 & 0 & 1 & 0 & 0 \\ 0 & 0 & -1 & 0 & 1 & 0 & 0 \end{bmatrix} \begin{Bmatrix} 0 \\ u_2 \\ u_3 \\ u_4 \\ v \\ \lambda_1 \\ \lambda_2 \end{Bmatrix} = \begin{Bmatrix} f_1 \\ 0 \\ 0 \\ P \\ 0 \\ 0 \\ 0 \end{Bmatrix} \tag{73}$$

Solving this system of equations:

$$f_1 = -P \tag{74}$$

$$\lambda_1 = P \tag{75}$$

$$\lambda_2 = -P \tag{76}$$

$$u_2 = u_3 = v = \frac{L}{E_1 A_1} P \tag{77}$$

$$u_4 = \frac{L}{E_1 A_1} P + \frac{L}{E_2 A_2} P \tag{78}$$

3.2.2 Penalty Method

In the penalty method the displacement continuity constraint is imposed through

two penalty parameters γ_1 and γ_2. Thus the TPE of the system in this study changes its form.

$$\pi = \pi_1 + \pi_2 + \frac{1}{2}\gamma_1 \cdot (v - u_2)^2 + \frac{1}{2}\gamma_2 \cdot (v - u_3)^2 \tag{79}$$

where π_1, π_2 are, respectively, the TPE of the first and of the second bar.

$$\pi = \int_{V_1} \frac{1}{2}(\sigma_x \cdot \varepsilon_x) dV + \int_{V_2} \frac{1}{2}(\sigma_x \cdot \varepsilon_x) dV - \sum_{i=1}^{4} f_i \cdot u_i + \frac{1}{2}\gamma_1 \cdot (v - u_2)^2 + \frac{1}{2}\gamma_2 \cdot (v - u_3)^2 \tag{80}$$

$$\pi = \frac{1}{2} \cdot \int_0^{L} E_1 A_1 \left(\frac{du}{dx}\right)^2 dx + \frac{1}{2} \cdot \int_{L}^{2L} E_2 A_2 \left(\frac{du}{dx}\right)^2 dx - \sum_{i=1}^{4} f_i \cdot u_i + \frac{1}{2}\gamma_1 \cdot (v - u_2)^2 + \frac{1}{2}\gamma_2 \cdot (v - u_3)^2 \tag{81}$$

The linear Lagrange interpolation functions are used.

$$u = \sum_{j=1}^{2} u_j N_j = u_1 \left(1 - \frac{x}{L}\right) + u_2 \left(\frac{x}{L}\right) \tag{82}$$

Substituting:

$$\pi = \frac{E_1 A_1}{2} \cdot \int_0^{L} \left(\sum_i u_i \frac{dN_i}{dx}\right)\left(\sum_j u_j \frac{dN_j}{dx}\right) dx + \frac{E_2 A_2}{2} \cdot \int_{L}^{2L} \left(\sum_i u_i \frac{dN_i}{dx}\right)\left(\sum_j u_j \frac{dN_j}{dx}\right) dx - P \cdot u_4 + \frac{1}{2}\gamma_1 \cdot (v - u_2)^2 + \frac{1}{2}\gamma_2 \cdot (v - u_3)^2 \tag{83}$$

The first variations of π assume the subsequent forms:

$$\frac{\partial \pi}{\partial u_1} = E_1 A_1 \cdot \int_0^{L} \left(\frac{dN_1}{dx}\right)\left(\sum_j u_j \frac{dN_j}{dx}\right) dx = 0 \tag{84}$$

$$\frac{\partial \pi}{\partial u_2} = E_1 A_1 \cdot \int_0^{L} \left(\frac{dN_2}{dx}\right)\left(\sum_j u_j \frac{dN_j}{dx}\right) dx - \gamma_1 \cdot (v - u_2) = 0 \tag{85}$$

$$\frac{\partial \pi}{\partial u_3} = E_2 A_2 \cdot \int_0^{L} \left(\frac{dN_1}{dx}\right)\left(\sum_j u_j \frac{dN_j}{dx}\right) dx - \gamma_2 \cdot (v - u_3) = 0 \tag{86}$$

$$\frac{\partial \pi}{\partial u_4} = E_2 A_2 \cdot \int_0^{l_2} \left(\frac{dN_2}{dx} \right) \left(\sum_J u_J \frac{dN_J}{dx} \right) dx - P = 0 \tag{87}$$

$$\frac{\partial \pi}{\partial v} = \gamma_1 \cdot (v - u_2) + \gamma_2 \cdot (v - u_3) = 0 \tag{88}$$

Thus, the FE model is determined.

$$\begin{bmatrix} \frac{E_1 A_1}{L} & -\frac{E_1 A_1}{L} & 0 & 0 & 0 \\ -\frac{E_1 A_1}{L} & \frac{E_1 A_1}{L} + \gamma_1 & 0 & 0 & -\gamma_1 \\ 0 & 0 & \frac{E_2 A_2}{L} + \gamma_2 & -\frac{E_2 A_2}{L} & -\gamma_2 \\ 0 & 0 & -\frac{E_2 A_2}{L} & \frac{E_2 A_2}{L} & 0 \\ 0 & -\gamma_1 & -\gamma_2 & 0 & \gamma_1 + \gamma_2 \end{bmatrix} \begin{Bmatrix} 0 \\ u_2 \\ u_3 \\ u_4 \\ v \end{Bmatrix} = \begin{Bmatrix} f_1 \\ 0 \\ 0 \\ P \\ 0 \end{Bmatrix} \tag{89}$$

The solution to this system of equations takes the following form:

$$f_1 = -P \tag{90}$$

$$u_2 = \frac{L}{E_1 A_1} P \tag{91}$$

$$v = \left(\frac{1}{\gamma_1} + \frac{L}{E_1 A_1} \right) P \tag{92}$$

$$u_3 = \left(\frac{L}{E_1 A_1} + \frac{1}{\gamma_1} + \frac{1}{\gamma_2} \right) P \tag{93}$$

$$u_4 = \left(\frac{L}{E_1 A_1} + \frac{1}{\gamma_1} \right) P + \left(\frac{L}{E_2 A_2} + \frac{1}{\gamma_2} \right) P \tag{94}$$

3.2.3 Comparison between the Two Methods

The convergence to the Lagrange solution when penalty parameters approach infinite is verified.

$$\underset{\gamma_1\to\infty}{Limit}\, v = \underset{\gamma_1\to\infty}{Limit}\left(\frac{1}{\gamma_1}+\frac{L}{E_1A_1}\right)P = \left(\frac{L}{E_1A_1}\right)P \tag{95}$$

$$\underset{\gamma_1,\gamma_2\to\infty}{Limit}\, u_3 = \underset{\gamma_1,\gamma_2\to\infty}{Limit}\left(\frac{L}{E_1A_1}+\frac{1}{\gamma_1}+\frac{1}{\gamma_2}\right)P = \left(\frac{L}{E_1A_1}\right)P \tag{96}$$

$$\underset{\gamma_1,\gamma_2\to\infty}{Limit}\, u_4 = \underset{\gamma_1,\gamma_2\to\infty}{Limit}\left(\frac{L}{E_1A_1}+\frac{1}{\gamma_1}\right)P+\left(\frac{L}{E_2A_2}+\frac{1}{\gamma_2}\right)P = \left(\frac{L}{E_1A_1}+\frac{L}{E_2A_2}\right)P \tag{97}$$

The constraints we have enforced are:

$$\begin{aligned} G_1\left(u_1,u_2,u_3,u_4,v\right) &= \left(v-u_2\right) \\ G_2\left(u_1,u_2,u_3,u_4,v\right) &= \left(v-u_3\right) \end{aligned} \tag{98}$$

Then, as in the previous paragraph, if we define $u_{1\gamma},u_{2\gamma},u_{3\gamma},u_{4\gamma},v_\gamma$ as the solutions derived from the Penalty formulation, it is possible to verify the well-known relation between the Lagrange multipliers and the penalty parameters:

$$\lambda_1 = \gamma_1\cdot G_1\left(u_{1\gamma},u_{2\gamma},u_{3\gamma},u_{4\gamma},v_\gamma\right) = \gamma_1\cdot\left(v_\gamma-u_{2\gamma}\right) = \gamma_1\cdot\left[\left(\frac{1}{\gamma_1}+\frac{L}{E_1A_1}\right)P-\frac{L}{E_1A_1}P\right] = P \tag{99}$$

$$\begin{aligned} \lambda_2 &= \gamma_2\cdot G_2\left(u_{1\gamma},u_{2\gamma},u_{3\gamma},u_{4\gamma},v_\gamma\right) = \gamma_2\cdot\left(v_\gamma-u_{3\gamma}\right) = \\ &= \gamma_2\cdot\left[\left(\frac{1}{\gamma_1}+\frac{L}{E_1A_1}\right)P-\left(\frac{1}{\gamma_1}+\frac{L}{E_1A_1}+\frac{1}{\gamma_2}\right)P\right] = -P \end{aligned} \tag{100}$$

3.2.4 Relation between Penalty Parameter and Beam Properties

Like in the single beam case, the exact theoretical displacement of the tip of the beam matches that from the Lagrange multiplier finite element formulation.

$$u_4^{exact} = \frac{L}{E_1A_1}P+\frac{L}{E_2A_2}P \tag{101}$$

The Penalty parameter solution $u_4^{penalty}$ differs from the exact one due to the presence of

two additional terms (P/γ_1) and (P/γ_2).

$$u_4^{penalty} = \left(\frac{L}{E_1 A_1} + \frac{1}{\gamma_1}\right)P + \left(\frac{L}{E_2 A_2} + \frac{1}{\gamma_2}\right)P \tag{102}$$

The ratio of $u_4^{penalty}$ to u_4^{exact} is evaluated in order to underline the dependencies between the two solutions.

$$\frac{u_4^{penalty}}{u_4^{exact}} = \frac{\left(\frac{L}{E_1 A_1} + \frac{1}{\gamma_1}\right)P + \left(\frac{L}{E_2 A_2} + \frac{1}{\gamma_2}\right)P}{\left(\frac{L}{E_1 A_1} + \frac{L}{E_2 A_2}\right)P} = 1 + \frac{\left(\frac{1}{\gamma_1} + \frac{1}{\gamma_2}\right)}{\left(\frac{L}{E_1 A_1} + \frac{L}{E_2 A_2}\right)} \tag{103}$$

Now, if the penalty parameters γ_1 and γ_2 are substituted by:

$$\gamma_1 = \beta \cdot \left(\frac{E_1 A_1}{L}\right) \tag{104}$$

$$\gamma_2 = \beta \cdot \left(\frac{E_2 A_2}{L}\right) \tag{105}$$

the ratio between the solutions becomes independent of material and geometrical properties of the beams.

$$\frac{u_4^{penalty}}{u_4^{exact}} = 1 + \frac{2}{\beta} \tag{106}$$

3.3 Bending Loads – One Element – Full Integration

The conventionally formulated linear finite element model of the Timoshenko beam is generally not used in commercial finite element codes due to its shear locking behavior. Instead, a Consistent Interpolation Element (CIE) or Reduced Integration Element (RIE) is adopted. For this reason, only the 1 element case is studied with a

conventional FE formulation. The purpose is to compare the results with those generated by the Reduced Integration Element.

Now, we will focus our attention on the deflection of a beam under typical bending loads: transversely distributed load F, concentrated moment M and concentrated force Q applied at the tip.

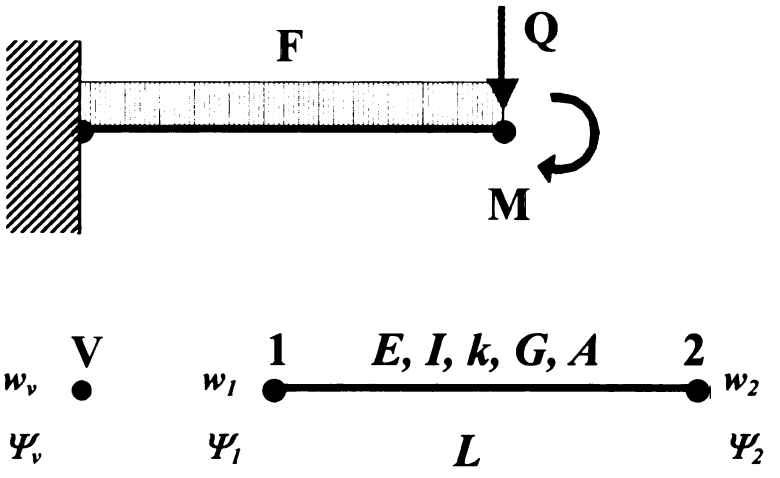

Figure 4. ***Beam under bending loads – One Element***

This case is analyzed using a single linear Timoshenko beam element connected to one fixed point V by a displacement continuity constraint; this is imposed through a Lagrange multiplier or a Penalty parameter. The configuration of the geometry and the mesh is depicted in Figure 4.

3.3.1 Lagrange Multipliers Method

The hybrid interface method introduces two Lagrange multipliers λ_1 and λ_2 in the total potential energy (TPE) of the system to satisfy the continuity conditions for transverse displacement and rotation. Thus the TPE of the system in this study assumes the following form.

$$\pi = \pi_1 + \lambda_1 \cdot (w_v - w_1) + \lambda_2 \cdot (\Psi_v - \Psi_1) - r_1 \cdot w_v - m_1 \cdot \Psi_v \tag{107}$$

Where π_1 is the TPE of the bar; r_1 and m_1 are, respectively, the vertical reaction force and the reaction moment at V.

$$\pi_1 = \frac{1}{2}\int_0^L \left[EI\left(\frac{\partial \Psi}{\partial x}\right)^2 + kGA\left(\Psi + \frac{\partial w}{\partial x}\right)^2 \right] dx - \int_0^L [F \cdot w]\, dx - \sum_{i=1}^{2} Q_i \cdot w_i - \sum_{i=1}^{2} M_i \cdot \Psi_i \tag{108}$$

The first variations of π_1 take the following form.

$$\begin{aligned} \delta\pi_1 = & \int_0^L \left[EI\left(\frac{\partial \Psi}{\partial x}\right)\frac{\partial \delta\Psi}{\partial x} + kGA\left(\Psi + \frac{\partial w}{\partial x}\right)\left(\delta\Psi + \frac{\partial \delta w}{\partial x}\right) \right] dx - \\ & \int_0^L (F \cdot \delta w)\, dx - \sum_{i=1}^{2} Q_i \cdot w_i - \sum_{i=1}^{2} M_i \cdot \Psi_i \end{aligned} \tag{109}$$

The Lagrange linear interpolation functions are used.

$$w = \sum_{j=1}^{2} w_j N_j = w_1\left(1 - \frac{x}{L}\right) + w_2\left(\frac{x}{L}\right) \tag{110}$$

$$\Psi = \sum_{j=1}^{2} \Psi_j N_j = \Psi_1\left(1 - \frac{x}{L}\right) + \Psi_2\left(\frac{x}{L}\right) \tag{111}$$

Thus, π_1 can be written:

$$\begin{aligned} & \delta\pi_1 = \\ & \int_0^L \left\{ EI\left(\sum_j \Psi_j \frac{dN_j}{dx}\right)\left(\sum_i \delta\Psi_i \frac{dN_i}{dx}\right) + kGA\left(\sum_j \Psi_j N_j + \sum_j w_j \frac{dN_j}{dx}\right)\left(\sum_i \delta\Psi_i \frac{dN_i}{dx}\right) \right\} dx + \\ & + \int_0^L \left\{ kGA\left(\sum_j \Psi_j N_j + \sum_j w_j \frac{dN_j}{dx}\right)\left(\sum_i \delta w_i \frac{dN_i}{dx}\right) \right\} dx - \int_0^L \left(F \cdot \sum_i \delta w_i \cdot N_i \right) dx - \\ & - \sum_{i=1}^{2} Q_i \cdot w_i - \sum_{i=1}^{2} M_i \cdot \Psi_i \end{aligned} \tag{112}$$

Taking the first variation of π with respect all the DOFs and setting them to zero:

$$\frac{\partial \pi}{\partial w_1} = \int_0^L \left\{ kGA\left(\sum_j \Psi_j N_j \frac{dN_1}{dx} + \sum_j w_j \frac{dN_j}{dx}\frac{dN_1}{dx}\right) \right\} dx - \int_0^L (F \cdot N_1)\, dx - \lambda_1 = 0 \tag{113}$$

$$\frac{\partial \pi}{\partial \Psi_1} = \int_0^L \left\{ EI\left(\sum_J \Psi_J \frac{dN_J}{dx}\frac{dN_1}{dx} \right) + kGA\left(\sum_J \Psi_J N_J N_1 + \sum_J w_J \frac{dN_J}{dx} N_1 \right) \right\} dx - \lambda_2 = 0 \quad (114)$$

$$\frac{\partial \pi}{\partial w_2} = \int_0^L \left\{ kGA\left(\sum_J \Psi_J N_J \frac{dN_2}{dx} + \sum_J w_J \frac{dN_J}{dx}\frac{dN_2}{dx} \right) \right\} dx + \int_0^L (F \cdot N_2)\, dx + Q = 0 \quad (115)$$

$$\frac{\partial \pi}{\partial \Psi_2} = \int_0^L \left\{ EI\left(\sum_J \Psi_J \frac{dN_J}{dx}\frac{dN_2}{dx} \right) + kGA\left(\sum_J \Psi_J N_J N_2 + \sum_J w_J \frac{dN_J}{dx} N_2 \right) \right\} dx - M = 0 \quad (116)$$

$$\frac{\partial \pi}{\partial w_v} = \lambda_1 - r_1 = 0 \quad (117)$$

$$\frac{\partial \pi}{\partial \Psi_v} = \lambda_2 - m_1 = 0 \quad (118)$$

$$\frac{\partial \pi}{\partial \lambda_1} = w_v - w_1 = 0 \quad (119)$$

$$\frac{\partial \pi}{\partial \lambda_2} = \Psi_v - \Psi_1 = 0 \quad (120)$$

Then, the resulting FE model is:

$$\begin{bmatrix} \frac{kAG}{L} & -\frac{kAG}{2} & -\frac{kAG}{L} & -\frac{kAG}{2} & 0 & 0 & -1 & 0 \\ -\frac{kAG}{2} & \frac{EI}{L}+\frac{kAGL}{3} & \frac{kAG}{2} & \frac{kAGL}{6}-\frac{EI}{L} & 0 & 0 & 0 & -1 \\ -\frac{kAG}{L} & \frac{kAG}{2} & \frac{kAG}{L} & \frac{kAG}{2} & 0 & 0 & 0 & 0 \\ -\frac{kAG}{2} & \frac{kAGL}{6}-\frac{EI}{L} & \frac{kAG}{2} & \frac{EI}{L}+\frac{kAGL}{3} & 0 & 0 & 0 & 0 \\ 0 & 0 & 0 & 0 & 0 & 0 & 1 & 0 \\ 0 & 0 & 0 & 0 & 0 & 0 & 0 & 1 \\ -1 & 0 & 0 & 0 & 1 & 0 & 0 & 0 \\ 0 & -1 & 0 & 0 & 0 & 1 & 0 & 0 \end{bmatrix} \cdot \begin{bmatrix} w_1 \\ \Psi_1 \\ w_2 \\ \Psi_2 \\ w_v \\ \Psi_v \\ \lambda_1 \\ \lambda_2 \end{bmatrix} = \begin{bmatrix} -\left(\frac{FL}{2}\right) \\ 0 \\ -Q-\left(\frac{FL}{2}\right) \\ M \\ r_1 \\ m_1 \\ 0 \\ 0 \end{bmatrix} \quad (121)$$

Taking into consideration that V is fixed ($w_v = 0$ and $\Psi_v = 0$), the system can be solved.

For the purposes of this study it is convenient to identify contribution to the solution

coming f

If only th

Instead, v

changes t

Finally,

coming from the three types of loads.

If only the concentrated moment M at the tip is present, the solution is:

$$w_1 = 0 \tag{122}$$

$$\Psi_1 = 0 \tag{123}$$

$$w_2 = -\frac{6ML^2}{12EI + kAGL^2} \tag{124}$$

$$\Psi_2 = \frac{12ML^2}{12EI + kAGL^2} \tag{125}$$

$$\lambda_1 = 0 \tag{126}$$

$$\lambda_2 = -M \tag{127}$$

Instead, when only the concentrated transverse load Q at the tip is applied, the solution changes to:

$$w_1 = 0 \tag{128}$$

$$\Psi_1 = 0 \tag{129}$$

$$w_2 = -\frac{\left(12EIL + 4kAGL^3\right)Q}{kAG\left(12EI + kAGL^2\right)} \tag{130}$$

$$\Psi_2 = \frac{6L^2Q}{\left(12EI + kAGL^2\right)} \tag{131}$$

$$\lambda_1 = Q \tag{132}$$

$$\lambda_2 = -LQ \tag{133}$$

Finally, a transversely distributed load F yields the following outcome.

$$w_1 = 0 \tag{134}$$

$$\Psi_1 = 0 \tag{135}$$

In

exact theo

3.3.2 Pe

In

through tw

becomes:

with π eq

$$\pi_i = \frac{1}{2}$$

The displ

Setting

$$w_2 = -\frac{\left(6EIL^2 + 2kAGL^4\right)F}{12EIkAG + \left(kAGL\right)^2} \tag{136}$$

$$\Psi_2 = \frac{3L^3F}{12EI + kAGL^2} \tag{137}$$

$$\lambda_1 = LF \tag{138}$$

$$\lambda_2 = -\frac{L^2F}{2} \tag{139}$$

In this case the solutions provided by the hybrid interface method are not the exact theoretical ones.

3.3.2 Penalty Method

In the penalty method the displacement continuity constraints are imposed through two penalty parameters γ_1 and γ_2. Thus the TPE of the system in this study becomes:

$$\pi = \pi_1 + \frac{1}{2}\gamma_1 \cdot \left(w_v - w_1\right)^2 + \frac{1}{2}\gamma_2 \cdot \left(\Psi_v - \Psi_1\right)^2 - r_1 \cdot w_v - m_1 \cdot \Psi_v \tag{140}$$

with π_1 equal to:

$$\pi_1 = \frac{1}{2}\int_0^L \left[EI\left(\frac{\partial \Psi}{\partial x}\right)^2 + kGA\left(\Psi + \frac{\partial w}{\partial x}\right)^2 \right] dx - \int_0^L [F \cdot w]dx - \sum_{i=1}^{2} Q_i \cdot w_i - \sum_{i=1}^{2} M_i \cdot \Psi_i \tag{141}$$

The displacements are approximated linearly:

$$w = \sum_{j=1}^{2} w_j N_j = w_1\left(1 - \frac{x}{L}\right) + w_2\left(\frac{x}{L}\right) \tag{142}$$

$$\Psi = \sum_{j=1}^{2} \Psi_j N_j = \Psi_1\left(1 - \frac{x}{L}\right) + \Psi_2\left(\frac{x}{L}\right) \tag{143}$$

Setting the first variation of π with respect to all the DOFs to zero we get:

$$\frac{\partial z}{\partial \Psi_2}$$

Then, th

$k4$
L
k
k
k
$($

Knowing

Concent

$$\frac{\partial \pi}{\partial w_1} = \int_0^L \left\{ kGA\left(\sum_j \Psi_j N_j \frac{dN_1}{dx} + \sum_j w_j \frac{dN_j}{dx}\frac{dN_1}{dx} \right) \right\} dx - \int_0^L (F \cdot N_1)\, dx - \gamma_1 \cdot (w_v - w_1) = 0 \quad (144)$$

$$\frac{\partial \pi}{\partial \Psi_1} = \int_0^L \left\{ EI\left(\sum_j \Psi_j \frac{dN_j}{dx}\frac{dN_1}{dx} \right) + kGA\left(\sum_j \Psi_j N_j N_1 + \sum_j w_j \frac{dN_j}{dx} N_1 \right) \right\} dx - \quad (145)$$
$$-\gamma_2 \cdot (\Psi_v - \Psi_1) = 0$$

$$\frac{\partial \pi}{\partial w_2} = \int_0^L \left\{ kGA\left(\sum_j \Psi_j N_j \frac{dN_2}{dx} + \sum_j w_j \frac{dN_j}{dx}\frac{dN_2}{dx} \right) \right\} dx + \int_0^L (F \cdot N_2)\, dx + Q = 0 \quad (146)$$

$$\frac{\partial \pi}{\partial \Psi_2} = \int_0^L \left\{ EI\left(\sum_j \Psi_j \frac{dN_j}{dx}\frac{dN_2}{dx} \right) + kGA\left(\sum_j \Psi_j N_j N_2 + \sum_j w_j \frac{dN_j}{dx} N_2 \right) \right\} dx - M = 0 \quad (147)$$

$$\frac{\partial \pi}{\partial w_v} = \gamma_1 \cdot (w_v - w_1) - r_1 = 0 \quad (148)$$

$$\frac{\partial \pi}{\partial \Psi_v} = \gamma_2 \cdot (\Psi_v - \Psi_1) - m_1 = 0 \quad (149)$$

Then, the resulting FE model is:

$$\begin{bmatrix} \frac{kAG}{L}+\gamma_1 & -\frac{kAG}{2} & -\frac{kAG}{L} & -\frac{kAG}{2} & -\gamma_1 & 0 \\ -\frac{kAG}{2} & \frac{EI}{L}+\frac{kAGL}{3}+\gamma_2 & \frac{kAG}{2} & \frac{kAGL}{6}-\frac{EI}{L} & 0 & \gamma_2 \\ -\frac{kAG}{L} & \frac{kAG}{2} & \frac{kAG}{L} & \frac{kAG}{2} & 0 & 0 \\ -\frac{kAG}{2} & \frac{kAGL}{6}-\frac{EI}{L} & \frac{kAG}{2} & \frac{EI}{L}+\frac{kAGL}{3} & 0 & 0 \\ -\gamma_1 & 0 & 0 & 0 & \gamma_1 & 0 \\ 0 & -\gamma_2 & 0 & 0 & 0 & \gamma_2 \end{bmatrix} \cdot \begin{bmatrix} w_1 \\ \Psi_1 \\ w_2 \\ \Psi_2 \\ w_v \\ \Psi_v \end{bmatrix} = \begin{bmatrix} -\left(\frac{FL}{2}\right) \\ 0 \\ -Q-\left(\frac{FL}{2}\right) \\ M \\ r_1 \\ m_1 \end{bmatrix} \quad (150)$$

Knowing that V is fixed ($w_v = 0$ and $\Psi_v = 0$), the system is solved.

Concentrated moment M:

$$w_1 = 0 \quad (151)$$

$$\Psi_1 = \frac{M}{\gamma_2} \tag{152}$$

$$w_2 = -\frac{\left(12EIL + kAGL^3 + 6L^2\gamma_2\right)M}{\left(12EI + kAGL^2\right)\gamma_2} \tag{153}$$

$$\Psi_2 = \frac{\left(12EI + kAGL^2 + 12L\gamma_2\right)M}{\left(12EI + kAGL^2\right)\gamma_2} \tag{154}$$

Concentrated transverse load Q:

$$w_1 = -\frac{Q}{\gamma_1} \tag{155}$$

$$\Psi_1 = -\frac{LQ}{\gamma_2} \tag{156}$$

$$w_2 = -\frac{\left[12EIL\gamma_1\gamma_2 + \left(kAGL\right)^2 \cdot \left(L^2\gamma_1 + \gamma_2\right) + 4kAG \cdot \left(3EIL^2\gamma_1 + 3EI\gamma_2 + L^3\gamma_1\gamma_2\right)\right]Q}{kAG\left(12EI + kAGL^2\right)\gamma_1\gamma_2} \tag{157}$$

$$\Psi_2 = \frac{\left(12EIL + kAGL^3 + 6L^2\gamma_2\right)Q}{\left(12EI + kAGL^2\right)\gamma_2} \tag{158}$$

Transversely distributed load F:

$$w_1 = -\frac{FL}{\gamma_1} \tag{159}$$

$$\Psi_1 = \frac{FL^2}{2\gamma_2} \tag{160}$$

$$w_2 = -\frac{\left[12EIL\gamma_1\gamma_2 + \left(kAGL\right)^2 \cdot \left(L^2\gamma_1 + 2\gamma_2\right) + 4kAG \cdot \left(3EIL^2\gamma_1 + 6EI\gamma_2 + L^3\gamma_1\gamma_2\right)\right]LQ}{2kAG\left(12EI + kAGL^2\right)\gamma_1\gamma_2} \tag{161}$$

$$\Psi_2 = \frac{\left(12EIL + kAGL^3 + 6L^2\gamma_2\right)LQ}{2\left(12EI + kAGL^2\right)\gamma_2} \tag{162}$$

3.3.3 Comparison between the Two Methods

When the penalty parameters approach infinity the Penalty method solutions tend to the Lagrange ones. Only the outcome regarding node 2 will be considered for brevity.

Concentrated moment M:

$$\underset{\gamma_2\to\infty}{Limit}\, w_2 = \underset{\gamma_2\to\infty}{Limit}\left[-\frac{\left(12EIL + kAGL^3 + 6L^2\gamma_2\right)M}{\left(12EI + kAGL^2\right)\gamma_2}\right] = \frac{-6ML^2}{12EI + kAGL^2} \tag{163}$$

$$\underset{\gamma_2\to\infty}{Limit}\, \Psi_2 = \underset{\gamma_2\to\infty}{Limit}\left[\frac{\left(12EI + kAGL^2 + 12L\gamma_2\right)M}{\left(12EI + kAGL^2\right)\gamma_2}\right] = \frac{12ML^2}{12EI + kAGL^2} \tag{164}$$

Concentrated transverse load Q:

$$\underset{\gamma_1,\gamma_2\to\infty}{Limit}\, \Psi_2 = \underset{\gamma_1,\gamma_2\to\infty}{Limit}\left\{\frac{\left(12EIL + kAGL^3 + 6L^2\gamma_2\right)Q}{\left(12EI + kAGL^2\right)\gamma_2}\right\} = \frac{6L^2P}{\left(12EI + kAGL^2\right)} \tag{165}$$

Transversely distributed load F:

$$\underset{\gamma_1,\gamma_2\to\infty}{Limit}\, w_2 =$$

$$\underset{\gamma_1,\gamma_2\to\infty}{Limit}\left\{-\frac{\left[12EIL\gamma_1\gamma_2 + \left(kAGL\right)^2\cdot\left(L^2\gamma_1 + \gamma_2\right) + 4kAG\cdot\left(3EIL^2\gamma_1 + 3EI\gamma_2 + L^3\gamma_1\gamma_2\right)\right]Q}{kAG\left(12EI + kAGL^2\right)\gamma_1\gamma_2}\right\} \tag{166}$$

$$= \frac{\left(12EIL + 4kAGL^3\right)P}{kAG\left(12EI + kAGL^2\right)}$$

$$\underset{\gamma_1,\gamma_2\to\infty}{Limit}\, \Psi_2 = \underset{\gamma_1,\gamma_2\to\infty}{Limit}\left\{\frac{\left(12EIL + kAGL^3 + 6L^2\gamma_2\right)LQ}{2\left(12EI + kAGL^2\right)\gamma_2}\right\} = \frac{3L^3P}{\left(12EI + kAGL^2\right)} \tag{167}$$

As before, the relations between the Lagrange multipliers and the penalty parameters are verified. The constraints we have enforced are:

$$G_1 = \left(w_v - w_1\right) \tag{168}$$

$$G_2 = \left(\Psi_v - \Psi_1\right) \tag{169}$$

Concen

Concen

Transver

3.3.4 Re

A

material a

I

match th

Concen

between

Concentrated moment M:

$$\lambda_1 = \gamma_1 \cdot G_1 = \gamma_1 \cdot (w_v - w_1) = \gamma_1 \cdot [0 - 0] = 0 \tag{170}$$

$$\lambda_2 = \gamma_2 \cdot G_2 = \gamma_2 \cdot (\Psi_v - \Psi_1) = \gamma_2 \cdot \left[0 - \frac{M}{\gamma_2}\right] = -M \tag{171}$$

Concentrated transverse load Q:

$$\lambda_1 = \gamma_1 \cdot G_1 = \gamma_1 \cdot (w_v - w_1) = \gamma_1 \cdot \left[0 - \left(-\frac{Q}{\gamma_1}\right)\right] = Q \tag{172}$$

$$\lambda_2 = \gamma_2 \cdot G_2 = \gamma_2 \cdot (\Psi_v - \Psi_1) = \gamma_2 \cdot \left[0 - \left(\frac{LQ}{\gamma_2}\right)\right] = -LQ \tag{173}$$

Transversely distributed load F:

$$\lambda_1 = \gamma_1 \cdot G_1 = \gamma_1 \cdot (w_v - w_1) = \gamma_1 \cdot \left[0 - \left(-\frac{FL}{\gamma_1}\right)\right] = FL \tag{174}$$

$$\lambda_2 = \gamma_2 \cdot G_2 = \gamma_2 \cdot (\Psi_v - \Psi_1) = \gamma_2 \cdot \left[0 - \left(\frac{FL^2}{2\gamma_2}\right)\right] = -\frac{FL^2}{2} \tag{175}$$

3.3.4 Relation between Penalty Parameter and Beam Properties

As before, the obtained solutions are examined in order to find a relation between material and geometrical properties of the beam and the penalty parameter.

The exact theoretical solution for displacement of the tip of the beam does not match that from the Lagrange multiplier finite element formulation.

Concentrated Moment M:

The ratio $w_2^{penalty}$ to $w_2^{Lagrange}$ is evaluated in order to underline the dependencies between the two solutions.

Now, if

The pre

beam.

Thus,

parameter

The re

Setting:

We get :

Concen

$$\frac{w_2^{penalty}}{w_2^{Lagrange}} = \frac{\dfrac{\left(12EIL + kAGL^3 + 6L^2\gamma_2\right)M}{\left(12EI + kAGL^2\right)\gamma_2}}{\dfrac{6ML^2}{12EI + kAGL^2}} = 1 + \frac{\left(12EI + kAGL^2\right)}{6L \cdot \gamma_2} \tag{176}$$

Now, if the penalty parameter γ_2 is substituted by:

$$\gamma_2 = \beta \cdot \frac{\left(12EI + kAGL^2\right)}{6L} \tag{177}$$

The previous ratio becomes independent of material and geometrical properties of the beam.

$$\frac{w_2^{penalty}}{w_2^{exact}} = 1 + \frac{1}{\beta} \tag{178}$$

Thus, the accuracy of the solution depends directly on the value assigned to the parameter β.

The ratio $\Psi_2^{penalty}$ over $\Psi_2^{Lagrange}$ is:

$$\frac{\Psi_2^{penalty}}{\Psi_2^{Lagrange}} = \frac{\dfrac{\left(12EI + kAGL^2 + 12L\gamma_2\right)M}{\left(12EI + kAGL^2\right)\gamma_2}}{\dfrac{12ML^2}{12EI + kAGL^2}} = 1 + \frac{\left(12EI + kAGL^2\right)}{12L \cdot \gamma_2} \tag{179}$$

Setting:

$$\gamma_2 = \beta \cdot \frac{\left(12EI + kAGL^2\right)}{12L} \tag{180}$$

We get the same relation found previously.

$$\frac{\Psi_2^{penalty}}{\Psi_2^{exact}} = 1 + \frac{1}{\beta} \tag{181}$$

Concentrated Transversal Load Q:

Now, if

The ratio

The ratio

Setting

It follo

The ratio $w_2^{penalty}$ over $w_2^{Lagrange}$ is:

$$\frac{w_2^{penalty}}{w_2^{Lagrange}} = \frac{\left[12EIL\gamma_1\gamma_2 + (kAGL)^2 \cdot \left(L^2\gamma_1 + \gamma_2\right) + 4kAG \cdot \left(3EIL^2\gamma_1 + 3EI\gamma_2 + L^3\gamma_1\gamma_2\right)\right]Q}{kAG\left(12EI + kAGL^2\right)\gamma_1\gamma_2} = \frac{\left(12EIL + 4kAGL^3\right)Q}{kAG\left(12EI + kAGL^2\right)} \tag{182}$$

$$= 1 + \frac{kAGL^2\left(12EI + kAGL^2\right)}{\left(12EIL + 4kAGL^3\right)\gamma_1} + \frac{kAG\left(12EI + kAGL^2\right)}{\left(12EIL + 4kAGL^3\right)\gamma_2}$$

Now, if the penalty parameters γ_1 and γ_2 are substituted by:

$$\gamma_1 = \beta \cdot \frac{2kAG\left(12EI + kAGL^2\right)}{\left(12EIL + 4kAGL^3\right)} \tag{183}$$

$$\gamma_2 = \beta \cdot \frac{2kAGL^2\left(12EI + kAGL^2\right)}{\left(12EIL + 4kAGL^3\right)} \tag{184}$$

The ratio between the solutions becomes:

$$\frac{w_2^{penalty}}{w_2^{exact}} = 1 + \frac{1}{2\beta} + \frac{1}{2\beta} = 1 + \frac{1}{\beta} \tag{185}$$

The ratio $\Psi_2^{penalty}$ over $\Psi_2^{Lagrange}$ is:

$$\frac{\Psi_2^{penalty}}{\Psi_2^{Lagrange}} = \frac{\left(12EIL + kAGL^3 + 6L^2\gamma_2\right)Q}{\left(12EI + kAGL^2\right)\gamma_2} = 1 + \frac{\left(12EI + kAGL^2\right)}{6L\gamma_2} \tag{186}$$

Setting:

$$\gamma_2 = \beta \cdot \frac{\left(12EI + kAGL^2\right)}{6L} \tag{187}$$

It follows:

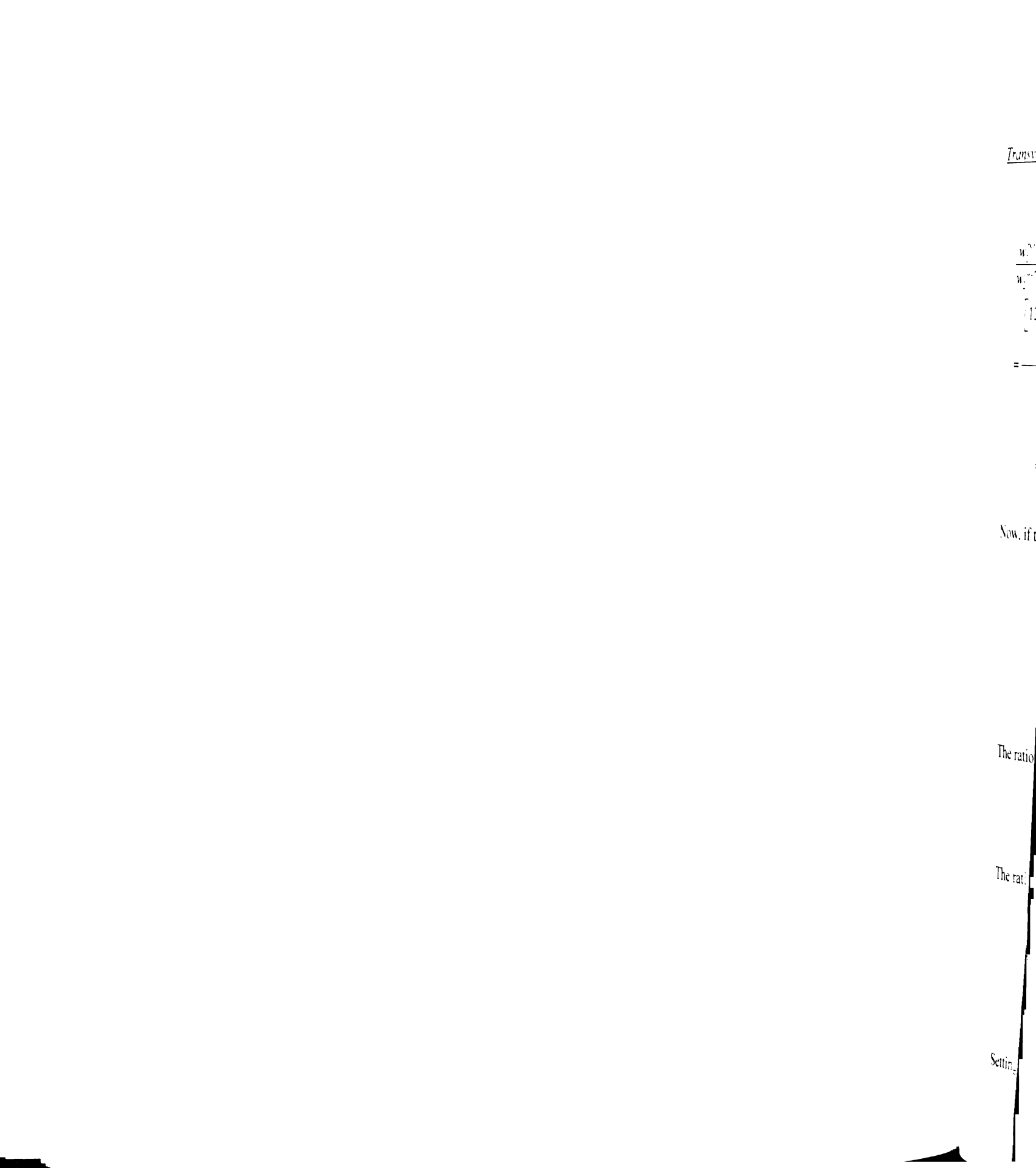

$$\frac{\Psi_2^{penalty}}{\Psi_2^{exact}} = 1 + \frac{1}{\beta} \tag{188}$$

Transversely Distributed Load F:

The ratio $w_2^{penalty}$ over $w_2^{Lagrange}$ is:

$$\frac{w_2^{penalty}}{w_2^{Lagrange}} = \frac{\left[12EIL\gamma_1\gamma_2 + (kAGL)^2 \cdot \left(L^2\gamma_1 + 2\gamma_2\right) + 4kAG \cdot \left(3EIL^2\gamma_1 + 6EI\gamma_2 + L^3\gamma_1\gamma_2\right)\right]FL}{\dfrac{2kAG\left(12EI + kAGL^2\right)\gamma_1\gamma_2}{\left(6EIL + 2kAGL^3\right)FL}} = \tag{189}$$

$$= 1 + \frac{kAG\left(24EI + 2kAGL^2\right)}{\left(12EIL + 4kAGL^3\right)\gamma_1} + \frac{kAGL^2\left(12EI + kAGL^2\right)}{\left(12EIL + 4kAGL^3\right)\gamma_2}$$

Now, if the penalty parameters γ_1 and γ_2 are substituted by:

$$\gamma_1 = \beta \cdot \frac{2kAG\left(24EI + 2kAGL^2\right)}{\left(12EIL + 4kAGL^3\right)} \tag{190}$$

$$\gamma_2 = \beta \cdot \frac{2kAGL^2\left(12EI + kAGL^2\right)}{\left(12EIL + 4kAGL^3\right)} \tag{191}$$

The ratio between the solutions turns into:

$$\frac{w_2^{penalty}}{w_2^{exact}} = 1 + \frac{1}{2\beta} + \frac{1}{2\beta} = 1 + \frac{1}{\beta} \tag{192}$$

The ratio $\Psi_2^{penalty}$ over $\Psi_2^{Lagrange}$ is:

$$\frac{\Psi_2^{penalty}}{\Psi_2^{Lagrange}} = \frac{\left(12EIL + kAGL^3 + 6L^2\gamma_2\right)FL}{\dfrac{\left(12EI + kAGL^2\right)\gamma_2}{3L^2F}} = 1 + \frac{\left(12EI + kAGL^2\right)}{6L\gamma_2} \tag{193}$$

Setting:

It follow

3.4 B

3.4.1 I

total pote

displacem

following

$\pi_i =$

The first

The La

$$\gamma_2 = \beta \cdot \frac{\left(12EI + kAGL^2\right)}{6L} \tag{194}$$

It follows:

$$\frac{\Psi_2^{penalty}}{\Psi_2^{exact}} = 1 + \frac{1}{\beta} \tag{195}$$

3.4 Bending Loads – One Element – Reduced Integration

3.4.1 Lagrange Multipliers Method

The hybrid interface method introduces two Lagrange multiplier λ_1 and λ_2 in the total potential energy (TPE) of system to satisfy the continuity conditions for transverse displacement and rotation. Thus the TPE of the system in this study assumes the following form.

$$\pi = \pi_1 + \lambda_1 \cdot \left(w_v - w_1\right) + \lambda_2 \cdot \left(\Psi_v - \Psi_1\right) - r_1 \cdot w_v - m_1 \cdot \Psi_v \tag{196}$$

$$\pi_1 = \frac{1}{2}\int_0^L \left[EI\left(\frac{\partial \Psi}{\partial x}\right)^2 + kGA\left(\Psi + \frac{\partial w}{\partial x}\right)^2 \right] dx - \int_0^L [F \cdot w]\, dx - \sum_{i=1}^{2} Q_i \cdot w_i - \sum_{i=1}^{2} M_i \cdot \Psi_i \tag{197}$$

The first variations of π is:

$$\begin{aligned} \delta\pi_1 = \int_0^L \left[EI\left(\frac{\partial \Psi}{\partial x}\right)\frac{\partial \delta\Psi}{\partial x} + kGA\left(\Psi + \frac{\partial w}{\partial x}\right)\left(\delta\Psi + \frac{\partial \delta w}{\partial x}\right) \right] dx - \int_0^L \left(F \cdot \delta w\right) dx - \\ \sum_{i=1}^{2} Q_i \cdot w_i - \sum_{i=1}^{2} M_i \cdot \Psi_i \end{aligned} \tag{198}$$

The Lagrange linear interpolation functions are used to approximate Ψ in:

$$\frac{1}{2}\int_0^L \left[EI\left(\frac{\partial \Psi}{\partial x}\right)^2 \right] dx \tag{199}$$

Instead, in the expression:

$$\frac{1}{2}\int_0^L \left[kGA\left(\Psi + \frac{\partial w}{\partial x} \right)^2 \right] dx \tag{200}$$

the term $\left(\Psi + \frac{\partial w}{\partial x} \right)$ will be substituted by $\left(\frac{\Psi_1 + \Psi_2}{2} + \frac{w_2 - w_1}{L} \right)$.

This operation will produce the same finite element model as the Reduced Integration procedure.

Thus, $\delta\pi_1$ is:

$$\begin{aligned} \delta\pi_1 = & \int_0^L \left\{ EI\left(\sum_J \Psi_J \frac{dN_J}{dx} \right)\left(\sum_I \delta\Psi_I \frac{dN_I}{dx} \right) \right\} dx + \\ & + \int_0^L \left\{ kGA\left(\frac{\Psi_1 + \Psi_2}{2} + \frac{w_2 - w_1}{L} \right)\left(\frac{1}{2}\delta\Psi_1 + \frac{1}{2}\delta\Psi_2 + \frac{1}{L}\delta w_2 - \frac{1}{L}\delta w_1 \right) \right\} dx - \\ & - \int_0^L \left(F \cdot \sum_I \delta w_I \cdot N_I \right) dx - \sum_{I=1}^{2} Q_I \cdot w_I - \sum_{I=1}^{2} M_I \cdot \Psi_I \end{aligned} \tag{201}$$

Taking the first variation of π with respect all the DOFs and setting them to zero we get:

$$\frac{\partial \pi}{\partial w_1} = kGA\left(\frac{w_1}{L} - \frac{\Psi_1}{2} - \frac{w_2}{L} - \frac{\Psi_2}{2} \right) - \int_0^L (F \cdot N_1)\, dx - \lambda_1 = 0 \tag{202}$$

$$\frac{\partial \pi}{\partial \Psi_1} = kGA\left(-\frac{w_1}{2} + \frac{L\Psi_1}{4} + \frac{w_2}{2} + \frac{L\Psi_2}{4} \right) + \int_0^L \left\{ EI\left(\sum_J \Psi_J \frac{dN_J}{dx}\frac{dN_1}{dx} \right) \right\} dx - \lambda_2 = 0 \tag{203}$$

$$\frac{\partial \pi}{\partial w_2} = kGA\left(-\frac{w_1}{L} + \frac{\Psi_1}{2} + \frac{w_2}{L} + \frac{\Psi_2}{2} \right) + \int_0^L (F \cdot N_2)\, dx + Q = 0 \tag{204}$$

$$\frac{\partial \pi}{\partial \Psi_2} = \left(-\frac{w_1}{2} + \frac{L\Psi_1}{4} + \frac{w_2}{2} + \frac{L\Psi_2}{4} \right) + \int_0^L \left\{ EI\left(\sum_J \Psi_J \frac{dN_J}{dx}\frac{dN_2}{dx} \right) \right\} dx - M = 0 \tag{205}$$

$$\frac{\partial \pi}{\partial w_v} = \lambda_1 - r_1 = 0 \tag{206}$$

$$\frac{\partial \pi}{\partial \Psi_v} = \lambda_2 - m_1 = 0 \tag{207}$$

$$\frac{\partial \pi}{\partial \lambda_1} = w_v - w_1 = 0 \tag{208}$$

$$\frac{\partial \pi}{\partial \lambda_2} = \Psi_v - \Psi_1 = 0 \tag{209}$$

Then, the resulting FE model is:

$$\begin{bmatrix} \frac{kAG}{L} & -\frac{kAG}{2} & -\frac{kAG}{L} & -\frac{kAG}{2} & 0 & 0 & -1 & 0 \\ -\frac{kAG}{2} & \frac{EI}{L}+\frac{kAGL}{4} & \frac{kAG}{2} & \frac{kAGL}{4}-\frac{EI}{L} & 0 & 0 & 0 & -1 \\ -\frac{kAG}{L} & \frac{kAG}{2} & \frac{kAG}{L} & \frac{kAG}{2} & 0 & 0 & 0 & 0 \\ -\frac{kAG}{2} & \frac{kAGL}{4}-\frac{EI}{L} & \frac{kAG}{2} & \frac{EI}{L}+\frac{kAGL}{4} & 0 & 0 & 0 & 0 \\ 0 & 0 & 0 & 0 & 0 & 0 & 1 & 0 \\ 0 & 0 & 0 & 0 & 0 & 0 & 0 & 1 \\ -1 & 0 & 0 & 0 & 1 & 0 & 0 & 0 \\ 0 & -1 & 0 & 0 & 0 & 1 & 0 & 0 \end{bmatrix} \cdot \begin{bmatrix} w_1 \\ \Psi_1 \\ w_2 \\ \Psi_2 \\ w_v \\ \Psi_v \\ \lambda_1 \\ \lambda_2 \end{bmatrix} = \begin{bmatrix} -\left(\frac{FL}{2}\right) \\ 0 \\ -Q-\left(\frac{FL}{2}\right) \\ M \\ r_1 \\ m_1 \\ 0 \\ 0 \end{bmatrix} \tag{210}$$

Taking into consideration that V is fixed ($w_v = 0$ and $\Psi_v = 0$), the system can be solved.

Concentrated moment M:

$$w_1 = 0 \tag{211}$$

$$\Psi_1 = 0 \tag{212}$$

$$w_2 = -\frac{ML^2}{EI} \tag{213}$$

$$\Psi_2 = \frac{ML}{EI} \tag{214}$$

$$\lambda_1 = 0 \tag{215}$$

$$\lambda_2 = -M \tag{216}$$

Concentrated transverse load Q:

$$w_1 = 0 \tag{217}$$

$$\Psi_1 = 0 \tag{218}$$

$$w_2 = -\left(\frac{QL^3}{4EI} + \frac{QL}{kAG}\right) \tag{219}$$

$$\Psi_2 = \frac{L^2 Q}{2EI} \tag{220}$$

$$\lambda_1 = Q \tag{221}$$

$$\lambda_2 = -LQ \tag{222}$$

Transversely distributed load F:

$$w_1 = 0 \tag{223}$$

$$\Psi_1 = 0 \tag{224}$$

$$w_2 = -\left(\frac{FL^4}{8EI} + \frac{FL^2}{2kAG}\right) \tag{225}$$

$$\Psi_2 = \frac{L^3 F}{4EI^2} \tag{226}$$

$$\lambda_1 = LF \tag{227}$$

$$\lambda_2 = -\frac{L^2 F}{2} \tag{228}$$

Also in this case, the solutions provided by the hybrid interface method are not the exact theoretical ones.

3.4.2 Penalty Method

In the penalty method the displacement continuity constraint is imposed through

two penalty parameters γ_1 and γ_2. Thus the TPE of the system in this study becomes:

$$\pi = \pi_1 + \frac{1}{2}\gamma_1 \cdot (w_v - w_1)^2 + \frac{1}{2}\gamma_2 \cdot (\Psi_v - \Psi_1)^2 - r_1 \cdot w_v - m_1 \cdot \Psi_v \qquad (229)$$

Here π_1 is equal to:

$$\pi_1 = \frac{1}{2}\int_0^L \left[EI\left(\frac{\partial \Psi}{\partial x}\right)^2 + kGA\left(\Psi + \frac{\partial w}{\partial x}\right)^2 \right] dx - \int_0^L [F \cdot w]dx - \sum_{i=1}^{2} Q_i \cdot w_i - \sum_{i=1}^{2} M_i \cdot \Psi_i \qquad (230)$$

Approximating the displacements as in the previous case.

$$\begin{aligned} \delta\pi_1 = & \int_0^L \left\{ EI\left(\sum_j \Psi_j \frac{dN_j}{dx}\right)\left(\sum_i \delta\Psi_i \frac{dN_i}{dx}\right)\right\} dx + \\ & + \int_0^L \left\{ kGA\left(\frac{\Psi_1 + \Psi_2}{2} + \frac{w_2 - w_1}{L}\right)\left(\frac{1}{2}\delta\Psi_1 + \frac{1}{2}\delta\Psi_2 + \frac{1}{L}\delta w_2 - \frac{1}{L}\delta w_1\right)\right\} dx - \\ & - \int_0^L \left(F \cdot \sum_i \delta w_i \cdot N_i \right) dx - \sum_{i=1}^{2} Q_i \cdot w_i - \sum_{i=1}^{2} M_i \cdot \Psi_i \end{aligned} \qquad (231)$$

Taking the first variation of π with respect all the DOFs, but not the penalty parameters, and setting them to zero we get:

$$\frac{\partial \pi}{\partial w_1} = kGA\left(\frac{w_1}{L} - \frac{\Psi_1}{2} - \frac{w_2}{L} - \frac{\Psi_2}{2}\right) - \int_0^L (F \cdot N_1)dx - \gamma_1 \cdot (w_v - w_1) = 0 \qquad (232)$$

$$\begin{aligned} \frac{\partial \pi}{\partial \Psi_1} = & kGA\left(-\frac{w_1}{2} + \frac{L\Psi_1}{4} + \frac{w_2}{2} + \frac{L\Psi_2}{4}\right) + \int_0^L \left\{ EI\left(\sum_j \Psi_j \frac{dN_j}{dx}\frac{dN_1}{dx}\right)\right\} dx - \\ & \gamma_2 \cdot (\Psi_v - \Psi_1) = 0 \end{aligned} \qquad (233)$$

$$\frac{\partial \pi}{\partial w_2} = kGA\left(-\frac{w_1}{L} + \frac{\Psi_1}{2} + \frac{w_2}{L} + \frac{\Psi_2}{2}\right) + \int_0^L (F \cdot N_2)dx + Q = 0 \qquad (234)$$

$$\frac{\partial \pi}{\partial \Psi_2} = \left(-\frac{w_1}{2} + \frac{L\Psi_1}{4} + \frac{w_2}{2} + \frac{L\Psi_2}{4}\right) + \int_0^L \left\{ EI\left(\sum_j \Psi_j \frac{dN_j}{dx}\frac{dN_2}{dx}\right)\right\} dx - M = 0 \qquad (235)$$

$$\frac{\partial \pi}{\partial w_v} = \gamma_1 \cdot (w_v - w_1) - r_1 = 0 \qquad (236)$$

$$\frac{\partial \pi}{\partial \Psi_v} = \gamma_2 \cdot (\Psi_v - \Psi_1) - m_1 = 0 \tag{237}$$

Then, the resulting FE model is:

$$\begin{bmatrix} \frac{kAG}{L}+\gamma_1 & -\frac{kAG}{2} & -\frac{kAG}{L} & -\frac{kAG}{2} & -\gamma_1 & 0 \\ -\frac{kAG}{2} & \frac{EI}{L}+\frac{kAGL}{4}+\gamma_2 & \frac{kAG}{2} & \frac{kAGL}{4}-\frac{EI}{L} & 0 & -\gamma_2 \\ -\frac{kAG}{L} & \frac{kAG}{2} & \frac{kAG}{L} & \frac{kAG}{2} & 0 & 0 \\ -\frac{kAG}{2} & \frac{kAGL}{4}-\frac{EI}{L} & \frac{kAG}{2} & \frac{EI}{L}+\frac{kAGL}{4} & 0 & 0 \\ -\gamma_1 & 0 & 0 & 0 & \gamma_1 & 0 \\ 0 & -\gamma_2 & 0 & 0 & 0 & \gamma_2 \end{bmatrix} \cdot \begin{bmatrix} w_1 \\ \Psi_1 \\ w_2 \\ \Psi_2 \\ w_v \\ \Psi_v \end{bmatrix} = \begin{bmatrix} -\left(\frac{FL}{2}\right) \\ 0 \\ -Q-\left(\frac{FL}{2}\right) \\ M \\ r_1 \\ m_1 \end{bmatrix} \tag{238}$$

Taking into consideration that V is fixed ($w_v = 0$ and $\Psi_v = 0$), the system can be solved.

Concentrated moment M:

$$w_1 = 0 \tag{239}$$

$$\Psi_1 = \frac{M}{\gamma_2} \tag{240}$$

$$w_2 = -\left(\frac{L^2}{2EI}+\frac{L}{\gamma_2}\right)M \tag{241}$$

$$\Psi_2 = \left(\frac{L}{EI}+\frac{1}{\gamma_2}\right)M \tag{242}$$

Concentrated transverse load Q:

$$w_1 = -\frac{Q}{\gamma_1} \tag{243}$$

$$\Psi_1 = \frac{LQ}{\gamma_2} \tag{244}$$

$$w_2 = -\left(\frac{L^3}{4EI}+\frac{L}{kAG}+\frac{1}{\gamma_1}+\frac{L^2}{\gamma_2}\right)Q \tag{245}$$

$$\Psi_2 = \left(\frac{L^2}{2EI} + \frac{L}{\gamma_2} \right) Q \tag{246}$$

Transversely distributed load F:

$$w_1 = -\frac{LF}{\gamma_1} \tag{247}$$

$$\Psi_1 = \frac{L^2 F}{2\gamma_2} \tag{248}$$

$$w_2 = -\left(\frac{L^4}{8EI} + \frac{L^2}{2kAG} + \frac{L}{\gamma_1} + \frac{L^3}{2\gamma_2} \right) F \tag{249}$$

$$\Psi_2 = \left(\frac{L^3}{4EI} + \frac{L^2}{2\gamma_2} \right) F \tag{250}$$

3.4.3 Comparison between the Two Methods

When the penalty parameters approach infinity the Penalty method solutions tend to the Lagrange ones. Only the outcome regarding node 2 will be considered for brevity.

Concentrated moment M:

$$\underset{\gamma_2 \to \infty}{Limit}\, w_2 = \underset{\gamma_2 \to \infty}{Limit} \left[-\left(\frac{L^2}{2EI} + \frac{L}{\gamma_2} \right) M \right] = \frac{-ML^2}{2EI} \tag{251}$$

$$\underset{\gamma_2 \to \infty}{Limit}\, \Psi_2 = \underset{\gamma_2 \to \infty}{Limit} \left[\left(\frac{L}{EI} + \frac{1}{\gamma_2} \right) M \right] = \frac{ML}{EI} \tag{252}$$

Concentrated transverse load Q:

$$\underset{\gamma_1, \gamma_2 \to \infty}{Limit}\, w_2 = \underset{\gamma_1, \gamma_2 \to \infty}{Limit} \left\{ -\left(\frac{L^3}{4EI} + \frac{L}{kAG} + \frac{1}{\gamma_1} + \frac{L^2}{\gamma_2} \right) Q \right\} = -\left(\frac{L^3}{4EI} + \frac{L}{kAG} \right) Q \tag{253}$$

$$\underset{\gamma_1,\gamma_2\to\infty}{Limit}\,\Psi_2 = \underset{\gamma_1,\gamma_2\to\infty}{Limit}\left\{\left(\frac{L^2}{2EI}+\frac{L}{\gamma_2}\right)Q\right\} = \left(\frac{L^2}{2EI}\right)Q \tag{254}$$

Transversely distributed load F:

$$\underset{\gamma_1,\gamma_2\to\infty}{Limit}\,w_2 = \underset{\gamma_1,\gamma_2\to\infty}{Limit}\left\{-\left(\frac{L^4}{8EI}+\frac{L^2}{2kAG}+\frac{L}{\gamma_1}+\frac{L^3}{2\gamma_2}\right)F\right\} = -\left(\frac{L^4}{8EI}+\frac{L^2}{2kAG}\right)F \tag{255}$$

$$\underset{\gamma_1,\gamma_2\to\infty}{Limit}\,\Psi_2 = \underset{\gamma_1,\gamma_2\to\infty}{Limit}\left\{\left(\frac{L^3}{4EI}+\frac{L^2}{2\gamma_2}\right)F\right\} = \left(\frac{L^3}{4EI}\right)F \tag{256}$$

The constraints we have enforced are:

$$G_1 = \left(w_v - w_1\right) \tag{257}$$

$$G_2 = \left(\Psi_v - \Psi_1\right) \tag{258}$$

Now, the relations between the Lagrange multipliers and the penalty parameters are verified.

Concentrated moment M:

$$\lambda_1 = \gamma_1 \cdot G_1 = \gamma_1 \cdot \left(w_v - w_1\right) = \gamma_1 \cdot [0-0] = 0 \tag{259}$$

$$\lambda_2 = \gamma_2 \cdot G_2 = \gamma_2 \cdot \left(\Psi_v - \Psi_1\right) = \gamma_2 \cdot \left[0 - \frac{M}{\gamma_2}\right] = -M \tag{260}$$

Concentrated transverse load Q:

$$\lambda_1 = \gamma_1 \cdot G_1 = \gamma_1 \cdot \left(w_v - w_1\right) = \gamma_1 \cdot \left[0 - \left(-\frac{Q}{\gamma_1}\right)\right] = Q \tag{261}$$

$$\lambda_2 = \gamma_2 \cdot G_2 = \gamma_2 \cdot \left(\Psi_v - \Psi_1\right) = \gamma_2 \cdot \left[0 - \left(\frac{LQ}{\gamma_2}\right)\right] = -LQ \tag{262}$$

Transversely distributed load F:

$$\lambda_1 = \gamma_1 \cdot G_1 = \gamma_1 \cdot (w_v - w_1) = \gamma_1 \cdot \left[0 - \left(-\frac{FL}{\gamma_1}\right)\right] = FL \tag{263}$$

$$\lambda_2 = \gamma_2 \cdot G_2 = \gamma_2 \cdot (\Psi_v - \Psi_1) = \gamma_2 \cdot \left[0 - \left(\frac{FL^2}{2\gamma_2}\right)\right] = -\frac{FL^2}{2} \tag{264}$$

3.4.4 Relation between Penalty Parameter and Beam Properties

As before, the obtained solutions are explored in order to find a relation between material and geometrical properties of the beam and the penalty parameter. The exact theoretical solution for displacement of the tip of the beam does not match that from the Lagrange multiplier Finite element formulation.

Concentrated Moment M:

The ratio of $w_2^{penalty}$ to $w_2^{Lagrange}$ is evaluated in order to underline the dependencies between the two solutions.

$$\frac{w_2^{penalty}}{w_2^{Lagrange}} = \frac{\left(\frac{L^2}{2EI} + \frac{L}{\gamma_2}\right)M}{\frac{ML^2}{2EI}} = 1 + \frac{2EI}{L \cdot \gamma_2} \tag{265}$$

Now, if the penalty parameter γ_2 is substituted by:

$$\gamma_2 = \beta \cdot \frac{2EI}{L} \tag{266}$$

The ratio between the solutions becomes independent of material and geometrical properties of the beam.

$$\frac{w_2^{penalty}}{w_2^{exact}} = 1 + \frac{1}{\beta} \tag{267}$$

Thus, the accuracy of the solution depends directly on the value assigned to the

parameter β.

The ratio $\Psi_2^{penalty}$ over $\Psi_2^{Lagrange}$ is:

$$\frac{\Psi_2^{penalty}}{\Psi_2^{Lagrange}} = \frac{\left(\frac{L}{EI} + \frac{1}{\gamma_2}\right)M}{\frac{ML}{EI}} = 1 + \frac{EI}{L \cdot \gamma_2} \tag{268}$$

Setting:

$$\gamma_2 = \beta \cdot \frac{EI}{L} \tag{269}$$

We get the same relation found previously:

$$\frac{\Psi_2^{penalty}}{\Psi_2^{exact}} = 1 + \frac{1}{\beta} \tag{270}$$

Concentrated Transverse Load Q:

The ratio $w_2^{penalty}$ over $w_2^{Lagrange}$ is:

$$\frac{w_2^{penalty}}{w_2^{Lagrange}} = \frac{\left(\frac{L^3}{4EI} + \frac{L}{kAG} + \frac{1}{\gamma_1} + \frac{L^2}{\gamma_2}\right)Q}{\left(\frac{L^3}{4EI} + \frac{L}{kAG}\right)Q} = 1 + \frac{1}{\left(\frac{L^3}{4EI} + \frac{L}{kAG}\right)\gamma_1} + \frac{L^2}{\left(\frac{L^3}{4EI} + \frac{L}{kAG}\right)\gamma_2} \tag{271}$$

Now, if the penalty parameters γ_1 and γ_2 are substituted by:

$$\gamma_1 = \beta \cdot \frac{2}{\left(\frac{L^3}{4EI} + \frac{L}{kAG}\right)} \tag{272}$$

$$\gamma_2 = \beta \cdot \frac{2L^2}{\left(\frac{L^3}{4EI} + \frac{L}{kAG}\right)} \tag{273}$$

The ratio between the solutions becomes independent of material and geometrical properties of the beam.

$$\frac{w_2^{penalty}}{w_2^{exact}} = 1 + \frac{1}{2\beta} + \frac{1}{2\beta} = 1 + \frac{1}{\beta} \tag{274}$$

The ratio $\Psi_2^{penalty}$ over $\Psi_2^{Lagrange}$ is:

$$\frac{\Psi_2^{penalty}}{\Psi_2^{Lagrange}} = \frac{\left(\frac{L^2}{2EI} + \frac{L}{\gamma_2}\right)Q}{\left(\frac{L^2}{2EI}\right)Q} = 1 + \frac{2EI}{L\gamma_2} \tag{275}$$

Setting:

$$\gamma_2 = \beta \cdot \frac{2EI}{L} \tag{276}$$

It follows:

$$\frac{\Psi_2^{penalty}}{\Psi_2^{exact}} = 1 + \frac{1}{\beta} \tag{277}$$

Transversely Distributed Load F:

The ratio $w_2^{penalty}$ over $w_2^{Lagrange}$ is:

$$\frac{w_2^{penalty}}{w_2^{Lagrange}} = \frac{\left(\frac{L^4}{8EI} + \frac{L^2}{2kAG} + \frac{L}{\gamma_1} + \frac{L^3}{2\gamma_2}\right)Q}{\left(\frac{L^4}{8EI} + \frac{L^2}{2kAG}\right)Q} = 1 + \frac{L}{\left(\frac{L^4}{8EI} + \frac{L^2}{2kAG}\right)\gamma_1} + \frac{L^3}{2\left(\frac{L^4}{8EI} + \frac{L^2}{2kAG}\right)\gamma_2} \tag{278}$$

Now, if the penalty parameters γ_1 and γ_2 are substituted by:

$$\gamma_1 = \beta \cdot \frac{2L}{\left(\frac{L^4}{8EI} + \frac{L^2}{2kAG}\right)} \tag{279}$$

$$\gamma_2 = \beta \cdot \frac{L^3}{\left(\frac{L^4}{8EI} + \frac{L^2}{2kAG}\right)} \tag{280}$$

The ratio between the solutions becomes independent of material and geometrical properties of the beam.

$$\frac{w_2^{penalty}}{w_2^{exact}} = 1 + \frac{1}{2\beta} + \frac{1}{2\beta} = 1 + \frac{1}{\beta} \tag{281}$$

The ratio $\Psi_2^{penalty}$ over $\Psi_2^{Lagrange}$ is:

$$\frac{\Psi_2^{penalty}}{\Psi_2^{Lagrange}} = \frac{\left(\frac{L^3}{4EI} + \frac{L^2}{2\gamma_2}\right)Q}{\left(\frac{L^3}{4EI}\right)Q} = 1 + \frac{2EI}{L\gamma_2} \tag{282}$$

Setting:

$$\gamma_2 = \beta \cdot \frac{2EI}{L} \tag{283}$$

It follows:

$$\frac{\Psi_2^{penalty}}{\Psi_2^{exact}} = 1 + \frac{1}{\beta} \tag{284}$$

3.5 Bending Loads – Two Element – Reduced integration

A useful problem to our purpose is that of two linear beams elements connected using a Lagrange multiplier or a Penalty parameter continuity constraint, fixed in the center and loaded with bending loads symmetric with respect the joining point. The configuration of the geometry and the mesh are plotted in Figure 5.

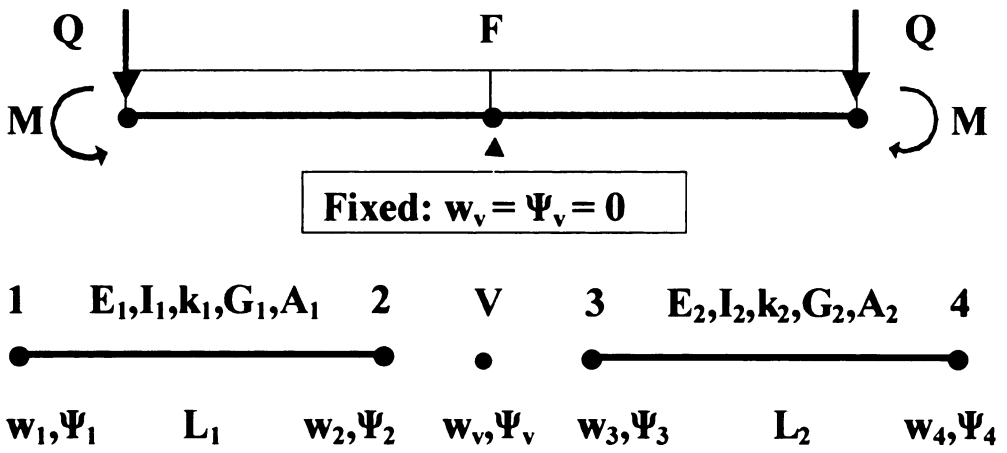

Figure 5. ***Beam under bending loads – Two Elements***

3.5.1 Lagrange Multiplier Method

The total potential energy of system is:

$$\pi = \pi_1 + \pi_2 + \lambda_1 \cdot (w_v - w_2) + \lambda_2 \cdot (\Psi_v - \Psi_2) + \lambda_3 \cdot (w_v - w_3) + \lambda_4 \cdot (\Psi_v - \Psi_3) \tag{285}$$

Where π_1, π_2 are, respectively, the TPE of the first and of the second bars.

The Lagrange linear interpolation functions are used to approximate Ψ in:

$$\frac{1}{2}\int_0^L \left[EI \left(\frac{\partial \Psi}{\partial x} \right)^2 \right] dx \tag{286}$$

Instead, in the expression:

$$\frac{1}{2}\int_0^L \left[kGA \left(\Psi + \frac{\partial w}{\partial x} \right)^2 \right] dx \tag{287}$$

the term $\left(\Psi + \frac{\partial w}{\partial x} \right)$ will be approximated by $\left(\frac{\Psi_1 + \Psi_2}{2} + \frac{w_2 - w_1}{L} \right)$.

$$\delta\pi_1 = \int_0^L \left\{ EI \left(\sum_J \Psi_J \frac{dN_J}{dx} \right) \left(\sum_I \delta\Psi_I \frac{dN_I}{dx} \right) \right\} dx +$$
$$+ \int_0^L \left\{ kGA \left(\frac{\Psi_1 + \Psi_2}{2} + \frac{w_2 - w_1}{L} \right) \left(\frac{1}{2}\delta\Psi_1 + \frac{1}{2}\delta\Psi_2 + \frac{1}{L}\delta w_2 - \frac{1}{L}\delta w_1 \right) \right\} dx - \quad (288)$$
$$- \int_0^L \left(F \cdot \sum_I \delta w_I \cdot N_I \right) dx - \sum_{I=1}^{2} Q_I \cdot w_I - \sum_{I=1}^{2} M_I \cdot \Psi_I$$

Taking the first variation of π with respect all the DOFs and setting them to zero we get:

$$\frac{\partial\pi}{\partial w_1} = k_1 G_1 A_1 \left(\frac{w_1}{L_1} - \frac{\Psi_1}{2} - \frac{w_2}{L_1} - \frac{\Psi_2}{2} \right) + \int_0^{L_1} (F \cdot N_1)\, dx = 0 \quad (289)$$

$$\frac{\partial\pi}{\partial\Psi_1} = k_1 G_1 A_1 \left(-\frac{w_1}{2} + \frac{L_1\Psi_1}{4} + \frac{w_2}{2} + \frac{L_1\Psi_2}{4} \right) + \int_0^{L_1} \left\{ E_1 I_1 \left(\sum_J \Psi_J \frac{dN_J}{dx} \frac{dN_1}{dx} \right) \right\} dx = 0 \quad (290)$$

$$\frac{\partial\pi}{\partial w_2} = k_1 G_1 A_1 \left(-\frac{w_1}{L_1} + \frac{\Psi_1}{2} + \frac{w_2}{L_1} + \frac{\Psi_2}{2} \right) + \int_0^{L_1} (F \cdot N_2)\, dx - \lambda_1 = 0 \quad (291)$$

$$\frac{\partial\pi}{\partial\Psi_2} = k_1 G_1 A_1 \left(-\frac{w_1}{2} + \frac{L_1\Psi_1}{4} + \frac{w_2}{2} + \frac{L_1\Psi_2}{4} \right) + \int_0^{L_1} \left\{ E_1 I_1 \left(\sum_J \Psi_J \frac{dN_J}{dx} \frac{dN_2}{dx} \right) \right\} dx - \lambda_2 = 0 \quad (292)$$

$$\frac{\partial\pi}{\partial w_3} = k_2 G_2 A_2 \left(\frac{w_1}{L_2} - \frac{\Psi_1}{2} - \frac{w_2}{L_2} - \frac{\Psi_2}{2} \right) + \int_0^{L_2} (F \cdot N_1)\, dx - \lambda_3 = 0 \quad (293)$$

$$\frac{\partial\pi}{\partial\Psi_3} = k_2 G_2 A_2 \left(-\frac{w_1}{2} + \frac{L_2\Psi_1}{4} + \frac{w_2}{2} + \frac{L_2\Psi_2}{4} \right) + \int_0^{L_2} \left\{ E_2 I_2 \left(\sum_J \Psi_J \frac{dN_J}{dx} \frac{dN_1}{dx} \right) \right\} dx - \lambda_4 = 0 \quad (294)$$

$$\frac{\partial\pi}{\partial w_4} = k_2 G_2 A_2 \left(-\frac{w_1}{L_2} + \frac{\Psi_1}{2} + \frac{w_2}{L_2} + \frac{\Psi_2}{2} \right) + \int_0^{L_2} (F \cdot N_2)\, dx + Q = 0 \quad (295)$$

$$\frac{\partial\pi}{\partial\Psi_2} = k_2 G_2 A_2 \left(-\frac{w_1}{2} + \frac{L_2\Psi_1}{4} + \frac{w_2}{2} + \frac{L_2\Psi_2}{4} \right) + \int_0^{L_2} \left\{ E_2 I_2 \left(\sum_J \Psi_J \frac{dN_J}{dx} \frac{dN_2}{dx} \right) \right\} dx - M = 0 \quad (296)$$

$$\frac{\partial\pi}{\partial w_v} = \lambda_1 + \lambda_3 = 0 \quad (297)$$

$$\frac{\partial \pi}{\partial \Psi_v} = \lambda_2 + \lambda_4 = 0 \tag{298}$$

$$\frac{\partial \pi}{\partial \lambda_1} = w_v - w_2 = 0 \tag{299}$$

$$\frac{\partial \pi}{\partial \lambda_2} = \Psi_v - \Psi_2 = 0 \tag{300}$$

$$\frac{\partial \pi}{\partial \lambda_3} = w_v - w_3 = 0 \tag{301}$$

$$\frac{\partial \pi}{\partial \lambda_4} = \Psi_v - \Psi_3 = 0 \tag{302}$$

The FE model is easily derived.

$$[K]\{u\} = \{f\} \tag{303}$$

where:

$$[K] = \begin{bmatrix}
\frac{k_1 A_1 G_1}{l_1} & -\frac{k_1 A_1 G_1}{2} & -\frac{k_1 A_1 G_1}{l_1} & -\frac{k_1 A_1 G_1}{2} & 0 & 0 & 0 & 0 & 0 & 0 & 0 & 0 & 0 & 0 \\
-\frac{k_1 A_1 G_1}{2} & \frac{E_1 I_1}{l_1} + \frac{k_1 A_1 G_1 l_1}{4} & \frac{k_1 A_1 G_1}{2} & \frac{k_1 A_1 G_1 l_1}{4} - \frac{E_1 I_1}{l_1} & 0 & 0 & 0 & 0 & 0 & 0 & 0 & 0 & 0 & 0 \\
-\frac{k_1 A_1 G_1}{l_1} & \frac{k_1 A_1 G_1}{2} & \frac{k_1 A_1 G_1}{l_1} & \frac{k_1 A_1 G_1}{2} & 0 & 0 & 0 & 0 & 0 & 0 & -1 & 0 & 0 & 0 \\
-\frac{k_1 A_1 G_1}{2} & \frac{k_1 A_1 G_1 l_1}{4} - \frac{E_1 I_1}{l_1} & \frac{k_1 A_1 G_1}{2} & \frac{E_1 I_1}{l_1} + \frac{k_1 A_1 G_1 l_1}{4} & 0 & 0 & 0 & 0 & 0 & 0 & 0 & -1 & 0 & 0 \\
0 & 0 & 0 & 0 & \frac{k_2 A_2 G_2}{l_2} & -\frac{k_2 A_2 G_2}{2} & -\frac{k_2 A_2 G_2}{l_2} & -\frac{k_2 A_2 G_2}{2} & 0 & 0 & 0 & 0 & -1 & 0 \\
0 & 0 & 0 & 0 & -\frac{k_2 A_2 G_2}{2} & \frac{E_2 I_2}{l_2} + \frac{k_2 A_2 G_2 l_2}{4} & \frac{k_2 A_2 G_2}{2} & \frac{k_2 A_2 G_2 l_2}{4} - \frac{E_2 I_2}{l_2} & 0 & 0 & 0 & 0 & 0 & -1 \\
0 & 0 & 0 & 0 & -\frac{k_2 A_2 G_2}{l_2} & \frac{k_2 A_2 G_2}{2} & \frac{k_2 A_2 G_2}{l_2} & \frac{k_2 A_2 G_2}{2} & 0 & 0 & 0 & 0 & 0 & 0 \\
0 & 0 & 0 & 0 & -\frac{k_2 A_2 G_2}{2} & \frac{k_2 A_2 G_2 l_2}{4} - \frac{E_2 I_2}{l_2} & \frac{k_2 A_2 G_2}{2} & \frac{E_2 I_2}{l_2} + \frac{k_2 A_2 G_2 l_2}{4} & 0 & 0 & 0 & 0 & 0 & 0 \\
0 & 0 & 0 & 0 & 0 & 0 & 0 & 0 & 0 & 0 & 1 & 0 & 1 & 0 \\
0 & 0 & 0 & 0 & 0 & 0 & 0 & 0 & 0 & 0 & 0 & 1 & 0 & 1 \\
0 & 0 & -1 & 0 & 0 & 0 & 0 & 0 & 1 & 0 & 0 & 0 & 0 & 0 \\
0 & 0 & 0 & -1 & 0 & 0 & 0 & 0 & 0 & 1 & 0 & 0 & 0 & 0 \\
0 & 0 & 0 & 0 & -1 & 0 & 0 & 0 & 1 & 0 & 0 & 0 & 0 & 0 \\
0 & 0 & 0 & 0 & 0 & -1 & 0 & 0 & 0 & 1 & 0 & 0 & 0 & 0
\end{bmatrix} \tag{304}$$

$$\{u\} = \{w_1 \quad \Psi_1 \quad w_2 \quad \Psi_2 \quad w_3 \quad \Psi_3 \quad w_4 \quad \Psi_4 \quad w_v \quad \Psi_v \quad \lambda_1 \quad \lambda_2 \quad \lambda_3 \quad \lambda_4\}^T \tag{305}$$

$$\{f\} = \left\{ -\frac{FL}{2} \quad 0 \quad -\frac{FL}{2} \quad 0 \quad -FL \quad 0 \quad \left(-Q - \frac{FL}{2}\right) \quad M \quad 0 \quad 0 \quad 0 \quad 0 \quad 0 \quad 0 \right\}^T \tag{306}$$

Taking into consideration that V is fixed ($w_v = 0$ and $\Psi_v = 0$), the system can be solved.

Concentrated moment M applied at the tip

$$w_1 = -\frac{ML_1^2}{2E_1 I_1} \tag{307}$$

$$\Psi_1 = -\frac{ML_1}{E_1 I_1} \tag{308}$$

$$w_2 = 0 \tag{309}$$

$$\Psi_2 = 0 \tag{310}$$

$$w_3 = 0 \tag{311}$$

$$\Psi_3 = 0 \tag{312}$$

$$w_4 = -\frac{ML_2^2}{2E_2 I_2} \tag{313}$$

$$\Psi_4 = \frac{ML_2}{E_2 I_2} \tag{314}$$

$$\lambda_1 = 0 \tag{315}$$

$$\lambda_2 = M \tag{316}$$

$$\lambda_3 = 0 \tag{317}$$

$$\lambda_4 = -M \tag{318}$$

Concentrated transverse load Q applied at the tip

$$w_1 = -\frac{QL_1^3}{4E_1 I_1} - \frac{L_1 Q}{A_1 G_1 k_1} \tag{319}$$

$$\Psi_1 = -\frac{QL_1^2}{2E_1I_1} \tag{320}$$

$$w_2 = 0 \tag{321}$$

$$\Psi_2 = 0 \tag{322}$$

$$w_3 = 0 \tag{323}$$

$$\Psi_3 = 0 \tag{324}$$

$$w_4 = -\frac{QL_2^3}{4E_2I_2} - \frac{L_2Q}{A_2G_2k_2} \tag{325}$$

$$\Psi_4 = \frac{QL_2^2}{2E_2I_2} \tag{326}$$

$$\lambda_1 = Q \tag{327}$$

$$\lambda_2 = QL_1 \tag{328}$$

$$\lambda_3 = Q \tag{329}$$

$$\lambda_4 = -QL_2 \tag{330}$$

Transversely distributed load F

$$w_1 = -\frac{FL_1^4}{8E_1I_1} - \frac{FL_1^2}{2A_1G_1k_1} \tag{331}$$

$$\Psi_1 = -\frac{FL_1^3}{4E_1I_1} \tag{332}$$

$$w_2 = 0 \tag{333}$$

$$\Psi_2 = 0 \tag{334}$$

$$w_3 = 0 \tag{335}$$

$$\Psi_3 = 0 \tag{336}$$

$$w_4 = -\frac{FL_2^3}{8E_2I_2} - \frac{L_2^2F}{2A_2G_2k_2} \tag{337}$$

$$\Psi_4 = \frac{FL_2^3}{4E_2I_2} \tag{338}$$

$$\lambda_1 = FL_1 \tag{339}$$

$$\lambda_2 = FL_1^2 \tag{340}$$

$$\lambda_3 = FL_2 \tag{341}$$

$$\lambda_4 = -FL_2^2 \tag{342}$$

3.5.2 Penalty Method

The total potential energy of system is:

$$\pi = \pi_1 + \pi_2 + \frac{1}{2}\gamma_1 \cdot (w_v - w_2)^2 + \frac{1}{2}\gamma_2 \cdot (\Psi_v - \Psi_2)^2 + \frac{1}{2}\gamma_3 \cdot (w_v - w_3)^2 + \frac{1}{2}\gamma_4 \cdot (\Psi_v - \Psi_3)^2 \tag{343}$$

Following the same procedure as in the previous paragraph, the first variations of π with respect all the DOFs produce:

$$\frac{\partial \pi}{\partial w_1} = \frac{\partial \pi_1}{\partial w_1} + \frac{\partial \pi_2}{\partial w_1} = 0 \tag{344}$$

$$\frac{\partial \pi}{\partial \Psi_1} = \frac{\partial \pi_1}{\partial \Psi_1} + \frac{\partial \pi_2}{\partial \Psi_1} = 0 \tag{345}$$

$$\frac{\partial \pi}{\partial w_2} = \frac{\partial \pi_1}{\partial w_2} + \frac{\partial \pi_2}{\partial w_2} - \gamma_1 \cdot (w_v - w_2) = 0 \tag{346}$$

$$\frac{\partial \pi}{\partial \Psi_2} = \frac{\partial \pi_1}{\partial \Psi_2} + \frac{\partial \pi_2}{\partial \Psi_2} - \gamma_2 \cdot (\Psi_v - \Psi_2) = 0 \tag{347}$$

$$\frac{\partial \pi}{\partial w_3} = \frac{\partial \pi_1}{\partial w_3} + \frac{\partial \pi_2}{\partial w_3} - \gamma_3 \cdot (w_v - w_3) = 0 \tag{348}$$

$$\frac{\partial \pi}{\partial \Psi_3} = \frac{\partial \pi_1}{\partial \Psi_3} + \frac{\partial \pi_2}{\partial \Psi_3} - \gamma_4 \cdot (\Psi_v - \Psi_4) = 0 \tag{349}$$

$$\frac{\partial \pi}{\partial w_4} = \frac{\partial \pi_1}{\partial w_4} + \frac{\partial \pi_2}{\partial w_4} = 0 \tag{350}$$

$$\frac{\partial \pi}{\partial \Psi_4} = \frac{\partial \pi_1}{\partial \Psi_4} + \frac{\partial \pi_2}{\partial \Psi_4} = 0 \tag{351}$$

$$\frac{\partial \pi}{\partial w_v} = \gamma_1 \cdot (w_v - w_2) + \gamma_3 \cdot (w_v - w_3) = 0 \tag{352}$$

$$\frac{\partial \pi}{\partial \Psi_v} = \gamma_2 \cdot (\Psi_v - \Psi_2) + \gamma_4 \cdot (\Psi_v - \Psi_3) = 0 \tag{353}$$

The FE model is easily derived.

$$[K]\{u\} = \{f\} \tag{354}$$

where:

$$\{u\} = \{w_1 \quad \Psi_1 \quad w_2 \quad \Psi_2 \quad w_3 \quad \Psi_3 \quad w_4 \quad \Psi_4 \quad w_v \quad \Psi_v\}^T \tag{355}$$

$$\{f\} = \left\{-\frac{FL}{2} \quad 0 \quad -\frac{FL}{2} \quad 0 \quad -\frac{FL}{2} \quad 0 \quad -Q - \frac{FL}{2} \quad M \quad 0 \quad 0\right\}^T \tag{356}$$

and the stiffness matrix K is:

Taking in

Concentra

$$\begin{bmatrix}
\frac{kAG}{L} & -\frac{kAG}{2} & -\frac{kAG}{L} & -\frac{kAG}{2} & 0 & 0 & 0 & 0 & 0 & 0 \\
-\frac{kAG}{2} & \frac{EI}{L}+\frac{kAGL}{4} & \frac{kAG}{2} & \frac{kAGL}{4}-\frac{EI}{L} & 0 & 0 & 0 & 0 & 0 & 0 \\
-\frac{kAG}{L} & \frac{kAG}{2} & \frac{kAG}{L}+\gamma_1 & \frac{kAG}{2} & 0 & 0 & 0 & 0 & -\gamma_1 & 0 \\
-\frac{kAG}{2} & \frac{kAGL}{4}-\frac{EI}{L} & \frac{kAG}{2} & \frac{EI}{L}+\frac{kAGL}{4}+\gamma_2 & 0 & 0 & 0 & 0 & 0 & -\gamma_2 \\
0 & 0 & 0 & 0 & \frac{kAG}{L}+\gamma_3 & -\frac{kAG}{2} & -\frac{kAG}{L} & -\frac{kAG}{2} & -\gamma_3 & 0 \\
0 & 0 & 0 & 0 & -\frac{kAG}{2} & \frac{EI}{L}+\frac{kAGL}{4}+\gamma_4 & \frac{kAG}{2} & \frac{kAGL}{4}-\frac{EI}{L} & 0 & -\gamma_4 \\
0 & 0 & 0 & 0 & -\frac{kAG}{L} & \frac{kAG}{2} & \frac{kAG}{L} & \frac{kAG}{2} & 0 & 0 \\
0 & 0 & 0 & 0 & -\frac{kAG}{2} & \frac{kAGL}{4}-\frac{EI}{L} & \frac{kAG}{2} & \frac{EI}{L}+\frac{kAGL}{4} & 0 & 0 \\
0 & 0 & -\gamma_1 & 0 & -\gamma_3 & 0 & 0 & 0 & \gamma_1+\gamma_3 & 0 \\
0 & 0 & 0 & -\gamma_2 & 0 & -\gamma_4 & 0 & 0 & 0 & \gamma_2+\gamma_4
\end{bmatrix} \tag{357}$$

Taking into consideration that V is fixed ($w_v = 0$ and $\Psi_v = 0$), the system can be solved.

Concentrated moment M:

$$w_1 = -\frac{ML_1^2}{2E_1I_1} - \frac{ML_1}{\gamma_2} \tag{358}$$

$$\Psi_1 = -\frac{ML_1}{E_1I_1} - \frac{M}{\gamma_2} \tag{359}$$

$$w_2 = 0 \tag{360}$$

$$\Psi_2 = -\frac{M}{\gamma_2} \tag{361}$$

$$w_3 = 0 \tag{362}$$

$$\Psi_3 = \frac{M}{\gamma_4} \tag{363}$$

$$w_4 = -\frac{ML_2^2}{2E_2I_2} - \frac{ML_2}{\gamma_4} \tag{364}$$

$$\Psi_4 = \frac{ML_2}{E_2I_2} - \frac{M}{\gamma_4} \tag{365}$$

Concentrated transverse load Q :

$$w_1 = -\frac{QL_1^3}{4E_1I_1} - \frac{L_1Q}{A_1G_1k_1} - \frac{Q}{\gamma_1} - \frac{QL_1^2}{\gamma_2} \tag{366}$$

$$\Psi_1 = -\frac{QL_1^2}{2E_1I_1} - \frac{QL_1}{\gamma_2} \tag{367}$$

$$w_2 = -\frac{Q}{\gamma_1} \tag{368}$$

$$\Psi_2 = -\frac{QL_1}{\gamma_2} \tag{369}$$

$$w_3 = -\frac{Q}{\gamma_3} \tag{370}$$

$$\Psi_3 = \frac{QL_2}{\gamma_4} \tag{371}$$

$$w_4 = -\frac{QL_2^3}{4E_2I_2} - \frac{L_2Q}{A_2G_2k_2} - \frac{Q}{\gamma_3} - \frac{QL_2^2}{\gamma_4} \tag{372}$$

$$\Psi_4 = \frac{QL_2^2}{2E_2I_2} - \frac{QL_2}{\gamma_4} \tag{373}$$

Transversely distributed load F:

$$w_1 = -\frac{FL_1^4}{8E_1I_1} - \frac{FL_1^2}{2A_1G_1k_1} - \frac{FL_1}{\gamma_1} - \frac{FL_1^3}{2\gamma_2} \tag{374}$$

$$\Psi_1 = -\frac{FL_1^3}{4E_1I_1} - \frac{FL_1^2}{2\gamma_2} \tag{375}$$

$$w_2 = -\frac{FL_1}{\gamma_1} \tag{376}$$

$$\Psi_2 = -\frac{FL_1^2}{2\gamma_2} \tag{377}$$

3.6 F

conventi

particula

and beam

the contr

strain. w

possible

function

beam e

marked

Concer

In this

$$w_3 = -\frac{FL_2}{\gamma_3} \tag{378}$$

$$\Psi_3 = \frac{FL_2^2}{\gamma_4} \tag{379}$$

$$w_4 = -\frac{FL_2^3}{8E_2I_2} - \frac{L_2^2F}{2A_2G_2k_2} - \frac{FL_2}{\gamma_3} - \frac{FL_2^3}{2\gamma_4} \tag{380}$$

$$\Psi_4 = \frac{FL_2^3}{4E_2I_2} - \frac{FL_2^2}{2\gamma_4} \tag{381}$$

3.6 Full versus Reduced Integration

As we said previously, we want to compare the results produced by use of a conventional FE formulation with those generated by the Reduced Integration one. In particular, we want to examine the difference in the relations among penalty parameters and beam properties. The following outcomes show that these relations always differ for the contribution of a term of the type $kAGL$. This term accounts for the transverse shear strain, which is usually very small compared to the bending deformation. Thus, it is possible to conclude that in the two methods the expressions for penalty parameters, as function of the beam properties, are similar.

The penalty parameters from the conventional full-integrated linear Timoshenko beam element are identified by the subscript "FI", while the reduced integration ones are marked by "RI".

Concentrated Moment M:

In this case, the ratio $\frac{w_2^{penalty}}{w_2^{exact}}$ produces:

While,

Concen

From $\frac{w}{w}$

$\chi_1^{\prime\prime} = /$

$\chi_2^{\prime\prime} = /$

While,

$$\gamma_2^{FI} = \beta \cdot \left(\frac{2EI}{L} + \frac{kAGL}{6} \right) \tag{382}$$

$$\gamma_2^{RI} = \beta \cdot \left(\frac{2EI}{L} \right) \tag{383}$$

While, the ratio $\frac{\Psi_2^{penalty}}{\Psi_2^{exact}}$ requires:

$$\gamma_2^{FI} = \beta \cdot \left(\frac{EI}{L} + \frac{kAGL}{12} \right) \tag{384}$$

$$\gamma_2^{RI} = \beta \cdot \left(\frac{EI}{L} \right) \tag{385}$$

Concentrated Transversal Load Q:

From $\frac{w_2^{penalty}}{w_2^{exact}}$ we have:

$$\gamma_1^{FI} = \beta \cdot \frac{2kAG\left(12EI + kAGL^2\right)}{\left(12EIL + 4kAGL^3\right)} = \beta \cdot 2\left[\frac{kAGEI}{\left(EIL + \frac{1}{3}kAGL^3 \right)} + \frac{\left(kAGL\right)^2}{\left(12EIL + 4kAGL^3\right)} \right] \tag{386}$$

$$\gamma_1^{RI} = \beta \cdot \frac{2kAGEI}{\left(EIL + \frac{1}{4}kAGL^3 \right)} \tag{387}$$

$$\gamma_2^{FI} = \beta \cdot \frac{2kAGL^2\left(12EI + kAGL^2\right)}{\left(12EIL + 4kAGL^3\right)} = \beta \cdot 2\left[\frac{kAGEIL^2}{\left(EIL + \frac{1}{3}kAGL^3 \right)} + \frac{\left(kAG\right)^2 \cdot L^4}{\left(12EIL + 4kAGL^3\right)} \right] \tag{388}$$

$$\gamma_2^{RI} = \beta \cdot \frac{2kAGEIL^2}{\left(EIL + \frac{1}{4}kAGL^3 \right)} \tag{389}$$

While, the ratio $\frac{\Psi_2^{penalty}}{\Psi_2^{exact}}$ produces:

Transv

In this

$\gamma^{*} =$

$\gamma_{\cdot} = \beta$

While,

$$\gamma_2^{FI} = \beta \cdot \left(\frac{2EI}{L} + \frac{kAGL}{6} \right) \tag{390}$$

$$\gamma_2^{RI} = \beta \cdot \left(\frac{2EI}{L} \right) \tag{391}$$

Transversely Distributed Load F:

In this case, the ratio $\frac{w_2^{penalty}}{w_2^{exact}}$ produces:

$$\gamma_1^{FI} = \beta \cdot \frac{2kAG\left(12EI + kAGL^2\right)}{\left(12EIL + 4kAGL^3\right)} = \beta \cdot 2\left[\frac{kAGEI}{\left(EIL + \frac{1}{3}kAGL^3 \right)} + \frac{(kAGL)^2}{\left(12EIL + 4kAGL^3\right)} \right] \tag{392}$$

$$\gamma_1^{RI} = \beta \cdot \frac{2kAGEI}{\left(EIL + \frac{1}{4}kAGL^3 \right)} \tag{393}$$

$$\gamma_2^{FI} = \beta \cdot \frac{2kAGL^2\left(12EI + kAGL^2\right)}{\left(12EIL + 4kAGL^3\right)} = \beta \cdot 2\left[\frac{kAGEIL^2}{\left(EIL + \frac{1}{3}kAGL^3 \right)} + \frac{(kAG)^2 \cdot L^4}{\left(12EIL + 4kAGL^3\right)} \right] \tag{394}$$

$$\gamma_2^{RI} = \beta \cdot \frac{2kAGEIL^2}{\left(EIL + \frac{1}{4}kAGL^3 \right)} \tag{395}$$

While, the ratio $\frac{\Psi_2^{penalty}}{\Psi_2^{exact}}$ produces:

$$\gamma_2^{FI} = \beta \cdot \left(\frac{2EI}{L} + \frac{kAGL}{6} \right) \tag{396}$$

$$\gamma_2^{RI} = \beta \cdot \left(\frac{2EI}{L} \right) \tag{397}$$

3.7 I

the stif

2) to ch

3.7.1

assemb

paramet

consecu

The int

of free

Chang

3.7 Interface Element

The work done so far gives us the tools to achieve two different tasks: 1) to define the stiffness matrix of an "Interface" element for the linear Timoshenko beam elements; 2) to choose automatically the best values of the penalty parameters.

3.7.1 Stiffness Matrix

We first consider the uniaxial load case. We observe the stiffness matrix of the assembled system (Section 3.2.2) composed by two beams connected through the penalty parameter. We notice that the matrix could be seen as the result of assembling three consecutive elements.

$$\begin{bmatrix} \frac{E_1A_1}{L} & -\frac{E_1A_1}{L} & 0 & 0 & 0 \\ -\frac{E_1A_1}{L} & \frac{E_1A_1}{L}+\gamma_1 & 0 & 0 & -\gamma_1 \\ 0 & 0 & \frac{E_2A_2}{L}+\gamma_2 & -\frac{E_2A_2}{L} & -\gamma_2 \\ 0 & 0 & -\frac{E_2A_2}{L} & \frac{E_2A_2}{L} & 0 \\ 0 & -\gamma_1 & -\gamma_2 & 0 & \gamma_1+\gamma_2 \end{bmatrix} \begin{Bmatrix} 0 \\ u_2 \\ u_3 \\ u_4 \\ v \end{Bmatrix} = \begin{Bmatrix} f_1 \\ 0 \\ 0 \\ P \\ 0 \end{Bmatrix} \tag{398}$$

The intermediate interface element would be constituted by three points with one degree of freedom each, and would have the following stiffness matrix and displacement vector.

$$\begin{bmatrix} \gamma_1 & 0 & -\gamma_1 \\ 0 & \gamma_2 & -\gamma_2 \\ -\gamma_1 & -\gamma_2 & \gamma_1+\gamma_2 \end{bmatrix} \begin{Bmatrix} u_2 \\ u_3 \\ v \end{Bmatrix} \tag{399}$$

Changing the order of the axial displacements, it is:

$$\begin{bmatrix} \gamma_1 & -\gamma_1 & 0 \\ -\gamma_1 & \gamma_1+\gamma_2 & -\gamma_2 \\ 0 & -\gamma_2 & \gamma_2 \end{bmatrix} \begin{Bmatrix} u_2 \\ v \\ u_3 \end{Bmatrix} \tag{400}$$

element

and loac

nodes wi

u

Figure 6.

To write

parameter

Table 1.

The same path can be followed starting from our study of the two linear beam elements connected using a Penalty parameter continuity constraint, fixed in the center and loaded with bending loads (Section 3.5.2). In this case the outcome is:

$$\begin{bmatrix} \gamma_1 & 0 & -\gamma_1 & 0 & 0 & 0 \\ 0 & \gamma_2 & 0 & -\gamma_2 & 0 & 0 \\ -\gamma_1 & 0 & \gamma_1+\gamma_3 & 0 & -\gamma_3 & 0 \\ 0 & -\gamma_2 & 0 & \gamma_2+\gamma_4 & 0 & -\gamma_4 \\ 0 & 0 & -\gamma_3 & 0 & \gamma_3 & 0 \\ 0 & 0 & 0 & -\gamma_4 & 0 & \gamma_4 \end{bmatrix} \begin{Bmatrix} w_1 \\ \Psi_1 \\ w_v \\ \Psi_v \\ w_2 \\ \Psi_2 \end{Bmatrix} \tag{401}$$

Now, if we join the two stiffness matrices, an interface element made of three nodes with three DOFs each would be defined, as in Figure 6.

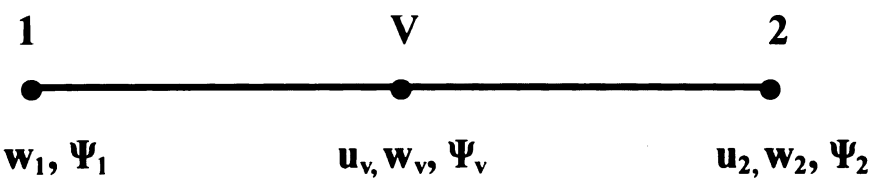

Figure 6. ***Interface element for the Timoshenko beam element***

To write the new 9x9 stiffness matrix, we need first to redefine the name of the penalty parameters to be associated with each of the constraints. Table 1 achieves this task.

Table 1. ***Penalty parameters associated with each of the constraints enforced***

Penalty parameter	Constraint enforced
γ_{11}	$(u_v - u_1)$
γ_{21}	$(w_v - w_1)$
γ_{31}	$(\Psi_v - \Psi_1)$
γ_{12}	$(u_v - u_2)$
γ_{22}	$(w_v - w_2)$
γ_{32}	$(\Psi_v - \Psi_2)$

Thus, the stiffness matrix and the displacement vector of the interface element are:

$$\begin{bmatrix} \gamma_{11} & 0 & 0 & -\gamma_{11} & 0 & 0 & 0 & 0 & 0 \\ 0 & \gamma_{21} & 0 & 0 & -\gamma_{21} & 0 & 0 & 0 & 0 \\ 0 & 0 & \gamma_{31} & 0 & 0 & -\gamma_{31} & 0 & 0 & 0 \\ -\gamma_{11} & 0 & 0 & \gamma_{11}+\gamma_{12} & 0 & 0 & -\gamma_{12} & 0 & 0 \\ 0 & -\gamma_{21} & 0 & 0 & \gamma_{22}+\gamma_{21} & 0 & 0 & -\gamma_{22} & 0 \\ 0 & 0 & -\gamma_{31} & 0 & 0 & \gamma_{31}+\gamma_{32} & 0 & 0 & -\gamma_{32} \\ 0 & 0 & 0 & -\gamma_{12} & 0 & 0 & \gamma_{12} & 0 & 0 \\ 0 & 0 & 0 & 0 & -\gamma_{22} & 0 & 0 & \gamma_{22} & 0 \\ 0 & 0 & 0 & 0 & 0 & -\gamma_{32} & 0 & 0 & \gamma_{32} \end{bmatrix} \begin{Bmatrix} u_1 \\ w_1 \\ \Psi_1 \\ u_v \\ w_v \\ \Psi_v \\ u_2 \\ w_2 \\ \Psi_2 \end{Bmatrix} \quad (402)$$

3.7.2 Best Values of the Penalty Parameters

Consider the problem, plotted in Figure 7, of two linear Timoshenko beams connected through an interface element.

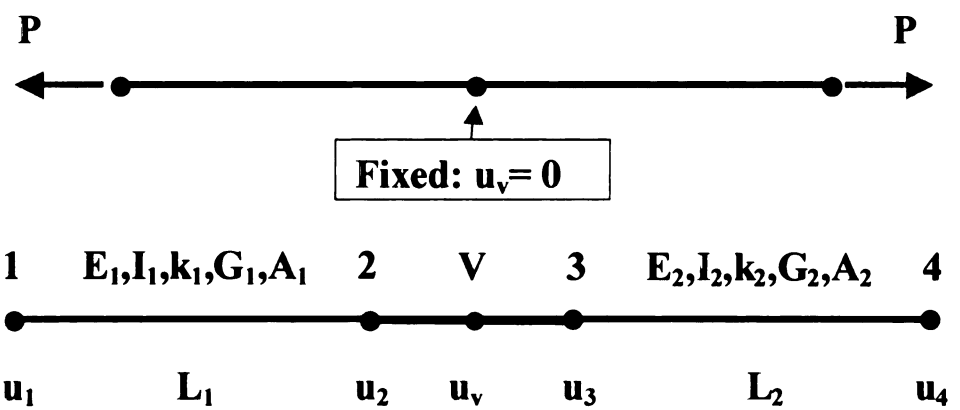

Figure 7. ***Beam under axial loads – Two Elements***

Results obtained in sections 3.1.4 and 3.2.4 lead us to affirm that the penalty parameters γ_{11} and γ_{12} should be:

$$\gamma_{11} = \beta \cdot \left(\frac{E_1 A_1}{L_1} \right) \quad (403)$$

$$\gamma_{12} = \beta \cdot \left(\frac{E_2 A_2}{L_2} \right) \tag{404}$$

The ratio between the solutions of the problem becomes independent of material and geometrical properties of the beams.

$$\frac{u_1^{penalty}}{u_1^{exact}} = \frac{u_4^{penalty}}{u_4^{exact}} = 1 + \frac{1}{\beta} \tag{405}$$

Based on the results of sections 3.4.4 and 3.5.2, for the other two DOFs, w and Ψ, a similar conclusion can be reached for each kind of bending load. However, in this case we cannot find the values of the penalty parameters that make true both of the following equations:

$$\frac{w_1^{penalty}}{w_1^{Lagrange}} = \frac{w_4^{penalty}}{w_4^{Lagrange}} = 1 + \frac{1}{\beta} \tag{406}$$

$$\frac{\Psi_1^{penalty}}{\Psi_1^{Lagrange}} = \frac{\Psi_4^{penalty}}{\Psi_4^{Lagrange}} = 1 + \frac{1}{\beta} \tag{407}$$

We can satisfy exactly only one of the two equations, and assign to the other one a value of the penalty parameter greater than required.

Concentrated Moment M

In order to get equation (406) to be true in the presence of a concentrated moment M, we need the following.

$$\gamma_{31} = \beta \cdot \frac{2E_1 I_1}{L_1} \tag{408}$$

$$\gamma_{32} = \beta \cdot \frac{2E_2 I_2}{L_2} \tag{409}$$

Instead, to fulfill the relation (407), it is required that:

A cho

option

As a c

Conce

Eq

While eq

$$\gamma_{31} = \beta \cdot \frac{E_1 I_1}{L_1} \tag{410}$$

$$\gamma_{32} = \beta \cdot \frac{E_2 I_2}{L_2} \tag{411}$$

A choice needs to be taken between the two groups of two values. The most reasonable option is to take the higher value and satisfy (406), that is:

$$\gamma_{31} = \beta \cdot \frac{2E_1 I_1}{L_1}, \quad \gamma_{32} = \beta \cdot \frac{2E_2 I_2}{L_2} \tag{412}$$

As a consequence, this selection determines the next equation to be true.

$$\frac{\Psi_1^{penalty}}{\Psi_1^{Lagrange}} = \frac{\Psi_4^{penalty}}{\Psi_4^{Lagrange}} = 1 + \frac{1}{2\beta} \tag{413}$$

Concentrated Transverse Load Q

Equation (406) requires:

$$\gamma_{21} = \beta \cdot \frac{2}{\left(\frac{L_1^3}{4E_1 I_1} + \frac{L_1}{k_1 A_1 G_1}\right)} \tag{414}$$

$$\gamma_{31} = \beta \cdot \frac{2L_1^2}{\left(\frac{L_1^3}{4E_1 I_1} + \frac{L_1}{k_1 A_1 G_1}\right)} \tag{415}$$

$$\gamma_{22} = \beta \cdot \frac{2}{\left(\frac{L_2^3}{4E_2 I_2} + \frac{L_2}{k_2 A_2 G_2}\right)} \tag{416}$$

$$\gamma_{32} = \beta \cdot \frac{2L_2^2}{\left(\frac{L_2^3}{4E_2 I_2} + \frac{L_2}{k_2 A_2 G_2}\right)} \tag{417}$$

While equation (407) specifies:

There

which

only w

known.

Transv

require

While e

$$\gamma_{31} = \beta \cdot \frac{E_1 I_1}{L_1} \tag{418}$$

$$\gamma_{32} = \beta \cdot \frac{E_2 I_2}{L_2} \tag{419}$$

There are no simple relations between the two expressions for γ_{31} and γ_{32} to tell us which to choose. Then, it is convenient to compare their values and take the bigger one only when the material and geometrical properties of the two beams being connected are known.

Transversely Distributed Load F

Results for this load case are similar to those of the previous. Equation (406) requires:

$$\gamma_{21} = \beta \cdot \frac{2L_1}{\left(\frac{L_1^4}{8E_1 I_1} + \frac{L_1^2}{2k_1 A_1 G_1}\right)} \tag{420}$$

$$\gamma_{31} = \beta \cdot \frac{2L_1^3}{\left(\frac{L_1^4}{4E_1 I_1} + \frac{L_1^2}{k_1 A_1 G_1}\right)} \tag{421}$$

$$\gamma_{22} = \beta \cdot \frac{2L_2}{\left(\frac{L_2^4}{8E_2 I_2} + \frac{L_2^2}{2k_2 A_2 G_2}\right)} \tag{422}$$

$$\gamma_{32} = \beta \cdot \frac{2L_2^3}{\left(\frac{L_2^4}{4E_2 I_2} + \frac{L_2^2}{k_2 A_2 G_2}\right)} \tag{423}$$

While equation (407) specifies:

$$\gamma_{31} = \beta \cdot \frac{2E_1 I_1}{L_1} \tag{424}$$

$$\gamma_{32} = \beta \cdot \frac{2E_2 I_2}{L_2} \tag{425}$$

Again, no simple relations exist between the two expressions for γ_{31} and γ_{32} to tell us which to choose. When the material and geometrical properties of the two beams is known the bigger one can be identified and chosen.

Table 2 summarizes the all relations among the penalty parameters and model characteristics.

Table 2. ***Penalty parameters relations for a Timoshenko beam element.***

	Axial load	**Moment applied at the tip**	**Transverse load applied at the tip**	**Transversely Distributed Load**
γ_{u1}	$\beta \cdot \left(\frac{E_1 A_1}{L_1} \right)$	-	-	-
γ_{w1}	-	-	$\beta \cdot \frac{2}{\left(\frac{L_1^3}{4E_1 I_1} + \frac{L_1}{k_1 A_1 G_1} \right)}$	$\beta \cdot \frac{2L_1}{\left(\frac{L_1^4}{8E_1 I_1} + \frac{L_1^2}{2k_1 A_1 G_1} \right)}$
$\gamma_{\psi 1}$	-	$\beta \cdot \frac{2E_1 I_1}{L_1}$	$\beta \cdot \frac{2L_1^2}{\left(\frac{L_1^3}{4E_1 I_1} + \frac{L_1}{k_1 A_1 G_1} \right)}$ or $\beta \cdot \frac{E_1 I_1}{L_1}$	$\beta \cdot \frac{2L_1^3}{\left(\frac{L_1^4}{4E_1 I_1} + \frac{L_1^2}{k_1 A_1 G_1} \right)}$ or $\beta \cdot \frac{2E_1 I_1}{L_1}$
γ_{u2}	$\beta \cdot \left(\frac{E_2 A_2}{L_2} \right)$	-	-	-
γ_{w2}	-	-	$\beta \cdot \frac{2}{\left(\frac{L_2^3}{4E_2 I_2} + \frac{L_2}{k_2 A_2 G_2} \right)}$	$\beta \cdot \frac{2L_2}{\left(\frac{L_2^4}{8E_2 I_2} + \frac{L_2^2}{2k_2 A_2 G_2} \right)}$
$\gamma_{\psi 2}$	-	$\beta \cdot \frac{2E_2 I_2}{L_2}$	$\beta \cdot \frac{2L_2^2}{\left(\frac{L_2^3}{4E_2 I_2} + \frac{L_2}{k_2 A_2 G_2} \right)}$ or $\beta \cdot \frac{E_2 I_2}{L_2}$	$\beta \cdot \frac{2L_2^3}{\left(\frac{L_2^4}{4E_2 I_2} + \frac{L_2^2}{k_2 A_2 G_2} \right)}$ or $\beta \cdot \frac{2E_2 I_2}{L_2}$

3.8 Numerical Results

To test the behavior of the relations just obtained for an automatic choice of the penalty parameters, the developed Interface element has been implemented in the commercial finite element code "ABAQUS".

The User Element Subroutine (UEL) receives all the necessary information about geometry and material properties of the two connected Timoshenko beams from the input file. Then, the stiffness matrix of the interface element is built. Inside the subroutine, that is written in Fortran 77, a series of "IF" structures select the appropriate values of penalty parameters in all cases where a choice is required.

3.8.1 One Element – Clamped Beam

We will test first the resulting displacements of a beam under: axial load P, transversely distributed load F, concentrated moment M and force Q applied at the tip.

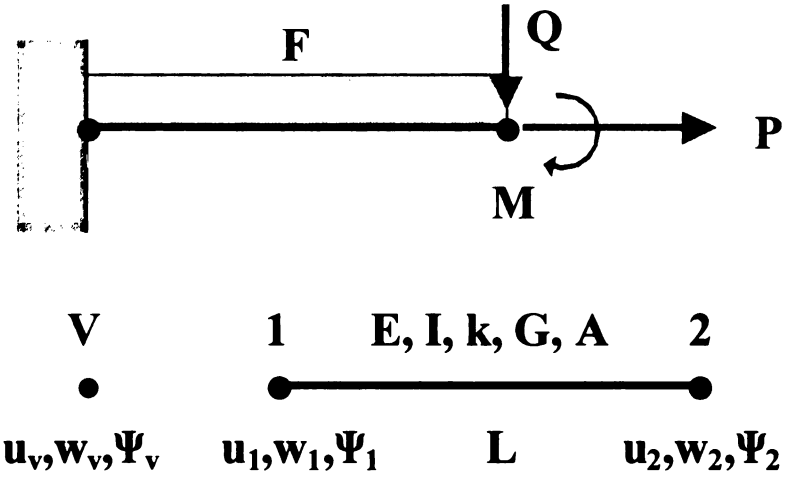

Figure 8. ***Beam under bending loads – One Element***

This case is analyzed using a single linear Timoshenko beam element connected to an undeformable structure by an interface element. The configuration of the geometry and the mesh is plotted in Figure 8. The beam properties are:

Length=0.5, thickness=0.1, width=0.1, Young's modulus=200.E9, shear correction factor=0.85

In Table 3 the results for various combinations of load are presented. The word "Abaqus" marks the outcomes obtained without using the interface element, that in this case means to set $w_1 = 0$ and $\Psi_1 = 0$. Instead, the word "UEL" indicates the use of the interface element.

Table 3. ***Single beam clamped - Outcomes***

	w_2 Abaqus	w_2 UEL	w_2^{Abaqus} / w_2^{UEL}	Ψ_2 Abaqus	Ψ_2 UEL	$\Psi_2^{Abaqus} / \Psi_2^{UEL}$
P	5.0000E-08	5.0050E-08	9.9900E-01	0	0	1
M	-3.0000E-03	-3.0030E-03	9.9900E-01	-6.0000E-03	-6.0030E-03	9.9950E-01
Q	-1.7942E-03	-1.7972E-03	9.9833E-01	-3.0000E-03	-3.0015E-03	9.9950E-01
F	-8.9712E-04	-8.9937E-04	9.9750E-01	-1.5000E-03	-1.5008E-03	9.9947E-01
M+Q	-4.7942E-03	-4.7972E-03	9.9937E-01	-9.0000E-03	-9.0020E-03	9.9978E-01
M+Q+F	-5.6914E-03	-5.6941E-03	9.9953E-01	-1.0500E-02	-1.0502E-02	9.9981E-01

We assumed all the loads to have the magnitude 1 and $\beta = 1000$.

3.8.2 Two Elements – Clamped Beam

Consider the problem wherein two linear beam elements are connected using an interface element and clamped at the tip of one beam. The configuration of the geometry and the mesh are plotted in Figure 9.

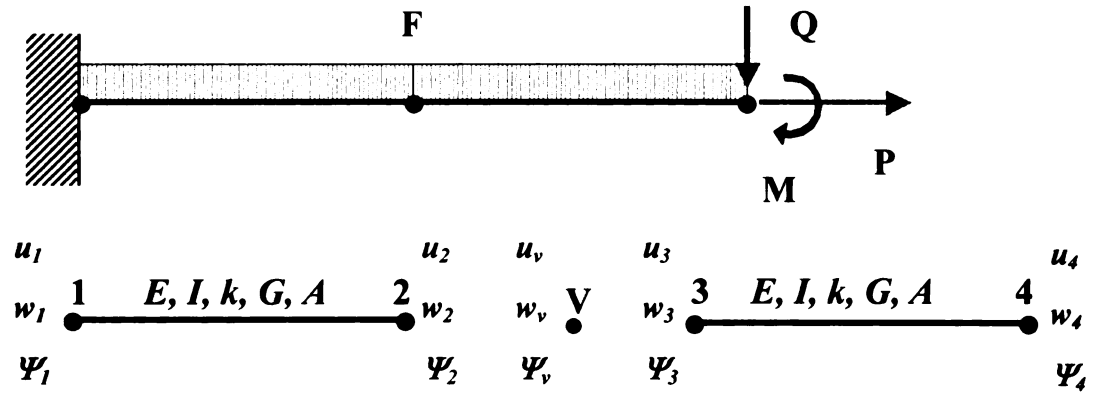

Figure 9. ***Two beam elements joined through an interface element***

The two beams are made of the same material, whose properties are:

Length=0.5, thickness=0.1, width=0.1, Young's modulus=200.E9, shear correction factor=0.85

Table 4. ***Two beams clamped - Outcomes***

	w_4 Abaqus	w_4 UEL	w_4^{Abaqus} / w_4^{UEL}	Ψ_4 Abaqus	Ψ_4 UEL	$\Psi_4^{Abaqus} / \Psi_4^{UEL}$
A	5.0000E-05	5.0050E-05	9.9900E-01	0	0	1.0000E+00
M	-3.0000E-03	-3.0020E+00	9.9933E-04	-6.0000E-03	-6.0030E+00	9.9950E-04
Q	-1.9486E-03	-1.9494E-03	9.9959E-01	-3.0000E-03	-3.0008E-03	9.9973E-01
F	-7.8682E-04	-7.8710E-04	9.9964E-01	-1.1250E-03	-1.1252E-03	9.9982E-01
M+Q	-4.9486E-03	-4.9497E-03	9.9978E-01	-9.0000E-03	-9.0015E-03	9.9983E-01
M+Q+F	-5.7355E-03	-5.7362E-03	9.9988E-01	-1.0125E-02	-1.0126E-02	9.9990E-01

In Table 3 the results for various combinations of load are presented. We assumed all the loads to have the magnitude 1 and $\beta = 1000$.

3.8.3 Two Elements – Two Materials – Clamped Beam

Consider two linear beams elements connected using an interface element and clamped at the tip of one beam. The configuration of the geometry and the mesh are plotted in Figure 10. The two beams are made of two different materials, whose

properties are:

Beam 1

Length=0.5, thickness=0.1, width=0.1, Young's Modulus=200.E9, shear correction factor=0.85

Beam 2

Length=0.5, thickness=0.05, width=0.05, Young's Modulus=1.E9, shear correction factor=0.85

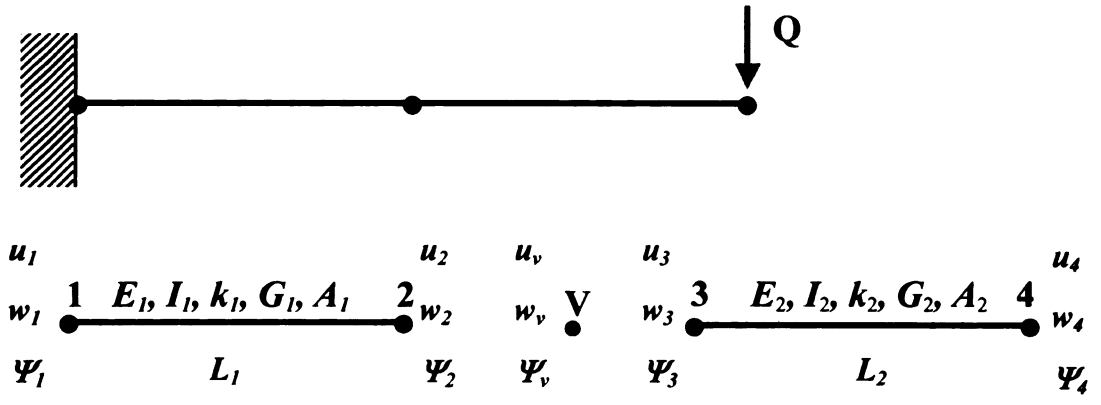

Figure 10. ***Two beam elements joined through an interface element***

In Table 5 the results for a concentrated force Q of magnitude 1 applied at the tip of the beam are presented for various values of β.

Table 5. ***Two beams – two materials - clamped - Outcomes***

	w_4 Abaqus	w_4 UEL	w_4^{Abaqus} / w_4^{UEL}	Ψ_4 Abaqus	Ψ_4 UEL	$\Psi_4^{Abaqus} / \Psi_4^{UEL}$
β=1E3	-7.2408E-05	-7.2529E-05	9.9833E-01	-2.4022E-04	-2.4035E-04	9.9946E-01
β=1E4	-7.2408E-05	-7.2420E-05	9.9983E-01	-2.4022E-04	-2.4024E-04	9.9992E-01
β=1E5	-7.2408E-05	-7.2410E-05	9.9997E-01	-2.4022E-04	-2.4023E-04	9.9996E-01

3.8.4 Three Elements – Simply Supported Beam

Three linear beam elements are connected using two interface elements. All the

system is simply supported. The configuration and the mesh are plotted in Figure 11.

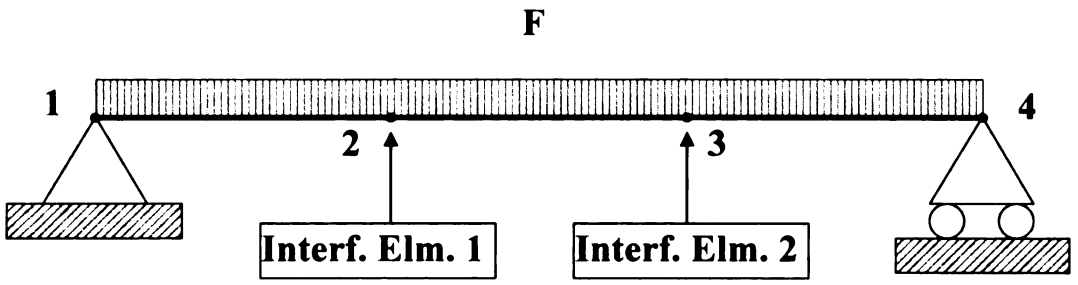

Figure 11. ***Three elements simply supported beam***

The three beams are made of three different materials, whose properties are:

Beam 1

Length=0.5, thickness=0.15, width=0.15, Young's Modulus=400.E9, shear correction factor=0.85

Beam 2

Length=0.5, thickness=0.1, width=0.1, Young's Modulus=200.E9, shear correction factor=0.85

Beam 3

Length=0.5, thickness=0.025, width=0.025, Young's Modulus=100.E9, shear correction factor=0.85

In Table 6 the results for a distributed force F of magnitude 1 are presented for $\beta = 1E4$.

Table 6. ***Three elements simply supported beam - Outcomes***

	w_4 Abaqus	w_4 UEL	w_4^{Abaqus} / w_4^{UEL}	Ψ_4 Abaqus	Ψ_4 UEL	$\Psi_4^{Abaqus} / \Psi_4^{UEL}$
Node 1	0.0000E+00	0.0000E+00	1.0000E+00	-3.8741E-06	-3.8746E-06	9.9987E-01
Node 2	-1.9364E-06	-1.9366E-06	9.9990E-01	-3.8704E-06	-3.8709E-06	9.9987E-01
Node 3	-3.8529E-06	-3.8533E-06	9.9990E-01	-3.7954E-06	-3.7959E-06	9.9987E-01
Node 4	0.0000E+00	0.0000E+00	1.0000E+00	1.5405E-05	1.5405E-05	1.0000E+00

CHAPTER 4 PLANE STRESS QUADRILATERAL ELEMENT

4.1 Finite Element Model

In this chapter an interface element for plane stress quadrilateral elements is developed. The plane elasticity problems are described by two coupled partial differential equations expressed in terms of the two components of the displacement vector u and v.

$$-\frac{\partial}{\partial x}(c_{11}\frac{\partial u}{\partial x}+c_{12}\frac{\partial v}{\partial y})-\frac{\partial}{\partial y}\left[c_{66}\left(\frac{\partial u}{\partial y}+\frac{\partial v}{\partial x}\right)\right]=f_x \tag{426}$$

$$-\frac{\partial}{\partial x}\left[c_{66}\left(\frac{\partial u}{\partial y}+\frac{\partial v}{\partial x}\right)\right]-\frac{\partial}{\partial y}(c_{12}\frac{\partial u}{\partial x}+c_{22}\frac{\partial v}{\partial y})=f_y \tag{427}$$

For an isotropic material the constant terms c_{ij} are defined in the plane stress stress-strain relations to be:

$$\begin{aligned} c_{11} &= c_{22} = \frac{Y}{1-\nu^2} \\ c_{12} &= \nu c_{11} \\ c_{66} &= G_{12} = \frac{Y}{2(1+\nu)} \end{aligned} \tag{428}$$

Where Y is the Young's modulus.

Appling the total potential energy principle, the weak form of the two governing

equations can be developed. The associated finite element model is:

$$\begin{bmatrix} [K^{11}] & [K^{12}] \\ [K^{12}]^T & [K^{22}] \end{bmatrix} \begin{Bmatrix} \{u\} \\ \{v\} \end{Bmatrix} = \begin{Bmatrix} \{F^1\} \\ \{F^2\} \end{Bmatrix} \tag{429}$$

Where:

$$K_{ij}^{11} = \int_{\Omega_e} h \left(c_{11} \frac{\partial N_i}{\partial x} \frac{\partial N_j}{\partial x} + c_{66} \frac{\partial N_i}{\partial y} \frac{\partial N_j}{\partial y} \right) dxdy \tag{430}$$

$$K_{ij}^{12} = \int_{\Omega_e} h \left(c_{12} \frac{\partial N_i}{\partial x} \frac{\partial N_j}{\partial y} + c_{66} \frac{\partial N_i}{\partial y} \frac{\partial N_j}{\partial x} \right) dxdy \tag{431}$$

$$K_{ij}^{21} = \left[K_{ij}^{12} \right]^T \tag{432}$$

$$K_{ij}^{22} = \int_{\Omega_e} h \left(c_{66} \frac{\partial N_i}{\partial x} \frac{\partial N_j}{\partial x} + c_{22} \frac{\partial N_i}{\partial y} \frac{\partial N_j}{\partial y} \right) dxdy \tag{433}$$

where h is the thickness of the structure.

In the following, the stiffness matrix defined above is computed for a rectangular element having the in plane dimensions shown in Figure 12 and a thickness equal to h.

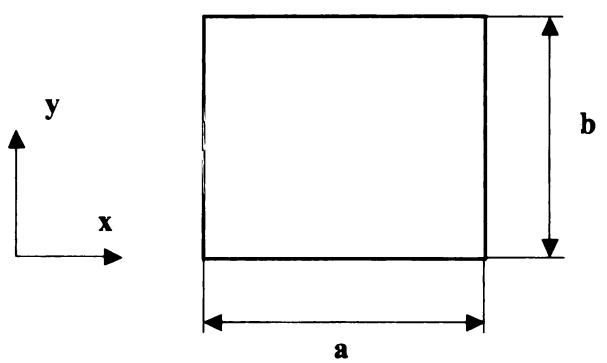

Figure 12. ***Geometrical dimensions of the rectangular element.***

Assuming the Poisson ratio ν to be zero, and the displacements to be approximated through the linear Lagrange interpolation functions, the matrices K_{ij} are:

$$K_{11} = h\left(Y \begin{matrix} b \\ 6a \end{matrix} \begin{pmatrix} 2 & -2 & -1 & 1 \\ -2 & 2 & 1 & -1 \\ -1 & 1 & 2 & -2 \\ 1 & -1 & -2 & 2 \end{pmatrix} + \begin{matrix} Y & a \\ 2 & 6b \end{matrix} \begin{pmatrix} 2 & 1 & -1 & -2 \\ 1 & 2 & -2 & -1 \\ -1 & -2 & 2 & 1 \\ -2 & -1 & 1 & 2 \end{pmatrix} \right) =$$

$$\begin{pmatrix} h\left(\frac{aY}{6b} + \frac{bY}{3a}\right) & h\left(\frac{aY}{12b} - \frac{bY}{3a}\right) & h\left(-\frac{aY}{12b} - \frac{bY}{6a}\right) & h\left(-\frac{aY}{6b} + \frac{bY}{6a}\right) \\ h\left(\frac{aY}{12b} - \frac{bY}{3a}\right) & h\left(\frac{aY}{6b} + \frac{bY}{3a}\right) & h\left(-\frac{aY}{6b} + \frac{bY}{6a}\right) & h\left(-\frac{aY}{12b} - \frac{bY}{6a}\right) \\ h\left(-\frac{aY}{12b} - \frac{bY}{6a}\right) & h\left(-\frac{aY}{6b} + \frac{bY}{6a}\right) & h\left(\frac{aY}{6b} + \frac{bY}{3a}\right) & h\left(\frac{aY}{12b} - \frac{bY}{3a}\right) \\ h\left(-\frac{aY}{6b} + \frac{bY}{6a}\right) & h\left(-\frac{aY}{12b} - \frac{bY}{6a}\right) & h\left(\frac{aY}{12b} - \frac{bY}{3a}\right) & h\left(\frac{aY}{6b} + \frac{bY}{3a}\right) \end{pmatrix} \quad (434)$$

$$K_{22} = h\left(\begin{matrix} Y & b \\ 2 & 6a \end{matrix} \begin{pmatrix} 2 & -2 & -1 & 1 \\ -2 & 2 & 1 & -1 \\ -1 & 1 & 2 & -2 \\ 1 & -1 & -2 & 2 \end{pmatrix} + Y \begin{matrix} a \\ 6b \end{matrix} \begin{pmatrix} 2 & 1 & -1 & -2 \\ 1 & 2 & -2 & -1 \\ -1 & -2 & 2 & 1 \\ -2 & -1 & 1 & 2 \end{pmatrix} \right) =$$

$$\begin{pmatrix} h\left(\frac{aY}{3b} + \frac{bY}{6a}\right) & h\left(\frac{aY}{6b} - \frac{bY}{6a}\right) & h\left(-\frac{aY}{6b} - \frac{bY}{12a}\right) & h\left(-\frac{aY}{3b} + \frac{bY}{12a}\right) \\ h\left(\frac{aY}{6b} - \frac{bY}{6a}\right) & h\left(\frac{aY}{3b} + \frac{bY}{6a}\right) & h\left(-\frac{aY}{3b} + \frac{bY}{12a}\right) & h\left(-\frac{aY}{6b} - \frac{bY}{12a}\right) \\ h\left(-\frac{aY}{6b} - \frac{bY}{12a}\right) & h\left(-\frac{aY}{3b} + \frac{bY}{12a}\right) & h\left(\frac{aY}{3b} + \frac{bY}{6a}\right) & h\left(\frac{aY}{6b} - \frac{bY}{6a}\right) \\ h\left(-\frac{aY}{3b} + \frac{bY}{12a}\right) & h\left(-\frac{aY}{6b} - \frac{bY}{12a}\right) & h\left(\frac{aY}{6b} - \frac{bY}{6a}\right) & h\left(\frac{aY}{3b} + \frac{bY}{6a}\right) \end{pmatrix} \quad (435)$$

$$K_{12} = h\left(Y \begin{matrix} 1 \\ 2 \end{matrix} \begin{pmatrix} \frac{1}{4} & -\frac{1}{4} & -\frac{1}{4} & \frac{1}{4} \\ \frac{1}{4} & -\frac{1}{4} & -\frac{1}{4} & \frac{1}{4} \\ -\frac{1}{4} & \frac{1}{4} & \frac{1}{4} & -\frac{1}{4} \\ -\frac{1}{4} & \frac{1}{4} & \frac{1}{4} & -\frac{1}{4} \end{pmatrix} \right) = \begin{pmatrix} \frac{hY}{8} & -\frac{hY}{8} & -\frac{hY}{8} & \frac{hY}{8} \\ \frac{hY}{8} & -\frac{hY}{8} & -\frac{hY}{8} & \frac{hY}{8} \\ -\frac{hY}{8} & \frac{hY}{8} & \frac{hY}{8} & -\frac{hY}{8} \\ -\frac{hY}{8} & \frac{hY}{8} & \frac{hY}{8} & -\frac{hY}{8} \end{pmatrix} \quad (436)$$

Finally, the stiffness matrix of the rectangular element can be defined.

$$K_{el} = \begin{pmatrix} h\left(\frac{aY}{6b} + \frac{bY}{3a}\right) & h\left(\frac{aY}{12b} - \frac{bY}{3a}\right) & h\left(-\frac{aY}{12b} - \frac{bY}{6a}\right) & h\left(-\frac{aY}{6b} + \frac{bY}{6a}\right) & \frac{hY}{8} & -\frac{hY}{8} & -\frac{hY}{8} & \frac{hY}{8} \\ h\left(\frac{aY}{12b} - \frac{bY}{3a}\right) & h\left(\frac{aY}{6b} + \frac{bY}{3a}\right) & h\left(-\frac{aY}{6b} + \frac{bY}{6a}\right) & h\left(-\frac{aY}{12b} - \frac{bY}{6a}\right) & \frac{hY}{8} & -\frac{hY}{8} & -\frac{hY}{8} & \frac{hY}{8} \\ h\left(-\frac{aY}{12b} - \frac{bY}{6a}\right) & h\left(-\frac{aY}{6b} + \frac{bY}{6a}\right) & h\left(\frac{aY}{6b} + \frac{bY}{3a}\right) & h\left(\frac{aY}{12b} - \frac{bY}{3a}\right) & -\frac{hY}{8} & \frac{hY}{8} & \frac{hY}{8} & -\frac{hY}{8} \\ h\left(-\frac{aY}{6b} + \frac{bY}{6a}\right) & h\left(-\frac{aY}{12b} - \frac{bY}{6a}\right) & h\left(\frac{aY}{12b} - \frac{bY}{3a}\right) & h\left(\frac{aY}{6b} + \frac{bY}{3a}\right) & -\frac{hY}{8} & \frac{hY}{8} & \frac{hY}{8} & -\frac{hY}{8} \\ \frac{hY}{8} & \frac{hY}{8} & -\frac{hY}{8} & -\frac{hY}{8} & h\left(\frac{aY}{3b} + \frac{bY}{6a}\right) & h\left(\frac{aY}{6b} - \frac{bY}{6a}\right) & h\left(-\frac{aY}{6b} - \frac{bY}{12a}\right) & h\left(-\frac{aY}{3b} + \frac{bY}{12a}\right) \\ -\frac{hY}{8} & -\frac{hY}{8} & \frac{hY}{8} & \frac{hY}{8} & h\left(\frac{aY}{6b} - \frac{bY}{6a}\right) & h\left(\frac{aY}{3b} + \frac{bY}{6a}\right) & h\left(-\frac{aY}{3b} + \frac{bY}{12a}\right) & h\left(-\frac{aY}{6b} - \frac{bY}{12a}\right) \\ -\frac{hY}{8} & -\frac{hY}{8} & \frac{hY}{8} & \frac{hY}{8} & h\left(-\frac{aY}{6b} - \frac{bY}{12a}\right) & h\left(-\frac{aY}{3b} + \frac{bY}{12a}\right) & h\left(\frac{aY}{3b} + \frac{bY}{6a}\right) & h\left(\frac{aY}{6b} - \frac{bY}{6a}\right) \\ \frac{hY}{8} & \frac{hY}{8} & -\frac{hY}{8} & -\frac{hY}{8} & h\left(-\frac{aY}{3b} + \frac{bY}{12a}\right) & h\left(-\frac{aY}{6b} - \frac{bY}{12a}\right) & h\left(\frac{aY}{6b} - \frac{bY}{6a}\right) & h\left(\frac{aY}{3b} + \frac{bY}{6a}\right) \end{pmatrix} \quad (437)$$

4.2 Cubic Spline Interpolation Functions

Spline functions [27-38] are mathematical tools able to build a curve constrained to pass smoothly through a set of data points. They exist in various orders, but cubic splines are the most widely used in engineering practice. They are expressed by third order interpolating polynomials that share the characteristic of having continuous first and second order derivatives. It follows that cubic splines do not have the "wiggle" problem associated with high-order interpolating polynomials.

In their general form, the cubic spline can interpolate as many data points as needed. However, because our search for the proper penalty parameters involved solving really large system of equations symbolically, we had to limit the number of DOFs by using few pseudo nodes to represent the interface elements. A natural cubic spline interpolation over three points appeared as the best choice for having a limited number of DOFs while maintaining a smooth approximation of interface displacements. The word *natural* indicates that the second derivatives at the end points are assumed to be zero, any extension of the spline beyond the ends would be straight. The Abaqus user element developed using the natural cubic spline interpolation behaves very well in most cases; it is also very computationally efficient. Nevertheless, for some categories of problems this approach can't achieve satisfactory results. In these cases, a general form of the cubic spline interpolation is adopted. Second derivatives at the end points are calculated by differentiating twice a cubic function which passes through the first four pseudo-nodes along the interface path and another cubic function that passes through the last four pseudo-nodes along the interface path. The Abaqus user element subroutine associated to general form of the cubic spline, allows the user to specify the desired number of nodes

composing the interface element.

Both cubic spline formulations are described in the following two sections, starting with the general form.

4.2.1 General Form of the Cubic Spline

The mathematical description of the cubic spline formulation can be found in several books [27-38]. Anyway, for an efficient implementation in our computer code we found very useful to adopt the matrix approach followed by Jonathan Ransom [40]. In this section, his methodology is reported.

Given a series of points x_i $(i = 0,1,\ldots,n)$ which are generally not evenly spaced, and the corresponding function values $f(x_i)$, the cubic spline function denoted $g(x)$ may be written as:

$$g(x) = \frac{g_{,xx}(x_i)}{6}\left[\frac{(x_{i+1}-x)^3}{\Delta x_i} - \Delta x_i (x_{i+1}-x)\right] + \frac{g_{,xx}(x_{i+1})}{6}\left[\frac{(x-x_i)^3}{\Delta x_i} - \Delta x_i (x-x_i)\right] + \\ + f(x_i)\left[\frac{(x_{i+1}-x)}{\Delta x_i}\right] + f(x_{i+1})\left[\frac{(x-x_i)}{\Delta x_i}\right] \tag{438}$$

where $\Delta x_i = x_{i+1} - x_i$ and $g_{,xx}$ denotes differentiation twice with respect to x. This equation provides the interpolating cubics over each interval for $i = 0,1,\ldots,n$ and may be given in matrix form as:

$$\mathbf{g} = \hat{\mathbf{T}}_1 \mathbf{g}_{,xx} + \hat{\mathbf{T}}_2 \mathbf{f} \tag{439}$$

For each of the k values of x at which the spline function is to be evaluated, $x_i \le x_k \le x_{i+1}$, $k = 1,2,\ldots,p$, and p is the number of evaluation points. The $\hat{\mathbf{T}}_1$ and $\hat{\mathbf{T}}_2$ matrices may be written in the form:

$$\hat{\mathbf{T}}_1 = \begin{bmatrix} (\hat{t}_1)_{1,1} & (\hat{t}_1)_{1,2} & \cdots & (\hat{t}_1)_{1,n+1} \\ (\hat{t}_1)_{2,1} & (\hat{t}_1)_{2,2} & \cdots & (\hat{t}_1)_{2,n+1} \\ \vdots & \vdots & \ddots & \vdots \\ (\hat{t}_1)_{p,1} & (\hat{t}_1)_{p,2} & \cdots & (\hat{t}_1)_{p,n+1} \end{bmatrix} \tag{440}$$

$$\hat{\mathbf{T}}_2 = \begin{bmatrix} (\hat{t}_2)_{1,1} & (\hat{t}_2)_{1,2} & \cdots & (\hat{t}_2)_{1,n+1} \\ (\hat{t}_2)_{2,1} & (\hat{t}_2)_{2,2} & \cdots & (\hat{t}_2)_{2,n+1} \\ \vdots & \vdots & \ddots & \vdots \\ (\hat{t}_2)_{p,1} & (\hat{t}_2)_{p,2} & \cdots & (\hat{t}_2)_{p,n+1} \end{bmatrix} \tag{441}$$

where

$$(\hat{t}_1)_{k,j} = \begin{cases} 0 & \text{for } x_k < x_i \text{ or } x_k > x_{i+1} \\ \dfrac{1}{6}\left[\dfrac{(x_{i+1}-x_k)^3}{\Delta x_i} - \Delta x_i (x_{i+1}-x_k)\right] & \text{for } x_i \le x_k \le x_{i+1} \text{ and } j = i+1 \\ \dfrac{1}{6}\left[\dfrac{(x_k-x_i)^3}{\Delta x_i} - \Delta x_i (x_k-x_i)\right] & \text{for } x_i \le x_k \le x_{i+1} \text{ and } j = i+2 \end{cases} \tag{442}$$

$$(\hat{t}_2)_{k,j} = \begin{cases} 0 & \text{for } x_k < x_i \text{ or } x_k > x_{i+1} \\ \dfrac{(x_{i+1}-x_k)}{\Delta x_i} & \text{for } x_i \le x_k \le x_{i+1} \text{ and } j = i+1 \\ \dfrac{(x_k-x_i)}{\Delta x_i} & \text{for } x_i \le x_k \le x_{i+1} \text{ and } j = i+2 \end{cases} \tag{443}$$

and

$$\mathbf{g}_{,xx} = \begin{Bmatrix} g_{,xx}(x_0) \\ g_{,xx}(x_1) \\ \vdots \\ g_{,xx}(x_n) \end{Bmatrix} \tag{444}$$

$$\mathbf{f} = \begin{Bmatrix} f(x_0) \\ f(x_1) \\ \vdots \\ f(x_n) \end{Bmatrix} \tag{445}$$

Note that there are, at most, two nonzero coefficients in each row of the $\hat{\mathbf{T}}_1$ and $\hat{\mathbf{T}}_2$ matrices given above.

Applying additional smoothness conditions (*i.e.*, equating the first and second derivatives of adjacent interpolating cubics at x_i) yields a set of simultaneous equations of the form:

$$\begin{aligned} &\left[\frac{\Delta x_{i-1}}{\Delta x_i}\right] g_{,xx}(x_{i-1}) + \left[\frac{2(x_{i+1}-x_i)}{\Delta x_i}\right] g_{,xx}(x_i) + [1] g_{,xx}(x_{i+1}) = \\ &6\left[\frac{f(x_{i+1})-f(x_i)}{(\Delta x_i)^2} - \frac{f(x_i)-f(x_{i-1})}{(\Delta x_i)(\Delta x_{i-1})}\right] \qquad i = 1,2,....,n-1 \end{aligned} \tag{446}$$

If the x_i are evenly separated with spacing Δx, then the Eq. (446) becomes:

$$[1] g_{,xx}(x_{i-1}) + [4] g_{,xx}(x_i) + [1] g_{,xx}(x_{i+1}) = 6\left[\frac{f(x_{i+1})-2f(x_i)+f(x_{i-1})}{(\Delta x_i)^2}\right] \tag{447}$$

Eqs. (446) and (B.4) may be written as:

$$\mathbf{A}\mathbf{g}_{,xx} = \mathbf{P}\mathbf{f} \tag{448}$$

The coefficients of matrices **A** and **P** are dependent upon the end conditions.

Whether the equations are of the form of Eq. (446) or Eq. (447), there are $n-1$ equations in the $n+1$ unknowns $g_{,xx}(x_0), g_{,xx}(x_1), \ldots, g_{,xx}(x_n)$. The two necessary additional equations are obtained by specifying conditions on $g_{,xx}(x_0)$ and $g_{,xx}(x_n)$. For a *natural spline*, $g_{,xx}(x_0) = g_{,xx}(x_n) = 0$. In general, these second derivatives are

calculated by differentiating (twice) a cubic function which passes through the first four pseudo-nodes along the interface path and another cubic function that passes through the last four pseudo-nodes along the interface path. Evaluating this cubic function:

$$g(x_0) = a_0 + a_1 x + a_2 x^2 + a_3 x^3 \tag{449}$$

at the first four points gives:

$$\begin{Bmatrix} g(x_0) \\ g(x_1) \\ g(x_2) \\ g(x_3) \end{Bmatrix} = \begin{bmatrix} 1 & x_0 & x_0^2 & x_0^3 \\ 1 & x_1 & x_1^2 & x_1^3 \\ 1 & x_2 & x_2^2 & x_2^3 \\ 1 & x_3 & x_3^2 & x_3^3 \end{bmatrix} \text{ or } \mathbf{Na} = \mathbf{g} \tag{450}$$

Solving for the coefficients yields $\mathbf{a} = \mathbf{N}^{-1}\mathbf{g}$ or

$$\begin{Bmatrix} a_0 \\ a_1 \\ a_2 \\ a_3 \end{Bmatrix} = \begin{bmatrix} n_{11} & n_{12} & n_{13} & n_{14} \\ n_{21} & n_{22} & n_{23} & n_{24} \\ n_{31} & n_{32} & n_{33} & n_{34} \\ n_{41} & n_{42} & n_{43} & n_{44} \end{bmatrix} \tag{451}$$

From the cubic function, $g_{,xx}(x) = 2a_2 + 6a_3 x$, where a_2 and a_3 are determined from Eq. (451). Equation (451) is valid for evenly spaced as well as arbitrarily spaced points. Similar expressions are obtained for the cubic function passing through the last four points where coefficients of the inverted matrix similar to those in Eq. (451) are denoted $\bar{n}_{kl}$ for $k,l = 1,\ldots,4$. With these end conditions, the matrices of Eq. (448) are given for equally-spaced points as:

$$\mathbf{A} = \begin{bmatrix} 1 & 0 & 0 & \cdots & & \\ 1 & 4 & 1 & \cdots & & \\ & 1 & 4 & 1 & & \\ & & & \ddots & & \\ & & \cdots & 1 & 4 & 1 \\ & & \cdots & 0 & 0 & 1 \end{bmatrix}_{(n+1\times n+1)} \tag{452}$$

and

$$\mathbf{P}=\begin{bmatrix} p_1 & p_2 & p_3 & p_4 & \cdots & \\ \frac{6}{\Delta x} & -\frac{12}{\Delta x} & \frac{6}{\Delta x} & & \cdots & \\ & \frac{6}{\Delta x} & -\frac{12}{\Delta x} & \frac{6}{\Delta x} & \cdots & \\ & & & \ddots & & \\ & & \cdots & & \ddots & \\ & \cdots & \overline{p}_1 & \overline{p}_2 & \overline{p}_3 & \overline{p}_4 \end{bmatrix}_{(n+1\times n+1)} \tag{453}$$

where $P_k(x)=2n_{3k}+6n_{4k}x_1$ and $\overline{P}_k(x)=2n_{3k}+6n_{4k}x_{n+1}$ for $k,l=1,\ldots,4$. For unevenly spaced points, the tridiagonal **A** and **P** matrices may readily be obtained from Eq. (446).

In Eq. (439), the spline function g(x) is expressed in terms of the functional values $f(x_i)$ as well as second derivatives of the spline function, $g_{,xx}(x_i)$. However, it is desirable to express $g(x)$ in terms of the function values $f(x_i)$ only. This manipulation is done by solving for $g_{,xx}(x_i)$ in Eq. (448) yielding:

$$\mathbf{g}_{,xx}=\mathbf{A}^{-1}\mathbf{P}\mathbf{f} \tag{454}$$

Substituting in Eq. (439) yields

$$\mathbf{g}(x)=\hat{\mathbf{T}}_1\mathbf{A}^{-1}\mathbf{P}\mathbf{f}+\hat{\mathbf{T}}_2\mathbf{f}=\left(\hat{\mathbf{T}}_1\mathbf{A}^{-1}\mathbf{P}+\hat{\mathbf{T}}_2\right)\mathbf{f}=\mathbf{T}\mathbf{f} \tag{455}$$

4.2.2 Natural Cubic Spline over Three Points

In the literature it is possible to find two kinds of natural cubic splines. One type interpolates the given data using a single function for the entire domain, while another one defines different functions for each interval between two data points.

To the first category belongs, for example, the following type of cubic splines interpolations functions:

$$
\begin{aligned}
T_1(x) &= \frac{1}{4} - \frac{1}{2}y(x) + \frac{1}{8}|y(x)|^3 - \frac{1}{4}|y(x)-1|^3 + \frac{1}{8}|y(x)-2|^3 \\
T_2(x) &= \frac{3}{2} - \frac{1}{4}|y(x)|^3 + \frac{1}{2}|y(x)-1|^3 - \frac{1}{4}|y(x)-2|^3 \\
T_3(x) &= -\frac{3}{4} + \frac{1}{2}y(x) + \frac{1}{8}|y(x)|^3 - \frac{1}{4}|y(x)-1|^3 + \frac{1}{8}|y(x)-2|^3 \\
&with: \quad y(x) = 2\frac{x}{L}
\end{aligned}
\tag{456}
$$

We have tested this particular set of functions, built to interpolate three equally spaced data points over an interval of length L, in an interface element composed by three nodes. The displacement field V of the entire interface frame was approximated in terms of the nodal displacements as:

$$V(x) = T_1(x)\, q_1^s + T_2(x)\, q_2^s + T_3(x)\, q_3^s \tag{457}$$

Though it is very easy to implement into a computer code, this set of cubic splines doesn't allow an exact numerical integration to be obtained for several intervals of integration. For this reason, in our path for programming an interface element, we decided to replace this type of cubic splines with one of the second type.

For a three equally spaced points interface frame, if x is the coordinate along the interface, the interpolation functions over the first interval are:

$$
\begin{aligned}
T_1(x) &= 1 - \frac{5(x-x_1)}{4h} + \frac{(x-x_1)^3}{4h^3} \\
T_2(x) &= \frac{3(x-x_1)}{2h} - \frac{(x-x_1)^3}{2h^3} \\
T_3(x) &= -\frac{(x-x_1)}{4h} + \frac{(x-x_1)^3}{4h^3}
\end{aligned}
\tag{458}
$$

Where x_1 is the coordinate of the first node and h is the distance between two points. Figure 13 plots these functions over the first interval for the case where: $h = 1$, $x_1 = 0$.

Figure

Figure 1

Similarly

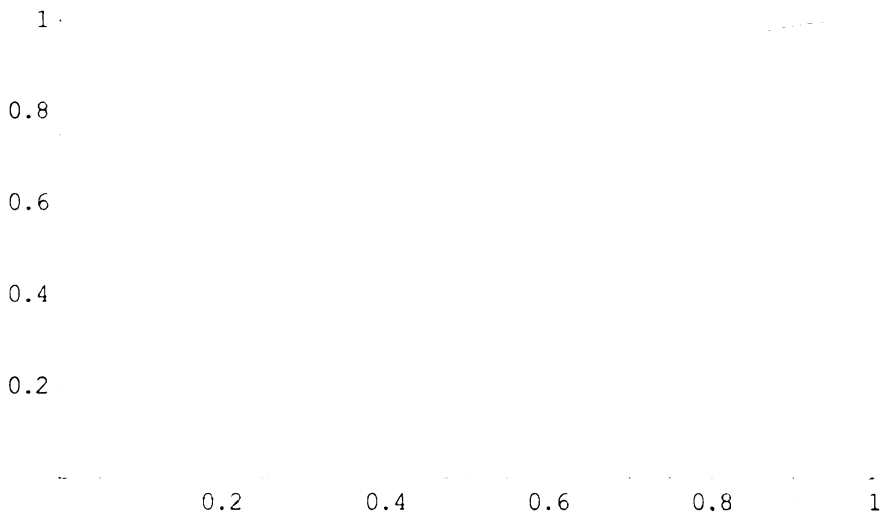

Figure 13. ***Representation of the cubic splines over the first interval***

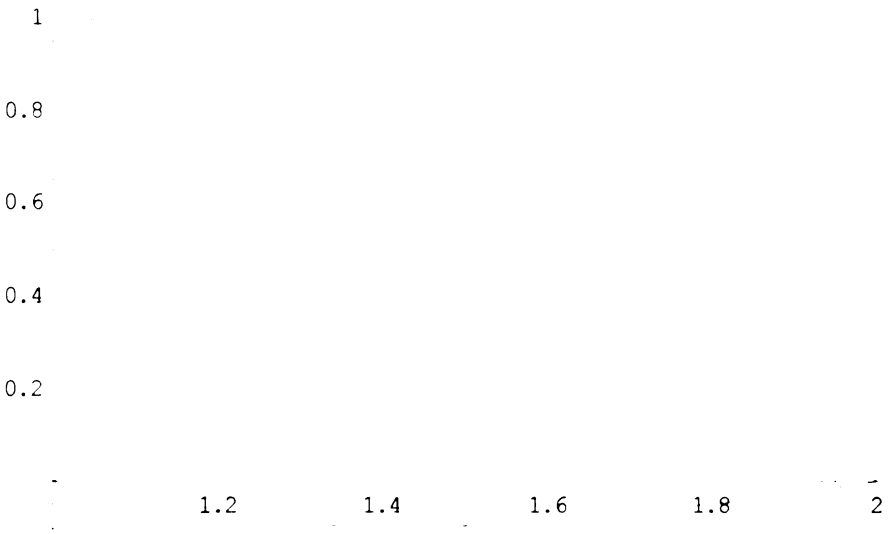

Figure 14. ***Representation of the cubic splines over the second interval***

Similarly, the interpolation functions over the second interval are:

$$T_1(x) = -\frac{(x-x_2)}{2h} + \frac{3(x-x_2)^2}{4h^2} - \frac{(x-x_2)^3}{4h^3} \tag{459}$$

$$T_2(x) = 1 - \frac{3(x-x_2)^2}{2h^2} + \frac{(x-x_2)^3}{2h^3} \tag{460}$$

$$T_3(x) = \frac{(x-x_2)}{2h} + \frac{3(x-x_2)^2}{4h^2} - \frac{(x-x_2)^3}{4h^3} \tag{461}$$

Where x_1 is the coordinate of the first node and h is the distance between two points. Figure 14 plots these functions over the second interval for the case where: $h = 1, x_1 = 0$.

4.3 2D Beam with a Vertical Interface – Single Variable

We now provide a numerical example of application of the Penalty Frame Method. In order to avoid large matrices, we first show the solution to a single variable 2-D problem.

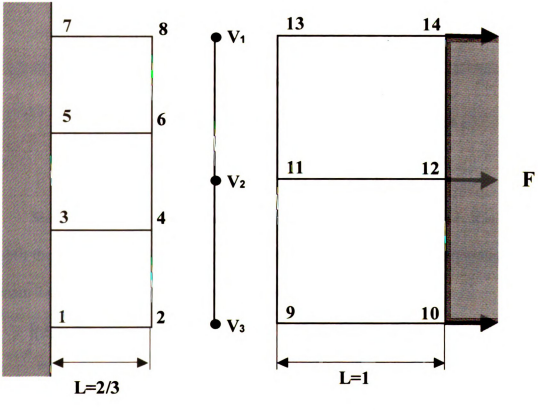

Figure 15. ***2D Cantilever beam under axial load applied at the tip.***

The extension of a cantilever beam under a uniform load F applied at the tip is

analyzed using two groups of bi-linear rectangular elements connected to each other by a three noded interface frame. The configuration of the geometry and the mesh are plotted in Figure 15. The single dependent variable involved in this FE problem is the axial displacement u.

We have shown in Chapter 2 that in the Penalty Frame Method the displacement continuity constraint is imposed through two penalty parameter γ_1 and γ_2. Thus, the TPE of the system in this study is given in the following form.

$$\pi = \pi_{\Omega_1} + \pi_{\Omega_2} + \frac{1}{2}\gamma_1 \int_S (V - u_1)^2 \, ds + \frac{1}{2}\gamma_2 \int_S (V - u_2)^2 \, ds \tag{462}$$

Taking the first variation of π and setting it to zero it follows:

$$\delta\pi\big|_{q_1'', q_1', q_S, q_2'', q_2'} = 0 \tag{463}$$

$$\begin{aligned} \delta\pi = {} & \delta\pi_{\Omega_1} + \delta\pi_{\Omega_2} + \gamma_1 \int_S (\delta u_1 \, u_1) \, ds + \gamma_1 \int_S (\delta V \, V) \, ds - \\ & - \gamma_1 \int_S (\delta u_1 \, V) \, ds - \gamma_1 \int_S (\delta V \, u_1) \, ds + \gamma_2 \int_S (\delta u_2 \, u_2) \, ds + \\ & + \gamma_2 \int_S (\delta V \, V) \, ds - \gamma_2 \int_S (\delta u_2 \, V) \, ds - \gamma_2 \int_S (\delta V \, u_2) \, ds \end{aligned} \tag{464}$$

Since there are three elements on the interface of the sub-domain 1, it is necessary to split the related integral in three parts. In the same way, the integral regarding the sub-domain 2 needs to be divided in two parts. For example:

$$\begin{aligned} & \gamma_1 \int_S (\delta u_1 \, u_1) \, ds = \\ & = \gamma_1 \int_0^{2/3} (\delta u_1 \, u_1) \, ds + \gamma_1 \int_{2/3}^{4/3} (\delta u_1 \, u_1) \, ds + \gamma_1 \int_{4/3}^{2} (\delta u_1 \, u_1) \, ds = \\ & = \gamma_1 \int_0^{2/3} (\delta q_1 N_1 + \delta q_2 N_2)(q_1 N_1 + q_2 N_2) \, ds + \gamma_1 \int_{2/3}^{4/3} (\delta q_2 N_1 + \delta q_3 N_2)(q_2 N_1 + q_3 N_2) \, ds + \\ & + \gamma_1 \int_{4/3}^{2} (\delta q_3 N_1 + \delta q_4 N_2)(q_3 N_1 + q_4 N_2) \, ds \end{aligned} \tag{465}$$

$$\gamma_2 \int_S (\delta u_2\, u_2)\, ds = \gamma_2 \int_0^1 (\delta u_2\, u_2)\, ds + \gamma_2 \int_1^2 (\delta u_2\, u_2)\, ds =$$
$$= \gamma_2 \int_0^1 (\delta q_1 N_1 + \delta q_2 N_2)(q_1 N_1 + q_2 N_2)\, ds + \gamma_2 \int_1^2 (\delta q_2 N_1 + \delta q_3 N_2)(q_2 N_1 + q_3 N_2)\, ds \tag{466}$$

Where in the integral over the sub-domain 1 the DOFs q_1, q_2, q_3, q_4 are, respectively, the axial displacements of the nodes: 2, 4, 6, 8. While, in the sub-domain 2 q_1, q_2, q_3 correspond, respectively, to the axial displacements of the nodes: 9, 11, 13. N_1 and N_2 are the linear Lagrange interpolation functions.

For the present problem, V is approximated on the entire interface frame in terms of the axial nodal displacements v_1, v_2, v_3 of the pseudo nodes V_1, V_2, V_3 as:

$$V = T_1 v_1 + T_2 v_2 + T_3 v_3 \tag{467}$$

Where T_1, T_2, T_3 are the natural cubic spline interpolation functions defined over the interval $V_1 - V_2$ by:

$$\begin{aligned} T_1(y) &= 1 - \frac{5(y - y_1)}{4h} + \frac{(y - y_1)^3}{4h^3} \\ T_2(y) &= \frac{3(y - y_1)}{2h} - \frac{(y - y_1)^3}{2h^3} \\ T_3(y) &= -\frac{(y - y_1)}{4h} + \frac{(y - y_1)^3}{4h^3} \end{aligned} \tag{468}$$

and over the interval $V_2 - V_3$ by:

$$\begin{aligned} T_1(y) &= -\frac{(y - y_2)}{2h} + \frac{3(y - y_2)^2}{4h^2} - \frac{(y - y_2)^3}{4h^3} \\ T_2(y) &= 1 - \frac{3(y - y_2)^2}{2h^2} + \frac{(y - y_2)^3}{2h^3} \\ T_3(y) &= \frac{(y - y_2)}{2h} + \frac{3(y - y_2)^2}{4h^2} - \frac{(y - y_2)^3}{4h^3} \end{aligned} \tag{469}$$

The five elements meshing our model are all square. Then, assuming the Young's Modulus to be 1, for a single-variable square element the stiffness matrix is equal to:

$$K_{el} = \begin{pmatrix} \frac{2}{3} & -\frac{1}{6} & -\frac{1}{3} & -\frac{1}{6} \\ -\frac{1}{6} & \frac{2}{3} & -\frac{1}{6} & -\frac{1}{3} \\ -\frac{1}{3} & -\frac{1}{6} & \frac{2}{3} & -\frac{1}{6} \\ -\frac{1}{6} & -\frac{1}{3} & -\frac{1}{6} & \frac{2}{3} \end{pmatrix} \tag{470}$$

The Boolean matrix for assembling the mesh is:

$$boolean = \begin{pmatrix} 1 & 2 & 4 & 3 \\ 3 & 4 & 6 & 5 \\ 5 & 6 & 8 & 7 \\ 9 & 10 & 12 & 11 \\ 11 & 12 & 14 & 13 \end{pmatrix} \tag{471}$$

We saw previously that the global system of equation of the Penalty Frame Method assumes the following form:

$$\begin{bmatrix} K_1^{oo} & K_1^{oi} & 0 & 0 & 0 \\ K_1^{io} & K_1^{ii} + G_1^{ii} & -G_1^{is} & 0 & 0 \\ 0 & -G_1^{si} & G_1^{ss} + G_2^{ss} & -G_2^{si} & 0 \\ 0 & 0 & -G_2^{is} & K_2^{ii} + G_2^{ii} & K_2^{io} \\ 0 & 0 & 0 & K_2^{oi} & K_2^{oo} \end{bmatrix} \begin{Bmatrix} q_1^o \\ q_1^i \\ q_s \\ q_2^i \\ q_2^o \end{Bmatrix} = \begin{Bmatrix} f_1^o \\ f_1^i \\ 0 \\ f_2^i \\ f_2^o \end{Bmatrix} \tag{472}$$

Where $[K_1]$ is the stiffness matrix for the domain on the left three elements, while $[K_2]$ is the stiffness of the two elements on the right. The $[G]$ matrices need to be evaluated by the following integrals.

$$\begin{aligned} G_J^{ii} &= \gamma_J \int_S \left(N_J^T N_J \right) ds \\ G_J^{is} &= \gamma_J \int_S \left(N_J^T T_J \right) ds \\ G_J^{si} &= \left[G_J^{is} \right]^T \\ G_J^{ss} &= \gamma_J \int_S \left(T_J^T T_J \right) ds \end{aligned} \tag{473}$$

The degrees of freedom q_1'' are equal to zero, since points 1, 3, 5 and 7 are clamped.

Thus, in order to find axial displacements of the unconstrained nodes, only the $\left[K_1''\right]$ part of the matrix $\left[K_1\right]$ is needed. $\left[K_1''\right]$ is associated to the DOFs of the points 2, 4, 6 and 8 and can be evaluated to be.

$$K_1^{ii} = \begin{pmatrix} \frac{2}{3} & -\frac{1}{6} & 0 & 0 \\ -\frac{1}{6} & \frac{2}{3}+\frac{2}{3} & -\frac{1}{6} & 0 \\ 0 & -\frac{1}{6} & \frac{2}{3}+\frac{2}{3} & -\frac{1}{6} \\ 0 & 0 & -\frac{1}{6} & \frac{2}{3} \end{pmatrix} \tag{474}$$

The matrix $\left[K_2\right]$, related to the axial displacements of the nodes 9, 11, 13, 10, 12 and 14, is computed as:

$$K_2 = \begin{pmatrix} \frac{2}{3} & -\frac{1}{6} & 0 & -\frac{1}{6} & -\frac{1}{3} & 0 \\ -\frac{1}{6} & \frac{2}{3}+\frac{2}{3} & -\frac{1}{6} & -\frac{1}{3} & -\frac{2}{6} & -\frac{1}{3} \\ 0 & -\frac{1}{6} & \frac{2}{3} & 0 & -\frac{1}{3} & -\frac{1}{6} \\ -\frac{1}{6} & -\frac{1}{3} & 0 & \frac{2}{3} & -\frac{1}{6} & 0 \\ -\frac{1}{3} & -\frac{2}{6} & -\frac{1}{3} & -\frac{1}{6} & \frac{2}{3}+\frac{2}{3} & -\frac{1}{6} \\ 0 & -\frac{1}{3} & -\frac{1}{6} & 0 & -\frac{1}{6} & \frac{2}{3} \end{pmatrix} \tag{475}$$

In order to provide an example of the integration of the $\left[G\right]$ matrixes, the $\left[G_{is}^1\right]$ matrix is calculated in the following lines. The four rows of the matrix, in order from row 1 to row 4, are:

$$\int_0^{\frac{2}{3}} \left(1 - \frac{x}{\frac{2}{3}}\right) (T_1[x]\, v_1 + T_2[x]\, v_2 + T_3[x]\, v_3)\, dx = \frac{197\, v1}{810} + \frac{43\, v2}{405} - \frac{13\, v3}{810} \tag{476}$$

$$\int_0^{\frac{2}{3}}\left(3\ \frac{x}{2}\right)(T_1[x]\,v_1+T_2[x]\,v_2+T_3[x]\,v_3)\,dx+$$

$$\int_{2/3}^{4/3}\left(\frac{4}{3}\ -x\ \frac{2}{3}\right)(T_1[x]\,v_1+T_2[x]\,v_2+T_3[x]\,v_3)\,dx=\frac{1199\,v1}{6480}+\frac{1681\,v2}{3240}-\frac{241\,v3}{6480} \tag{477}$$

$$\int_{\frac{2}{3}}^{\frac{4}{3}}\left(x-\frac{2}{3}\ \frac{2}{3}\right)(T_1[x]\,v_1+T_2[x]\,v_2+T_3[x]\,v_3)\,dx+$$

$$\int_{4/3}^{2}\left(2-x\ \frac{2}{3}\right)*(T_1[x]\,v_1+T_2[x]\,v_2+T_3[x]\,v_3)\,dx=-\frac{241\,v1}{6480}+\frac{1681\,v2}{3240}+\frac{1199\,v3}{6480} \tag{478}$$

$$\int_{\frac{4}{3}}^{2}\left(x-\frac{4}{3}\ \frac{2}{3}\right)(T_1[x]\,v_1+T_2[x]\,v_2+T_3[x]\,v_3)\,dx=-\frac{13\,v1}{810}+\frac{43\,v2}{405}+\frac{197\,v3}{810} \tag{479}$$

In our case the matrix $\left[G_{is}^{1}\right]$ determines the contribution to the axial displacement of the points 2, 4, 6, 8 by the interface points v_1, v_2, v_3.

$$G_1^{is}=\gamma_1\begin{pmatrix}\frac{197}{810} & \frac{43}{405} & -\frac{13}{810}\\ \frac{1199}{6480} & \frac{1681}{3240} & -\frac{241}{6480}\\ -\frac{241}{6480} & \frac{1681}{3240} & \frac{1199}{6480}\\ -\frac{13}{810} & \frac{43}{405} & \frac{197}{810}\end{pmatrix} \tag{480}$$

The other $[G]$ matrices are calculated to be:

$$G_1^{ii}=\frac{\gamma_1}{9}\begin{pmatrix}2 & 1 & 0 & 0\\ 1 & 4 & 1 & 0\\ 0 & 1 & 4 & 1\\ 0 & 0 & 1 & 2\end{pmatrix} \tag{481}$$

$$G_1^{si}=\gamma_1\begin{pmatrix}\frac{197}{810} & \frac{1199}{6480} & -\frac{241}{6480} & -\frac{13}{810}\\ \frac{43}{405} & \frac{1681}{3240} & \frac{1681}{3240} & \frac{43}{405}\\ -\frac{13}{810} & -\frac{241}{6480} & \frac{1199}{6480} & \frac{197}{810}\end{pmatrix} \tag{482}$$

$$G_1^{ss} = \gamma_1 \begin{pmatrix} \frac{239}{840} & \frac{39}{280} & -\frac{41}{840} \\ \frac{39}{280} & \frac{34}{35} & \frac{39}{280} \\ -\frac{41}{840} & \frac{39}{280} & \frac{239}{840} \end{pmatrix} \tag{483}$$

$$G_2^{ss} = \gamma_2 \begin{pmatrix} \frac{239}{840} & \frac{39}{280} & -\frac{41}{840} \\ \frac{39}{280} & \frac{34}{35} & \frac{39}{280} \\ -\frac{41}{840} & \frac{39}{280} & \frac{239}{840} \end{pmatrix} \tag{484}$$

$$G_2^{ii} = \frac{\gamma_2}{6} \begin{pmatrix} 2 & 1 & 0 \\ 1 & 4 & 1 \\ 0 & 1 & 2 \end{pmatrix} \tag{485}$$

$$G_2^{is} = \gamma_2 \begin{pmatrix} \frac{73}{240} & \frac{9}{40} & -\frac{7}{240} \\ \frac{1}{10} & \frac{4}{5} & \frac{1}{10} \\ -\frac{7}{240} & \frac{9v2}{40} & \frac{73}{240} \end{pmatrix} \tag{486}$$

$$G_2^{si} = \gamma_2 \begin{pmatrix} \frac{73}{240} & \frac{1}{10} & -\frac{7}{240} \\ \frac{9}{40} & \frac{4}{5} & \frac{9v2}{40} \\ -\frac{7}{240} & \frac{1}{10} & \frac{73}{240} \end{pmatrix} \tag{487}$$

Then, the "stiffness" matrix associated with the interface element is:

$$K_{Glue} = \begin{pmatrix} \frac{2\gamma_1}{9} & \frac{\gamma_1}{9} & 0 & 0 & -\frac{197\gamma_1}{810} & -\frac{43\gamma_1}{405} & \frac{13\gamma_1}{810} & 0 & 0 & 0 \\ \frac{\gamma_1}{9} & \frac{4\gamma_1}{9} & \frac{\gamma_1}{9} & 0 & -\frac{1199\gamma_1}{6480} & -\frac{1681\gamma_1}{3240} & \frac{241\gamma_1}{6480} & 0 & 0 & 0 \\ 0 & \frac{\gamma_1}{9} & \frac{4\gamma_1}{9} & +\frac{\gamma_1}{9} & \frac{241\gamma_1}{6480} & -\frac{1681\gamma_1}{3240} & -\frac{1199\gamma_1}{6480} & 0 & 0 & 0 \\ 0 & 0 & \frac{\gamma_1}{9} & \frac{2\gamma_1}{9} & \frac{13\gamma_1}{810} & -\frac{43\gamma_1}{405} & -\frac{197\gamma_1}{810} & 0 & 0 & 0 \\ -\frac{197\gamma_1}{810} & -\frac{1199\gamma_1}{6480} & \frac{241\gamma_1}{6480} & \frac{13\gamma_1}{810} & \frac{239(\gamma_1+\gamma_2)}{840} & \frac{39(\gamma_1+\gamma_2)}{280} & -\frac{41(\gamma_1+\gamma_2)}{840} & -\frac{73\gamma_2}{240} & -\frac{\gamma_2}{10} & \frac{7\gamma_2}{240} \\ -\frac{43\gamma_1}{405} & -\frac{1681\gamma_1}{3240} & -\frac{1681\gamma_1}{3240} & -\frac{43\gamma_1}{405} & \frac{39(\gamma_1+\gamma_2)}{280} & \frac{34(\gamma_1+\gamma_2)}{35} & \frac{39(\gamma_1+\gamma_2)}{280} & -\frac{9\gamma_2}{40} & -\frac{4\gamma_2}{5} & -\frac{9\gamma_2}{40} \\ \frac{13\gamma_1}{810} & \frac{241\gamma_1}{6480} & -\frac{1199\gamma_1}{6480} & -\frac{197\gamma_1}{810} & -\frac{41(\gamma_1+\gamma_2)}{840} & \frac{39(\gamma_1+\gamma_2)}{280} & \frac{239(\gamma_1+\gamma_2)}{840} & \frac{7\gamma_2}{240} & -\frac{\gamma_2}{10} & -\frac{73\gamma_2}{240} \\ 0 & 0 & 0 & 0 & -\frac{73\gamma_2}{240} & -\frac{9\gamma_2}{40} & \frac{7\gamma_2}{240} & \frac{\gamma_2}{3} & \frac{\gamma_2}{6} & 0 \\ 0 & 0 & 0 & 0 & -\frac{\gamma_2}{10} & -\frac{4\gamma_2}{5} & -\frac{\gamma_2}{10} & \frac{\gamma_2}{6} & \frac{2\gamma_2}{3} & \frac{\gamma_2}{6} \\ 0 & 0 & 0 & 0 & \frac{7\gamma_2}{240} & -\frac{9\gamma_2}{40} & -\frac{73\gamma_2}{240} & 0 & \frac{\gamma_2}{6} & \frac{2}{3}+\frac{\gamma_2}{3} \end{pmatrix} \tag{488}$$

And the global system of equations associated to the problem in this study becomes:

$$K = \begin{pmatrix}
\frac{2+2\gamma_1}{3} & \frac{-1+\gamma_1}{6} & 0 & 0 & \frac{-197\gamma_1}{810} & \frac{-43\gamma_1}{405} & \frac{13\gamma_1}{810} & 0 & 0 & 0 & 0 & 0 & 0 \\
\frac{-1+\gamma_1}{6} & \frac{4+4\gamma_1}{3} & \frac{-1+\gamma_1}{6} & 0 & \frac{-1199\gamma_1}{6480} & \frac{-1681\gamma_1}{3240} & \frac{241\gamma_1}{6480} & 0 & 0 & 0 & 0 & 0 & 0 \\
0 & \frac{-1+\gamma_1}{6} & \frac{4+4\gamma_1}{3} & \frac{-1+\gamma_1}{6} & \frac{241\gamma_1}{6480} & \frac{-1681\gamma_1}{3240} & \frac{-1199\gamma_1}{6480} & 0 & 0 & 0 & 0 & 0 & 0 \\
0 & 0 & \frac{-1+\gamma_1}{6} & \frac{2+2\gamma_1}{3} & \frac{13\gamma_1}{810} & \frac{-43\gamma_1}{405} & \frac{-197\gamma_1}{810} & 0 & 0 & 0 & 0 & 0 & 0 \\
\frac{-197\gamma_1}{810} & \frac{-1199\gamma_1}{6480} & \frac{241\gamma_1}{6480} & \frac{13\gamma_1}{810} & \frac{239(\gamma_1+\gamma_2)}{840} & \frac{39(\gamma_1+\gamma_2)}{280} & \frac{-41(\gamma_1+\gamma_2)}{840} & \frac{-73\gamma_2}{240} & \frac{-\gamma_2}{10} & \frac{73\gamma_2}{240} & 0 & 0 & 0 \\
\frac{-43\gamma_1}{405} & \frac{-1681\gamma_1}{3240} & \frac{-1681\gamma_1}{3240} & \frac{-43\gamma_1}{405} & \frac{39(\gamma_1+\gamma_2)}{280} & \frac{34(\gamma_1+\gamma_2)}{35} & \frac{39(\gamma_1+\gamma_2)}{280} & \frac{-9\gamma_2}{40} & \frac{-4\gamma_2}{5} & \frac{-9\gamma_2}{40} & 0 & 0 & 0 \\
\frac{13\gamma_1}{810} & \frac{241\gamma_1}{6480} & \frac{-1199\gamma_1}{6480} & \frac{-197\gamma_1}{810} & \frac{-41(\gamma_1+\gamma_2)}{840} & \frac{39(\gamma_1+\gamma_2)}{280} & \frac{239(\gamma_1+\gamma_2)}{840} & \frac{73\gamma_2}{240} & \frac{-\gamma_2}{10} & \frac{-73\gamma_2}{240} & 0 & 0 & 0 \\
0 & 0 & 0 & 0 & \frac{-73\gamma_2}{240} & \frac{-9\gamma_2}{40} & \frac{73\gamma_2}{240} & \frac{2+\gamma_2}{3} & \frac{-1+\gamma_2}{6} & 0 & \frac{-1}{6} & \frac{-1}{3} & 0 \\
0 & 0 & 0 & 0 & \frac{-\gamma_2}{10} & \frac{-4\gamma_2}{5} & \frac{-\gamma_2}{10} & \frac{-1+\gamma_2}{6} & \frac{4+2\gamma_2}{3} & \frac{-1+\gamma_2}{6} & \frac{-1}{3} & \frac{-2}{6} & \frac{-1}{3} \\
0 & 0 & 0 & 0 & \frac{73\gamma_2}{240} & \frac{-9\gamma_2}{40} & \frac{-73\gamma_2}{240} & 0 & \frac{-1+\gamma_2}{6} & \frac{2+\gamma_2}{3} & 0 & \frac{-1}{3} & \frac{-1}{6} \\
0 & 0 & 0 & 0 & 0 & 0 & 0 & \frac{-1}{6} & \frac{-1}{3} & 0 & \frac{2}{3} & \frac{-1}{6} & 0 \\
0 & 0 & 0 & 0 & 0 & 0 & 0 & \frac{-1}{3} & \frac{-2}{6} & \frac{-1}{3} & \frac{-1}{6} & \frac{2+2}{3} & \frac{-1}{6} \\
0 & 0 & 0 & 0 & 0 & 0 & 0 & 0 & \frac{-1}{3} & \frac{-1}{6} & 0 & \frac{-1}{6} & \frac{2}{3}
\end{pmatrix} \tag{489}$$

A force vector able to reproduce the axial load is applied as:

$$force = \left\{0,\ 0,\ 0,\ 0,\ 0,\ 0,\ 0,\ 0,\ 0,\ 0,\ \frac{q}{4},\ \frac{q}{2},\ \frac{q}{4}\right\} \tag{490}$$

Finally, if we choose the penalty parameters to be $\gamma_1 = \gamma_2 = 1000$ and $q = 1$, the system can be solved to obtain:

$$\begin{aligned}
u_2,\ u_4,\ u_6,\ u_8 &= \frac{1}{3} \\
v_1,\ v_2,\ v_3 &= \frac{2003}{6000} \\
u_9,\ u_{11},\ u_{13} &= \frac{1003}{3000} \\
u_{10},\ u_{12},\ u_{14} &= \frac{2503}{3000}
\end{aligned} \tag{491}$$

Here can be noticed that the error in the displacements due to the use of the penalty frame method is on the order of magnitude of $\frac{1}{\gamma}$.

4.4 *Clamped Rectangular Plane Stress Element*

The previous analysis, even if very useful to explain the method, does not produce any information on the possible relations among material and geometrical properties of the element and the optimal penalty parameter. That's why the next simple problem is solved through a symbolic calculation.

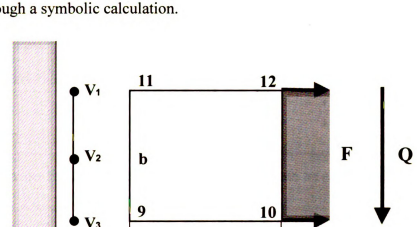

Figure 16. ***Single element beam connected to a fixed penalty frame***

Consider a rectangular plane stress element clamped to a fixed penalty frame along one side and loaded on the other. The geometry of the problem is shown in Figure 16.

We saw in Section 4.1 that the stiffness matrix of the rectangular element is:

$$K_{el} = \begin{pmatrix} h\left(\frac{aY}{6b}+\frac{bY}{3a}\right) & h\left(\frac{aY}{12b}-\frac{bY}{3a}\right) & h\left(-\frac{aY}{12b}-\frac{bY}{6a}\right) & h\left(-\frac{aY}{6b}+\frac{bY}{6a}\right) & \frac{hY}{8} & -\frac{hY}{8} & -\frac{hY}{8} & \frac{hY}{8} \\ h\left(\frac{aY}{12b}-\frac{bY}{3a}\right) & h\left(\frac{aY}{6b}+\frac{bY}{3a}\right) & h\left(\frac{aY}{6b}-\frac{bY}{6a}\right) & h\left(-\frac{aY}{12b}-\frac{bY}{6a}\right) & \frac{hY}{8} & -\frac{hY}{8} & -\frac{hY}{8} & \frac{hY}{8} \\ h\left(-\frac{aY}{12b}-\frac{bY}{6a}\right) & h\left(\frac{aY}{6b}-\frac{bY}{6a}\right) & h\left(\frac{aY}{6b}+\frac{bY}{3a}\right) & h\left(\frac{aY}{12b}-\frac{bY}{3a}\right) & -\frac{hY}{8} & \frac{hY}{8} & \frac{hY}{8} & -\frac{hY}{8} \\ h\left(-\frac{aY}{6b}+\frac{bY}{6a}\right) & h\left(-\frac{aY}{12b}-\frac{bY}{6a}\right) & h\left(\frac{aY}{12b}-\frac{bY}{3a}\right) & h\left(\frac{aY}{6b}+\frac{bY}{3a}\right) & -\frac{hY}{8} & \frac{hY}{8} & \frac{hY}{8} & -\frac{hY}{8} \\ \frac{hY}{8} & \frac{hY}{8} & -\frac{hY}{8} & -\frac{hY}{8} & h\left(\frac{aY}{3b}+\frac{bY}{6a}\right) & h\left(\frac{aY}{6b}-\frac{bY}{6a}\right) & h\left(-\frac{aY}{6b}-\frac{bY}{12a}\right) & h\left(-\frac{aY}{3b}+\frac{bY}{12a}\right) \\ -\frac{hY}{8} & \frac{hY}{8} & \frac{hY}{8} & \frac{hY}{8} & h\left(\frac{aY}{6b}-\frac{bY}{6a}\right) & h\left(\frac{aY}{3b}+\frac{bY}{6a}\right) & h\left(-\frac{aY}{3b}+\frac{bY}{12a}\right) & h\left(-\frac{aY}{6b}-\frac{bY}{12a}\right) \\ -\frac{hY}{8} & -\frac{hY}{8} & \frac{hY}{8} & \frac{hY}{8} & h\left(-\frac{aY}{6b}-\frac{bY}{12a}\right) & h\left(-\frac{aY}{3b}+\frac{bY}{12a}\right) & h\left(\frac{aY}{3b}+\frac{bY}{6a}\right) & h\left(\frac{aY}{6b}-\frac{bY}{6a}\right) \\ \frac{hY}{8} & \frac{hY}{8} & -\frac{hY}{8} & -\frac{hY}{8} & h\left(-\frac{aY}{3b}+\frac{bY}{12a}\right) & h\left(-\frac{aY}{6b}-\frac{bY}{12a}\right) & h\left(\frac{aY}{6b}-\frac{bY}{6a}\right) & h\left(\frac{aY}{3b}+\frac{bY}{6a}\right) \end{pmatrix} \tag{492}$$

In order to separate the DOFs on the interface from those outside the interface, the stiffness matrix is rearranged. To make this change clear, the first row and the last column of the new matrix show the associated DOFs.

$$K_{el} = \begin{array}{c} \begin{matrix} u9 & u11 & v9 & v11 & u10 & u12 & v10 & v12 \end{matrix} \\ \begin{pmatrix} h\left(\frac{aY}{6b}+\frac{bY}{3a}\right) & h\left(-\frac{aY}{6b}+\frac{bY}{6a}\right) & \frac{hY}{8} & \frac{hY}{8} & h\left(\frac{aY}{12b}-\frac{bY}{3a}\right) & h\left(-\frac{aY}{12b}-\frac{bY}{6a}\right) & -\frac{hY}{8} & -\frac{hY}{8} \\ h\left(-\frac{aY}{6b}+\frac{bY}{6a}\right) & h\left(\frac{aY}{6b}+\frac{bY}{3a}\right) & -\frac{hY}{8} & -\frac{hY}{8} & h\left(-\frac{aY}{12b}-\frac{bY}{6a}\right) & h\left(\frac{aY}{12b}-\frac{bY}{3a}\right) & \frac{hY}{8} & \frac{hY}{8} \\ \frac{hY}{8} & -\frac{hY}{8} & h\left(\frac{aY}{3b}+\frac{bY}{6a}\right) & h\left(-\frac{aY}{3b}+\frac{bY}{12a}\right) & \frac{hY}{8} & -\frac{hY}{8} & h\left(\frac{aY}{6b}-\frac{bY}{6a}\right) & h\left(-\frac{aY}{6b}-\frac{bY}{12a}\right) \\ \frac{hY}{8} & -\frac{hY}{8} & h\left(-\frac{aY}{3b}+\frac{bY}{12a}\right) & h\left(\frac{aY}{3b}+\frac{bY}{6a}\right) & \frac{hY}{8} & -\frac{hY}{8} & h\left(-\frac{aY}{6b}-\frac{bY}{12a}\right) & h\left(\frac{aY}{6b}-\frac{bY}{6a}\right) \\ h\left(\frac{aY}{12b}-\frac{bY}{3a}\right) & h\left(-\frac{aY}{12b}-\frac{bY}{6a}\right) & \frac{hY}{8} & \frac{hY}{8} & h\left(\frac{aY}{6b}+\frac{bY}{3a}\right) & h\left(-\frac{aY}{6b}+\frac{bY}{6a}\right) & -\frac{hY}{8} & -\frac{hY}{8} \\ h\left(-\frac{aY}{12b}-\frac{bY}{6a}\right) & h\left(\frac{aY}{12b}-\frac{bY}{3a}\right) & -\frac{hY}{8} & -\frac{hY}{8} & h\left(-\frac{aY}{6b}+\frac{bY}{6a}\right) & h\left(\frac{aY}{6b}+\frac{bY}{3a}\right) & \frac{hY}{8} & \frac{hY}{8} \\ -\frac{hY}{8} & \frac{hY}{8} & h\left(\frac{aY}{6b}-\frac{bY}{6a}\right) & h\left(-\frac{aY}{6b}-\frac{bY}{12a}\right) & -\frac{hY}{8} & \frac{hY}{8} & h\left(\frac{aY}{3b}+\frac{bY}{6a}\right) & h\left(-\frac{aY}{3b}+\frac{bY}{12a}\right) \\ -\frac{hY}{8} & \frac{hY}{8} & h\left(-\frac{aY}{6b}-\frac{bY}{12a}\right) & h\left(\frac{aY}{6b}-\frac{bY}{6a}\right) & -\frac{hY}{8} & \frac{hY}{8} & h\left(-\frac{aY}{3b}+\frac{bY}{12a}\right) & h\left(\frac{aY}{3b}+\frac{bY}{6a}\right) \end{pmatrix} \end{array} \begin{matrix} u9 \\ u11 \\ v9 \\ v11 \\ u10 \\ u12 \\ v10 \\ v12 \end{matrix} \tag{493}$$

The $[G]$ matrices related to the problem in this study can be easily computed to be:

$$G_2^{ii} = \frac{\gamma_1}{6}\begin{pmatrix} 2 & 1 \\ 1 & 2 \end{pmatrix} \tag{494}$$

$$G_2^{is} = \gamma_1 \begin{pmatrix} \frac{73}{240} & \frac{54}{240} & \frac{-7}{240} \\ \frac{4}{30} & \frac{12}{30} & \frac{-1}{30} \end{pmatrix} \tag{495}$$

$$G_2^{si} = \gamma_1 \begin{pmatrix} \frac{73}{240} & \frac{2}{15} \\ \frac{9}{40} & \frac{2}{5} \\ -\frac{7}{240} & -\frac{1}{30} \end{pmatrix} \tag{496}$$

$$G_2^{ss} = \gamma_1 \begin{pmatrix} \frac{47}{168} & \frac{51}{280} & -\frac{41}{1680} \\ \frac{51}{280} & \frac{17}{35} & -\frac{3}{70} \\ -\frac{41}{1680} & -\frac{3}{70} & \frac{1}{210} \end{pmatrix} \tag{497}$$

Thus, the global system of equations associated with this analysis is reported below. As before, the first row and the last column of the new matrix show the DOFs (for clarity).

$K =$ 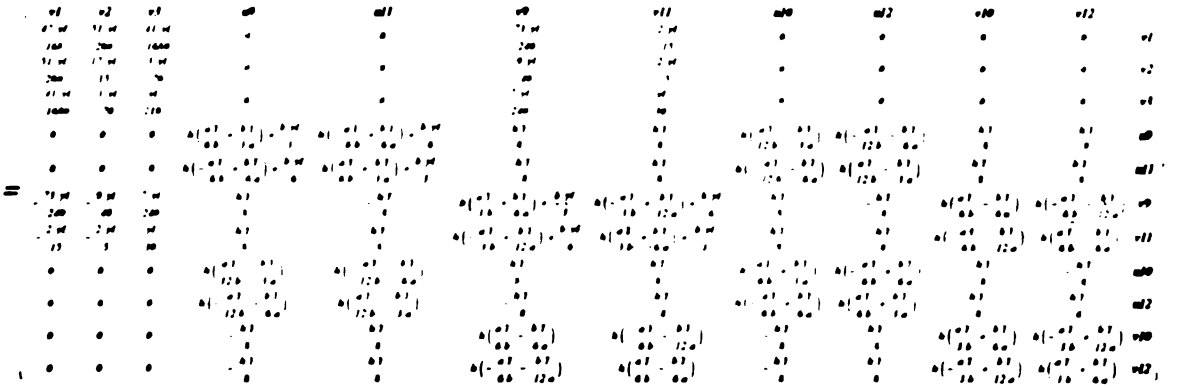

(498)

Taking advantage of the fact that the interface points v_1, v_2, v_3 are fixed, the global stiffness matrix reduces to:

$K =$ 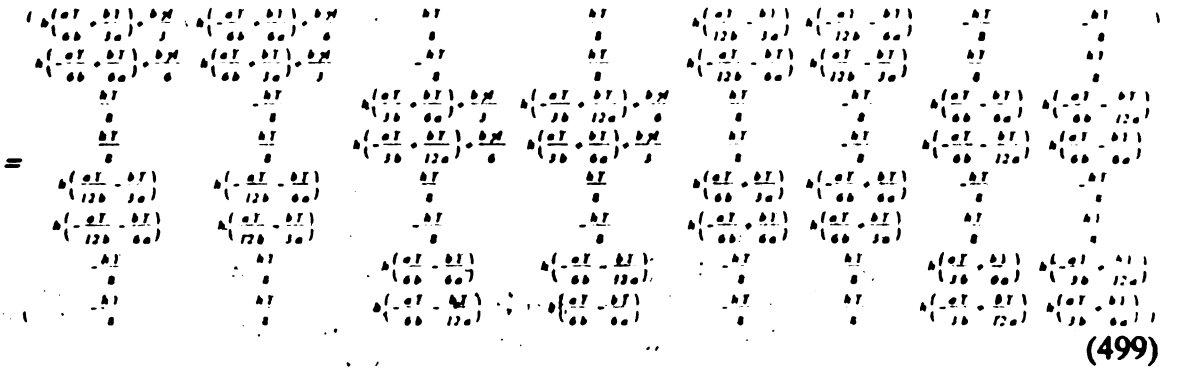

(499)

4.4.1 Axial Load

We are interested in solving this problem for two simple load cases: axial and transversal load. According to Figure 17, we consider the axial extension first.

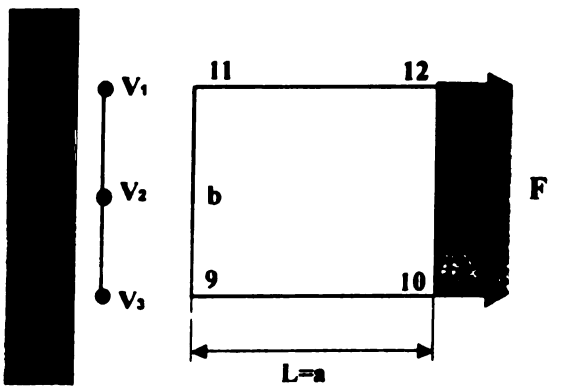

Figure 17. ***Single element beam under axial load***

A force v

Inverting

can be ev

containin

difficult t

A

nodes 9 a

direction

following

4.4.2 Tr

In

Figure 1

A force vector of the following kind is applied:

$$force = \left\{0,0,0,0,\frac{F}{2},\frac{F}{2},0,0\right\} \tag{500}$$

Inverting $[K]$ and multiplying by the force vector, the displacements of the four nodes can be evaluated in symbolic form. However, the results are very complex expressions containing the geometrical, material and penalty parameters. As a consequence, it is difficult to arrive at any conclusions based on those outcomes.

A reasonable simplification consists in imposing the vertical displacements of nodes 9 and 11 to be zero. In this case those nodes are directly fixed in the vertical direction without the interposition of the interface frame. Under this assumption the following solution is obtained:

$$u_9,\ u_{11} = \frac{F}{b\gamma_1} \tag{501}$$

$$u_{10},\ u_{12} = \frac{a\,F}{b\,h\,Y} + \frac{F}{b\gamma_1} \tag{502}$$

4.4.2 Transversal Load

In this section we consider the transversal load, as plotted in Figure 18.

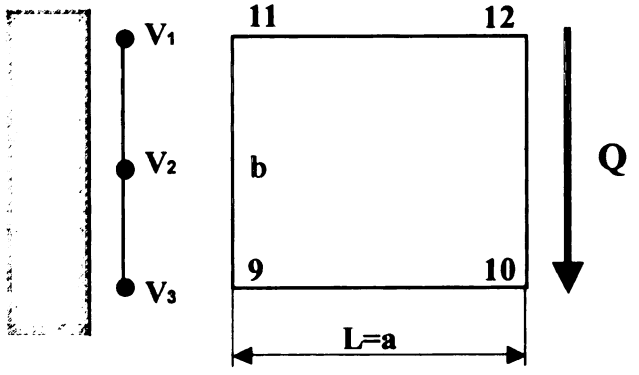

Figure 18. ***Single element beam under a transversal load***

A force vector of the following kind is applied:

$$force = \left\{0,0,0,0,0,0,\frac{Q}{2},\frac{Q}{2}\right\} \tag{503}$$

Inverting $[K]$ and multiplying by the force vector, the displacements of the four nodes can be evaluated in symbolic form. The same simplification applied to the axial case is assumed. This time the horizontal displacements of nodes 9 and 11 are set to zero. Under this assumption the following solution is obtained:

$$\begin{aligned} v_9,\ v_{11} &= \frac{Q}{b\gamma_1} \\ u_{10} &= \frac{6a^2Q}{a^2hY + 2b^2hY} \\ u_{12} &= \frac{-6a^2Q}{a^2hY + 2b^2hY} \\ v_{10} = v_{12} &= \frac{4a\left(2a^2 + b^2\right)Q}{b\left(a^2 + 2b^2\right)hY} + \frac{Q}{b\gamma_1} \end{aligned} \tag{504}$$

A numerical test has been performed in order to verify that the Abaqus quadrilateral plane stress element CPS4 behaves according to the finite element model developed above. The simple FE analysis of a single CPS4 element clamped on one side and loaded on the other was executed. Then, results from the penalty frame model were compared with those from conventional Abaqus FE solution. Results are nondimensionalized by the Abaqus FE solution. The penalty parameter is: $\gamma_1 = 1000$.

	ABAQUS	Interface	Interface with $\gamma_1 = \infty$
Vertical displacement of the tip	**1.0000**	**1.0001**	**1.0000**

This confirms that our FE model matches the one implemented in Abaqus.

4.5 Penalty Parameter and Element Properties

In this section the solutions obtained are investigated in order to find a relation between material and geometrical properties of the beam and the penalty parameter.

4.5.1 Axial Extension

The exact displacement of the tip is given by the expression:

$$u^{exact} = \frac{a}{Ybh} F \tag{505}$$

The penalty parameter solution $u^{penalty}$ differs from the exact one by the presence of an additional term $\frac{F}{b\gamma_1}$.

$$u^{penalty} = \left(\frac{a}{bhY} + \frac{1}{b\gamma_1} \right) F \tag{506}$$

The ratio $u^{penalty}$ over u^{exact} is evaluated in order to underline the dependences between the two solutions.

$$\frac{u^{penalty}}{u^{exact}} = \frac{\left(\frac{a}{bhY} + \frac{1}{b\gamma_1} \right) F}{\left(\frac{a}{bhY} \right) F} = 1 + \frac{\left(\frac{hY}{a} \right)}{\gamma_1} \tag{507}$$

Now, if the penalty parameter γ_1 is substituted by:

$$\gamma_1 = \beta \cdot \left(\frac{hY}{a} \right) \tag{508}$$

The ratio between the solutions becomes independent of material and geometrical properties of the element.

$$\frac{u^{penalty}}{u^{exact}} = 1 + \frac{1}{\beta} \tag{509}$$

The accuracy of the solution depends directly on the value assigned to the parameter β.

4.5.2 Vertical Flexure

As in the previous section, the obtained flexure solutions are examined in order to find a relation between material and geometrical properties of the element and the penalty parameter.

The exact theoretical solution for the vertical displacement of the tip of the element cannot match that from the Finite element formulation. The appropriate term of comparison is the outcome provided by the same element without using of the penalty interface frame. We call this solution w^{FE} :

$$w^{FE} = \frac{4a\left(2a^2 + b^2\right)Q}{b\left(a^2 + 2b^2\right)hY} \tag{510}$$

The ratio $w^{penalty}$ over w^{FE} is computed to be:

$$\frac{w^{penalty}}{w^{FE}} = \frac{\dfrac{4a\left(2a^2 + b^2\right)Q}{b\left(a^2 + 2b^2\right)hY} + \dfrac{Q}{b\gamma_1}}{\dfrac{4a\left(2a^2 + b^2\right)Q}{b\left(a^2 + 2b^2\right)hY}} = 1 + \frac{\left(a^2 + 2b^2\right)hY}{4a\left(2a^2 + b^2\right)Q} = \tag{511}$$

$$= 1 + \frac{a\,hY}{4\left(2a^2 + b^2\right)Q} + \frac{b^2 hY}{2a\left(2a^2 + b^2\right)Q}$$

Substituting penalty parameter γ_1 with:

$$\gamma_1 = \beta \cdot \frac{\left(a^2 + 2b^2\right)hY}{4a\left(2a^2 + b^2\right)} \tag{512}$$

The previous ratio becomes dependent only on β.

$$\frac{w^{penalty}}{w^{LE}} = 1 + \frac{1}{\beta} \tag{513}$$

Thus, as stated before, the accuracy of the solution depends directly on the value assigned to the parameter β.

4.6 Building an interface Element Using Abaqus UEL

So far, the way an interface element stiffness matrix is defined has been explained in detail. The evaluation of the matrices $[G]$ has been widely described too. The stiffness matrix and generalized vector of unknown displacements associated with the interface element are:

$$\begin{bmatrix} G_1^{tt} & -G_1^{ts} & 0 \\ -G_1^{st} & G_1^{ss} + G_2^{ss} & -G_2^{st} \\ 0 & -G_2^{ts} & G_2^{tt} \end{bmatrix} \begin{Bmatrix} q_1^t \\ q_s \\ q_2^t \end{Bmatrix} \tag{514}$$

We now have the complete set of information for building an Abaqus User Element Subroutine, UEL [39], able to connect different meshes of 2-D quadrilateral elements.

The subroutine receives all the necessary information about geometry and material properties of the two connected meshes from the input file. The parameters provided are: the nodes on the interface, thickness and Young's Modulus of the two domains. Two version of the computer code for 2-D quadrilateral elements has been developed.

One release has three equally spaced nodes along the interface whose displacement field is interpolated by natural splines. It is computationally very efficient, but it doesn't guarantee accurate results in some particular configurations. This happens

since the continuity of the second derivatives at the connection between different interface elements is not enforced.

The version of subroutine based on the general form of the spline interpolation, allows varying the number of points composing the interface element. It successfully connects long boundaries and many finite elements with only one interface element. It does always guarantee accurate results, but as the number of points grows the computational efficiency decreases very fast. For example, an interface element with 100 nodes has a stiffness matrix of 200x200, since the DOFs are two. The presence of one element with a big stiffness matrix, makes the global stiffness matrix less banded and strongly affects the time required by the solver.

The UEL subroutine is written in Fortran 77, according to the requirements stated in Abaqus Manuals [39]. All the variables are defined to be in double precision format, in order to minimize numerical round-off errors as much as possible.

In appendix A, a complete user manual for the interface element based on general form of the spline interpolation, is reported.

4.6.1 Automatic Choice of the Optimal Penalty Parameter

One of the objectives of this study is to establish an automatic choice of the optimal penalty parameter. The investigations in section 4.5 constitute the basis for pursuing this goal. However, it should be underlined that we don't need to get an exact value; we just need to know the right order of magnitude of the penalty parameter. In fact, even in the most complex FE analysis, there exists a range of values for this parameter for which the numerical outcomes change very little. This range can be equal to more than 12 orders of magnitude for simple analyses, but usually it doesn't reduce to

less than 2 orders of magnitude in any situations.

Taking into consideration the previous comments, we now recall the main results found in section 4.5. We saw that under conditions of axial load, the following expression of the penalty parameter would make the accuracy of the solution to depend only on the value assigned to the parameter β:

$$\gamma_1 = \beta \cdot \left(\frac{hY}{a} \right) \tag{515}$$

This expression is very simple, but still contains information that would be difficult to obtain, namely: the length of the element, a. Inside the UEL subroutine only the coordinates of the nodes on the interface are known. Moreover, along the interface the elements could have different lengths. Thus, taking advantage of the good practice in FE of using elements with aspect ratio not too distant from the square shape, we choose to approximate the dimension in the direction perpendicular to the interface with the one parallel to it. According to the adopted symbols, the expression for γ_1 becomes:

$$\gamma_1 = \beta \cdot \left(\frac{hY}{b} \right) \tag{516}$$

This simplification strongly affects the result regarding the flexural load case. The expression for γ_1 reduces to:

$$\gamma_1 = \left\{ \beta \cdot \left[\frac{\left(a^2 + 2b^2\right) hY}{4a\left(2a^2 + b^2\right)} \right] \right\} \xrightarrow{a=b} \gamma_1 = \left\{ \beta \cdot \left[\frac{hY}{4b} \right] \right\} \tag{517}$$

A final step is required in order to obtain a single expression for an automatic evaluation of the penalty parameter. It consists in eliminating the number *4* from the denominator of the last expression for γ_1. This simplification is important since the

interface could have any orientation, so it is better to not make any distinction between horizontal and vertical displacement DOFs.

In conclusion, we choose to make γ_1 to depend on the following parameter:

$$\gamma_1 = \beta \cdot \left(\frac{hY}{b} \right) \tag{518}$$

Where the value of β is usually assigned to be 1000.

4.7 Numerical Results

In this section the developed Abaqus User Element, UEL, for plane stress quadrilaterals, is employed to solve several problems. These FE analyses will test the precision and reliability of the proposed method.

4.7.1 Patch Test

A two dimensional rectangular region is assumed to be composed of two domains. The domains are meshed independently and joined by one interface element. The geometrical configuration of the problem is shown in Figure 19.

Other properties are: $E_1 = E_2 = 1$ and $thickness = 1$. In discretizing the two subdomains, four-noded bilinear plane stress elements are used. Three different conditions are investigated: uniform axial strain in direction 1, uniform axial strain in direction 2 and uniform shear strain. This problem is intended to serve as a patch test for the interface element developed herein. If the continuity constraint along the inclined interface is not correctly imposed by the interface model, then discontinuity of displacements and strains across the interface would result.

The condition of a uniform strain in direction 1 is obtained by assigning a displacement equal to 1.6 mm to all nodes on the right vertical side and constraining the opposite side against movements in the same direction.

The node at the bottom left corner is constrained against vertical motion. The results are in agreement with the exact solution to the number of significant digits available, i.e. axial strain is uniform in direction 1 and equal to 0.1 in all elements of the patch. The displacement distribution in direction 1 is reported in Figure 20. Similarly, the condition of a uniform strain in direction 2 is obtained by assigning a displacement equal to 1 mm to all nodes on the top horizontal side and constraining the opposite side against movements in direction 2. The node at the bottom left corner is constrained against horizontal motion.

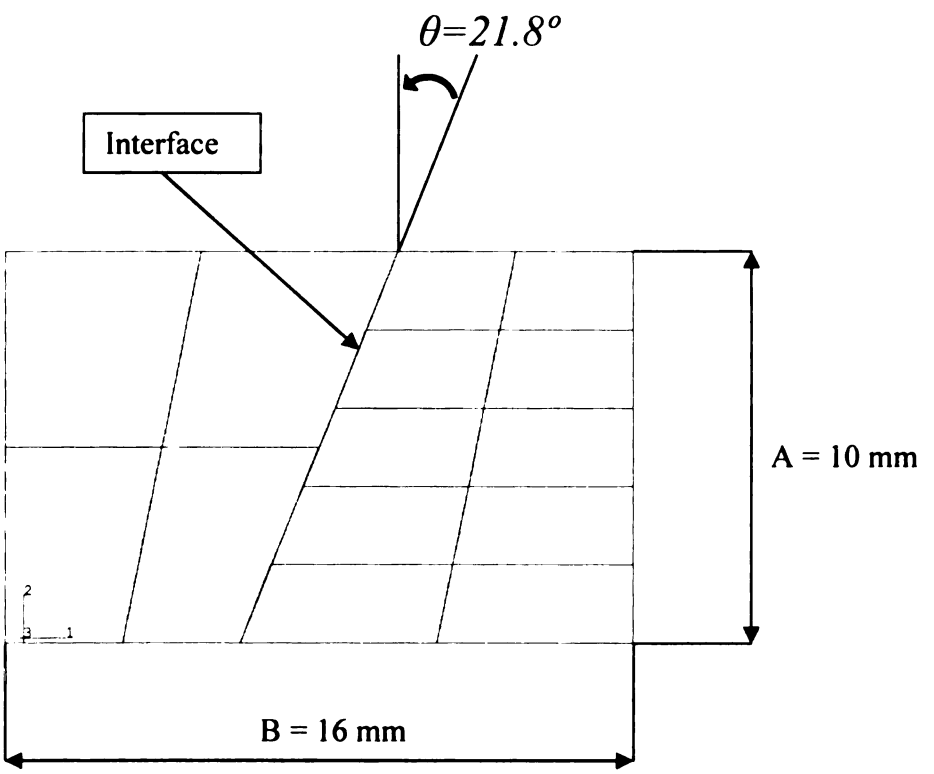

Figure 19. ***Patch of incompatible 2D meshes connected by one interface element.***

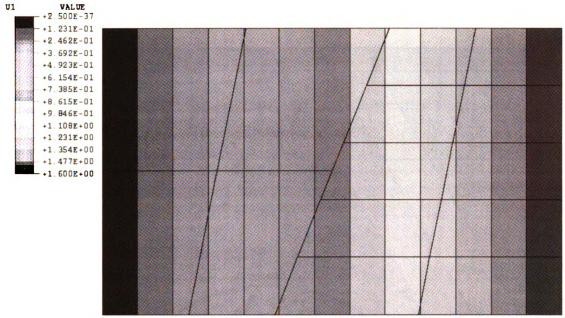

Figure 20. ***Patch of incompatible 2D meshes - Displacements distribution in the direction 1 (U_1).***

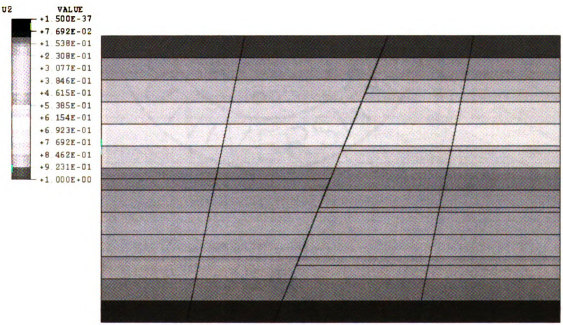

Figure 21. ***Patch of incompatible 2D meshes - Displacements distribution in the direction 2 (U_2).***

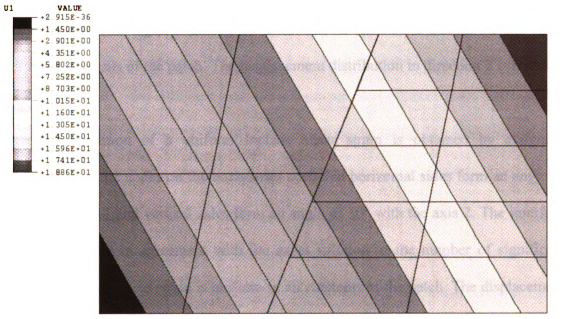

(a)

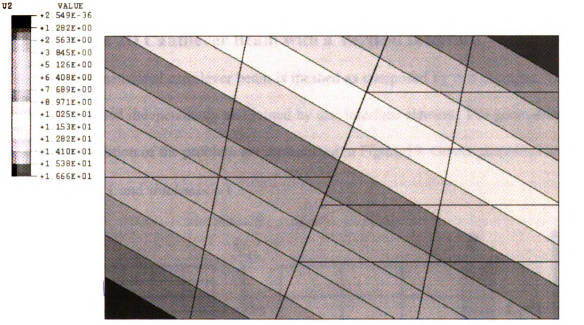

(b)

Figure 22. ***Patch of incompatible 2D meshes - Displacements distribution in the direction 1 (a) and in direction 2 (b) under uniform shear deformation.***

The interface element results are in agreement with the exact solution to the number of significant digits available, i.e. axial strain is uniform in direction 2 and equal to 0.1 in all elements of the patch. The displacement distribution in direction 2 is reported in Figure 21.

The condition of a uniform inplane shear strain is obtained by assigning displacements to the nodes on the boundaries such that horizontal sides form an angle of 30° with the axis 1 and vertical sides form an angle of 30° with the axis 2. The interface element results are in agreement with the exact solution to the number of significant digits available, i.e. shear strain is uniform in all elements of the patch. The displacement distributions in direction 1 and 2 are reported in Figures 22(a) and 22(b).

4.7.2 Isotropic 2D Cantilever Beam with a Vertical Interface

A two-dimensional cantilever beam is meshed as composed by two domains. The domains are meshed independently and joined by one interface element. The geometrical and load configuration of the problem are represented in Figure 19. Others properties are: $P = 1$, $E_1 = E_2 = 1$ and $thickness = 1$.

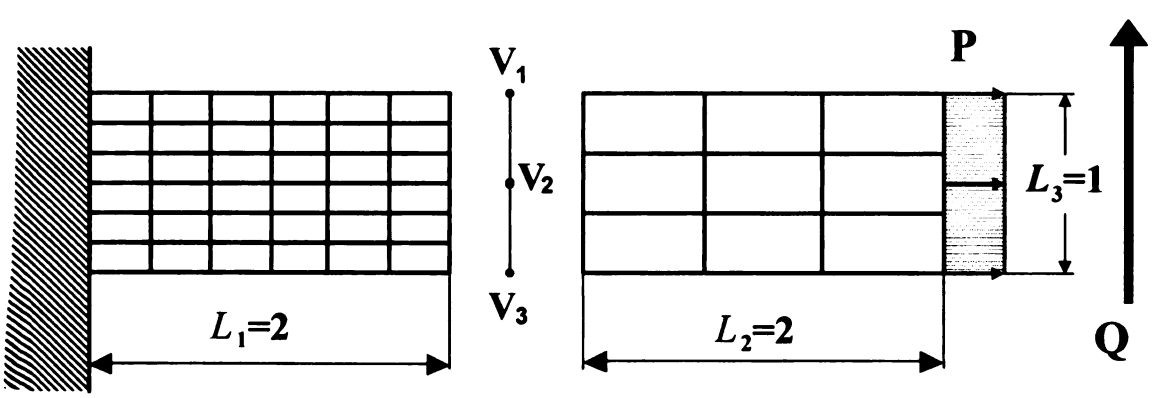

Figure 23. ***2D Cantilever beam with vertical interface***

Only one Interface element is adopted in this simple case, since more would not improve the solution accuracy. This element is identified by the vertical interface made of the three nodes V_1, V_2 and V_3. For discretizing the two domains, four-noded bilinear elements are used. Two different load conditions are investigated: axial and bending loads. This problem may be considered another form patch test for the element developed herein.

4.7.2.1 Axial Load

Under the condition of a uniform axial load applied at the free end of the beam, the interface element results are in complete agreement with the exact solution to the number of significant digits available. Results from two different beam discretizations are reported in Table 7.

Table 7. ***Tip axial displacement numerical results for beam extension.***

	Mesh	***Solution***
Abaqus	20x8	**4.000**
Abaqus with interface Element	10x8 Left / 10x2 Right 10x8 Left / 10x4 Right	**4.000** **4.000**
Classical	-	**4.000**

It is important to study the stability of the solution obtained by the new method for various values of the nondimensionalized penalty parameter γ / E. To run this test the automatic choice of the optimal parameter γ, described in section 4.7, has been disabled. Results are produced in tabular and graphical form in Table 8 and Figure 24.

It can be noticed that the solution is stable for a wide range of values of the nondimensionalized penalty parameter γ / E.

Table 8. ***2D Cantilever Beam under axial load – Mesh 10x8-10x4***

Variation of the solution accuracy with the decimal LOG of the penalty parameter															
0	**1**	**2**	**3**	**4**	**5**	**6**	**7**	**8**	**9**	**10**	**11**	**12**	**13**	**14**	**15**
6.00	4.20	4.02	4.00	4.00	4.00	4.00	4.00	4.00	4.00	4.00	4.00	4.00	4.02	4.13	7.42
Ratio Penalty/Exact															
0	**1**	**2**	**3**	**4**	**5**	**6**	**7**	**8**	**9**	**10**	**11**	**12**	**13**	**14**	**15**
1.50	1.05	1.01	1.00	1.00	1.00	1.00	1.00	1.00	1.00	1.00	1.00	1.00	1.01	1.03	1.86

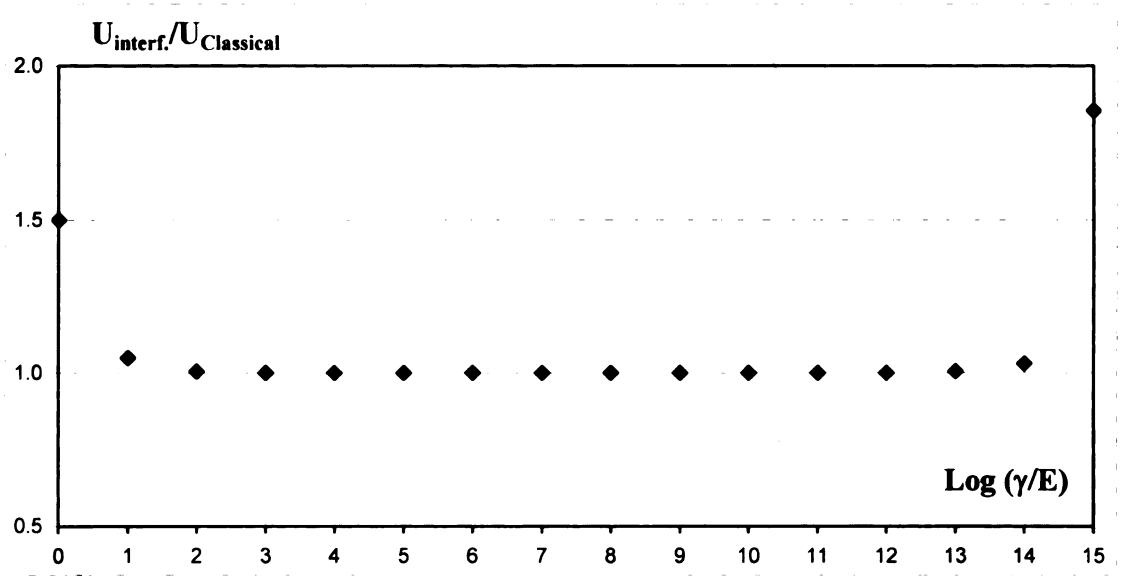

Figure 24. ***Stability of the solution for different values of γ - axial load.***

4.7.2.2 Bending Load

For the bending load case, the comparison is made to both the exact solution and a reference finite element solution. The coarse mesh of bilinear quadrilateral elements cannot exactly recover the classical solution. In Table 9 are results obtained from two different beam discretizations. The FE results, marked as Abaqus, are obtained from a traditional analysis using a compatible finite element model of the beam.

The stability of the solution obtained is tested also in this load case for various values of the nondimensionalized penalty parameter γ / E. Again the automatic choice of

the optimal parameter γ was temporarily disabled. Results are produced in graphical form in Figure 25. The method proves very reliable and stable for bending loads.

Table 9. ***Tip deflection numerical results for beam flexure.***

	Mesh	*Solution*
Abaqus	20x2	**258.800**
	20x4	**260.000**
	20x8	**260.400**
Abaqus with interface Element	10x8 Left / 10x2 Right	**259.500**
	10x8 Left / 10x4 Right	**261.100**
	10x8 Left / 10x8 Right	**260.400**
Classical	-	**265.6**

Table 10. ***Tip deflection in a 2D beam under bending load – mesh 10x8-10x4***

Variation of the solution accuracy with the decimal LOG of the penalty parameter														
0	**1**	**2**	**3**	**4**	**5**	**6**	**7**	**8**	**9**	**10**	**11**	**12**	**13**	**14**
358.2	269.9	261.1	261.1	260.1	260.1	260.1	260.1	260.1	260.1	260.1	260.3	263.2	306.4	481.8
Ratio Penalty/Classical														
0	**1**	**2**	**3**	**4**	**5**	**6**	**7**	**8**	**9**	**10**	**11**	**12**	**13**	**14**
1.349	1.016	0.983	0.983	0.979	0.979	0.979	0.979	0.979	0.979	0.979	0.980	0.991	1.154	1.814

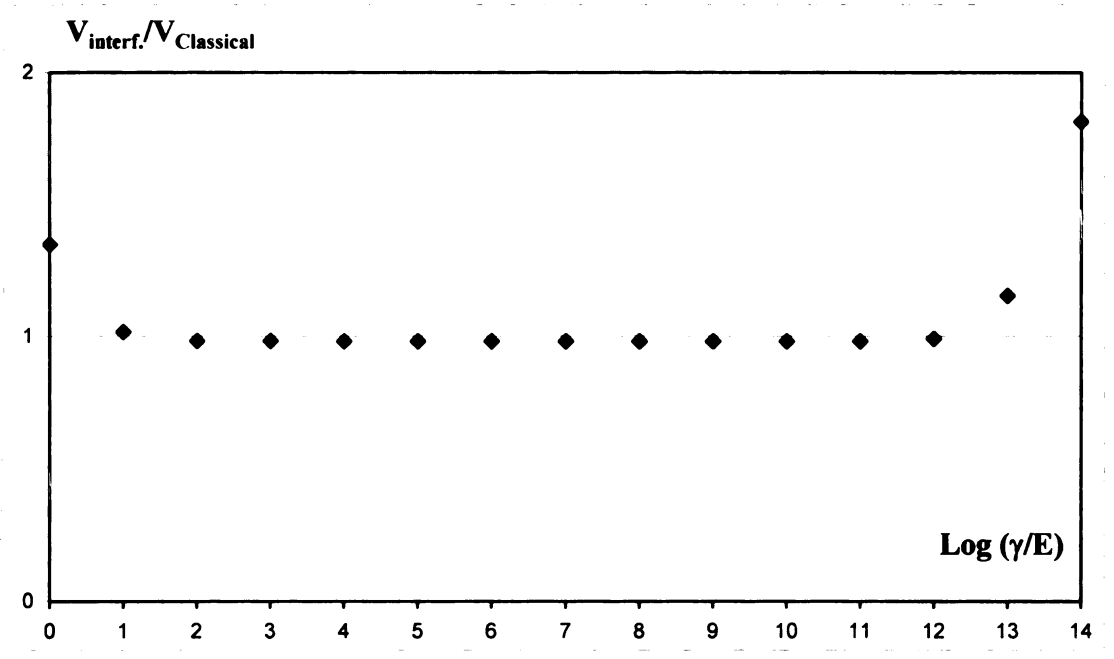

Figure 25. ***Stability of the solution for different values of γ - bending load***

4.7.3 Tension-Loaded Plate with a Central Circular Hole

A plate with a central circular hole is subjected to a uniform load at its edges. This well studied elasticity problem allows one to investigate the capability of the interface elements in performing global/local analysis. Geometrical and load configurations are plotted in Figure 26. The plate height and width are, respectively, $h = 100$ and $b = 200$; the radius of the hole is $r = 2.5$; the distance of the interface from the center of the hole is 5.

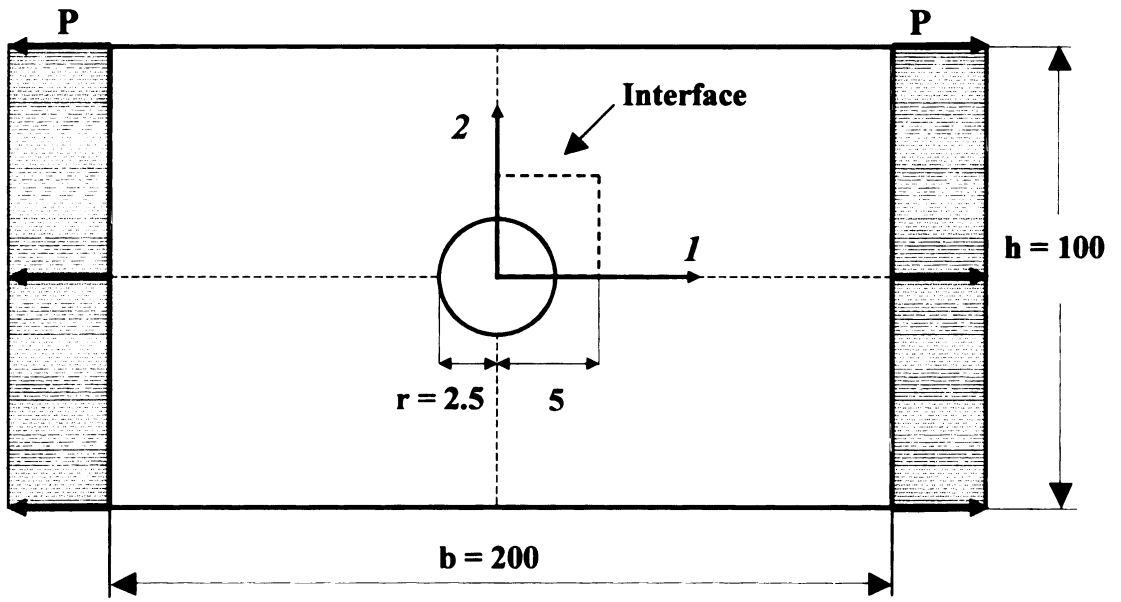

Figure 26. ***Tension-loaded plate with a central circular hole (not to scale).***

Taking advantage of symmetry, only one quarter of the plate is modeled. A fine mesh is applied in the area between the hole and the interface, while a much coarser mesh is adopted elsewhere. The complete finite element model is reported in Figure 27a. For a better view, the area near the hole is depicted in Figure 28a. A conventional FE model has been built with Abaqus in order to compare the maps of displacements and stresses,

see Figures 27b and 28b. The elements used to mesh the models are plane stress bilinear quadrilaterals, Abaqus CPS4. Five interface elements are employed along each segment of the interface.

Horizontal U_1 and vertical displacements U_2 do not show any change in their values across the interface, as plotted in Figures 29a and 30a. Figures 31a and 32a demonstrate that only light discontinuities in the values of stresses at the interface are present. Results from the Abaqus conventional FE model are reported in Figures 29b-32b. Comparing the maps of the displacements, it can be noticed that the interface elements does not affect at all their distribution. The maps of the stresses show just little differences among the models.

It is important to remember that through the penalty formulation continuity of displacements has been enforced, but not continuity of stresses. Therefore, some discontinuities across the interface are expected and do not depend on inaccuracies of the penalty model. The finite element interface technology developed at NASA LaRC [6-11], which uses Lagrange multipliers to enforce the interface constraint conditions exactly, is not able to do any better in preserving continuity of stresses across the interface.

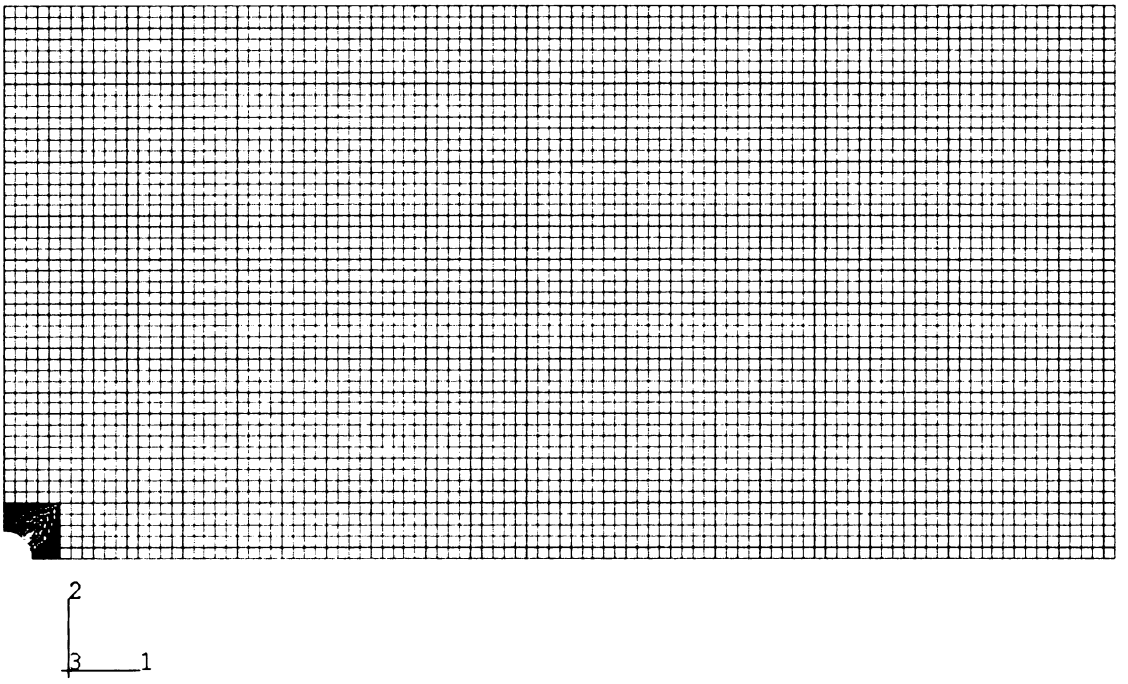

(a)

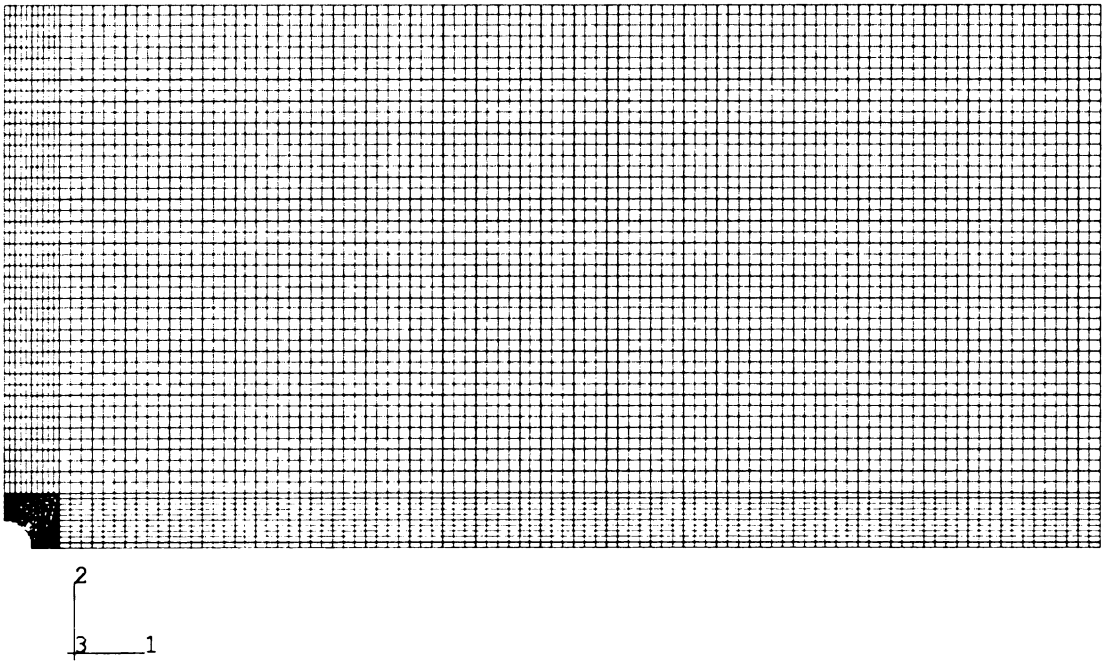

(b)

Figure 27. ***(a) Interface element and (b) conventional FE mesh.***

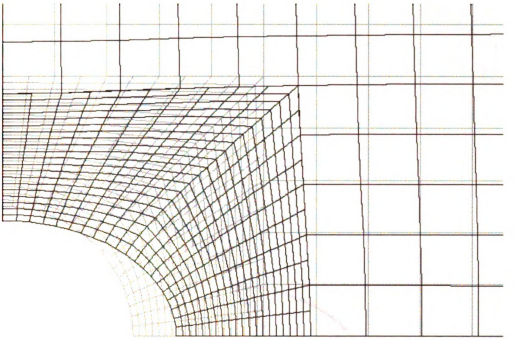

(a)

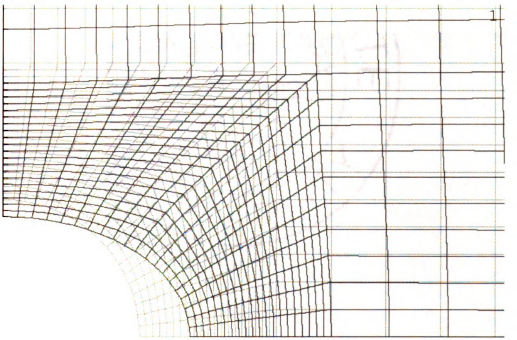

(b)

Figure 28. ***(a) Interface element and (b) conventional FE mesh - zoom of the deformed configuration.***

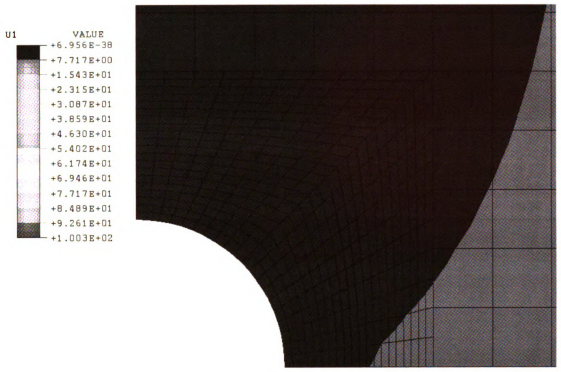

(a)

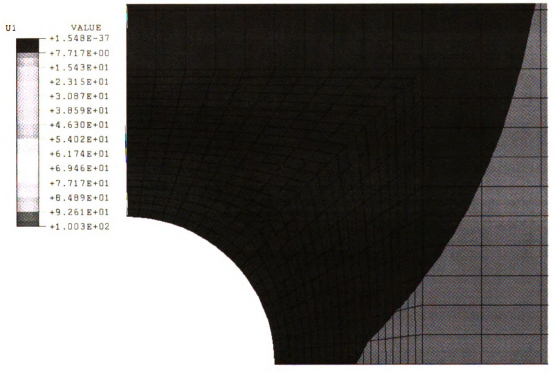

(b)

Figure 29. ***(a) Interface element and (b) conventional FE solution - horizontal displacement distribution (U_1).***

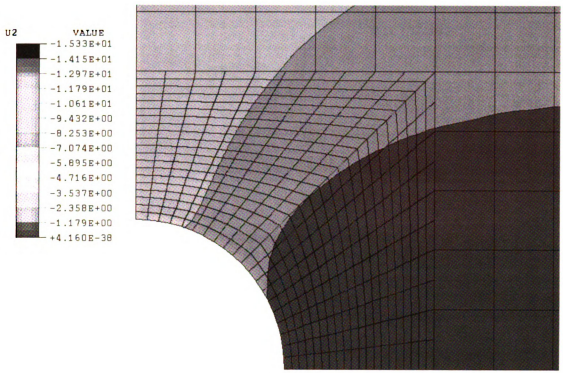

(a)

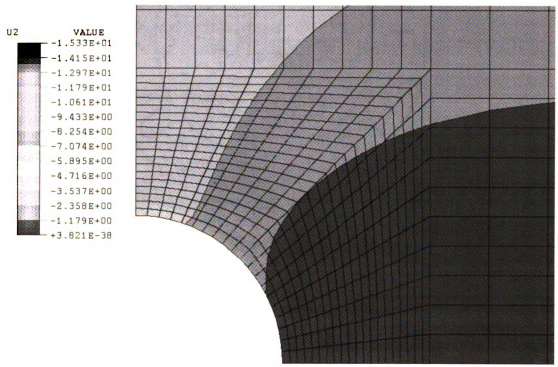

(b)

Figure 30. ***(a) Interface element and (b) conventional FE solution - vertical displacement distribution (U_2).***

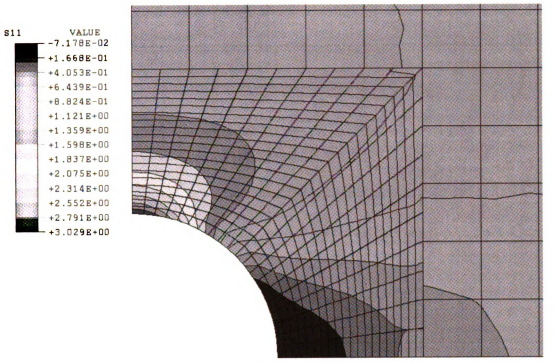

(a)

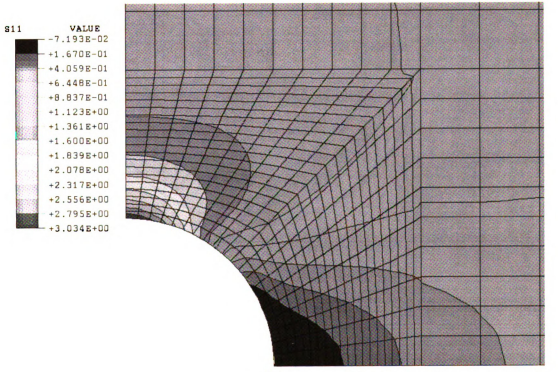

(b)

Figure 31. ***(a) Interface element and (b) conventional FE solution - stress distribution in the direction 1 (σ_{11}).***

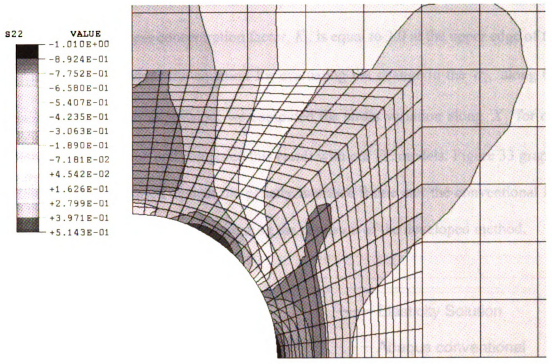

(a)

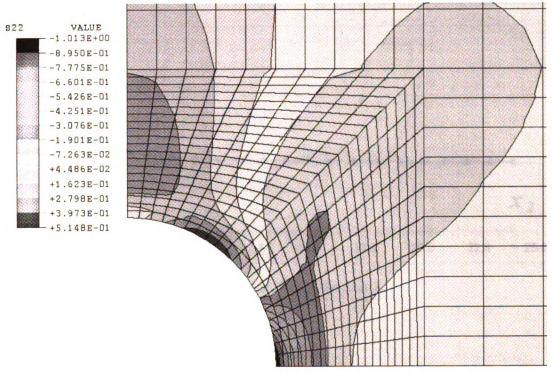

(b)

Figure 32. ***(a) Interface element and (b) conventional FE solution - stress distribution in the direction 2 (σ_{22}).***

tension

hole. M

line axi

geomet

the Ela

ones. T

Figur

The elasticity solution for an infinite plate with a central hole loaded in uniform tension says that the stress concentration factor, K_t, is equal to 3.0 at the upper edge of the hole. Moreover, it provides the equation for evaluating the change in the σ_{11} along the line axis X_2. Using this expression, we computed the stress variation along X_2 for our geometrical configuration and compared this result with our FE models. Figure 33 graphs the Elasticity exact solution against the penalty interface frame and the conventional FE ones. The results are all very near, validating the precision of the developed method.

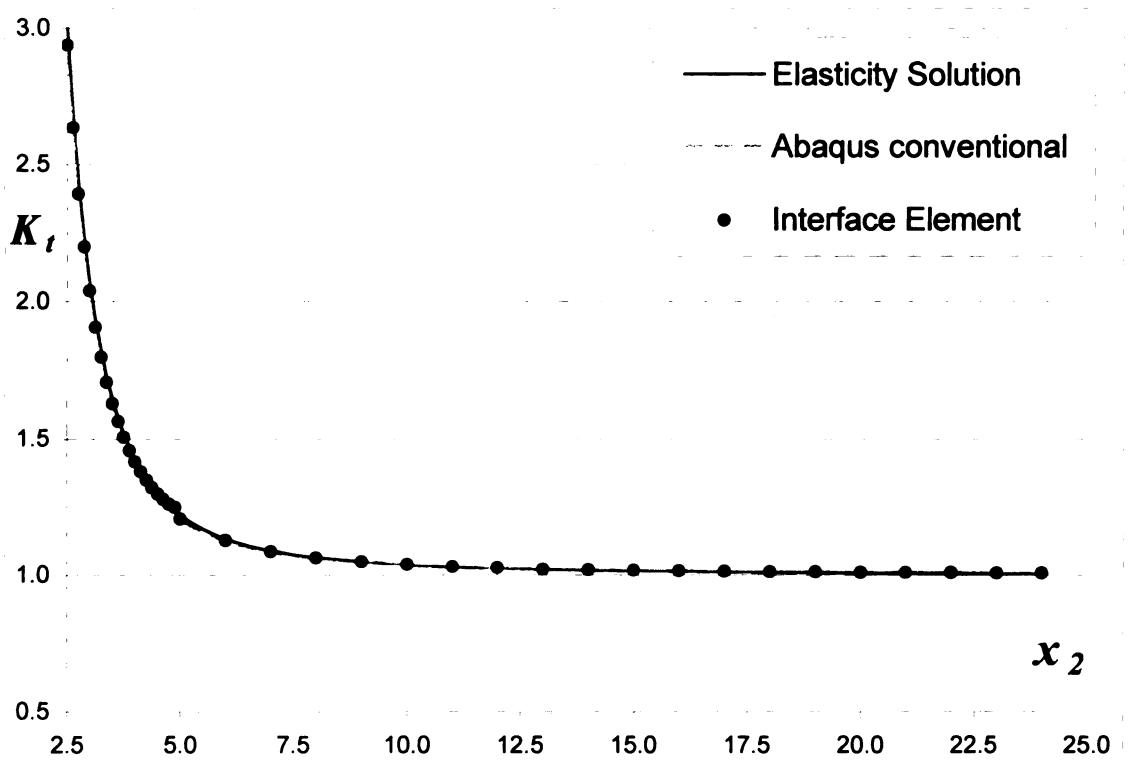

Figure 33. ***Stress Concentration Factor Along the axis 2.***

T

the hole.

mesh the

at same

Figure 3

model. C

interface

previous

confirm

incomp

The problem has also been studied with a different mesh for the area containing the hole. We wanted to prove that in order to get accurate results it is not necessary to mesh the connecting finite element models with some of the nodes at the interface placed at same location. The area near the hole of the new finite element model is shown in Figure 34; the mesh of the second subdomain is unchanged with respect to the previous model. One interface element of the general form is employed along each segment of the interface. Comparison is made to the same reference Abaqus conventional FE model used previously. Horizontal U_1 and vertical displacements U_2 plotted in Figures 35 and 36 confirm the remarkable accuracy of the method even in case of total nodal incompatibility at the interface.

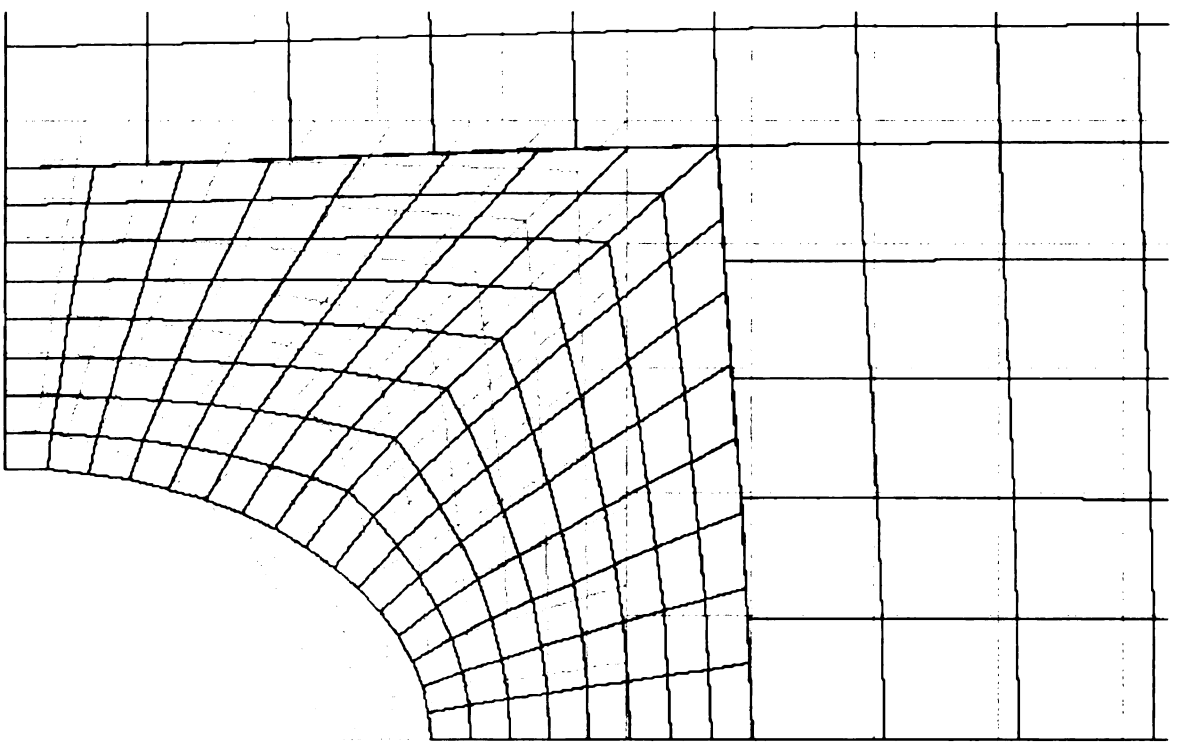

Figure 34. ***Interface element FE mesh #2 - zoom of the deformed configuration.***

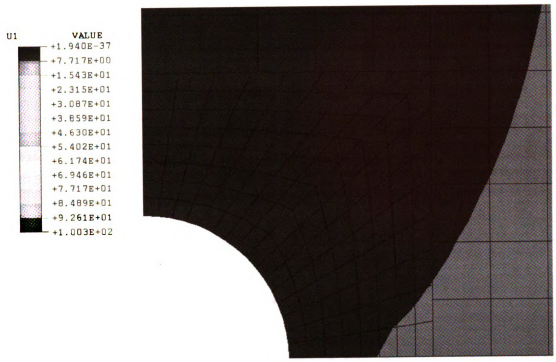

(a)

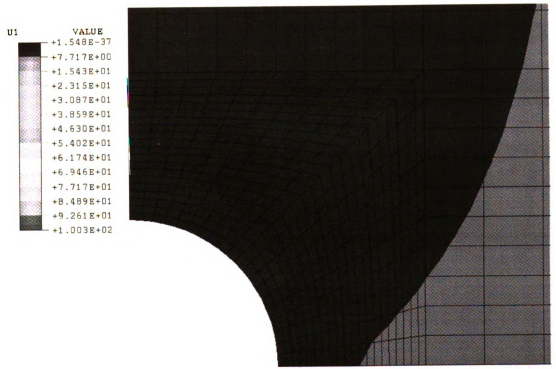

(b)

Figure 35. ***(a) Interface element and (b) conventional FE solution - horizontal displacement distribution (U_1).***

Figu

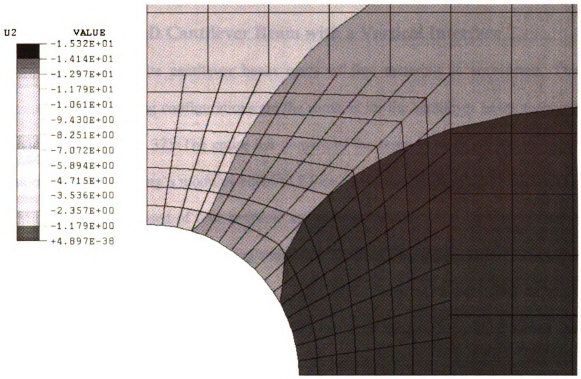

(a)

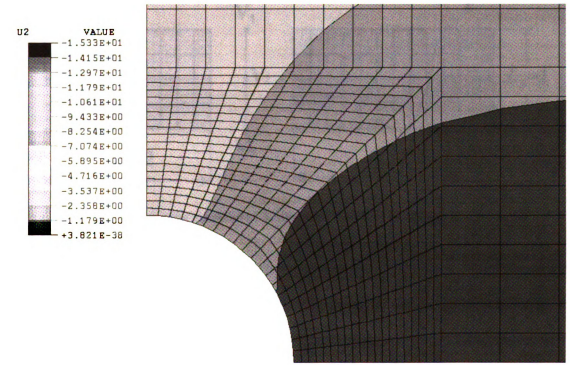

(b)

Figure 36. ***(a) Interface element and (b) conventional FE solution - vertical displacement distribution (U_2).***

4.7.4 Composite 2D Cantilever Beam with a Vertical Interface

A 2D composite cantilever beam made of five materials is considered. The geometrical and loading configurations are the same as for the cantilever beam analyzed previously (see Figure 37). The entire left domain of the beam is made of one isotropic material having a Young's modulus equal to 2.9E+7 MPa and Poisson's ratio 0.25. The right domain is composed of four isotropic layers of equal thickness. They have all the same Poisson ratio 0.25, but the Young's modulus E varies. Starting from the bottom, the layerwise E takes the values: 1E+6 MPa, 1E+7 MPa, 5E+6 MPa and 1E+8 MPa. A conventional finite element model (10x4-10x4) has been used as a baseline to test the results from the penalty interface method.

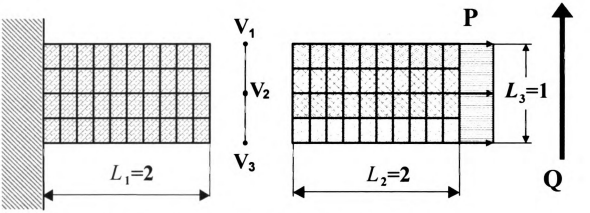

Figure 37. ***2D Composite cantilever beam with vertical interface***

Under these conditions the interface is expected to undergo abrupt changes of slope. An important property of the interface elements is the automatic choice of the penalty parameters. In fact, the interface elements can join the four different layers to the left domain with the dissimilar stiffness. This behavior can increase the accuracy of the results, avoiding the possible corrupting effect of an overestimated penalty parameter.

The results are shown for two possible interface discretizations: 1 interface element and 4 interface elements. Axial and vertical displacements at the free end of the beam under axial load are plotted in Figures 38 and 39. Similarly, deflections for transversal load case displacements at the free end of the beam are reported in Figures 40 and 41.

Displacements from the interface element model compare very well to those from the conventional finite element model. Only in the transversal load case, a single interface element appears to slightly overestimate the vertical displacements.

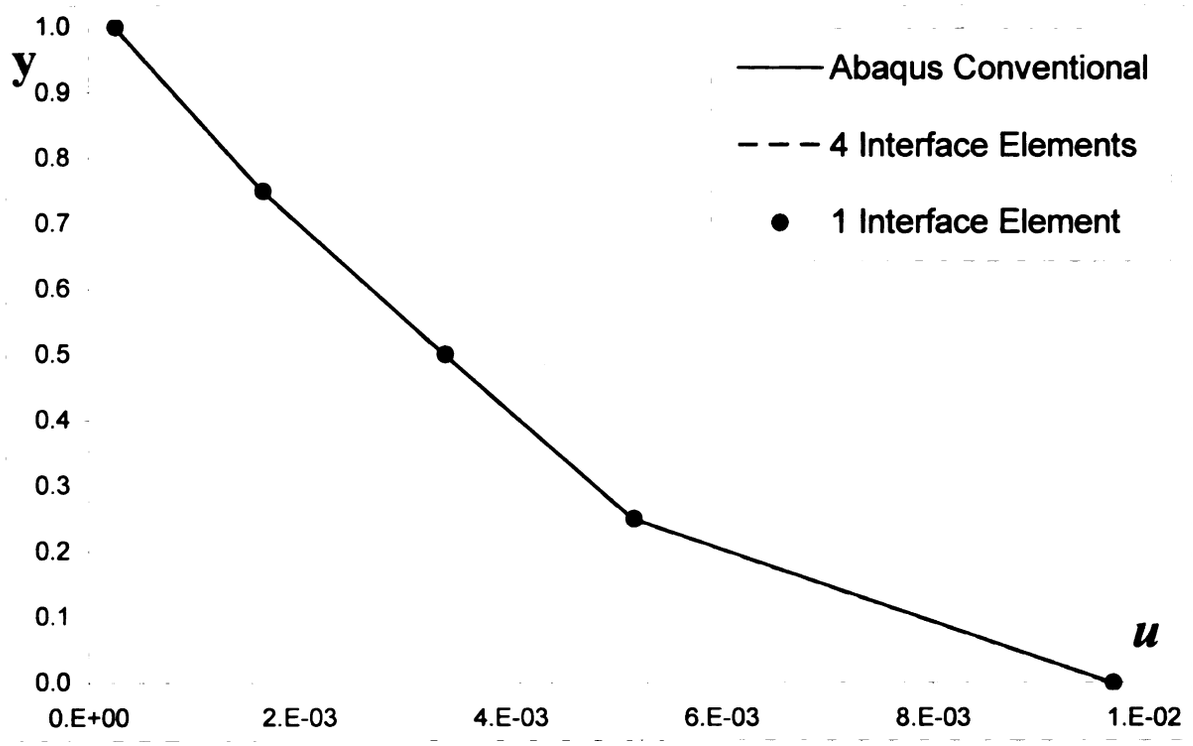

Figure 38. ***Beam extension along the thickness at the free end under axial load.***

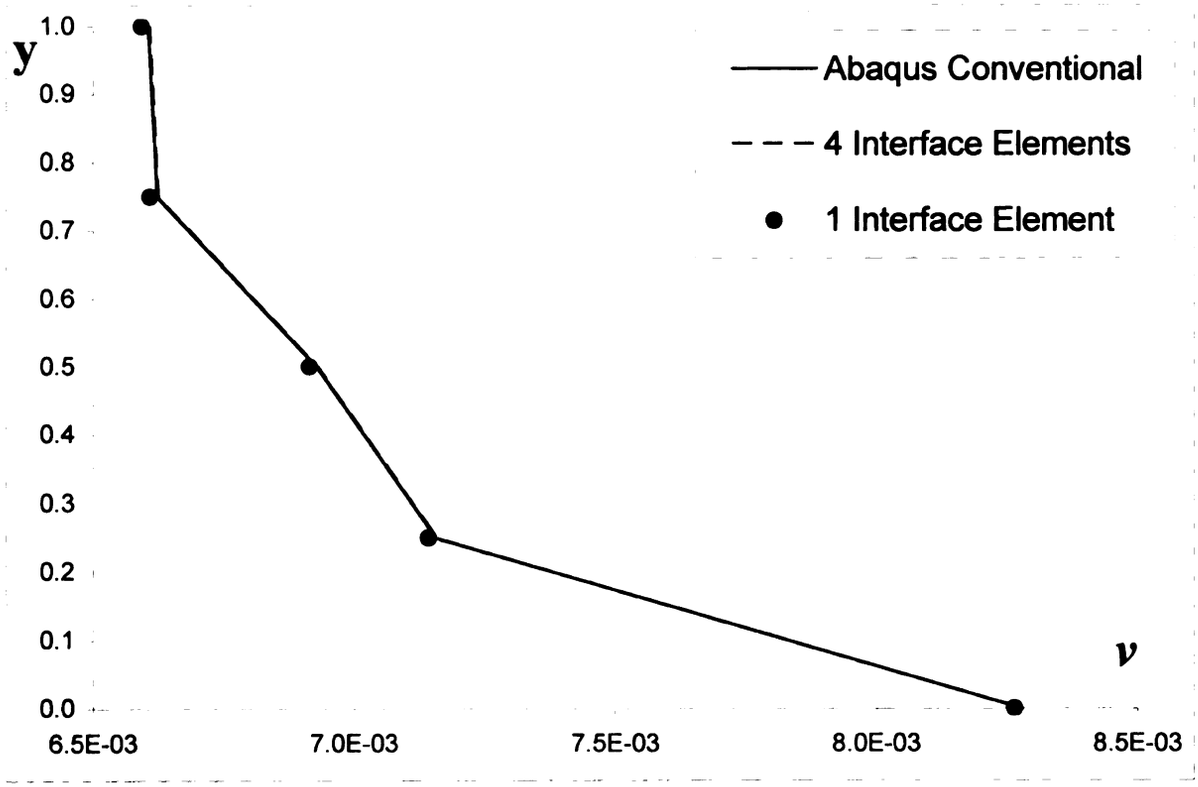

Figure 39. ***Beam vertical deflection along the thickness at the free end under axial load.***

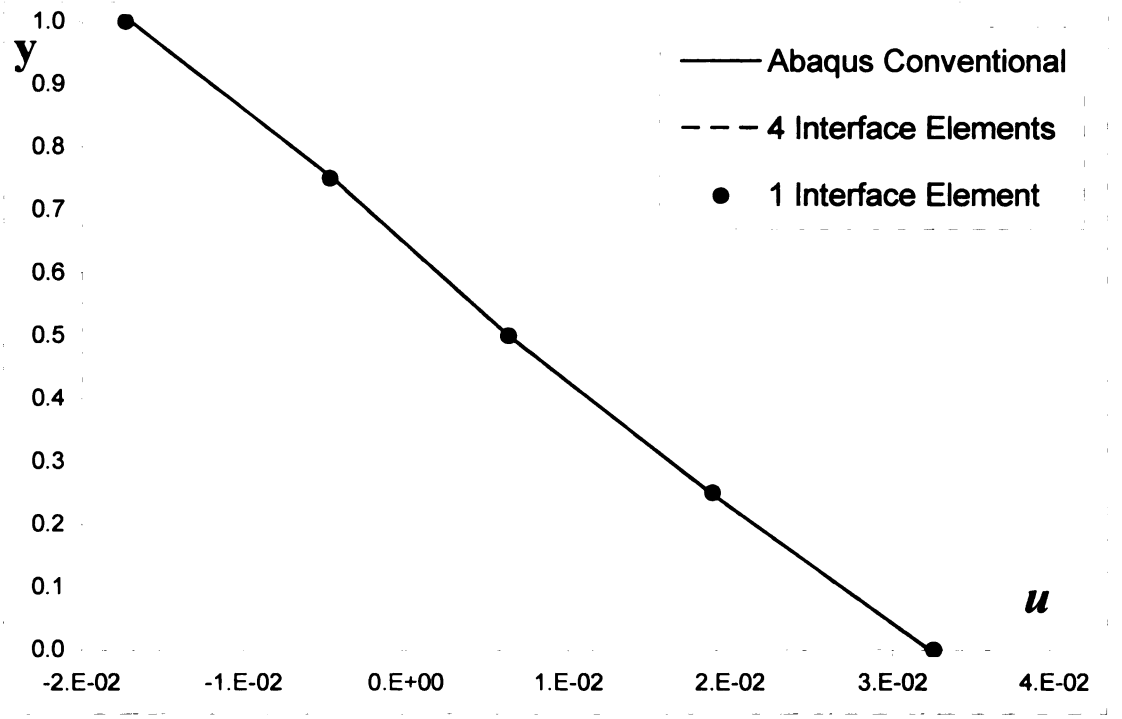

Figure 40. ***Beam extension along the thickness at the free end under transversal load.***

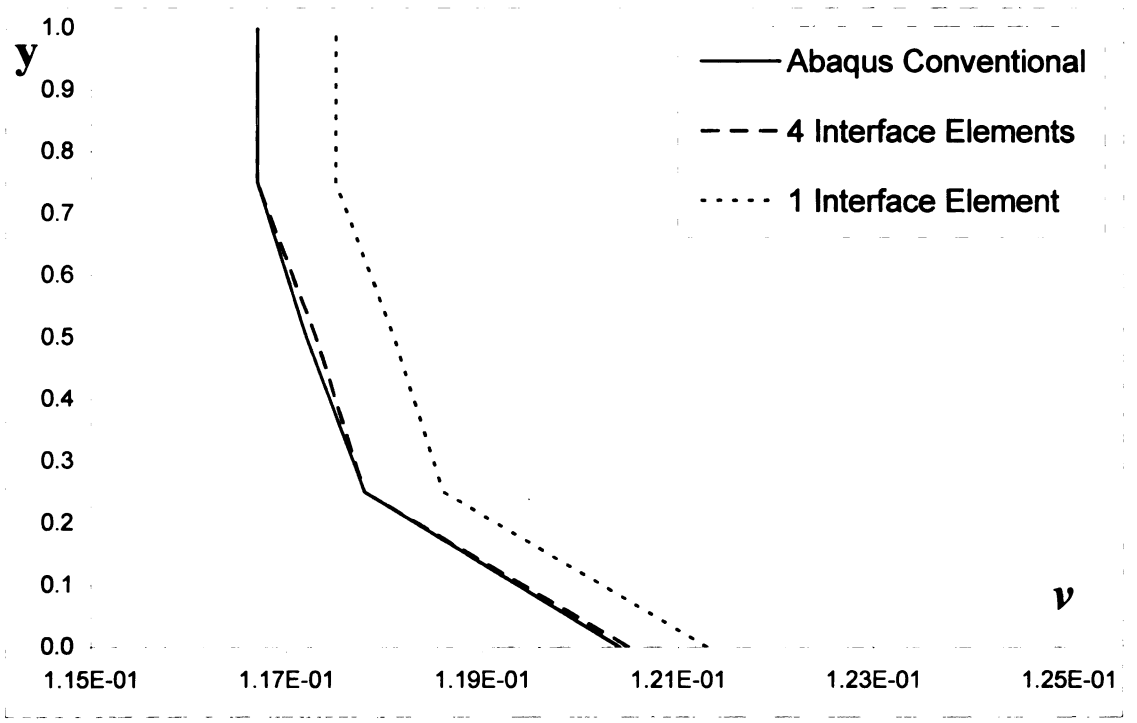

Figure 41. ***Beam vertical deflection along the thickness at the free end under transversal load.***

4.7.

conc

in [

posi

Figu

4.7.5 Clamped-Clamped Asymmetric Beam

In this section an asymmetric beam, clamped at both ends, is loaded with two concentrated loads applied at two different points of the mesh. This problem was studied in [4,13] to validate the proposed interface method. The geometry of the problem and the position of the two concentrated loads are shown in Figure 42.

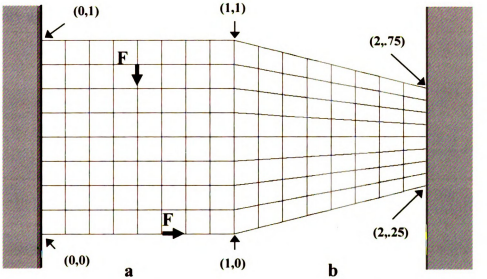

Figure 42. ***Clamped-clamped two-piece asymmetric beam. The data in parentheses represents the x and y coordinates of the points indicated***

The beam is meshed using two domains with different material properties. The ratio of the Young's modulus in the domains *a* and *b* is 0.2. The domain *a* is discretized with an 8 by 8 mesh; two different meshes are adopted for the domain *b*. The mesh used for the conventional FE analysis is set to be 8 by 8, so that at the interface there is the same number of nodes. A different mesh is needed for discretizing domain *b* in order to test the interface model's capabilities. An 8 by 12 mesh has been chosen. The two forces, having the same magnitude F=1 but different directions, produce a complex state of deformation with strong stress concentrations at the interface that can challenge the

interface element. Figures 43 and 44 compare the deformed configuration, produced by a conventional FEM, with that obtained using a FEM with four interface elements at the interface. No visible differences can be observed.

The test is completed by a comparison between the in-plane displacements u and v along the interface as shown in Figures 45 and 46. The four interface elements connect two interfaces with a different number of nodes. Both displacement components are in satisfactory agreement with the conventional analysis.

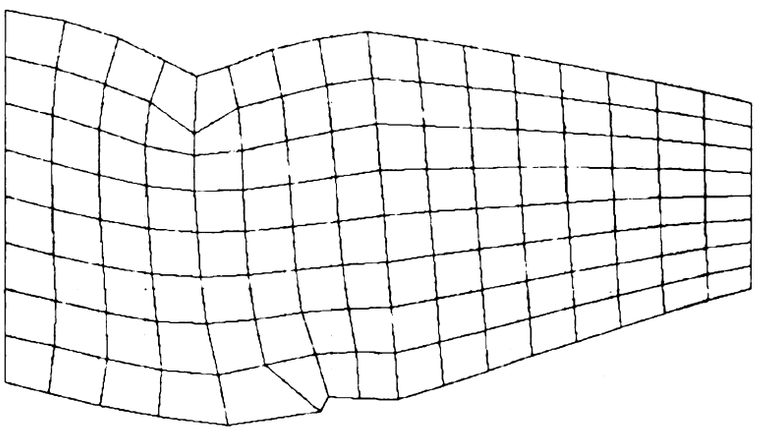

Figure 43. ***Deformed configuration obtained through conventional Abaqus FE solution.***

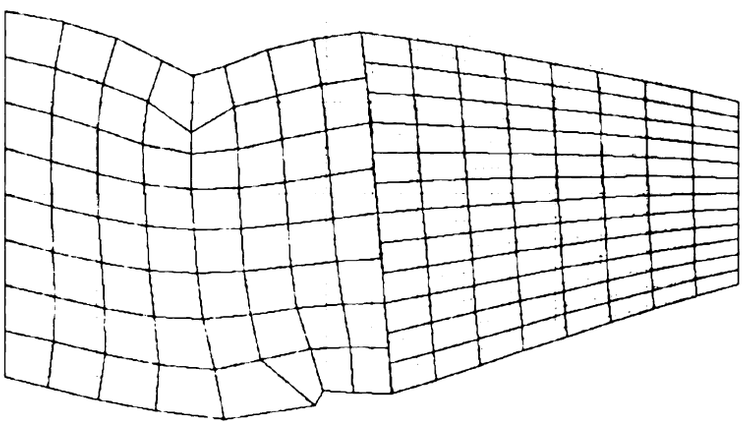

Figure 44. ***Deformed configuration obtained using interface elements approach.***

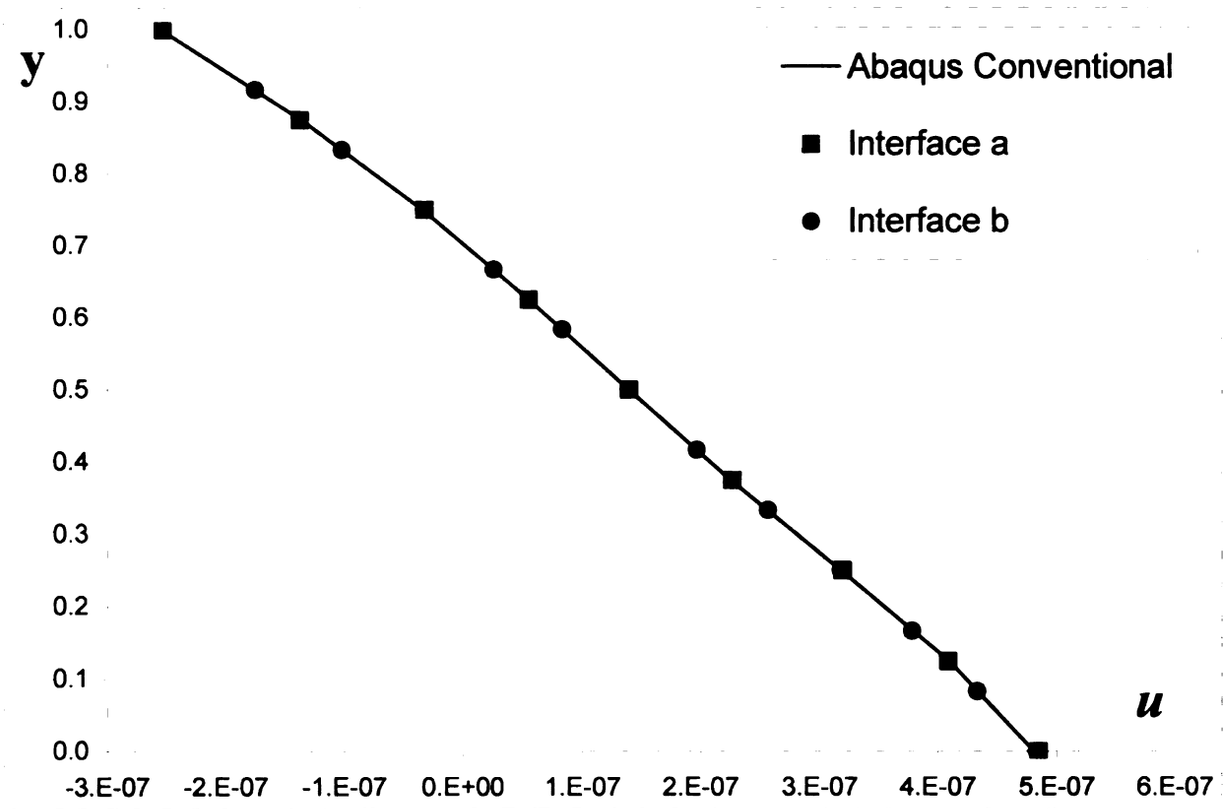

Figure 45. ***Axial displacements along the thickness at the interface***

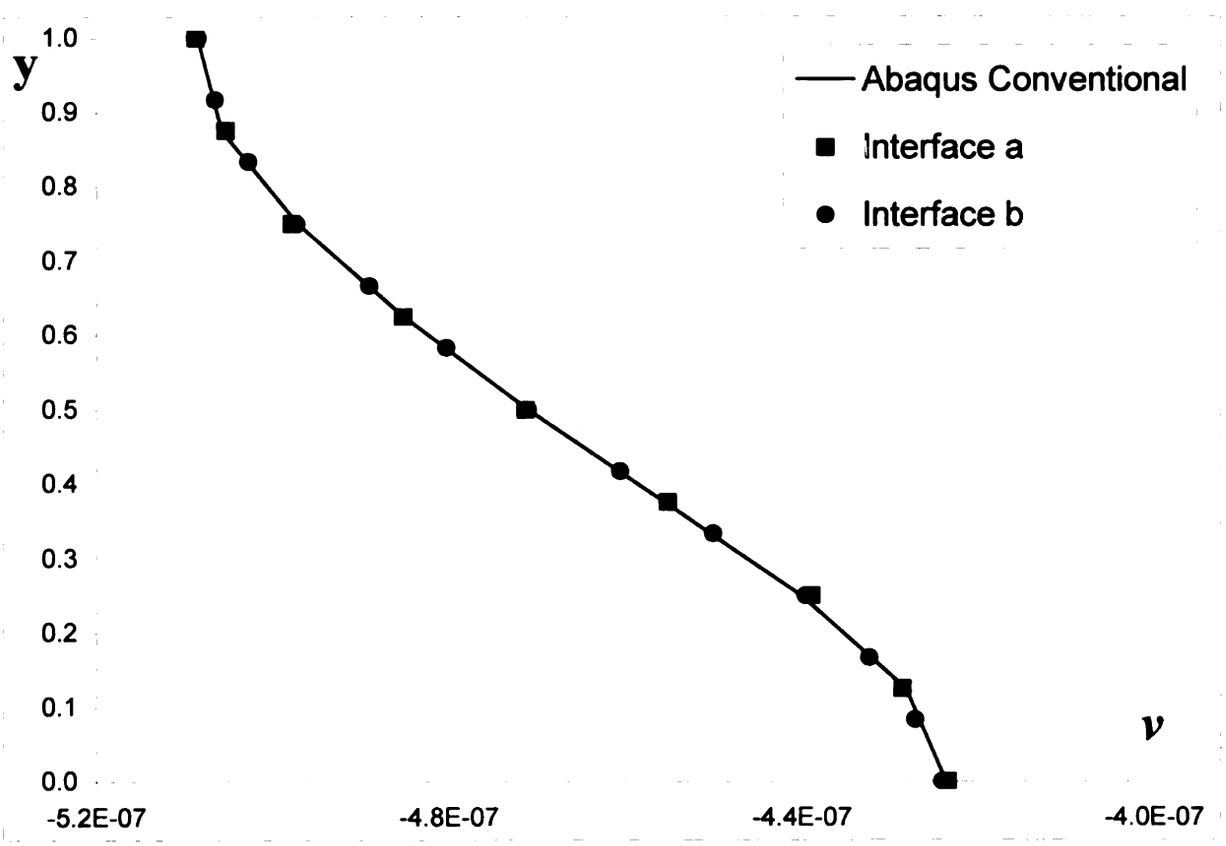

Figure 46. ***Transversal displacements along the thickness at the interface***

CHAPTER 5 PLATES

5.1 Finite Element Model

In this chapter an interface element for plate elements is developed. A definition of the finite element model associated with the plate element is provided in this section. Plate elements based on the First Order Shear Deformation theory, or Mindlin plate theory has been chosen for our research.

The degrees of freedom associated with this element are five for each node: u, v, w, θ_x, θ_y. However, the equations governing the in-plane displacements u and v are uncoupled from those governing the bending deflections w, θ_x, θ_y. It follows that all the results obtained from the study on the plane stress quadrilateral are valid for the in-plane displacements of the plate. Thus, we will focus our attention just on the bending DOFs w, θ_x, θ_y.

The First Order Shear Deformation Theory (FSDT) is based on the displacement field of Mindlin:

$$\begin{aligned} u &= u_0 - z\,\theta_y \\ v &= v_0 + z\,\theta_x \\ w &= w_0 \end{aligned} \tag{519}$$

The associated bending strains are:

$$\varepsilon_x = -z\frac{\partial \theta_y}{\partial x} \tag{520}$$

$$\varepsilon_y = z\frac{\partial \theta_x}{\partial y} \tag{521}$$

$$\varepsilon_z = 0 \tag{522}$$

$$\gamma_{yz} = \theta_x + \frac{\partial w_0}{\partial y} \tag{523}$$

$$\gamma_{xz} = -\theta_y + \frac{\partial w_0}{\partial x} \tag{524}$$

$$\gamma_{xy} = z\left(\frac{\partial \theta_x}{\partial x} - \frac{\partial \theta_y}{\partial y}\right) \tag{525}$$

For a single isotropic plate with Young's modulus Y, Poisson ratio ν and thickness t; the laminate stiffness is defined by the following relations.

$$\begin{Bmatrix} N_x \\ N_y \\ N_{xy} \\ M_x \\ M_y \\ M_{xy} \end{Bmatrix} = \begin{bmatrix} A & \nu A & 0 & 0 & 0 & 0 \\ \nu A & A & 0 & 0 & 0 & 0 \\ 0 & 0 & A\left(\frac{1-\nu}{2}\right) & 0 & 0 & 0 \\ 0 & 0 & 0 & D & \nu D & 0 \\ 0 & 0 & 0 & \nu D & D & 0 \\ 0 & 0 & 0 & 0 & 0 & D\left(\frac{1-\nu}{2}\right) \end{bmatrix} \begin{Bmatrix} \varepsilon_x^0 \\ \varepsilon_y^0 \\ \gamma_{xy}^0 \\ \chi_x \\ \chi_y \\ \chi_{xy} \end{Bmatrix} \tag{526}$$

$$\begin{Bmatrix} Q_x \\ Q_y \end{Bmatrix} = \begin{bmatrix} A_s & 0 \\ 0 & A_s \end{bmatrix} \begin{Bmatrix} -\theta_y + \frac{\partial w}{\partial x} \\ \theta_x + \frac{\partial w}{\partial y} \end{Bmatrix} \tag{527}$$

Where:

$$A_s = kGt \tag{528}$$

$$A = \frac{Y t}{1-\nu^2} \tag{529}$$

$$D = \frac{Y t^3}{12\left(1-\nu^2\right)} \tag{530}$$

$$\begin{cases} \varepsilon_x^0 = \dfrac{\partial u_0}{\partial x} \\ \varepsilon_y^0 = \dfrac{\partial v_0}{\partial y} \\ \gamma_{xy}^0 = \dfrac{\partial u_0}{\partial y} + \dfrac{\partial v_0}{\partial x} \\ \chi_x = -\dfrac{\partial \theta_y}{\partial x} \\ \chi_y = \dfrac{\partial \theta_x}{\partial x} \\ \chi_{xy} = \left(\dfrac{\partial \theta_x}{\partial x} - \dfrac{\partial \theta_y}{\partial y}\right) \end{cases} \tag{531}$$

Assuming finite element interpolation of w, θ_x and θ_y in the form:

$$\begin{aligned} w &= \sum_{j=1}^{n} w_i N_j \\ \theta_x &= \sum_{j=1}^{n} (\theta_x)_i N_j \\ \theta_y &= \sum_{j=1}^{n} (\theta_y)_i N_j \end{aligned} \tag{532}$$

We obtain the finite element model for bending.

$$\begin{bmatrix} [K^{11}] & [K^{12}] & [K^{13}] \\ [K^{12}]^T & [K^{22}] & [K^{23}] \\ [K^{13}]^T & [K^{23}]^T & [K^{33}] \end{bmatrix} \begin{Bmatrix} \{w\} \\ \{\theta_x\} \\ \{\theta_y\} \end{Bmatrix} = \begin{Bmatrix} \{F^1\} \\ \{F^2\} \\ \{F^3\} \end{Bmatrix} \tag{533}$$

Where:

$$K_{ij}^{11} = kGt \left\{ \int_{\Omega_e} \left(\frac{\partial N_i}{\partial x} \frac{\partial N_j}{\partial x} + \frac{\partial N_i}{\partial y} \frac{\partial N_j}{\partial y} \right) dx dy \right\} \tag{534}$$

$$K_{ij}^{12} = kGt\left\{\int_{\Omega_e}\left(\frac{\partial N_i}{\partial y}N_j\right)dxdy\right\} \tag{535}$$

$$K_{ij}^{13} = -kGt\left\{\int_{\Omega_e}\left(\frac{\partial N_i}{\partial x}N_j\right)dxdy\right\} \tag{536}$$

$$K_{ij}^{22} = \int_{\Omega_e}\left(\left(\frac{Yt^3}{24(1+\nu)}\right)\frac{\partial N_i}{\partial x}\frac{\partial N_j}{\partial x} + \left(\frac{Yt^3}{12(1-\nu^2)}\right)\frac{\partial N_i}{\partial y}\frac{\partial N_j}{\partial y} + kGt\left(N_iN_j\right)\right)dxdy \tag{537}$$

$$K_{ij}^{23} = -\int_{\Omega_e}\left(\left(\frac{\nu Yt^3}{12(1-\nu^2)}\right)\frac{\partial N_i}{\partial y}\frac{\partial N_j}{\partial x} + \left(\frac{Yt^3}{24(1+\nu)}\right)\frac{\partial N_i}{\partial x}\frac{\partial N_j}{\partial y}\right)dxdy \tag{538}$$

$$K_{ij}^{33} = \int_{\Omega_e}\left(\left(\frac{Yt^3}{12(1-\nu^2)}\right)\frac{\partial N_i}{\partial x}\frac{\partial N_j}{\partial x} + \left(\frac{Yt^3}{24(1+\nu)}\right)\frac{\partial N_i}{\partial y}\frac{\partial N_j}{\partial y} + (kGt)N_iN_j\right)dxdy \tag{539}$$

Now, the previous defined stiffness matrix is computed for a rectangular plate element having the in plane dimension shown in Figure 47 and a thickness equal to t.

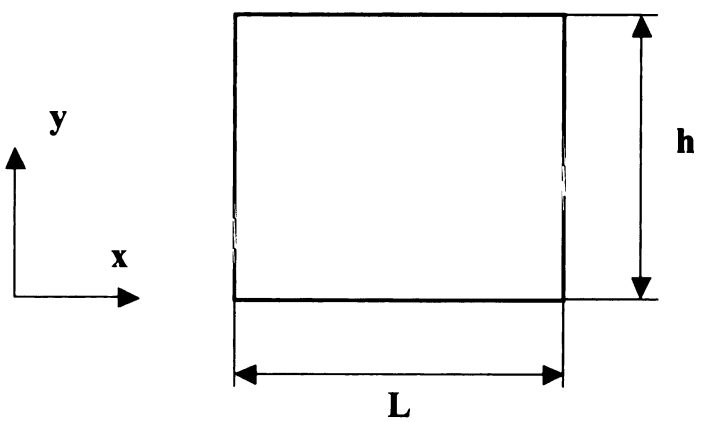

Figure 47. ***Geometrical dimensions of the plate element***

In the following lines the $[K]$ matrices composing the stiffness matrix are evaluated.

$$K_{11} = \begin{pmatrix} \frac{k\left(h^2+L^2\right)tY}{6hL(1+\nu)} & \frac{k\left(-2h^2+L^2\right)tY}{12hL(1+\nu)} & -\frac{k\left(h^2+L^2\right)tY}{12hL(1+\nu)} & \frac{k\left(h^2-2L^2\right)tY}{12hL(1+\nu)} \\ \frac{k\left(-2h^2+L^2\right)tY}{12hL(1+\nu)} & \frac{k\left(h^2+L^2\right)tY}{6hL(1+\nu)} & \frac{k\left(h^2-2L^2\right)tY}{12hL(1+\nu)} & -\frac{k\left(h^2+L^2\right)tY}{12hL(1+\nu)} \\ -\frac{k\left(h^2+L^2\right)tY}{12hL(1+\nu)} & \frac{k\left(h^2-2L^2\right)tY}{12hL(1+\nu)} & \frac{k\left(h^2+L^2\right)tY}{6hL(1+\nu)} & \frac{k\left(-2h^2+L^2\right)tY}{12hL(1+\nu)} \\ \frac{k\left(h^2-2L^2\right)tY}{12hL(1+\nu)} & -\frac{k\left(h^2+L^2\right)tY}{12hL(1+\nu)} & \frac{k\left(-2h^2+L^2\right)tY}{12hL(1+\nu)} & \frac{k\left(h^2+L^2\right)tY}{6hL(1+\nu)} \end{pmatrix} \tag{540}$$

$K_{22} =$

$$\begin{pmatrix} \frac{tY\left(-2L^2t^2+h^2\left(4kL^2+t^2\right)(-1+\nu)\right)}{72hL(-1+\nu)(1+\nu)} & -\frac{tY\left(L^2t^2-h^2\left(2kL^2-t^2\right)(-1+\nu)\right)}{72hL(-1+\nu)(1+\nu)} & \frac{tY\left(2L^2t^2+h^2\left(2kL^2-t^2\right)(-1+\nu)\right)}{144hL(-1+\nu)(1+\nu)} & \frac{tY\left(4L^2t^2+h^2\left(4kL^2+t^2\right)(-1+\nu)\right)}{144hL(-1+\nu)(1+\nu)} \\ -\frac{tY\left(L^2t^2-h^2\left(2kL^2-t^2\right)(-1+\nu)\right)}{72hL(-1+\nu)(1+\nu)} & \frac{tY\left(-2L^2t^2+h^2\left(4kL^2+t^2\right)(-1+\nu)\right)}{72hL(-1+\nu)(1+\nu)} & \frac{tY\left(4L^2t^2+h^2\left(4kL^2+t^2\right)(-1+\nu)\right)}{144hL(-1+\nu)(1+\nu)} & \frac{tY\left(2L^2t^2+h^2\left(2kL^2-t^2\right)(-1+\nu)\right)}{144hL(-1+\nu)(1+\nu)} \\ \frac{tY\left(2L^2t^2+h^2\left(2kL^2-t^2\right)(-1+\nu)\right)}{144hL(-1+\nu)(1+\nu)} & \frac{tY\left(4L^2t^2+h^2\left(4kL^2+t^2\right)(-1+\nu)\right)}{144hL(-1+\nu)(1+\nu)} & \frac{tY\left(-2L^2t^2+h^2\left(4kL^2+t^2\right)(-1+\nu)\right)}{72hL(-1+\nu)(1+\nu)} & -\frac{tY\left(L^2t^2-h^2\left(2kL^2-t^2\right)(-1+\nu)\right)}{72hL(-1+\nu)(1+\nu)} \\ \frac{tY\left(4L^2t^2+h^2\left(4kL^2+t^2\right)(-1+\nu)\right)}{144hL(-1+\nu)(1+\nu)} & \frac{tY\left(2L^2t^2+h^2\left(2kL^2-t^2\right)(-1+\nu)\right)}{144hL(-1+\nu)(1+\nu)} & -\frac{tY\left(L^2t^2-h^2\left(2kL^2-t^2\right)(-1+\nu)\right)}{72hL(-1+\nu)(1+\nu)} & \frac{tY\left(-2L^2t^2+h^2\left(4kL^2+t^2\right)(-1+\nu)\right)}{72hL(-1+\nu)(1+\nu)} \end{pmatrix} \tag{541}$$

$$K_{12} = \begin{pmatrix} -\frac{kLtY}{12(1+\nu)} & -\frac{kLtY}{24(1+\nu)} & -\frac{kLtY}{24(1+\nu)} & -\frac{kLtY}{12(1+\nu)} \\ -\frac{kLtY}{24(1+\nu)} & -\frac{kLtY}{12(1+\nu)} & -\frac{kLtY}{12(1+\nu)} & -\frac{kLtY}{24(1+\nu)} \\ \frac{kLtY}{24(1+\nu)} & \frac{kLtY}{12(1+\nu)} & \frac{kLtY}{12(1+\nu)} & \frac{kLtY}{24(1+\nu)} \\ \frac{kLtY}{12(1+\nu)} & \frac{kLtY}{24(1+\nu)} & \frac{kLtY}{24(1+\nu)} & \frac{kLtY}{12(1+\nu)} \end{pmatrix} \tag{542}$$

$K_{33} =$

$$\begin{pmatrix} \frac{tY\left(h^2\left(-2t^2+4kL^2(-1+\nu)\right)+L^2t^2(-1+\nu)\right)}{72hL(-1+\nu)(1+\nu)} & \frac{tY\left(4h^2\left(t^2+kL^2(-1+\nu)\right)+L^2t^2(-1+\nu)\right)}{144hL(-1+\nu)(1+\nu)} & \frac{tY\left(2h^2\left(t^2+kL^2(-1+\nu)\right)-L^2t^2(-1+\nu)\right)}{144hL(-1+\nu)(1+\nu)} \\ \frac{tY\left(4h^2\left(t^2+kL^2(-1+\nu)\right)+L^2t^2(-1+\nu)\right)}{144hL(-1+\nu)(1+\nu)} & \frac{tY\left(h^2\left(-2t^2+4kL^2(-1+\nu)\right)+L^2t^2(-1+\nu)\right)}{72hL(-1+\nu)(1+\nu)} & -\frac{tY\left(h^2\left(t^2-2kL^2(-1+\nu)\right)+L^2t^2(-1+\nu)\right)}{72hL(-1+\nu)(1+\nu)} \\ \frac{tY\left(2h^2\left(t^2+kL^2(-1+\nu)\right)-L^2t^2(-1+\nu)\right)}{144hL(-1+\nu)(1+\nu)} & -\frac{tY\left(h^2\left(t^2-2kL^2(-1+\nu)\right)+L^2t^2(-1+\nu)\right)}{72hL(-1+\nu)(1+\nu)} & \frac{tY\left(h^2\left(-2t^2+4kL^2(-1+\nu)\right)+L^2t^2(-1+\nu)\right)}{72hL(-1+\nu)(1+\nu)} \\ -\frac{tY\left(h^2\left(t^2-2kL^2(-1+\nu)\right)+L^2t^2(-1+\nu)\right)}{72hL(-1+\nu)(1+\nu)} & \frac{tY\left(2h^2\left(t^2+kL^2(-1+\nu)\right)-L^2t^2(-1+\nu)\right)}{144hL(-1+\nu)(1+\nu)} & \frac{tY\left(4h^2\left(t^2+kL^2(-1+\nu)\right)+L^2t^2(-1+\nu)\right)}{144hL(-1+\nu)(1+\nu)} \end{pmatrix}$$

$$\cdots$$

$$\begin{pmatrix} \frac{tY\left(4h^2\left(t^2+kL^2(-1+\nu)\right)+L^2t^2(-1+\nu)\right)}{144hL(-1+\nu)(1+\nu)} & \frac{tY\left(2h^2\left(t^2+kL^2(-1+\nu)\right)-L^2t^2(-1+\nu)\right)}{144hL(-1+\nu)(1+\nu)} & -\frac{tY\left(h^2\left(t^2-2kL^2(-1+\nu)\right)+L^2t^2(-1+\nu)\right)}{72hL(-1+\nu)(1+\nu)} \\ \frac{tY\left(h^2\left(-2t^2+4kL^2(-1+\nu)\right)+L^2t^2(-1+\nu)\right)}{72hL(-1+\nu)(1+\nu)} & -\frac{tY\left(h^2\left(t^2-2kL^2(-1+\nu)\right)+L^2t^2(-1+\nu)\right)}{72hL(-1+\nu)(1+\nu)} & \frac{tY\left(2h^2\left(t^2+kL^2(-1+\nu)\right)-L^2t^2(-1+\nu)\right)}{144hL(-1+\nu)(1+\nu)} \\ -\frac{tY\left(h^2\left(t^2-2kL^2(-1+\nu)\right)+L^2t^2(-1+\nu)\right)}{72hL(-1+\nu)(1+\nu)} & \frac{tY\left(h^2\left(-2t^2+4kL^2(-1+\nu)\right)+L^2t^2(-1+\nu)\right)}{72hL(-1+\nu)(1+\nu)} & \frac{tY\left(4h^2\left(t^2+kL^2(-1+\nu)\right)+L^2t^2(-1+\nu)\right)}{144hL(-1+\nu)(1+\nu)} \\ \frac{tY\left(2h^2\left(t^2+kL^2(-1+\nu)\right)-L^2t^2(-1+\nu)\right)}{144hL(-1+\nu)(1+\nu)} & \frac{tY\left(4h^2\left(t^2+kL^2(-1+\nu)\right)+L^2t^2(-1+\nu)\right)}{144hL(-1+\nu)(1+\nu)} & \frac{tY\left(h^2\left(-2t^2+4kL^2(-1+\nu)\right)+L^2t^2(-1+\nu)\right)}{72hL(-1+\nu)(1+\nu)} \end{pmatrix} \tag{543}$$

$$\cdots$$

$$K_{13} = \begin{pmatrix} \frac{hktY}{12(1+\nu)} & \frac{hktY}{12(1+\nu)} & \frac{hktY}{24(1+\nu)} & \frac{hktY}{24(1+\nu)} \\ -\frac{hktY}{12(1+\nu)} & -\frac{hktY}{12(1+\nu)} & -\frac{hktY}{24(1+\nu)} & -\frac{hktY}{24(1+\nu)} \\ -\frac{hktY}{24(1+\nu)} & -\frac{hktY}{24(1+\nu)} & -\frac{hktY}{12(1+\nu)} & -\frac{hktY}{12(1+\nu)} \\ \frac{hktY}{24(1+\nu)} & \frac{hktY}{24(1+\nu)} & \frac{hktY}{12(1+\nu)} & \frac{hktY}{12(1+\nu)} \end{pmatrix} \tag{544}$$

$$K_{23} = \begin{pmatrix} \frac{t^3 Y}{96(-1+\nu)} & \frac{t^3 Y(1-3\nu)}{96(-1+\nu^2)} & \frac{t^3 Y}{96-96\nu} & \frac{t^3 Y(-1+3\nu)}{96(-1+\nu^2)} \\ \frac{t^3 Y(-1+3\nu)}{96(-1+\nu^2)} & \frac{t^3 Y}{96-96\nu} & \frac{t^3 Y(1-3\nu)}{96(-1+\nu^2)} & \frac{t^3 Y}{96(-1+\nu)} \\ \frac{t^3 Y}{96-96\nu} & \frac{t^3 Y(-1+3\nu)}{96(-1+\nu^2)} & \frac{t^3 Y}{96(-1+\nu)} & \frac{t^3 Y(1-3\nu)}{96(-1+\nu^2)} \\ \frac{t^3 Y(1-3\nu)}{96(-1+\nu^2)} & \frac{t^3 Y}{96(-1+\nu)} & \frac{t^3 Y(-1+3\nu)}{96(-1+\nu^2)} & \frac{t^3 Y}{96-96\nu} \end{pmatrix} \quad (545)$$

5.2 *Clamped Rectangular Plate Element*

Following the same path as in the Plane Elasticity case, the solution for a rectangular plate element has been developed. Figures 48 and 49 show loading and geometrical configuration.

Analyzing a plate, nevertheless, requires the presence of 3 degrees of freedom for node. Having a total of 7 nodes, we should report a matrix with 21 rows and 21 columns, an effort that would be of little help in increasing our knowledge about the method. This since we would show nothing else that adding the same $[G]$ matrices to the global stiffness matrix of the system three times, one for each DOF. In fact, it should be clear that the $[G]$ matrixes depend only on the integration interval and on the approximation functions adopted. If all the DOFs are approximated by the linear Lagrange approximation functions and we adopt the same cubic splines, as before, all the $[G]$ matrices are unchanged.

In the following sections the results from our numerical study are reported. Two different penalty parameters are used: γ_w is associated to the transverse DOF *w*, instead γ_θ is related to the rotational DOF.

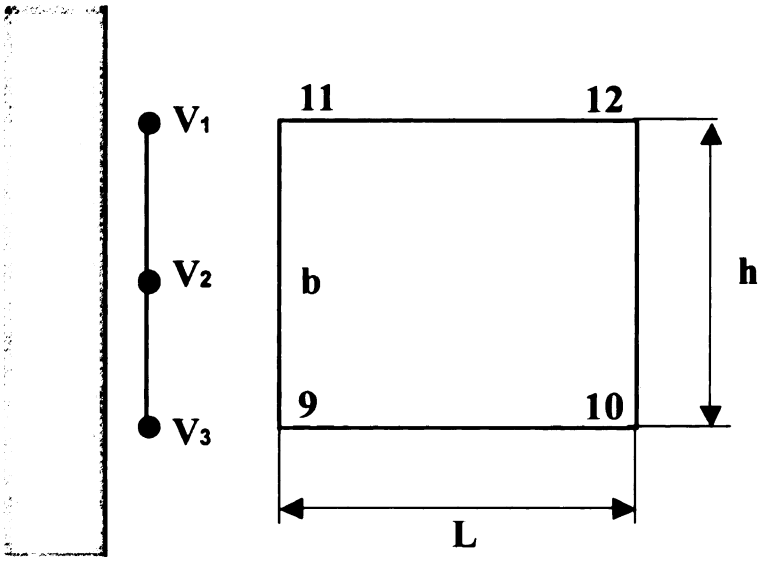

Figure 48. ***Single plate element connected to a fixed penalty frame – Top view***

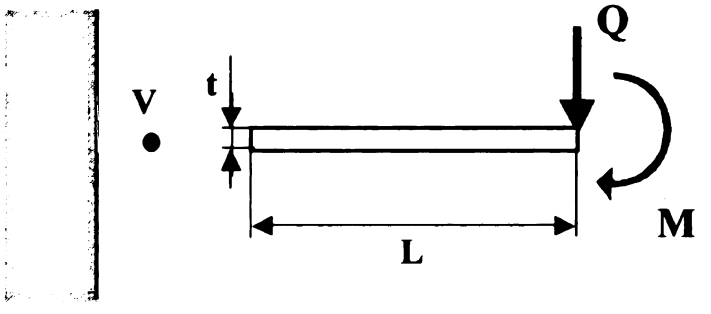

Figure 49. ***Single plate element connected to a fixed penalty frame – Lateral view***

5.2.1 Transversal Load

We are interested in solving this problem for two simple load cases: transversal load and a bending moment applied at the free edge. We consider the transversal load first, as shown in Figure 50.

The symbolic results obtained from the solution of the global system of equations associated with the problem in this study are quite complex expressions. However, keeping in mind that we only want to know the right order of magnitude of the penalty parameter, some reasonable simplifications can be applied. In this case, groups of terms,

whose contribution to the solution is small, have been eliminated.

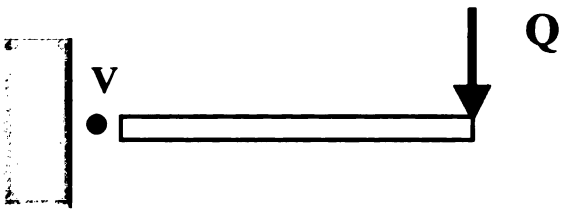

Figure 50. ***Single plate element under transversal load applied at the free side***

The solution obtained under these assumptions is proportional to that found in our study on the Timoshenko beam element. We should not be surprised by this achievement, since the Mindlin plate theory is an extension of the Timoshenko beam theory.

$$w_2 = w_3 \cong \left[\frac{L^3}{3Y\left(\frac{t^3 h}{12}\right)} + \frac{L}{k\frac{Y}{2}(th)} + \frac{1}{\gamma_w} + \frac{L^2}{\gamma_\theta} \right] Q = \left[\left(\frac{L^3}{3YI} + \frac{L}{kGA} \right) + \frac{1}{\gamma_w} + \frac{L^2}{\gamma_\theta} \right] Q \quad (546)$$

$$\left(\theta_y\right)_2 = \left(\theta_y\right)_3 \cong \left[\frac{L^2}{2Y\left(\frac{t^3 h}{12}\right)} + \frac{L}{\gamma_\theta} \right] Q = \left[\frac{L^2}{2YI} + \frac{L}{\gamma_\theta} \right] Q \quad (547)$$

Where I is the second moment of inertia, γ_w is the penalty parameter associated to the DOF w, and γ_θ is the penalty parameter associated to the rotational DOFs θ_x and θ_y.

5.2.2 Bending Moment

In this section we consider a concentrated bending moment applied at the tip, as plotted in Figure 51.

As in the previous analysis, the symbolic results computed from the global system of equations are quite complex expressions. But, applying the same kind of simplifications,

groups of terms whose contribution to the solution is small have been eliminated.

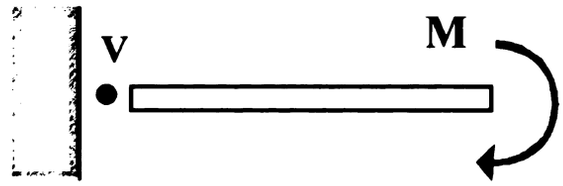

Figure 51. ***Single plate element under bending moment applied at the free side***

Again, the solution obtained is proportional to the Timoshenko beam element solution for the analogous load case.

$$w_2 = w_3 \cong \left[\frac{L^2}{2Y\left(\frac{t^3 h}{12}\right)} + \frac{L}{\gamma_\theta} \right] M = \left[\frac{L^2}{2YI} + \frac{L}{\gamma_\theta} \right] M \tag{548}$$

$$\left(\theta_x\right)_2 = \left(\theta_x\right)_3 \cong \left[\frac{L}{Y\left(\frac{t^3 h}{12}\right)} + \frac{1}{\gamma_\theta} \right] M = \left[\frac{L}{YI} + \frac{1}{\gamma_\theta} \right] M \tag{549}$$

5.3 Penalty Parameter and Element Properties

As for the plane stress quadrilateral, the obtained solutions are explored in order to find a relation between material and geometrical properties of the element and the penalty parameter.

5.3.1 Transversal Load

The proper term of comparison for the achieved solution is the outcome provided by the same element without using the penalty interface frame. Appling the same type of

simplification used in on the penalty solution, the FE results are:

$$w^{FE} \cong \frac{L^3 Q}{3Y\left(\frac{t^3 h}{12}\right)} + \frac{LQ}{k\frac{Y}{2}(th)} = \left[\left(\frac{L^3}{3YI} + \frac{L}{kGA}\right)\right]Q \tag{550}$$

$$\left(\theta_y\right)^{FE} \cong \frac{L^2 Q}{2Y\left(\frac{t^3 h}{12}\right)} = \left[\frac{L^2}{2YI}\right]Q \tag{551}$$

The ratio $w^{penalty}$ over w^{FE} is evaluated in order to underline the dependences between the two solutions.

$$\frac{w^{penalty}}{w^{FE}} = \frac{\left[\left(\frac{L^3}{3YI} + \frac{L}{kGA}\right) + \frac{1}{\gamma_w} + \frac{L^2}{\gamma_\theta}\right]Q}{\left[\left(\frac{L^3}{3YI} + \frac{L}{kGA}\right)\right]Q} = 1 + \frac{1}{\left(\frac{L^3}{3YI} + \frac{L}{kGA}\right)\gamma_w} + \frac{L^2}{\left(\frac{L^3}{3YI} + \frac{L}{kGA}\right)\gamma_\theta} \tag{552}$$

Now, if the penalty parameters γ_w and γ_θ are substituted by:

$$\gamma_w = \beta \cdot \frac{2}{\left(\frac{L^3}{3YI} + \frac{L}{kGA}\right)} \tag{553}$$

$$\gamma_\theta = \beta \cdot \frac{2L^2}{\left(\frac{L^3}{3YI} + \frac{L}{kGA}\right)} \tag{554}$$

The ratio between the solutions becomes independent of material and geometrical properties of the element.

$$\frac{w^{penalty}}{w^{FE}} = 1 + \frac{1}{2\beta} + \frac{1}{2\beta} = 1 + \frac{1}{\beta} \tag{555}$$

The ratio $\left(\theta_y\right)^{penalty}$ over $\left(\theta_y\right)^{FE}$ is:

$$\frac{(\theta_y)^{penalty}}{(\theta_y)^{F.E.}} = \frac{\left[\frac{L^2}{2YI} + \frac{L}{\gamma_\theta}\right]Q}{\left[\frac{L^2}{2YI}\right]Q} = 1 + \frac{2YI}{L\gamma_\theta} \tag{556}$$

Setting:

$$\gamma_\theta = \beta \cdot \frac{2YI}{L} \tag{557}$$

We reach our goal.

$$\frac{(\theta_y)^{penalty}}{(\theta_y)^{F.E.}} = 1 + \frac{1}{\beta} \tag{558}$$

5.3.2 Bending Moment

The finite element solution computed without using the penalty interface frame is proportional to:

$$w^{F.E.} \cong \frac{L^2}{2Y\left(\frac{t^3 h}{12}\right)} M = \frac{L^2}{2YI} M \tag{559}$$

$$(\theta_y)^{F.E.} \cong \frac{L}{Y\left(\frac{t^3 h}{12}\right)} M = \frac{L}{YI} M \tag{560}$$

The ratio $w^{penalty}$ over $w^{F.E.}$ is computed to be:

$$\frac{w^{penalty}}{w^{F.E.}} \cong \frac{\left[\frac{L^2}{2YI} + \frac{L}{\gamma_\theta}\right]M}{\left[\frac{L^2}{2YI}\right]M} = 1 + \frac{2YI}{L\gamma_\theta} \tag{561}$$

Substituting penalty parameter γ_θ with:

$$\gamma_\theta = \beta \cdot \frac{2YI}{L} \tag{562}$$

The previous ratio becomes dependent only on β.

$$\frac{w^{penalty}}{w^{FE}} = 1 + \frac{1}{\beta} \tag{563}$$

The ratio $(\theta_y)^{penalty}$ over $(\theta_y)^{FE}$ is:

$$\frac{(\theta_y)^{penalty}}{(\theta_y)^{FE}} = \frac{\left[\frac{L}{2YI} + \frac{1}{\gamma_\theta}\right]M}{\left[\frac{L}{2YI}\right]M} = 1 + \frac{YI}{L\gamma_\theta} \tag{564}$$

Setting:

$$\gamma_\theta = \beta \cdot \frac{YI}{L} \tag{565}$$

we reach our goal.

$$\frac{(\theta_y)^{penalty}}{(\theta_y)^{FE}} = 1 + \frac{1}{\beta} \tag{566}$$

5.4 Building an interface Element for Plates

The Abaqus User Element Subroutine UEL for the plates doesn't differ much from that for the 2-D quadrilateral plane stress elements. The subroutine for plate needs from the input file the same information as in the previous case. The parameters provided are: the nodes on the interface, thickness and Young's Modulus of the two domains.

Changes worth being mentioned are: (a) six DOFs per node are present; (b) the in-plane, transversal and rotational DOFs require different penalty parameters for optimal

behavior. The sixth DOF, θ_z, corresponds to the rotation about the *z*-axis, often defined as the "drilling" degree of freedom.

The statement in (b) results from our investigations on the penalty parameter. Six different penalty parameter are used, three for each domain. In particular: one, γ_u, is assigned to the in-plane DOFs (*u*, *v*), the second, γ_w, to the transverse DOF *w* and the third, γ_θ, is shared by all the rotational DOFs (θ_x, θ_y, θ_z).

5.4.1 Automatic Choice of an Optimal Penalty Parameter

It is important to underline once more that we need only the right order of magnitude of the penalty parameter. Taking into consideration the earlier comment, we now recall the main results found in section 5.3.

The penalty parameter related to the in-plane displacements, obviously, takes the same values assumed for the UEL dedicated to the 2-D quadrilateral plane stress element.

We saw that under conditions of transversal load applied at the tip, the following value of the penalty parameter would make the accuracy of the solution to depend only on the value assigned to the parameter β.

$$\gamma_w = \beta \cdot \frac{2}{\left(\frac{L^3}{3YI} + \frac{L}{kGA}\right)} \tag{567}$$

$$\gamma_\theta = \beta \cdot \frac{2L^2}{\left(\frac{L^3}{3YI} + \frac{L}{kGA}\right)} \tag{568}$$

And:

$$\gamma_\theta = \beta \cdot \frac{2YI}{L} \tag{569}$$

Clearly, these requirements are in conflict and there are no simple relations between the two expressions for γ_θ to tell us which to choose.

It has been discussed previously that the length of the element L is an unwanted presence in our expressions for γ. Thus, again we choose to approximate the dimension in the direction perpendicular to the interface with the one parallel to it. This means that in all the expressions it is assumed: $L = h$.

$$\gamma_w = \beta \cdot \frac{2}{\left(\frac{4h^3}{Yt^3} + \frac{1}{kGt}\right)}$$
$$\gamma_\theta = \beta \cdot \frac{2h^2}{\left(\frac{4h^3}{Yt^3} + \frac{1}{kGt}\right)} \tag{570}$$

And:

$$\gamma_\theta = \beta \cdot \frac{t^3 Y}{6} \tag{571}$$

When a bending moment is applied to the free side, in order to get the γ_θ independent from the element properties, we need:

$$\gamma_\theta = \beta \cdot \frac{2YI}{L} \tag{572}$$

and:

$$\gamma_\theta = \beta \cdot \frac{YI}{L} \tag{573}$$

We record another conflict in choosing γ_θ. But in this case the first expression is clearly the one determining the bigger value of the parameter, so it is our choice.

As we have just seen, after the necessary substitution $L = h$, this expression becomes:

$$\gamma_\theta = \beta \cdot \frac{t^3 Y}{6} \tag{574}$$

At this point it is obvious that the two different conditions, transversal load and bending moment, could require different values of γ_θ. A reasonable solution consists in choosing the parameter during the analysis using an IF clause. With all the necessary information about geometry and materials properties, the different values of γ_θ can be compared. The bigger value will be selected in order to obtain:

$$\frac{(\theta)^{penalty}}{(\theta)^{F.E.}} \leq 1 + \frac{1}{\beta} \tag{575}$$

Table 11 summarizes all the relations among the penalty parameters and model characteristics.

Table 11. ***Expression for computing the penalty parameters in a plate element.***

	All kind of loads
γ_{u1}	$\beta \cdot \left(\frac{E_1 t_1}{b_1} \right)$
γ_{v1}	$\beta \cdot \left(\frac{E_1 t_1}{b_1} \right)$
γ_{w1}	$\beta \cdot \frac{2}{\left(\frac{4b_1^3}{E_1 t_1^3} + \frac{1}{k_1 G_1 t_1} \right)}$
$\gamma_{\theta 1}$	$\beta \cdot \frac{2b_1^2}{\left(\frac{4b_1^3}{E_1 t_1^3} + \frac{1}{k_1 G_1 t_1} \right)}$ or $\beta \cdot \frac{t_1^3 E_1}{6}$
γ_{u2}	$\beta \cdot \left(\frac{E_2 t_2}{b_2} \right)$
γ_{v2}	$\beta \cdot \left(\frac{E_2 t_2}{b_2} \right)$
γ_{w2}	$\beta \cdot \frac{2}{\left(\frac{4b_2^3}{E_2 t_2^3} + \frac{1}{k_2 G_2 t_2} \right)}$
$\gamma_{\theta 2}$	$\beta \cdot \frac{2b_2^2}{\left(\frac{4b_2^3}{E_2 t_2^3} + \frac{1}{k_2 G_2 t_2} \right)}$ or $\beta \cdot \frac{t_2^3 E_2}{6}$

5.5 Numerical Results

In this section the developed Abaqus User Element UEL for plate elements, which we will again call interface element, is employed to solve example problems.

5.5.1 Plate Bending

Like the first analysis regarding the quadrilateral plane stress element, the following problem can be considered a patch test. A plate is divided in two domains discretized differently: 10 by 8 against 10 by 6. They are joined along the common interface through two Interface elements. Uniform bending moments, equal to 1 in magnitude, are applied at the opposite two edges. The four noded Abaqus shell element S4R is employed to mesh both domains. In-plane rigid body movements are avoided by applying the necessary constraints, moreover transverse displacements at the four corners are set to zero. Figure 52 plots deformed and original configurations of the plate. Others properties are: $E_1 = E_2 = 1E6$, $length = 4$, $width = 1$ and $thickness = 0.1$.

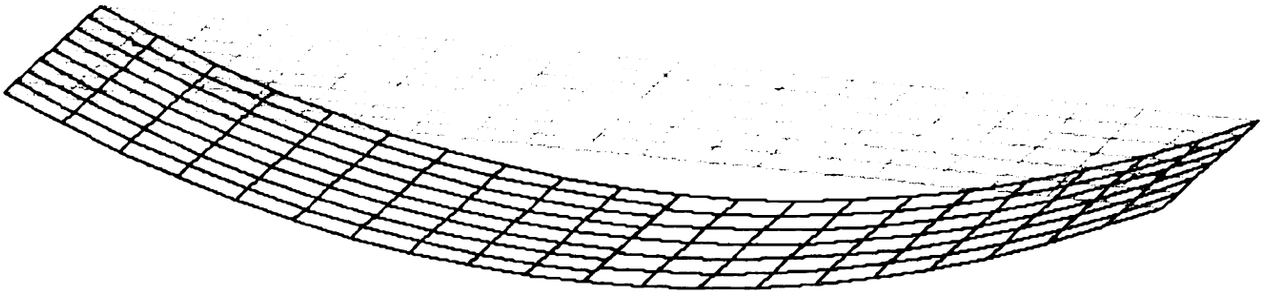

Figure 52. ***Original and deformed configurations of the plate***

This analysis would require the user to choose different orders of magnitude for the values of the penalty parameters related to transverse deflection w and rotational angles. However, the implemented ability of automatically choosing the appropriate penalty parameters for each DOF, saves this effort without sacrificing accuracy.

Table 11 reports the results from the penalty interface FEM, obtained with β =

1000 and β = 10000, compared to the classical solution. Values shown are nondimensionalized by the exact solution.

Table 12. ***Nondimensionalized results for the center deflection of the plate***

	Mesh a	Mesh b	w - $\beta = 1E3$	w - $\beta = 1E4$
Interface FEM	10x8	10x6	1.0004	1.0000

Outcomes confirm the reliability and the precision of the developed method.

5.5.2 Simply Supported Plate under Sinusoidal Load

A simply supported plate is subjected to a load distributed over the surface according to the following expression:

$$q = q_0 \sin\frac{\pi x}{a} \sin\frac{\pi y}{b} \tag{576}$$

In which q_0 represents the intensity of the load at the center of the plate. a and b are the plate dimensions, respectively, in the in-plane directions x and y.

We assume the plate to be square with side dimensions equal to two, $a = b = 2$. The value of q_0 is taken to be 1. Taking advantage of geometrical and loading symmetries, only a quarter of the plate is analyzed. As shown in Figure 53, a fine mesh is used for a square near the center, while the remaining surface adopts a coarse mesh. The four noded Abaqus shell element S4R is employed to mesh both domains. Four Interface elements are used to connect the two domains. Others properties are: $E_1 = E_2 = 1E6$, $\nu = 0.25$ and $thickness = 0.1$.

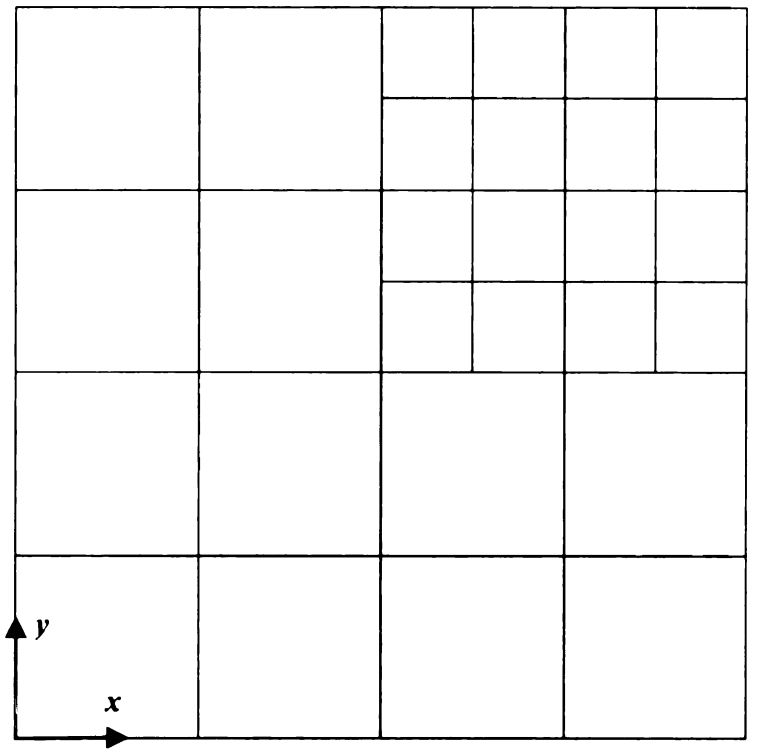

Figure 53. ***Penalty interface FE model of a flat plate.***

Figure 54 plots deformed and undeformed configurations of the FEM seen from the bottom.

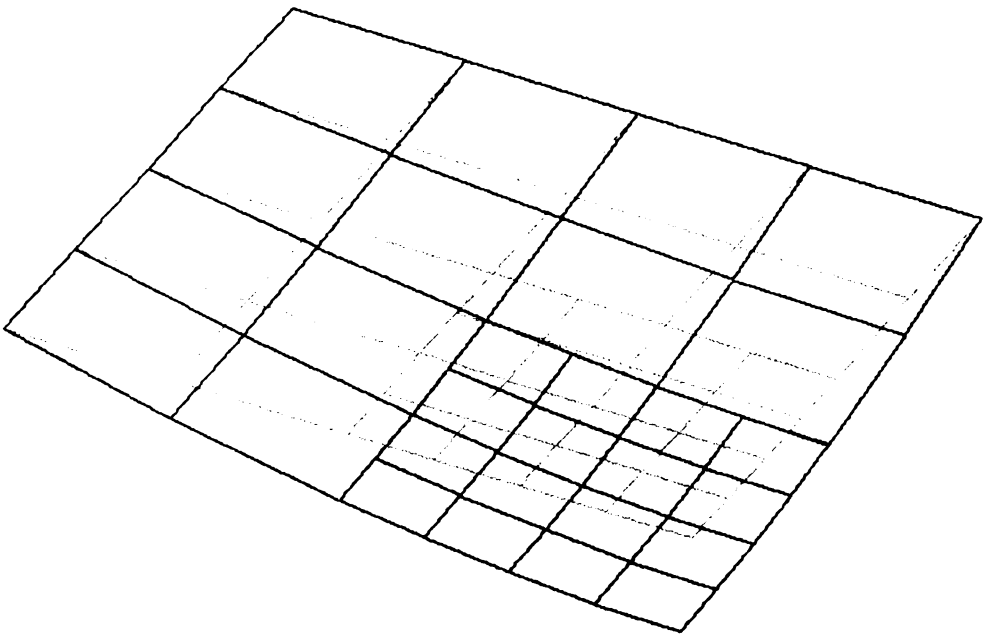

Figure 54. ***Original and deformed mesh as seen from the bottom of the plate.***

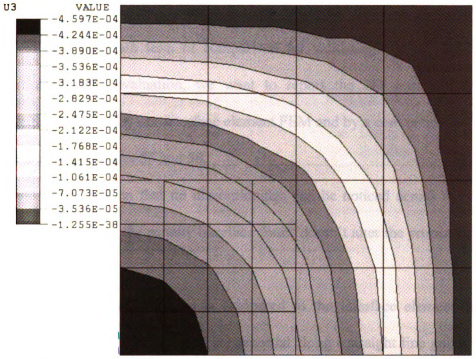

Figure 55. ***Distribution of traversal displacements w - Penalty interface frame FEM.***

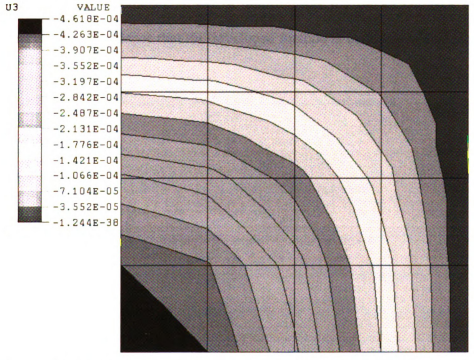

Figure 56. ***Distribution of traversal displacements w - Conventional FEM.***

An analytical elasticity solution to this problem exists in the literature. It obviously will be our main term of comparison for validating our results. However, before performing this evaluation, we want to report the 2D maps for transverse displacement w produced by our interface element FEM and by a conventional 4 by 4 FE. Results are shown in Figures 55 and 56.

These figures affirm that no discontinuities can be noticed across the interface. Moreover, the presence of the penalty interface frame doesn't alter the proper distribution of displacements.

Finally, the classical solution is compared to the interface element model. In Figure 57, the transverse displacements are reported along a straight line going from the middle of one side of the plate to the center. Since we are studying a quarter of the plate, this means that we are plotting w along one of the two sides of symmetry of the model. Even in the presence of a high gradient of deformation, the model behaves well. This further confirms our confidence that the developed method is both robust and accurate.

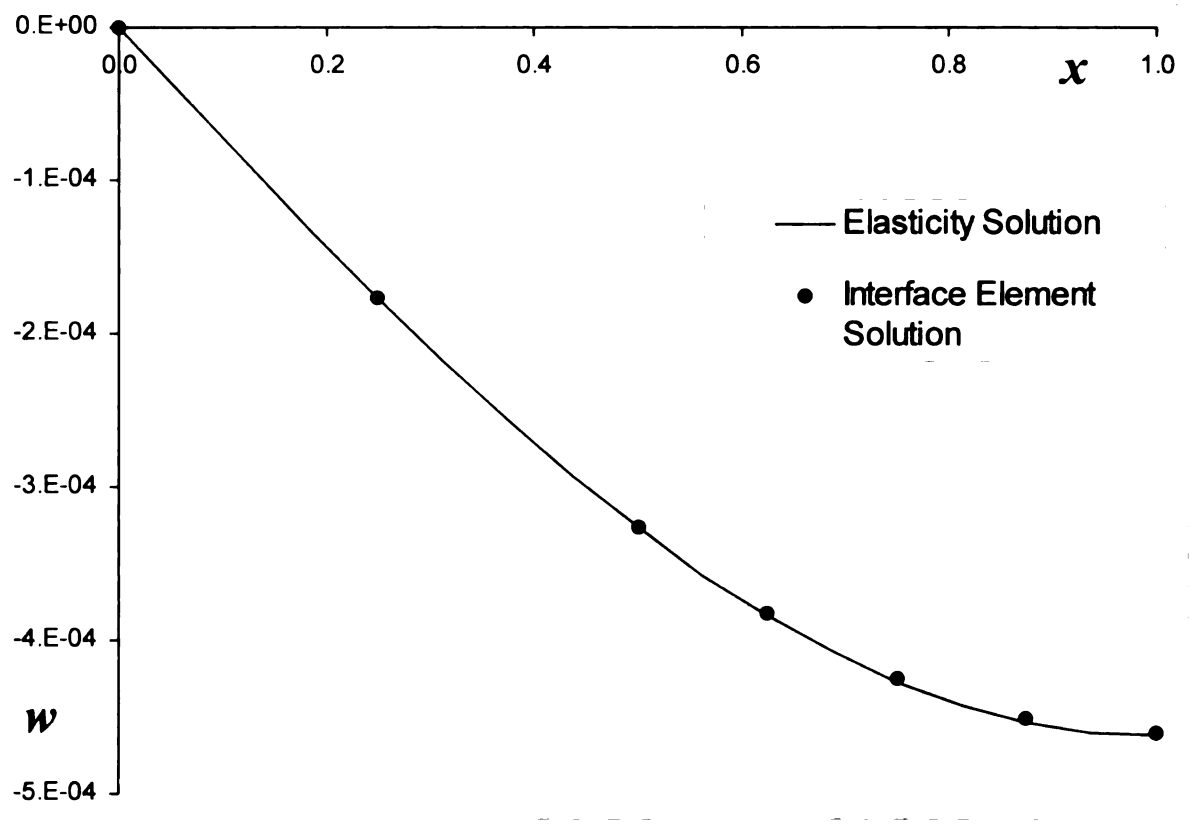

Figure 57. ***Variation of the transverse displacement w along one of the two sides of symmetry of the model***

CHAPTER 6 3D LINEAR BRICK ELEMENT

In this chapter an interface element for three-dimensional solid 8-node linear brick elements is developed. Each of the eight nodes has three displacement components *u*, *v* and *w*; a generic configuration of the brick element is shown in Figure 58.

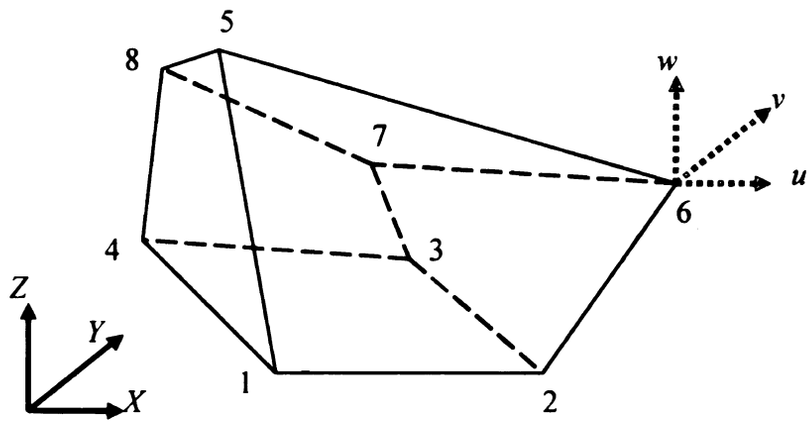

Figure 58. ***Three-dimensional solid 8-node linear brick element.***

6.1 Automatic Choice of the Penalty Parameter

The finite element model associated with this element can be found in several books [41-43] and is not difficult to derive. But, the task of computing and solving symbolically the system of equations associated with simple problems involving brick elements, overwhelms of the capabilities of the mathematical tools available to us. However, it seems reasonable to verify if the results obtained for the two-dimensional 4-

node quadrilateral element can be successfully applied to brick elements.

It has been derived in section 4.6.1, a single expression for an automatic evaluation of the penalty parameter in the case of the quadrilateral element. The relation among the penalty parameter γ and the properties of the finite element model, was found to be:

$$\gamma = \beta \cdot \left(\frac{hY}{b} \right) \tag{577}$$

Where the Y is the Young's modulus, b is the length of the element at the interface and while h is the thickness of the element.

The same relation with a few obvious updates may be adopted for the automatic choice of the penalty parameter in the interface formulation for brick elements. Let's consider the face of the brick element along the interface, see Figure 59.

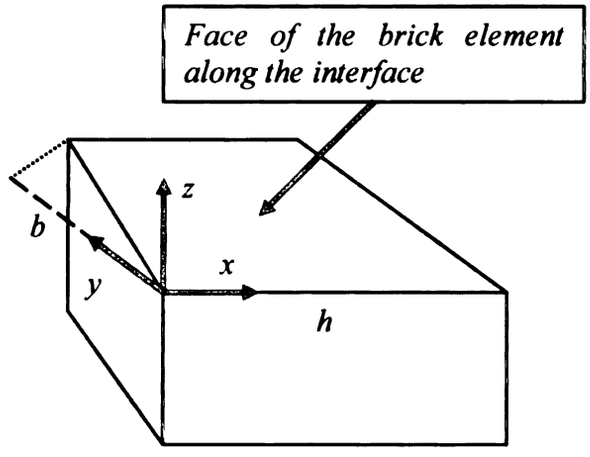

Figure 59. ***Definition of a local coordinate system***

It is possible to construct a local coordinate system such that the x and y direction are in the plane identified by the face and the x direction correspond to the bottom side of the quadrilateral face. Then, h would be the side length along x and b the component along y of the other side departing from the origin.

Several numerical tests have shown that the relation (577) can correctly evaluate the penalty parameters.

6.2 Cubic Spline Interpolation Functions

A 2-D interface element able to connect 3-D finite element meshes requires using two-dimensional interpolation functions [27-38]. Schumaker [30] and Prenter [31] proved that a two-dimensional version of the cubic splines, defined *bicubic* splines, can be constructed over a rectangular grid by taking the tensor product of one-dimensional splines. Their work also shows that the bicubic spline interpolation over a rectangular grid is smooth, having continuous second derivatives.

In order to allow the connection of finite element meshes whose interface boundaries are not rectangular, the bicubic spline interpolation is mapped from a square region to the interface quadrilateral area. The only limitation is that the boundaries of the interface area must form a quadrilateral region. It is important to remember that by using several quadrilateral elements it is possible to mesh every kind of interface surface. Thus, by employing several interface elements it is possible to connect meshes of every type. For example, among the numerical results, we have been able to test the connection of two circular shafts of different diameters.

The bicubic splines are constructed by taking the tensor product of one-dimensional splines in their general form described in section 4.2.1, not the natural cubic spline over three points. Thus, the Abaqus user element subroutine associated with the 2-D interface element, allows the user to specify the desired number of nodes for the interpolation of the two-dimensional displacement field V.

6.3 *Building an Interface Element for 8-Node Brick*

The Abaqus User Element Subroutine UEL for 8-node brick elements has some important differences with respect to the ones for the 2-D elements, but most of them are not visible to the user. As before, the parameters provided are: the nodes at the interface and Young's Modulus of the materials composing the two domains. Nevertheless, a great amount of programming work has been required to deal with the much higher level of complexity brought by the additional dimension. In particular, a very difficult task was the integration of the matrices G_{is}, which requires dividing the integral over the interface surface in several integrals over smaller areas. These areas are the intersections of the bicubic spline mesh with the finite element meshes.

As in the other cases, the UEL subroutine is written in Fortran 77. All the variables are defined to be in double precision format, in order to minimize numerical round-off errors as much as possible.

6.4 *Numerical Results*

In this section the developed Abaqus User Element, UEL, for 8-node brick elements is tested by several challenging problems.

6.4.1 3D Cantilever Beam with a Square Section

A three-dimensional cantilever beam is meshed as composed by two domains. The domains are meshed independently, 5x5x10 and 4x4x10 elements, and joined by one interface element. The geometrical configuration of the problem is represented in Figure 60. Others properties are $P = 1000N$ and $E_1 = E_2 = 1.MPa$.

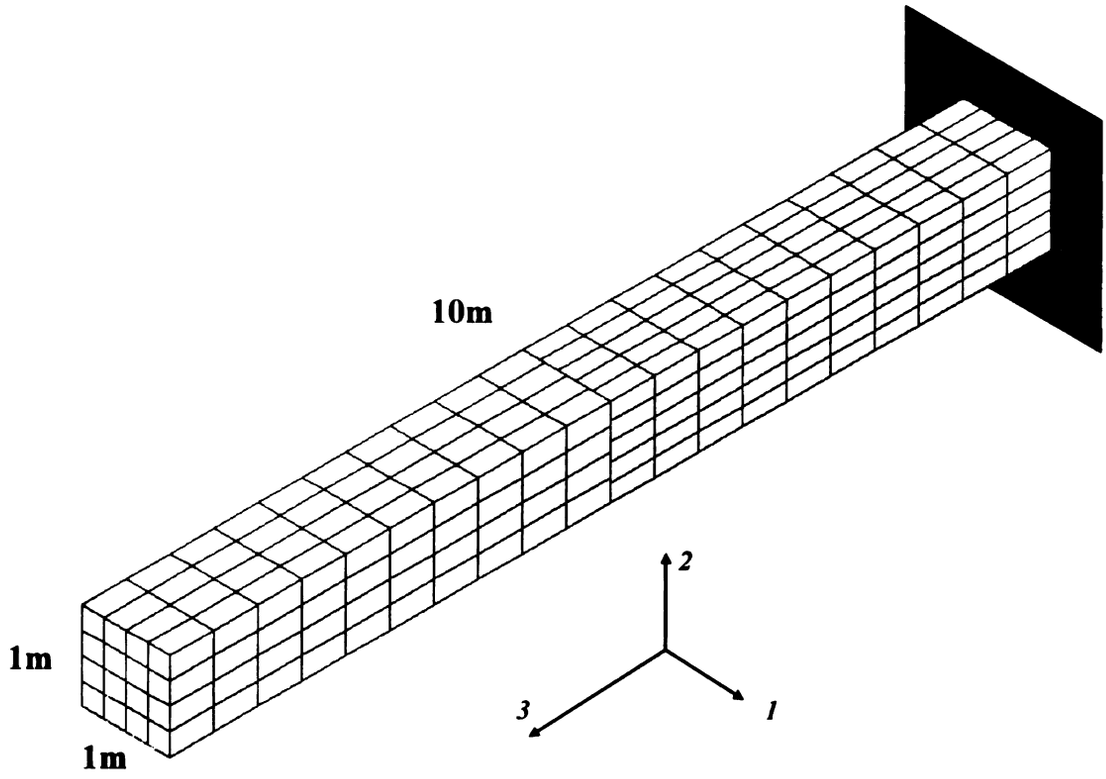

Figure 60. ***3D Cantilever beam with a square section***

The only interface element used, is made by a uniform square grid of 36 points (6x6). For discretizing the two domains, solid 8-node linear brick elements are used. Two different load conditions are investigated: axial and bending loads. In order to compare the results obtained from the multidomain analysis, a conventional finite element model without interface was created for the entire beam and its mesh discretization, 5x5x20 brick elements, is that of the finer subdomain. These problems may be considered a form of patch test for the element developed herein.

6.4.1.1 Axial Load

Under the condition of a uniform axial load applied at the free end of the beam, the interface element results are in complete agreement with the exact solution to the number of significant digits available, see Figures 61-65. There is no need to compare the

results with those obtained from a conventional mesh, since the solution to this linear problem is well known.

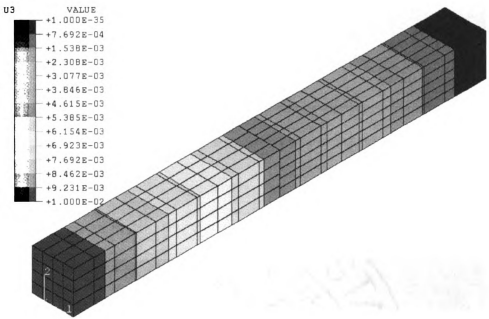

Figure 61. ***Cantilever beam with a square section – Axial displacement U3 – 3D view***

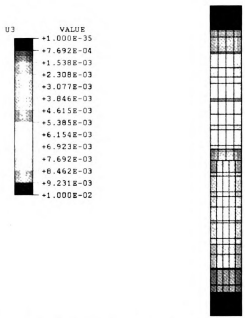

Figure 62. ***Cantilever beam with a square section – Axial displacement U3 – Side view***

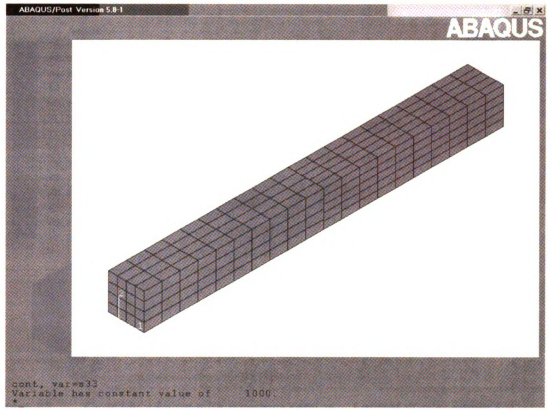

Figure 63. ***Cantilever beam with a square section – Stress S33***

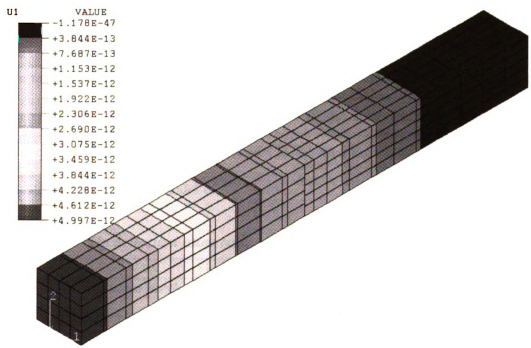

Figure 64. ***Cantilever beam with a square section – Lateral displacement U1***

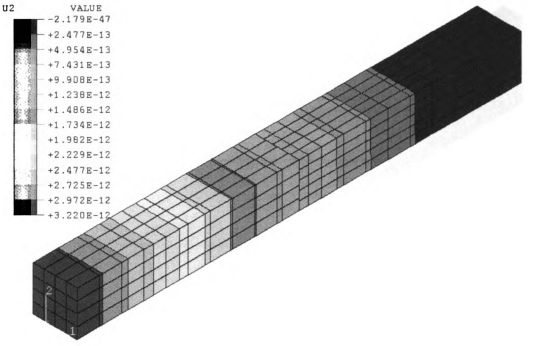

Figure 65. ***Cantilever beam with a square section – Lateral displacement U2***

6.4.1.2 Bending Load

For the bending load case, the comparison is made to both the classical solution and a reference finite element solution. The mesh of 8-node linear brick elements cannot exactly recover the classical solution. In Table 13 the tip deflection for beam flexure is reported. The FE result, marked as Abaqus, is obtained from a traditional analysis using a compatible finite element model of the beam.

Table 13. ***Tip deflection numerical results for beam flexure.***

	Mesh	***Solution***
Abaqus – conventional mesh	5x5x20	**4.023**
Interface Element	5x5x10 Left / 4x4x10 Right	**4.023**
Classical	-	**4.000**

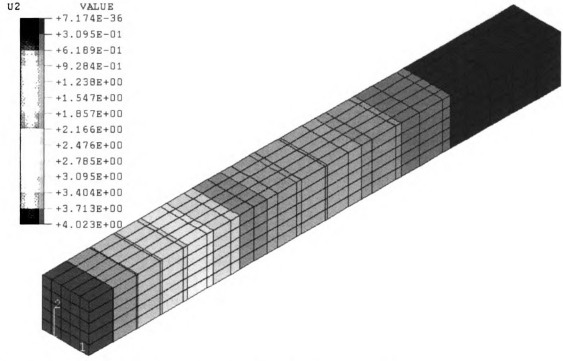

Figure 66. ***ABAQUS reference model – Displacement U2***

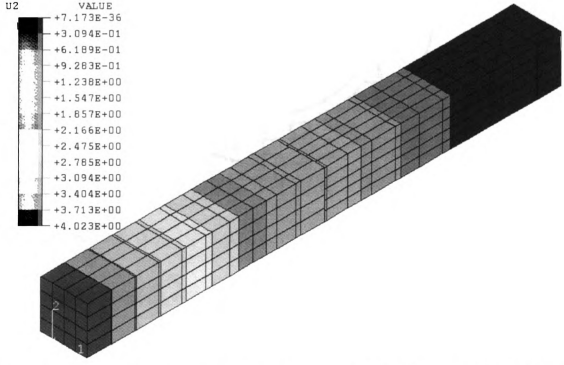

Figure 67. ***Interface element model – Displacement U2 - (Classical deflection = 4.0)***

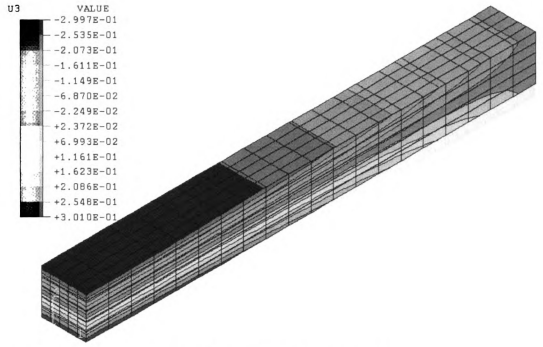

Figure 68. ***ABAQUS reference model – Displacement U3***

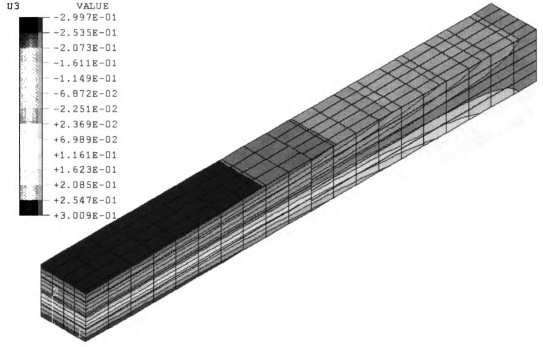

Figure 69. ***Interface element model – Displacement U3***

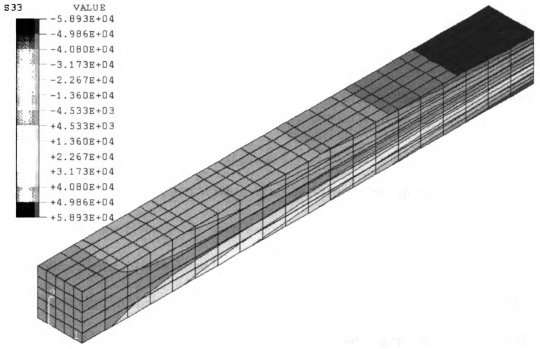

Figure 70. ***ABAQUS reference model – Stress S33 – (Classical = 6.0E+4)***

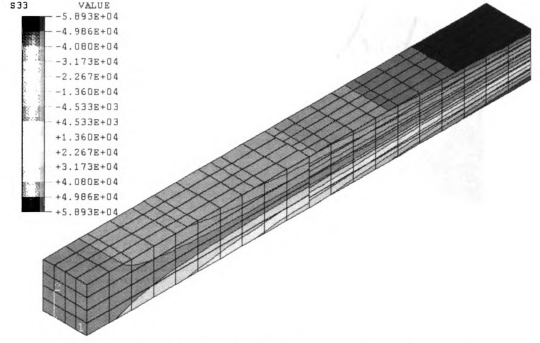

Figure 71. ***Interface element model – Stress S33 – (classical = 6.0E+4)***

Figures 66 to 69 demonstrate that the main components of displacements, U2 and U3, do not show any change in their values across the interface. The displacement field U1 is not reported since it is in the order of 1.E-14, almost zero as expected. Only light discontinuities in the values of main stresses σ_{33} at the interface are present, as plotted in Figures 70 and 71.

6.4.2 3D Cantilever Beam with a Quadrilateral Section

The interface element for solid 8-node linear brick elements is able to connect finite element meshes whose boundaries at the common interface are not rectangular. To test this capability, a three-dimensional cantilever beam with a distorted quadrilateral section is meshed as composed by two domains. The domains are meshed independently, 5x5x10 and 4x4x10 elements, and joined by one interface element. The geometrical configuration of the problem is represented in Figures 72 and 73.

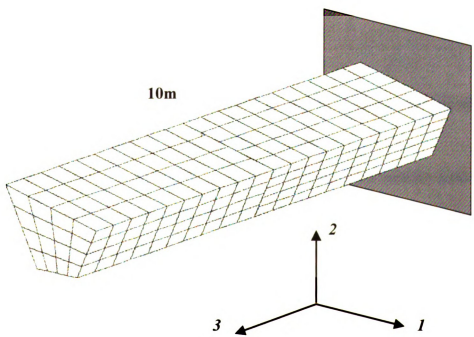

Figure 72. ***3D Cantilever beam with a quadrilateral section***

The Young's modulus of the materials composing the two domain of the beam are $E_1 = E_2 = 1.MPa$. A transversal load is applied in the 2-direction to the bottom four nodes at the tip of the beam and its total value is $P = 1000N$.

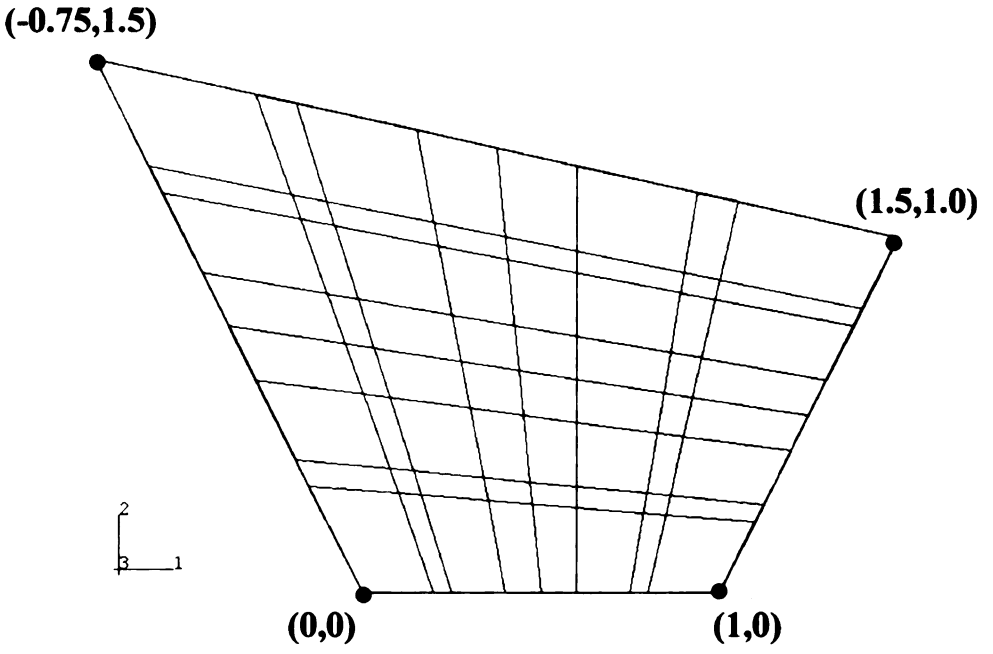

Figure 73. ***Quadrilateral section of the beam.***

In Figure 73 are shown at the same time the two different discretizations applied to the section of the beam; 5x5 and 4x4 brick elements.

Only one interface element is adopted; it is made by a uniform quadrilateral grid of 36 (6x6) points. For discretizing the two domains, solid 8-node linear brick elements are used. One load condition is reported: a bending load. Axial load results are not reported for brevity, but they are as good as in the previous case. In order to compare the results obtained from the multidomain analysis, a conventional finite element model without interface was created for the entire beam and its mesh discretization, 5x5x20

brick elements, is that of the finer subdomain.

Figure 74 shows the deformed configuration of the mesh with the interface element. Figures 75-80 demonstrate that all components of displacements are continuous across the interface. As before, it is possible to notice limited discontinuities in the values of main stresses σ_{33} at the interface, as plotted for the two lateral views in Figures 81 and 84.

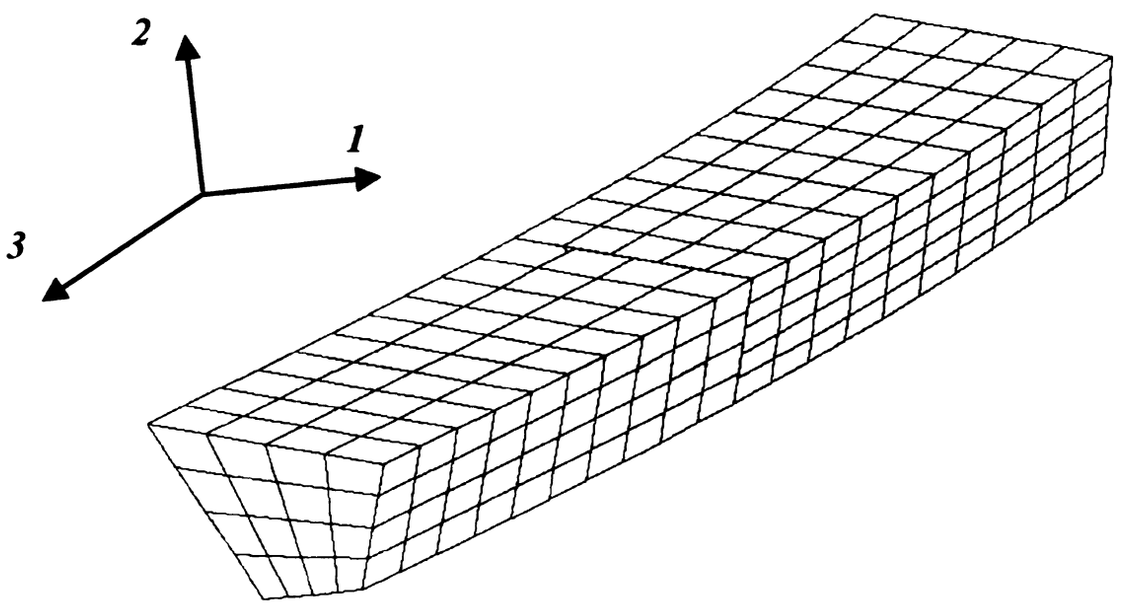

Figure 74. ***Deformed mesh***

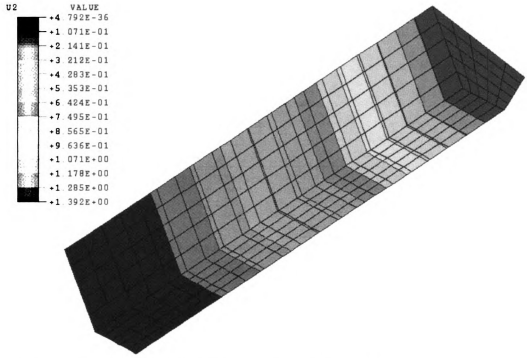

Figure 75. ***ABAQUS reference model – Displacement U2***

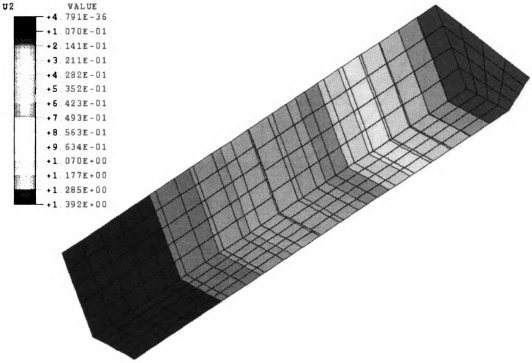

Figure 76. ***Interface element model – Displacement U2***

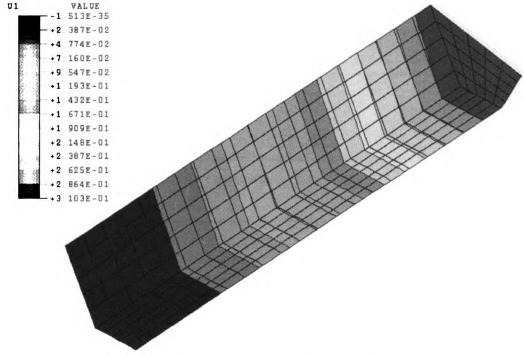

Figure 77. ***ABAQUS reference model – Displacement U1***

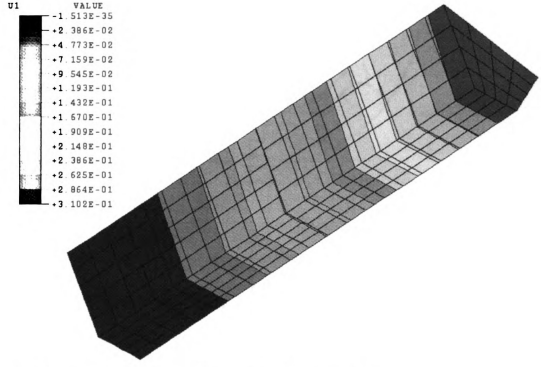

Figure 78. ***Interface element model – Displacement U1***

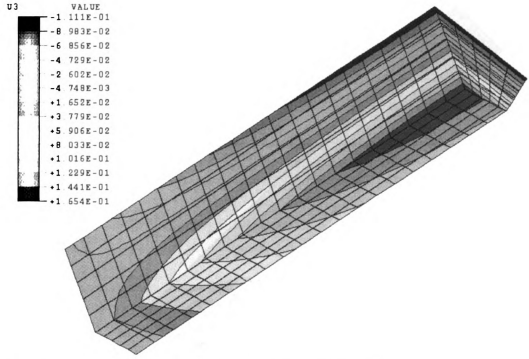

Figure 79. ***ABAQUS reference model – Displacement U3***

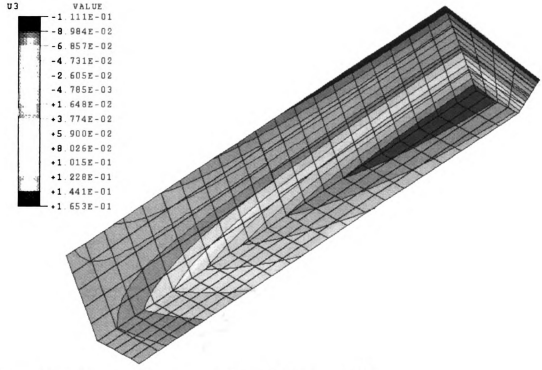

Figure 80. ***Interface element model – Displacement U3***

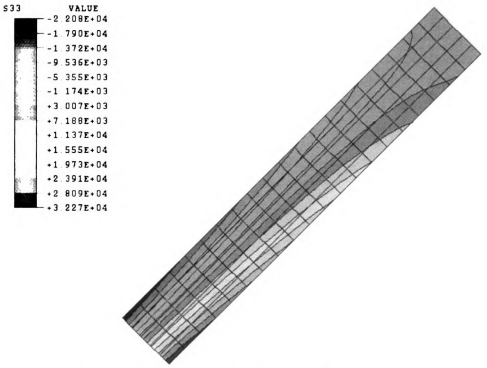

Figure 81. ***ABAQUS reference model – Lateral view 1 – Stress S33.***

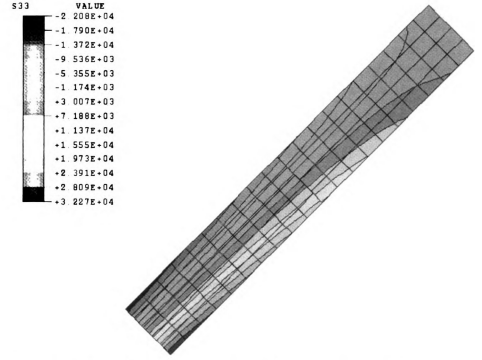

Figure 82. ***Interface element model – Lateral view 1 – Stress S33***

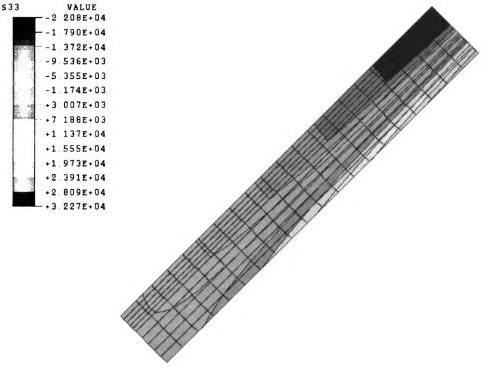

Figure 83. ***ABAQUS reference model – Lateral view 2 – Stress S33***

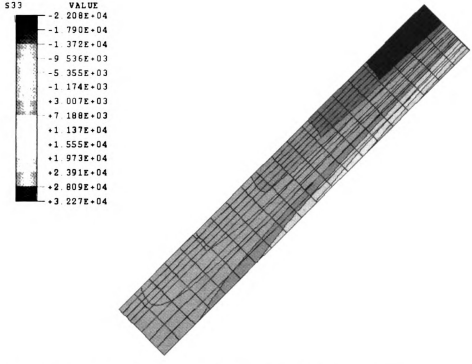

Figure 84. ***Interface element model – Lateral view 2 – Stress S33***

6.4.3 3D Shafts Assembly

Connecting shafts of different diameters is a problem of interest to the industry. It would be very useful to the designers to be able to connect shafts of varying dimensions without having to remesh the each section of the model each time. The presented interface technology would be very useful in solving this kind of problem, allowing a faster search for the optimal design.

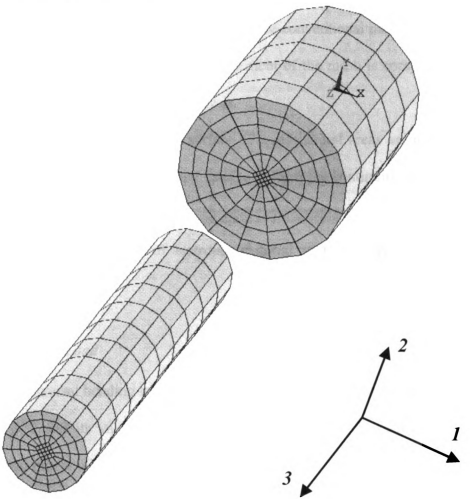

Figure 85. ***Shaft assembly.***

For the test analysis the configuration shown in Figure 85 has been considered.

The larger shaft has a diameter of 2 m and an axial length of 5 m, while the slender one has a diameter of 1 m and an axial length of 10 m. The larger shaft has the one face encastred and is meshed with 480 solid 8-node linear brick elements. The slender shaft has the load applied to the free end and is meshed with 800 solid 8-node linear brick elements. In Figure 85 is possible to notice the difference between the meshes at the interface of the two domains. The circle of 1m in diameter identifying the common interface, is discretized with 64 elements for the first shaft versus 80 for the second slender shaft. For comparison purposes a reference conventional model without interface elements was constructed. The level of refinement of the mesh is comparable to that of the slender shaft in the multidomain analysis.

Inside the common interface surface 17 quadrilateral areas are identified and an equal number of interface elements are used to enforce the continuity constraint between the incompatible meshes.

Both shafts are made of isotropic material with Young's modulus equal to $E_1 = E_2 = 1.MPa$.

6.4.3.1 Bending Load

A transversal bending load is applied to the bottom node at the tip of the beam, its direction is 2 and its value is $P = 100N$. The comparison is made to the reference conventional model without interface elements.

Figure 86 shows the original and deformed configurations of the mesh with the interface element.

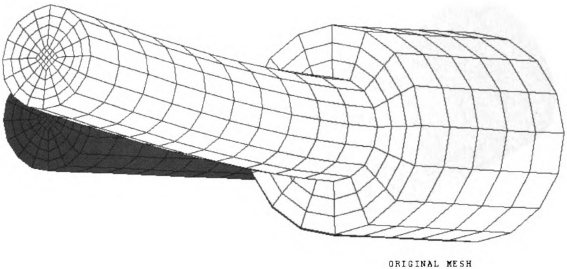

Figure 86. ***Original and deformed mesh under bending load.***

Figures 87 to 92 demonstrate that all the components of displacement are continuous across the interface. Also in the stress maps for the reference conventional model and for the finite element assembly with the interface elements, it is hard to notice any difference at all; see Figures 93 and 98.

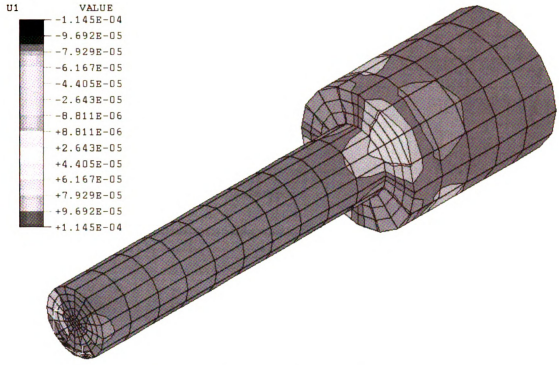

Figure 87. ***ABAQUS reference model – Displacement U1***

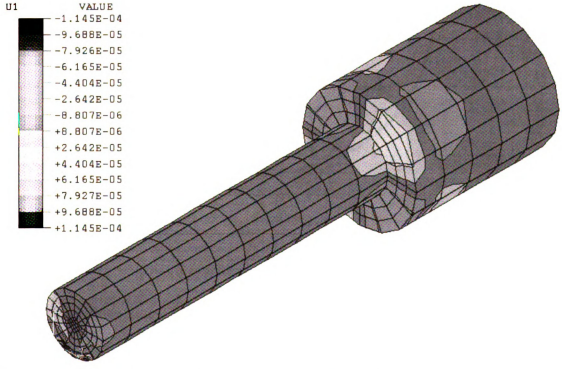

Figure 88. ***Interface element model – Displacement U1***

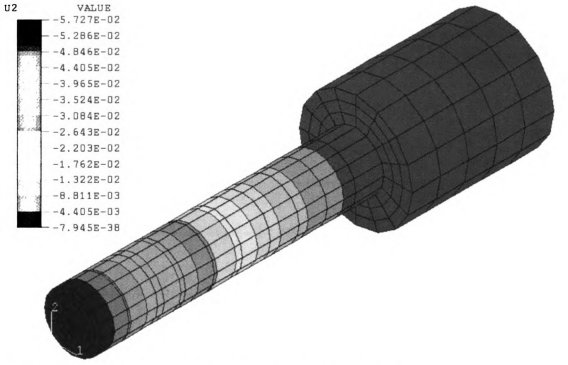

Figure 89. ***ABAQUS reference model – Displacement U2***

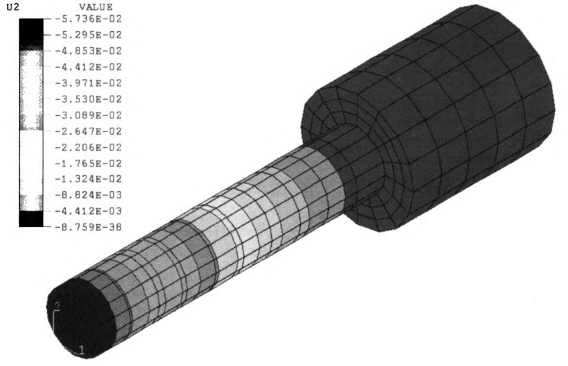

Figure 90. ***Interface element model – Displacement U2***

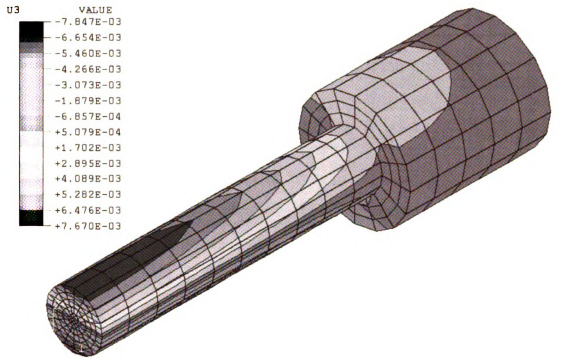

Figure 91. ***ABAQUS reference model – Displacement U3***

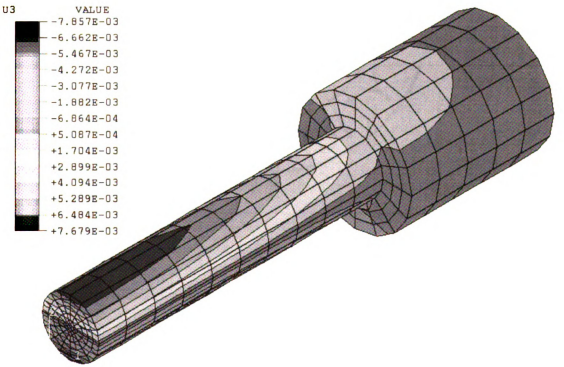

Figure 92. ***Interface element model – Displacement U3***

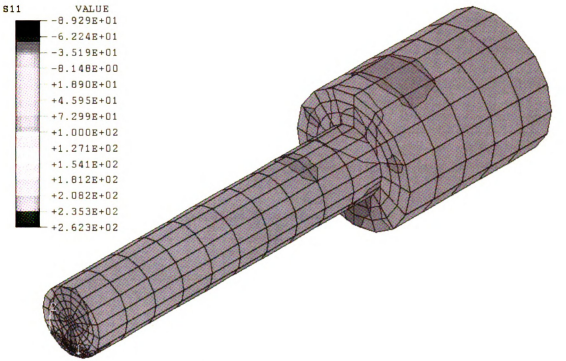

Figure 93. ***ABAQUS reference model – Stress S11***

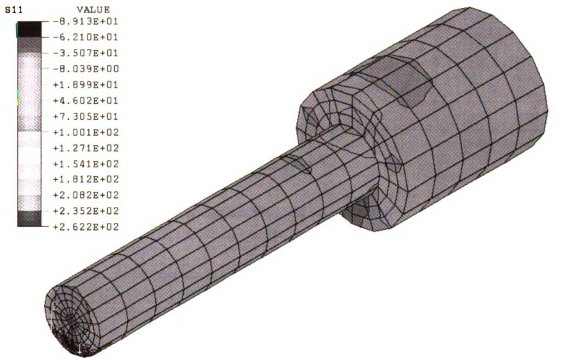

Figure 94. ***Interface element model – Stress S11***

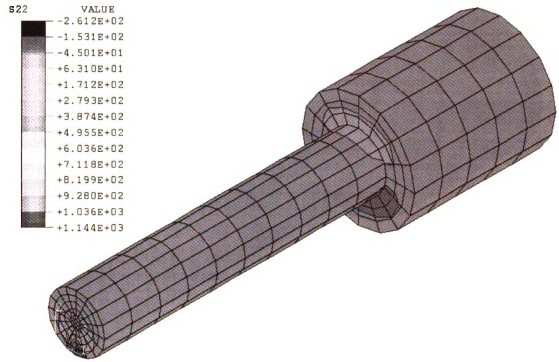

Figure 95. ***ABAQUS reference model – Stress S22***

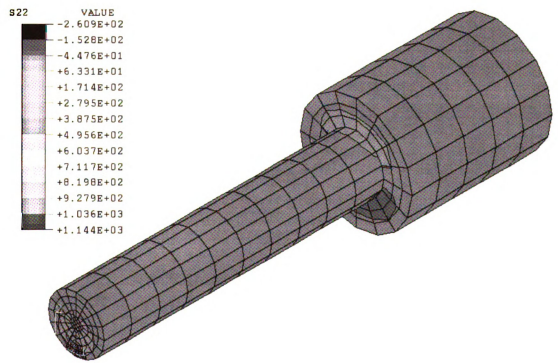

Figure 96. ***Interface element model – Stress S22***

Figur

Figu

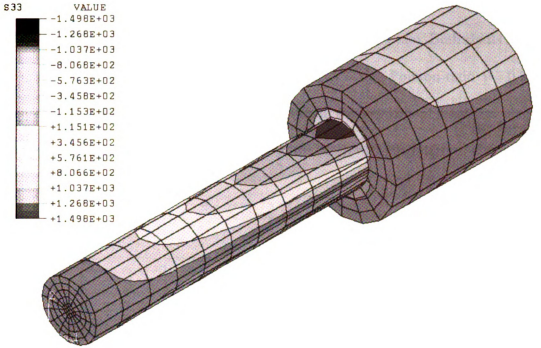

Figure 97. ***ABAQUS reference model – Stress S33***

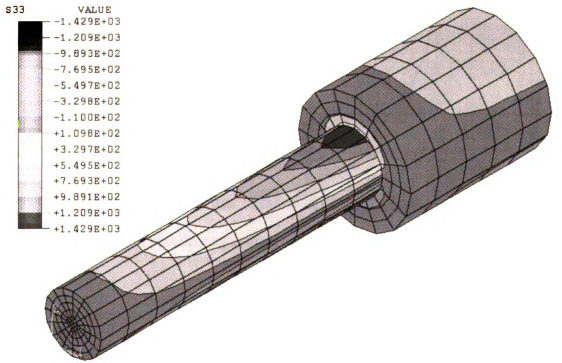

Figure 98. ***Interface element model – Stress S33***

6.4.3.2 Torsion

A torsion load is applied to the free end of the slender beam. Both shafts are made of isotropic material with Young's modulus $E = 1.MPa$ and Poisson ratio $\nu = 0.3$. The comparison is made to the reference conventional model without interface elements. Figure 99 shows the deformed configuration of the mesh with the interface element.

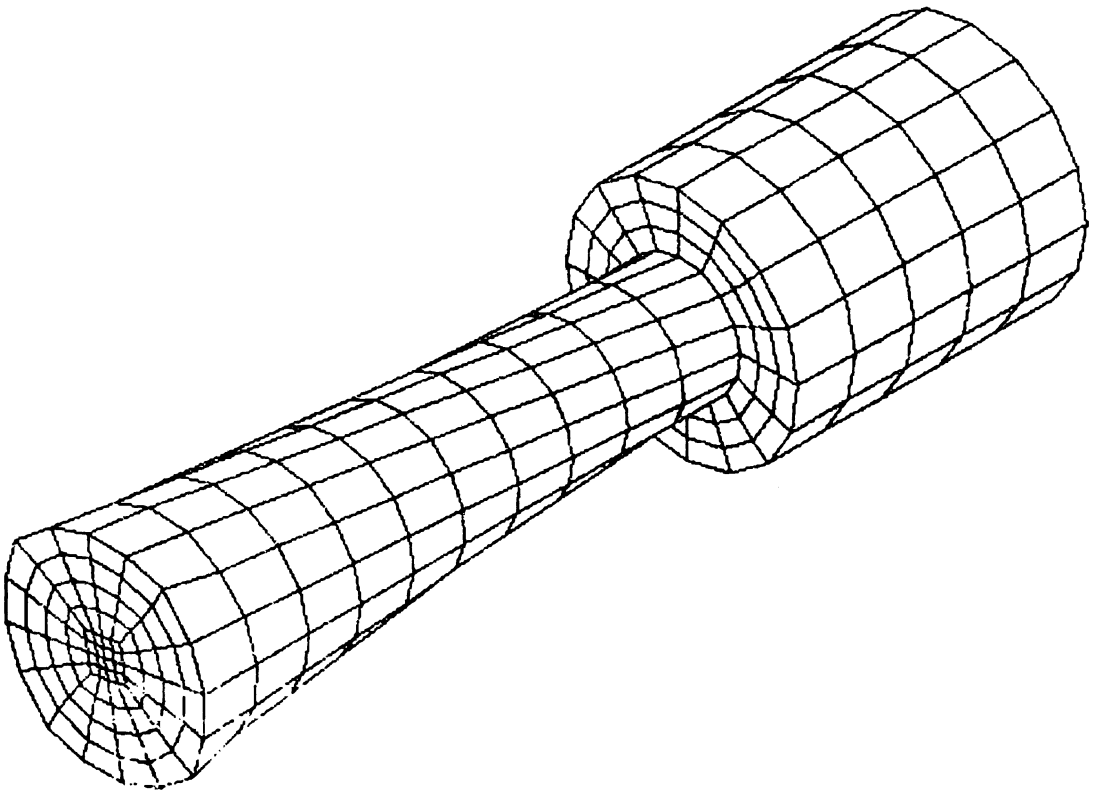

Figure 99. ***Deformed mesh under torsion load.***

Figures 100 to 113 shows that all the results from the multi-domain with interface elements analysis are in excellent agreement with those from the reference model.

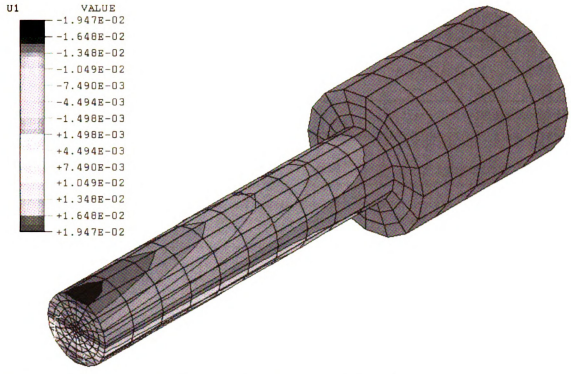

Figure 100. ***ABAQUS reference model – Displacement U1***

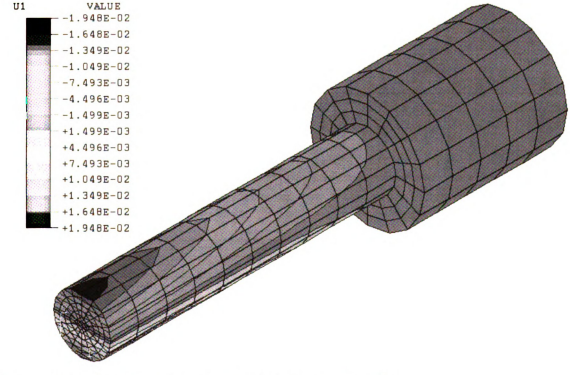

Figure 101. ***Interface element model – Displacement U1***

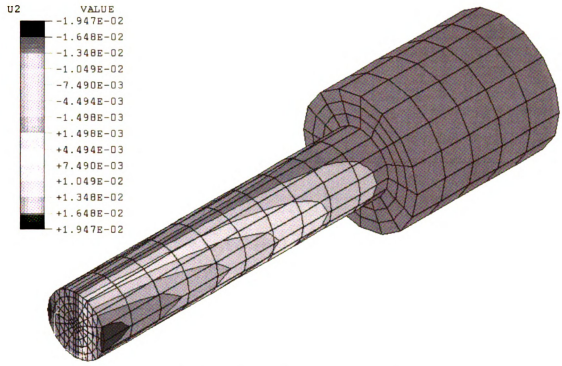

Figure 102. ***ABAQUS reference model – Displacement U2***

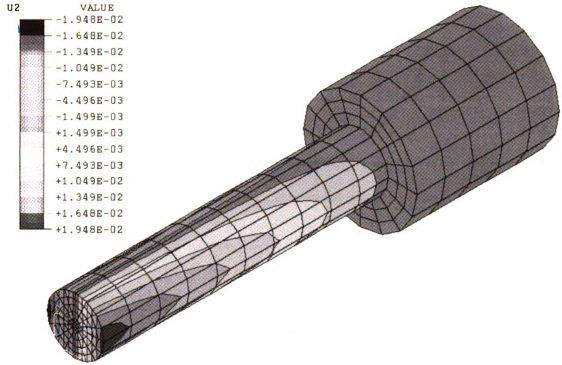

Figure 103. ***Interface element model – Displacement U2***

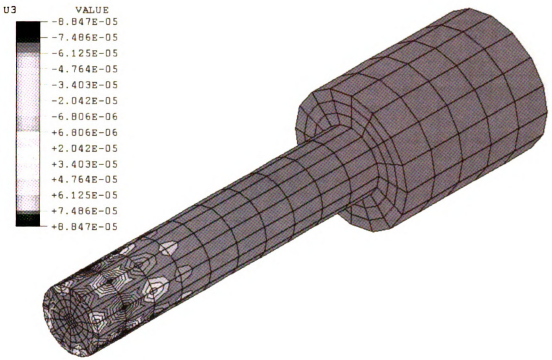

Figure 104. ***ABAQUS reference model – Displacement U3***

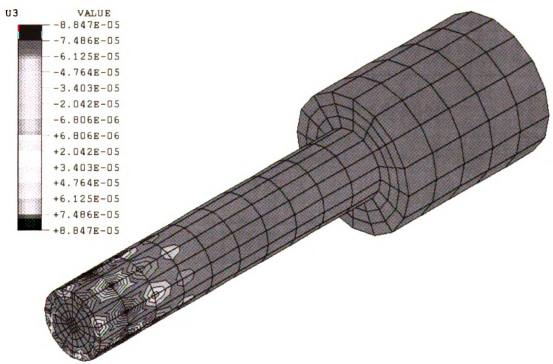

Figure 105. ***Interface element model – Displacement U3***

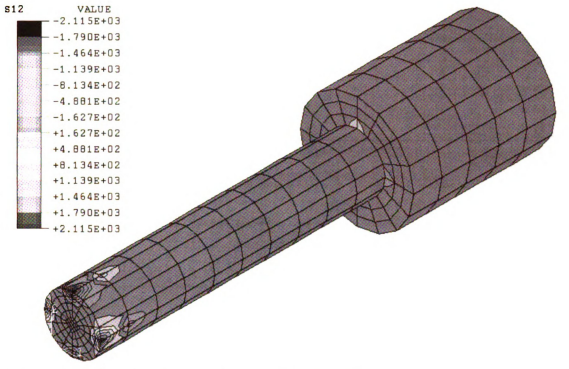

Figure 106. ***ABAQUS reference model – Stress S12***

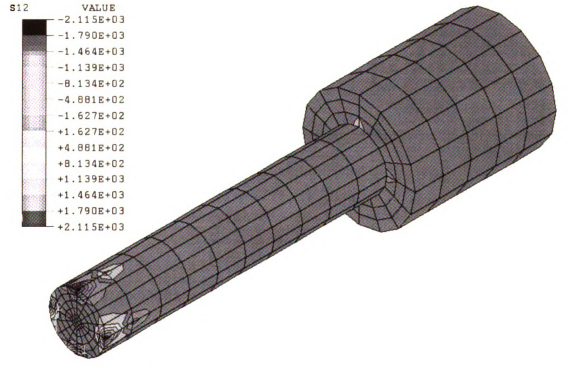

Figure 107. ***Interface element model – Stress S12***

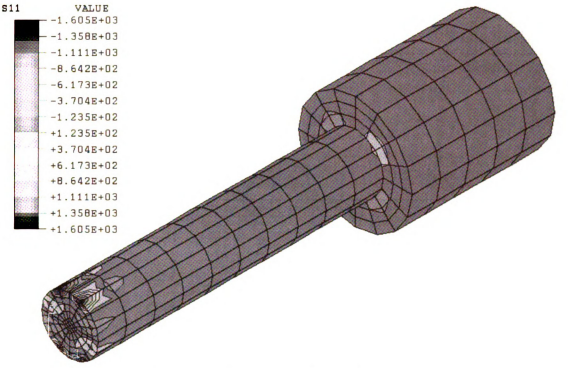

Figure 108. ***ABAQUS reference model – Stress S11***

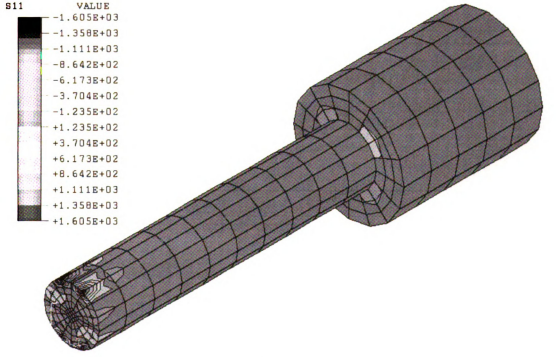

Figure 109. ***Interface element model – Stress S11***

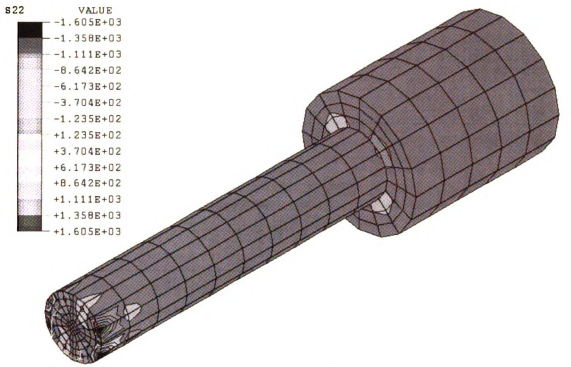

Figure 110. ***ABAQUS reference model – Stress S22***

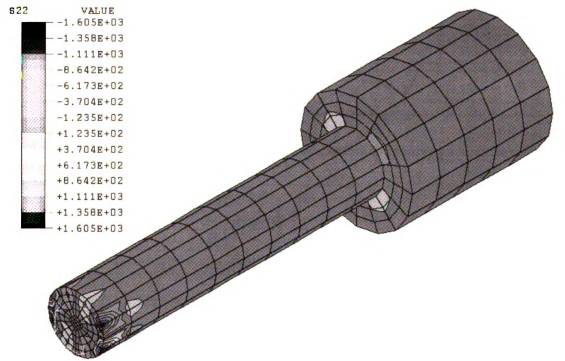

Figure 111. ***Interface element model – Stress S22***

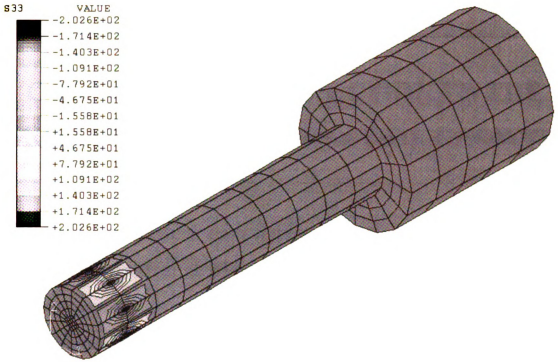

Figure 112. ***ABAQUS reference model – Stress S33***

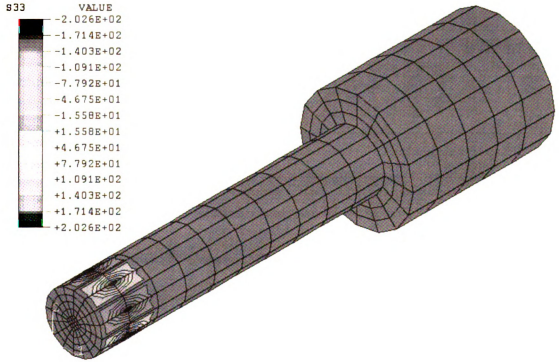

Figure 113. ***Interface element model – Stress S33***

CHAPTER 7 INTRODUCTION TO THE MODELING OF DELAMINATION GROWTH

Composite materials are widely used today because they enable high performance and low weight structures. However, due to the low tensile strength of the matrix, composite materials may experience delamination damage under service loading. This damage deteriorates load carrying capacity and can lead to premature fracture of the composite component. Extensive research has been performed in the attempt to better understand the major failure mechanisms for laminated composite delamination initiation and growth. The present chapter gives a brief review of the state of the art on the subject. The aspects considered first are the main causes of delamination. Then, computational techniques used in the literature to predict delamination initiation and growth are reported.

7.1 Causes of Delamination

In this section the main factors responsible for arising of interlaminar stresses able to originate delamination are examined.

7.1.1 Free-edge stresses

Delamination along the free edge of composite laminates has been studied since

the 1970s. Since then an important amount of work has been reported on the free edge problem in laminated composites, indicating that free edge delamination is attributed to the existence of interlaminar stresses near the free edges. These stresses occur due to the mismatch in engineering properties, i.e. mismatch in Poisson's ratio and coefficient of mutual influence between layers. In summary, three classes of interlaminar stress problems exist. Laminates of the type of [±θ] exhibit only shear-extension coupling (no Poisson mismatch between layers), so τ_{zx} is the only nonzero interlaminar stress. [0/90] laminates reveal only a Poisson mismatch between layers (no shear-extension coupling), so τ_{yz} and σ_z are the only nonzero interlaminar stresses. The mismatch in ν_{xy} give rises to interlaminar normal σ_z and shear τ_{yz} stresses. Laminates that are combinations of ±θ, 0° and 90°, for example [±θ$_1$/±θ$_2$] laminates, show both shear-extension coupling and Poisson mismatch between layers, so they have τ_{zx}, τ_{yz} and σ_z interlaminar stresses. Since high interlaminar shear is more likely to exist in the cases where the angle plies [±θ] are adjacent to each other, one should try to avoid placing them together in a laminate.

The other parameter affecting the interlaminar stresses is ply thickness. Thick plies tend to encourage higher interlaminar stresses thus causing early delamination.

7.1.2 Matrix cracks

Delamination is expected to occur at the interface where the predominant interlaminar stress component is computed unless there is a perturbation in the state of stress, probably induced by damage, prior to the onset of delamination. In most cases the delamination propagates in the axial direction along the same interface. In some other

cases, the delamination in the course of propagation turns into the neighboring ply. Several studies showed that under applied compression, all delamination initiated prior to any transverse cracking, in fact, in most of the cases the specimen failed without revealing any transverse crack. Under tensile loading, however, the delamination in most laminates, especially those containing 90° plies, is preceded by a number of transverse cracks. Because of the presence of the transverse cracks, the location of delamination is not unique. The path of delamination along the axial direction varies widely and depends upon the size and location of transverse cracks, type of laminate, material system, etc. The formation of the delamination in $[\pm\theta/90]_s$ and $[0/\pm\theta/90]_s$ laminates with θ in the 10°-45° range generally occurs in the following manner. Upon a further increase in applied load after transverse cracking, several delaminations in the form of axial cracks form at the mid-plane or interfaces between the $+\theta/-\theta$ layers or the $-\theta/90$ layers. Delaminations at the last two interfaces are nucleated by the transverse cracks. As the load increases, the delamination opens up further and either continues to run along the same interface or changes to other interfaces, normally at transverse cracks. At this time the delamination also propagates rapidly toward the middle of the specimen.

A finite element study [44] of transverse cracking investigated the behavior of two types of cross-ply laminates, $[90/0]_s$ and $[0/90]_s$ subjected to an extension ε_0. It was found that when the load increases, numerous transverse cracks running across the thickness of the laminate perpendicularly and possessing an approximately uniform spacing along the length of the laminate will occur. These transverse cracks terminate perpendicular to the ply interface because of the stronger 0° ply and then tend to develop delamination cracks along the ply interface if the load increases further. The ply material

is graphite epoxy T300/5208. For the $[90/0]_s$ the effects of the thickness of 90° ply on the stress distribution along the x-axis has been studied. When the thickness of the 90° ply increases, the strength of singular stresses near the crack tip is enhanced. A similar dependence on the thickness of the 90° ply is found for the $[90/0]_s$ laminate. Therefore, the thickness of 90° ply has an important influence on the growth of the delamination crack.

7.1.3 Impact

When a laminate is hit by an object or projectile, the material directly under is compressed and translates laterally in a time frame much less than that which is required for the overall response of the structure. The highly localized deformation gradient causes large transverse shear and normal stresses that can cause the damages to propagate and even failure of the laminate. Another effect of the impact is the creation of a compression stress wave, which travels from the impact surface through the thickness of the laminate. This wave is reflected from the back surface as a tension wave, which can cause failure at the first weak interface, resulting in chipping or splintering of the parts of the rear ply. Both internal stress waves and local out-of-plane deformations may initiate delamination at interfaces where there is major change in the angle between plies. The amount and type of the damage in the laminate depends upon the size, type and geometry of the laminate, impact energy and the loading on the laminate at the time of impact. At relatively low impact velocities, the laminate can respond by bending and failing either by shear resulting in delamination or flexural failure depending on short or long beam, respectively. At higher velocities somewhat different damage modes occur which may be caused by the combination of stress waves and the out of plane deformations. The

damage may result in delamination, fiber failure, matrix cracking, etc. If the velocity of the projectile is fairly high, the laminate acts as relatively rigid resulting in shear out and complete penetration of projectile.

7.1.4 Residual thermal stresses and moisture

Residual thermal stresses, caused by temperature and moisture changes, are always present due to cool down of the laminate from the elevated curing temperature and these may have considerable influence on interlaminar stresses.

7.2 Experimental Studies on Delamination Growth

Extensive research has been reported on the delamination testing of various composite materials. The majority of the work has been concerned with the determination of the critical strain energy release rates G. The reason why researchers are focusing on G is that, according to the fracture mechanics approach, delamination growth depends upon the stress state of the crack tip which is governed by the stress intensity factors K_I, K_{II} and K_{III} or the strain energy release rates G_I, G_{II} and G_{III}. Thus, it is essential towards the understanding of the reported results, to define the strain energy release rates G and to describe the testing equipment used to determine it. The goal of this section is to address this issue.

7.2.1 Definition of the strain energy release rate *G*

Energy rate analysis of the effects of flaws historically preceded crack-tip stress field analysis. The Griffith Theory [45] and later modifications by Irwin [46], termed the Griffith-Irwin Theory, made use of this approach [47-50]. Basically, these methods use

an energy balance analysis of crack extension. The total elastic energy made available per unit increase in crack surface area is denoted by G for the linear-elastic case. Physically, G may be viewed as the energy made available for the crack extension processes at the crack-tip as a result of the work from displacements of loading forces and/or reductions in strain energy in a body accompanying a unit increase in crack area. Alternatively, G can be regarded as a "generalized force" based on the potential energy change per unit forward displacement of a unit length of crack front, which results in G being defined as "the crack extension force". Following this line of argument, it is not difficult to show that for linear-elastic conditions:

$$G = -\frac{\partial U_T(\Delta_i, A)}{\partial A} \tag{578}$$

and

$$G = +\frac{\partial U_T(P_i, A)}{\partial A} \tag{579}$$

and

$$G = \frac{P^2}{2}\frac{\partial C}{\partial A} \tag{580}$$

where U_T is the total strain energy in a cracked body with a crack area A. U_T is alternately expressed in terms of A and load point displacements, Δ_i, or in terms of A and loads, P_i. In the last equation, C is the elastic compliance and the equation is written for a single loading force, but may be generalized for several forces. The G implied by the previous equations is the average value along a crack front weighted for the extent of crack extension involved for each increment of crack front in the three-dimensional sense. In two-dimensional situations, such as uniform extension of a straight-through crack in a thin plate subject to extension, G may be viewed as the value of a point quantity along the crack front. In several studies the critical value of G_c, required to cause the delamination

growth, is also defined as "delamination fracture toughness".

The Griffith criterion for fracture states that crack growth occurs if the total energy of the body remains constant or decreases as the crack length increases. In elastic solids, if W is the energy required for crack growth, then according to Griffith the necessary condition for crack growth can be expressed as:

$$G \geq \frac{dW}{dA} \tag{581}$$

It is common to replace $\frac{dW}{dA}$ by R the "crack resistance".

It needs to be underlined that the stress intensity factors K and the strain energy release rates G are not independent parameters, as the work of Irwin proved: the "energy-balance" approach to the characterization of fracture is equivalent to the "critical stress intensity factor" one. That means there exists a relationship between the strain energy release rate and the stress intensity factor:

$$G \propto K^2 \tag{582}$$

The constant of proportionality in the previous expression is a function of the elastic constants of the materials. This relationship relates the crack-tip stress field and the "energy-balance" criterion for crack growth, which can be interpreted in terms of a critical K value that is required for the crack to enlarge. Generally, researchers prefer to adopt the maximum total strain energy release rate criterion, which predicts the delamination will grow when G reaches the critical value G_c.

Another commonly recognized assumption is that the delamination can be characterized by linear elastic fracture mechanics (LEFM). The fundamental assumption of LEFM is that the behavior of the cracks, whether they grow or not, and how fast they

grow, is determined only by the stress field at the crack tip.

7.2.2 Test specimens for evaluating G

Interlaminar damage mechanism of composite materials results generally from mode I, mode II or mixed mode I+II loading. That is why the most adopted test specimens have been developed for studying crack propagation under the mentioned modes. A classification of the testing configurations can, consequently, be derived.

In all these specimens, the aim is to measure critical strain energy release rate G_c during onset or extension of delamination. Specimens are calibrated by means of a relation between G and compliance C.

$$G = \frac{P^2}{2b}\frac{\partial C}{\partial a} \tag{583}$$

where a is the crack length, b the width of the specimen, P the applied load and C is the compliance defined by the slope of the load P versus displacement δ curve for the specimen.

$$C = \frac{\delta}{P} \tag{584}$$

7.2.2.1 Test specimens for Mode I

Pure mode I, opening mode, caused by interlaminar normal stresses, is one of the most common delamination mode. Several investigators, i.e. [51-57], agree in recognizing the double cantilever beam (DCB) as an accurate pure mode I specimen.

A DCB, shown in Figures 114, is tested under displacement controlled conditions and P versus δ curves are obtained for various crack lengths a which are then used to obtain C and $\delta C/\delta a$. The value of G_c may then be determined using the critical load P_c for

the initiation of delamination and the values of $\delta C/\delta a$. Also, assuming DBC specimen to consist of two cantilever beams joined at the end of crack tip, the compliance may be expressed as:

$$C = \frac{8a^3}{bEh^3} \tag{585}$$

where E is longitudinal modulus and h is the thickness of each beam. Substituting this into the general expression for G, one obtains:

$$G = \frac{3P^2C}{2ba} \tag{586}$$

The beam relation can be used as long as the shear deformations can be ignored and the deflections are small, otherwise some corrections should be applied.

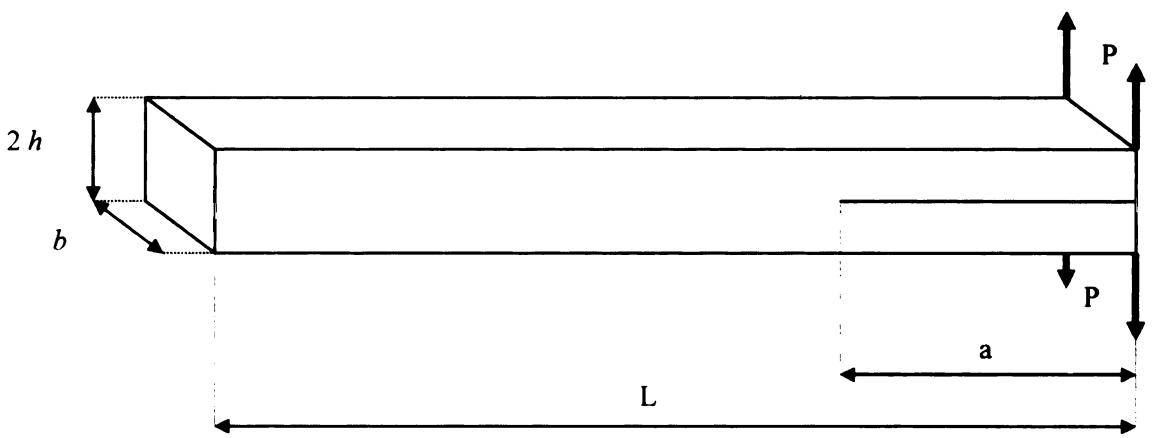

Figure 114. ***Double cantilever beam (DBC) specimen***

Only one other type of mode I specimen has been found [58] in the present review: the free edge delamination (FED). It seems FED specimen proposed provides a viable approach to determining delamination initiation, as it is relatively simple test specimen. However, because of the complex stress state in the free edge zone, the FED

specimen does not necessarily produce a pure mode I delamination. Therefore DCB is considered as most suitable to determine G_{Ic}.

7.2.2.2 Test specimen for Mode II

To characterize the mode II delamination, shearing mode, the end notched flexure (ENF) and end-loaded split (ELS) specimens have been proposed, i.e. [51-57]. ENF specimens are projected as developing pure mode II behavior. The specimen is the same as the DCB but it is loaded in a three-point flexure which results in almost pure in plane shear delamination growth mode.

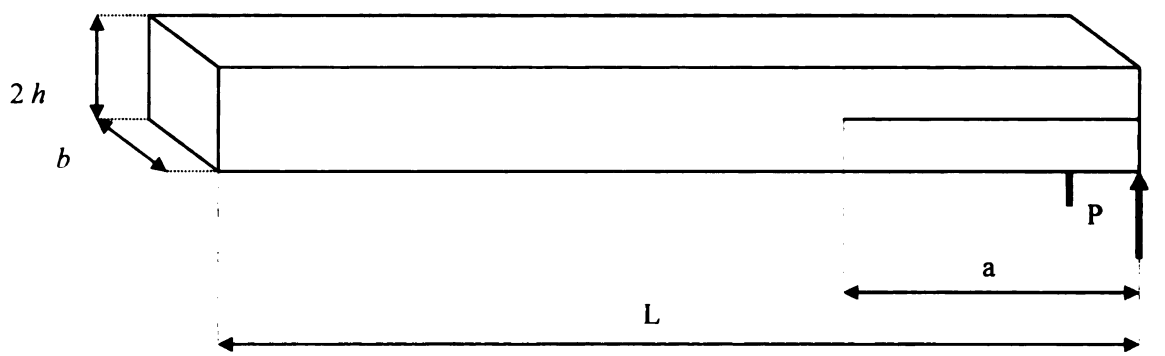

Figure 115. ***End-loaded split (ELS) specimen***

For the mode II end-loaded split (ELS) test, the specimen is held at one end and loaded at the other, as shown in Figure 115. For a given deflection and curvature, the arms of the beam are subject to the same bending moments.

7.2.2.3 Test specimen for Mixed Mode I+II

The present study reported that the mixed mode delamination, i.e. [51-57], has been explored by use of the following tests: fixed-ratio mixed mode FRMM, mixed mode bending MMB, cracked-lap shear test CLS and modified notched flexure MENF.

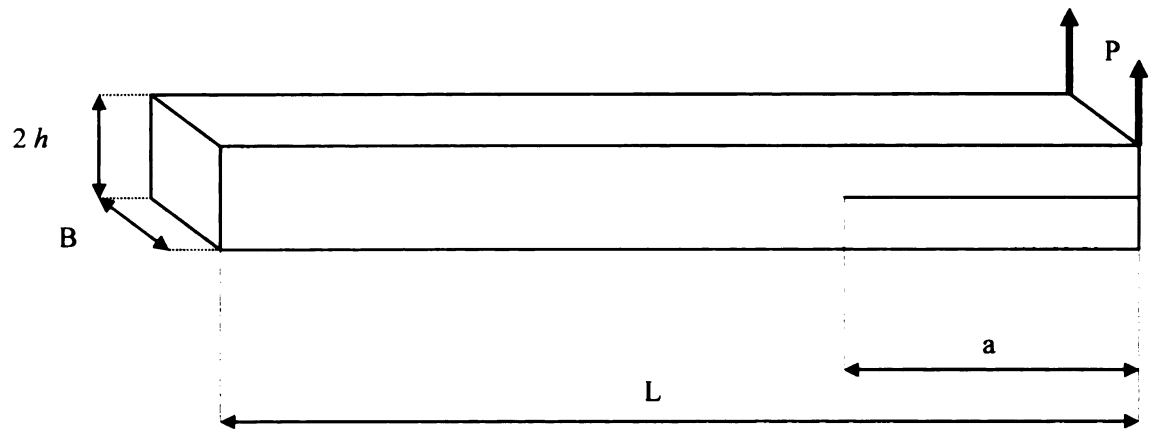

Figure 116. ***Fixed-ratio mixed-mode(FRMM) specimen.***

The fixed-ratio mixed-mode FRMM test containing a symmetrical crack is shown in Figure 116. For this symmetrically cracked FRMM test, the ratio of mode I to mode II loading is approximately constant throughout the test at 4:3; hence, the value of G_I/G_{II} is 1.33.

The mixed mode bending MMB specimens can provide a wide range of mixed mode I/II ratios by adjustment of the loading and lever fulcrum position.

Using the cracked-lap shear test CLS specimen, the P-δ curves may be obtained for various crack lengths and $\delta C/\delta a$ determined. The substitution of P_c and $\delta C/\delta a$ in equation for G give the value of G_c. CLS provides the total energy consisting of modes I and II.

7.3 Delamination Criteria

Initiation and evolution of the delamination may be predicted by a fracture mechanics approach or by interlaminar strength, introducing an interface constitutive law

between the layers. The two approaches are investigated separately in the next two sections.

Since interlaminar stresses τ_{zx}, τ_{yz} and σ_z are responsible for delamination, the accurate study of delamination requires a complete 3D stress analysis. However, it is difficult to calculate interlaminar stresses analytically. Also, it should be recognized that the stresses at the delamination front are singular. That's the reason why finite element analysis plays a dominant role in developing new criteria for predicting delamination. Consequently, the great majority of the works reviewed take advantage of the finite element method in some way.

7.3.1 Fracture Mechanics Based

As it has been discussed previously the fracture mechanics approach uses strain energy release rate as a parameter for assessing delamination, initiation and growth. In fracture mechanics approach, strain energy release rate per unit area delaminated is evaluated and compared with G_c. Thus, one of the main efforts of the researchers is to correctly evaluate strain energy release rate. There exists few well-tested numerical methods for obtaining G and they will be explained in the next subsection.

7.3.1.1 Numerical evaluation of the strain energy release rate

Different methods for evaluating the strain energy release rate G have been adopted in conjunction with finite element analysis: the virtual crack closure technique (VCCT), the crack closure method (CCM) and the J-integral method. The J-integral method can be used to analyze both linear and nonlinear problems. However, this method can't easily be applied to mixed-mode fracture problems. This is an important limitation

since delamination growth is a three-dimensional phenomenon with a general mixed-mode type of failure. The virtual crack closure technique (VCCT) does not have this restriction and, being simple and accurate, is almost universally adopted even if it can be used only for linear elastic problems. This choice is supported by several experimental results that well match numerical models based on the VCCT (i.e. Prathan and Tay [59]). The VCCT has been successfully used with both plate and 3D brick finite element models.

Calculation of the Strain Energy Release Rate by VCCT

In this section, classical definitions used in the calculation of the strain energy release rate by the VCCT method are reviewed.

In finite element analysis, the total strain energy release rate could be calculated from two finite element solutions, one with a crack length a and another with a slightly different crack length $a + \Delta a$. Using the difference form of the previous equation gives:

$$G = \frac{U_{a+\Delta a} - U_a}{\Delta a} \tag{587}$$

Where $U_{a+\Delta a}$ and U_a are the total strain energies of the finite element models with crack lengths $a + \Delta a$ and a, respectively. The value of G calculated from this relation is assigned as the strain energy release rate for a crack of length $a + \frac{\Delta a}{2}$. However, because of the difference approximation, the value of Δa needs to be very small. The formula is not attractive because (a) the computation involves differences of large numbers divided by a small number and consequently the resulting value is not accurate, and (b) this procedure involves two finite element runs. Hence, alternate forms of the formula for determining G have been proposed in the literature. These are based on the virtual crack

closure technique (VCCT) proposed by Irwin [46]. Elastic strain energy released during an incremental crack extension is equal to the work done in closing the incremental crack. When the crack is opened, the work done to close the crack opening could be written as:

$$\Delta W = \frac{1}{2}\int_0^{\Delta a} \hat{\sigma}\,\Delta\hat{u}\,da \tag{588}$$

$\Delta\hat{u}$ is the relative displacements between the crack surfaces along Δa when the crack is closed. On the basis of the crack closure equivalence, the available energy release rate G for a crack size a is expressed by:

$$G = \lim_{\Delta a\to 0}\frac{1}{2\Delta a}\int_0^{\Delta a} \hat{\sigma}\,\Delta\hat{u}\,da \tag{589}$$

Substituting in this equation the components of the surface stresses $\hat{\sigma}$ and the corresponding relative displacements $\Delta\hat{u}$ leads to the components of G.

In 2D problems modeled in the x-z plane, the mode-I and mode-II strain energy release rates are obtained from:

$$G_I = \lim_{\Delta a\to 0}\frac{1}{2\Delta a}\int_0^{\Delta a} \sigma_z(x,0)\,w(x-\Delta a,0)\,dx \tag{590}$$

$$G_{II} = \lim_{\Delta a\to 0}\frac{1}{2\Delta a}\int_0^{\Delta a} \sigma_{xz}(x,0)\,u(x-\Delta a,0)\,dx \tag{591}$$

Thus, the total strain energy release rate is:

$$G_{Total} = G_I + G_{II} \tag{592}$$

In the previous expressions, w and u are, respectively, the crack opening and sliding displacements; σ_z and σ_{xz} are the normal and shear stresses ahead of the crack tip.

In 3D analyses, the strain energy release rates can be calculated using VCCT as:

Thu

Wh

δy

are

con

to

the

the

reg

wi

ge

(

$$G_I = \lim_{\Delta a \to 0} \frac{1}{2\Delta a \delta y} \int_y^{y+\delta y} \left[\int_0^{\Delta a} \sigma_z(x, y, 0)\, w(x - \Delta a, y, 0)\, dx \right] dy \tag{593}$$

$$G_{II} = \lim_{\Delta a \to 0} \frac{1}{2\Delta a \delta y} \int_y^{y+\delta y} \left[\int_0^{\Delta a} \sigma_{xz}(x, y, 0)\, u(x - \Delta a, y, 0)\, dx \right] dy \tag{594}$$

$$G_{III} = \lim_{\Delta a \to 0} \frac{1}{2\Delta a \delta y} \int_y^{y+\delta y} \left[\int_0^{\Delta a} \sigma_{yz}(x, y, 0)\, v(x - \Delta a, y, 0)\, dx \right] dy \tag{595}$$

Thus, the total strain energy release rate is:

$$G_{Total} = G_I + G_{II} + G_{III} \tag{596}$$

Where w, u and v are the crack opening, sliding and tearing displacements, respectively. δy is the width of the crack front over which crack closure occurs, and σ_z, σ_{xz} and σ_{yz} are the normal and shear stresses on the crack plane and ahead of the crack front.

The crack closure representation is convenient for adaptation in numerical computation. That is another reason why several methods were proposed in the literature to calculate the strain energy release rates in finite element analyses using the VCCT. In the finite element method, continuous stress and displacement fields are approximated by their nodal values. Figure 117 (a) represents the finite element model near a crack-tip region. A crack of length a is shown with the crack tip at node o.

An incremental crack extension Δa is introduced replacing the crack tip node o with two separate nodes m and n as depicted in Figure 117 (b). For the new crack geometry the finite element solution for the nodal displacements (u_m, v_m, w_m) and (u_n, v_n, w_n) are found for nodes m and n, respectively.

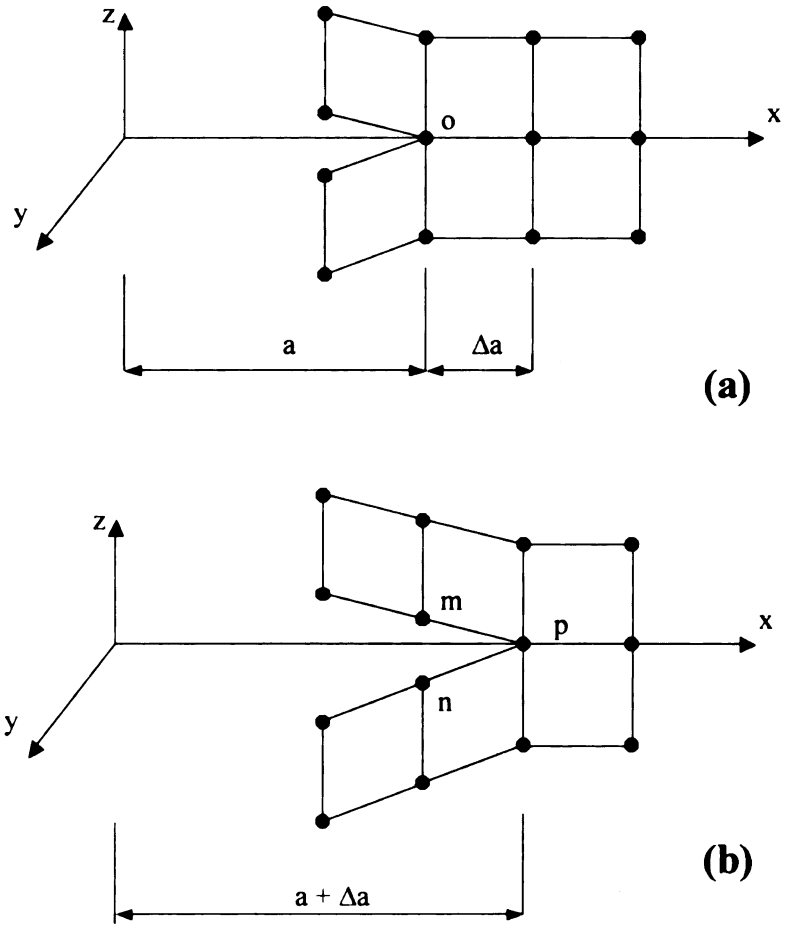

Figure 117. ***2D FEM before crack opening (a) and after crack opening (b)***

The corresponding load F_o, required to take the two bodies in contact for the delamination length a, is approximated to be the load F_p obtained from the same analysis at the node p. Therefore, it is assumed that the load distribution at the interface near the delamination tip remains the same during delamination extension from a to $a + \Delta a$. This assumption requires the finite element mesh to satisfy certain conditions: the mesh is symmetric on the crack plane and about the crack front, the element size Δa at the crack front should be small and normality of the FE mesh is maintained near the crack front. These requirements are often easy to satisfy.

Thus, the work required to close the crack opening is approximated by:

$$\Delta W \cong \frac{1}{2B_p}\left[F_x(u_m - u_n) + F_y(v_m - v_n) + F_z(w_m - w_n)\right] \tag{597}$$

Where F_x, F_y and F_z are the components of the nodal forces at p. B_p is the equivalent width apportioned to node p: the average of the dimensions in the y direction of the two adjacent elements sharing the node p.

Consequently, the energy release rate for the crack extension is approximated by:

$$G_I = \frac{1}{2\Delta a B_p}\left[F_z(w_m - w_n)\right] \tag{598}$$

$$G_{II} = \frac{1}{2\Delta a B_p}\left[F_x(u_m - u_n)\right] \tag{599}$$

$$G_{III} = \frac{1}{2\Delta a B_p}\left[F_y(v_m - v_n)\right] \tag{600}$$

In the literature, the virtual crack closure technique (VCCT) is employed in two ways: a) to evaluate the total strain energy release rate G across the width of the crack for various values of the crack dimensions, and b) to predict the crack growth. In the second case the total strain energy release rate G is computed for all the nodes in the original delamination front. The nodes with the largest values of G are released, simulating the advancement of the delamination front. Then, the strain energy release rate is recalculated along the new delamination front. The maximum value of G is found and the corresponding nodes are released. This procedure of determining G along the delamination front and subsequently releasing the corresponding nodes is repeated in order to simulate the progressive failure process.

Calculation of the Strain Energy Release Rate by CCM

The crack closure method CCM doesn't differ much from the virtual crack

closure technique VCCT. However, since the forces and displacements of the system must be carried out at two separate configurations it requires two finite element analyses. That's why it is much less used than the virtual crack closure technique VCCT.

Figure 117 (a) represents the finite element model near a crack-tip region. A crack of length a is shown with the crack tip at node o. Like in the VCCT approach, an incremental crack extension Δa is introduced replacing the crack tip node o with two separate nodes m and n as depicted in Figure 117 (b). For the new crack geometry the finite element solution for the nodal displacements (u_m, v_m, w_m) and (u_n, v_n, w_n) are found for nodes m and n, respectively. The crack opening is then collapsed by applying equal and opposite forces at nodes m and n such that they common displacements match those found earlier in o before it opens. Thus, the work required to close the crack opening is approximated by the same equation as in the VCCT:

$$\Delta W \cong \frac{1}{2B_p}\left[F_x(u_m - u_n) + F_y(v_m - v_n) + F_z(w_m - w_n)\right] \tag{601}$$

However, here F_x, F_y and F_z are the components of the nodal forces at o. B_p is the equivalent width apportioned to node p: the average of the dimensions in the y direction of the two adjacent elements sharing the node p.

Consequently, the energy release rate for the crack extension is approximated by:

$$G_I = \frac{1}{2\Delta a B_p}\left[F_z(w_m - w_n)\right] \tag{602}$$

$$G_{II} = \frac{1}{2\Delta a B_p}\left[F_x(u_m - u_n)\right] \tag{603}$$

$$G_{III} = \frac{1}{2\Delta a B_p}\left[F_y(v_m - v_n)\right] \tag{604}$$

7.3.1.2 Fracture mechanics based delamination criteria

As reported previously, the virtual crack closure technique (VCCT) is very often adopted for studying delamination initiation and growth.

In 1995 Hwu, Kao and Chang [60] conducted a set of experimental tests and finite element simulation in order to assess a delamination fracture criteria for composite material. For their investigation they employed the following specimens: the double-cantilever beam (DCB) test for mode I; the end-notched flexural (ENF) test for mode II; cracked-lap shear test CLS and the modified end-notched flexure (MENF) tests for mixed mode I+II. The finite element analysis implementing the VCCT was necessary in order to separate the total value of G obtained by the experiments into the sum of each mode. The authors assumed that unlike cracks in homogeneous bodies, the interface cracks always induce opening, shearing and tearing mode fracture simultaneously for a single mode loading. Hence, unlike the unidirectional composite specimen, it would not be guaranteed that the DCB test may measure G_I since the failure of DCB specimen may not only be determined by G_I, but may also be influenced by G_{II}. They had thought that before getting any experimental data from DCB test, one should only treat it like mixed mode failure test. But, results from the DCB tests confirmed that G_I is far bigger than G_{II} and G_{III}, and the test is an almost pure mode I delamination. Same result was found about the ENF test for mode II delamination.

According to our literature review, the most adopted [59, 61-70] mixed-mode interaction criterion is:

$$\left(\frac{G_I}{G_{Ic}}\right)^a + \left(\frac{G_{II}}{G_{IIc}}\right)^a + \left(\frac{G_{III}}{G_{IIIc}}\right)^a = Q^b \tag{605}$$

Where the value of the parameters a and b is usually 1 or 2. If $Q \geq 1$, then delamination occurs.

Kaczmarek, Wisnom, Jones [61] (1998) are among the authors computing the strain release rate implementing the VCCT method in finite element model. The computed values of the interlaminar fracture toughness G_c, critical value of G required to cause the delamination growth, has been used to study the free-edge delamination of glass/epoxy composite laminated beam loaded under bending.

In 1998 Pradhan and Tay [59] applied a 3D finite element analysis to the study of delamination growth in notched composite laminates under compression. The crack closure method CCM was chosen as approach for computing the strain energy release rate G in the three delamination modes.

Rinderknecht and Kroplin [63] in 1997, Wang and Raju [64] in 1996, Raju, Sistla and Krishnamurthy [65] in 1996 and Hitchings, Robinson and Javidrad [66] in 1994 developed similar finite element models for the analysis of delamination growth in composite plates. Obviously, the numerical models are different from each other, but the methodology for determining delamination initiation and growth is the same. The virtual crack closure technique (VCCT) is employed to compute the total energy release rate G, including contribution by all the three modes.

7.3.2 Interlaminar strength and mixed approaches

In strength of material approach, local state of stress at the interface is compared with relevant strengths. Use of finite element analysis makes the strength of material approach attractive, as the stresses can be evaluated quickly and efficiently, and interlaminar stresses can be easily compared with the measured strengths. However, unless delamination initiation is the only concern, failure criteria usually combine strength of material features with fracture mechanics ones.

Since the cohesive zone can still transfer load after the onset of damage, a softening model is required that describe how the stiffness is gradually reduced to zero after the interfacial stress reaches the interlaminar tensile strength. Reliable prediction of the softening behavior can be obtained relating the work of separation to the critical value of the strain energy release rate. It has been shown that if an individual interfacial location is considered, the area under the stress-relative displacement curve is equal the critical value of the strain energy release rate:

$$G_c = \int_0^{\delta_F} \sigma(\delta) d\delta \tag{606}$$

where δ_F is the relative displacement at failure and G_c is the critical strain energy release rate for the corresponding delamination mode.

Some stress-relative displacement models are illustrated in Figure 118. The material behavior is defined by the interfacial tensile strength σ_t, the relative displacement at the on set of damage δ_0, the relative displacement at failure δ_F. In single-mode delamination as the load is progressively increased, the relative displacement δ between bottom and top FE mesh grows accordingly to the value of the penalty stiffness. When δ_0 is reached the stress is at is maximum level, the interfacial tensile strength σ_t.

For higher relative displacements the interface accumulates damages and its ability to sustain stress decrease progressively. Once δ exceeds δ_F the interface is fully debonded and it is no more able to support any stress.

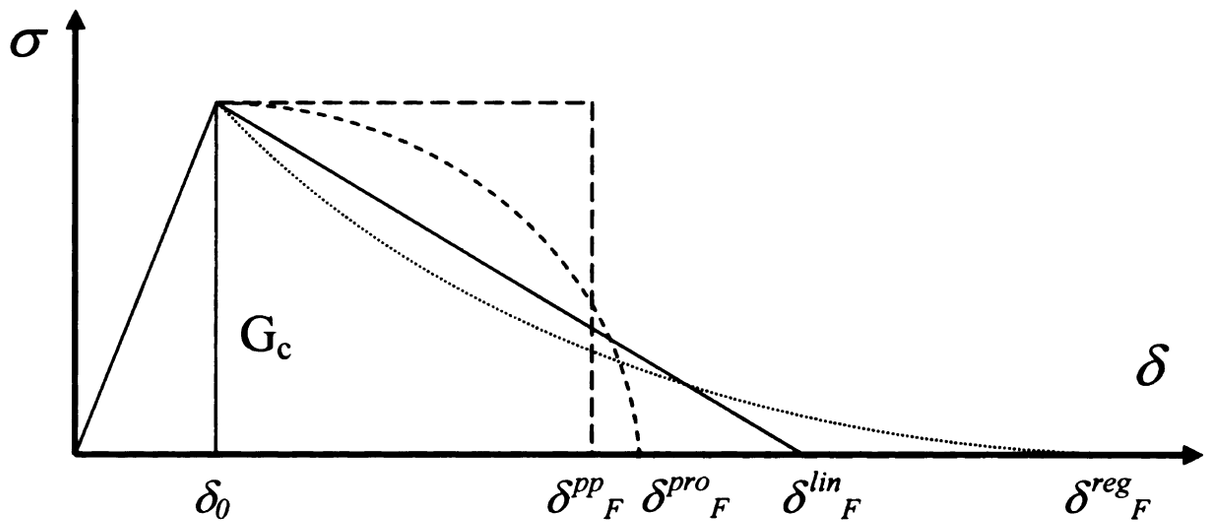

Figure 118. ***Interfacial constitutive model***

The delamination model just described is has been adopted by Reedy et al. [62] 1997, Davila et al. [67] 2001, Mi et al. [68] 1998, Chen et al. [69] 1999, and Alfano et al. [70] 2001, Lammerant and Verpoest [71] 1996, Schellekens and Boerst [72] 1993 and Schipperen and Lingen [73] 1999, Moorthy and Reddy [74] 1999. Interface elements are introduced to connect the individual plies of a composite laminate, but the way this connection is realized can differ. Two groups can be identify: point to point interface elements acting like spring and connecting pairs of nodes, continuous interface elements connecting pairs of two or three dimensional finite elements.

The work of Allix and Corigliano [75] 1999, Point and Sacco [76] 1996, Ladevèze [77] 1992, Bottega [78] 1983 clearly shares the same basic methodology, as

their references confirm. A constitutive law for the interface material, able to handle the delamination phenomenon, has been obtained starting from an adhesion model. It is based on the very simple physical idea of the behavior of the interface. In fact, it has been assumed that when two points on the surfaces in contact are in adhesion, their relative displacement must be zero. According to the work of Point and Sacco [75] the main feature of their delamination approach consists in the possibility of mathematically recovering fracture mechanics theory. Ladevèze [77] defined the damaged strain energy density in the interface layer as:

$$E_D = \frac{1}{2}\left[\frac{\langle\sigma_{33}\rangle_-^2}{k^0} + \frac{\langle\sigma_{33}\rangle_+^2}{k^0(1-d_I)} + \frac{\sigma_{32}^2}{k_2^0(1-d_{II})} + \frac{\sigma_{31}^2}{k_1^0(1-d_{III})}\right] \tag{607}$$

where d_I, d_{II} and d_{III} are the internal damage variable correspondent to the associated delamination mode. Differentiation of E_D with respect to each damage variable yields the associated thermodynamic forces Y_I, Y_{II} and Y_{III}. At this point a variety of damage evolution laws can be considered using a function $Y(Y_I, Y_{II}, Y_{III})$, like:

$$Y = \sup\big|_{\tau\leq t}\left(Y_I + \gamma_1 Y_{II} + \gamma_2 Y_{III}\right)^{\frac{1}{2}} \tag{608}$$

Then, the internal damage variables are computed by means of a material function $w(Y)$. Delay effects are usually introduced in the function $w(Y)$, because without their implementation the model would be accurate in the prediction of initiation but not in its evolution. The numerical procedure has been used for beam and plate problems. The results obtained using the finite element method seems to agree with the analytical solution. But, comparison with experimental results appears necessary to validate their approach.

The concept of interface model is also present in the work of Petrossian and Wisnom [79] 1998. They developed an interface element to model the resin-rich layers between plies, using plasticity theory. The element is able to behave elastically, yield under a changing mode ratio with either a perfectly plastic or work softening type response, and finally fail when a certain amount of plastic work has been done. According to the authors, when there is more then one possible delamination site the approach has a significant advantage over the conventional fracture mechanics methods such as the virtual crack closure technique, since it is not necessary to assume where or at what rates the cracks will propagate.

Chakraborty and Pradhan [80] performed a fully 3D finite element analysis to study delamination at the interface GR/E and GL/E laminates with broken central plies. The interface between the broken and continues plies has been modeled with a resin rich layer. Their methodology for predicting delamination employs contemporarily strength and fracture mechanics approaches. The strength of material approach adopted is the most common one, the quadratic failure criterion:

$$\left[\frac{\bar{\sigma}_{zz}}{Z}\right]^2+\left[\frac{\bar{\tau}_{zx}}{X}\right]^2+\left[\frac{\bar{\tau}_{zy}}{Y}\right]^2=Q \tag{609}$$

Where Z, X and Y are the transverse tensile strength, longitudinal shear strength and lateral shear strength, respectively. If $Q \geq 1$, then delamination initiation occurs. This same criterion for identifying delamination initiation has been adopted by Joo and Sun [81] (1994). In this expression $\bar{\sigma}_{zz}$, $\bar{\tau}_{zx}$ and $\bar{\tau}_{zy}$ are the average stress at the delamination

front and are give by:

$$\left[\bar{\sigma}_{zz}, \bar{\tau}_{zx}, \bar{\tau}_{zy}\right] = \frac{1}{x_c}\int_0^{x_c}\left[\sigma_{zz}, \tau_{zx}, \tau_{zy}\right]dx \tag{610}$$

where x_c is the critical distance over which the interlaminar stresses are averaged. The recommended value of x_c is twice the ply thickness. As fracture mechanics approach the crack closure method CCM is used. The delamination is assumed to takes place if $Q \geq 1$ or if the strain energy release rate $G=G_c$. Effects of important parameters like ply thickness, fibre angle, location of the break and stiffness of the interfacial resin has been studied. Delamination evolution is not explored.

Ko, Lin and Chin [82] (1992), S. Mohammadi, Owen and Peric [83] (1998), Zhao, Hoa, Xiao and Hanna [84] (1999) and Chang and Springer [85] (1986) predicted delamination initiation by a strength approach very similar to the one of Chakraborty and Pradhan [80]. Here, the mathematical form changes to:

$$\left[\frac{\bar{\sigma}_{zz}}{Z}\right]^2 + \left[\frac{\bar{\tau}_{zx}}{X}\right]^2 + \left[\frac{\bar{\tau}_{zy}}{Y}\right]^2 = e^2 \tag{611}$$

If $e \geq 1$, then delamination initiation occurs.

In [82, 85] delamination evolution is not explored, while in [83] the crack growth is studied with the same methodology like in [62].

A three-dimensional finite-deformation cohesive element and a class of irreversible cohesive laws was developed by M Ortiz and A. Pandolfi [86] (1999) and A. Pandolfi, P. Krysl and M Ortiz [87] (1999). The element has some unique characteristics,

but the interfacial constitutive model is of the familiar form summarized in Figure 118.

Moes, Dolbow and Belytschko [88] (1999) presented an innovative finite element able to account for crack growth inside the element. The numerical model is quite complicate and will not be described here. The approach adopted for delamination initiation and growth is based upon the maximum circumferential stress criterion. Stresses are computed by the classical fracture mechanics equation for the stress distribution at the crack tip.

This finite element type of approach, also referred as *singularity element* approach, was also used by M.A. Aminpour and K. A. Hosapple [89] (1991) and Jin Lee and Huajian Gao [90] (1995).

CHAPTER 8 A NOVEL INTERFACE TECHNOLOGY FOR MODELING DELAMINATION

The interface element developed in the present study can be readily employed for the analysis of delamination growth in composite laminates. In addition, the present interface element approach would have several advantages over the conventional FE one. A special feature, which is useful in simulating delamination, is the ability of releasing desired portions of the interface smaller than the finite element length, determining the crack advance. This can be achieved by changing the extreme values of the interval of integration of the interface element or by reducing the value of the penalty parameter for that interval. Also, within each interface sub-region it is possible to evaluate forces at the interface and to reduce the value of the penalty parameter as needed. Thus, it is possible to overcome the limitation common to the delamination techniques found in the literature, which requires delamination growth to be simulated in a discretized form by releasing nodes of the FE model. Moreover, the ability of estimating the normal force at the interface, allows for the development of an accurate and mesh independent friction model.

8.1 Damage Model

The damage model implemented in the developed interface element is one that is commonly adopted [62, 67-74]. It mixes features of strength of materials approaches and fracture mechanics. A bilinear softening model has been implemented in the present model, see Figure 119.

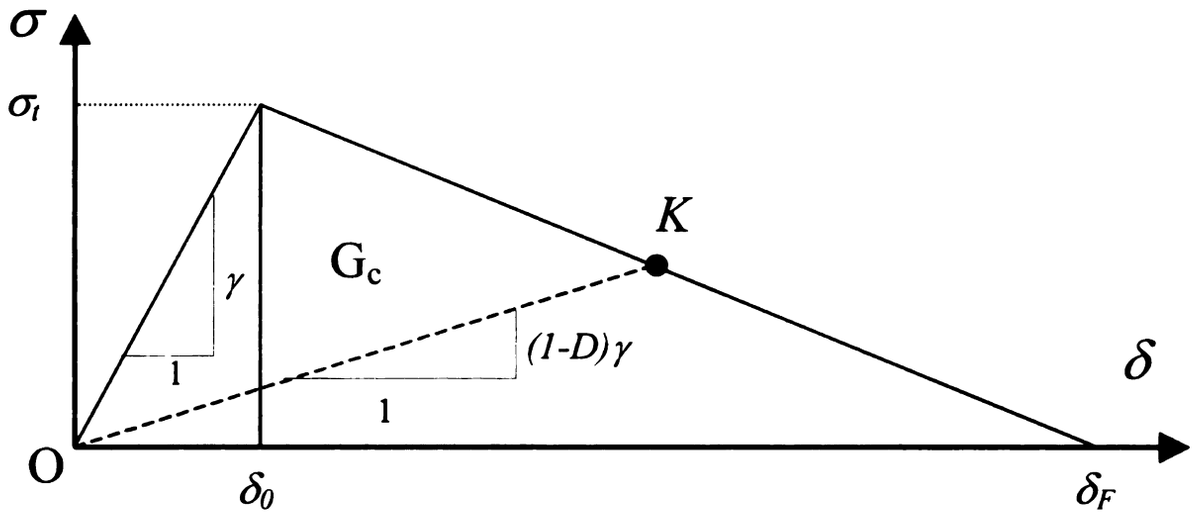

Figure 119. ***Bilinear interfacial constitutive damage model.***

In single-mode delamination, as the load is progressively increased, the relative displacement δ between the bottom and top FE mesh grows proportionally according to the value of the penalty stiffness γ. When δ_0 is reached the stress is equal to the interfacial tensile strength σ_t, the maximum stress level possible. For higher relative displacements the interface accumulates damage and its ability to sustain stress decreases progressively. Once δ exceeds δ_F the interface is fully debonded and it is no longer able to support any stress. If the load were removed after δ_0 has been exceeded but before δ_F has been reached, the model would unload to the origin. For example, if after reaching point *K* the load is reduced, the model unloads along the line *KO*. If the load is reapplied, the stress

grows with the relative displacement along the same line *KO*.

This behavior is obtained by an effective reduction in the penalty stiffness γ. In the present model, a new parameter D is introduced in order to signify the damage accumulated at the interface:

$$\sigma = (1 - D)\gamma\delta \tag{612}$$

Thus D is a damage parameter, whose initial value is zero. D starts growing when $\delta \geq \delta_0$ and reaches the value 1 when $\delta \geq \delta_F$.

The value of D is computed from geometry to be:

$$D(\delta) = \frac{\delta_F(\delta - \delta_0)}{\delta(\delta_F - \delta_0)} \tag{613}$$

The interfacial constitutive model is entirely defined when two of the following properties are known: G_c, σ_t, δ_0 and δ_F. The following two relations exist among these parameters:

$$G_c = \frac{\delta_F \sigma_t}{2} \tag{614}$$

$$\delta_0 = \frac{\sigma_t}{\gamma} \tag{615}$$

The bilinear interface model is applied to a sub-region of the interface between the two meshes; the smaller is the length of each sub-region the higher is the accuracy of the prediction. A conventional implementation of the discussed damage technique requires the model to be applied along the length of one finite element, wherein the crack can advance in a discrete way only by failing one element at a time. Both limitations necessitate the use of a refined finite element mesh. Thanks to the special features of the

interface element previously presented, the damage evolution scheme in our model is effectively mesh-independent, wherein sub-regions of the interface much smaller than the finite element length can be released.

Thus, the bilinear interface model can be applied to a desired fraction of the interface between the two meshes. If we divide the interface element into a given number of intervals n, each of them will obey the rules of the failure model independently from the others. This corresponds to changing the total potential energy of the system in the following way:

$$\pi = \pi_{\Omega_1} + \pi_{\Omega_2} + \frac{1}{2}\sum_{i=1}^{n}(1-D_i)\gamma_1 \int_{L_{i-1}}^{L_i}(V-u_1)^2\,ds + \sum_{i=1}^{n}(1-D_i)\gamma_2 \int_{L_{i-1}}^{L_i}(V-u_2)^2\,ds \quad (616)$$

where D_i is the damage parameter associated with the interval i, and the interval i is defined over the range (L_{i-1}, L_i). L_i is the value of the interface coordinate L at the end of the i^{th} interval. The value of the relative displacement δ is evaluated at the center of the interval i. By allowing crack advance in a more continuous way, a higher accuracy of the simulation can be achieved.

To illustrate this concept, consider the two incompatible meshes shown in Figure 120. They are joined by two interface elements whose length equals that of five conventional elements of the top mesh and four elements of the bottom mesh. Two forces F applied at the tip are responsible for affecting a mode I stress field at the interface. The interface element at the crack tip is shown in Figure 120(a) as divided in 10 intervals. The intervals don't need to match any of the nodes in the upper or lower mesh, but in this example some of them coincide. Moreover, the number of intervals in the interface

element is a parameter that can be changed as desired.

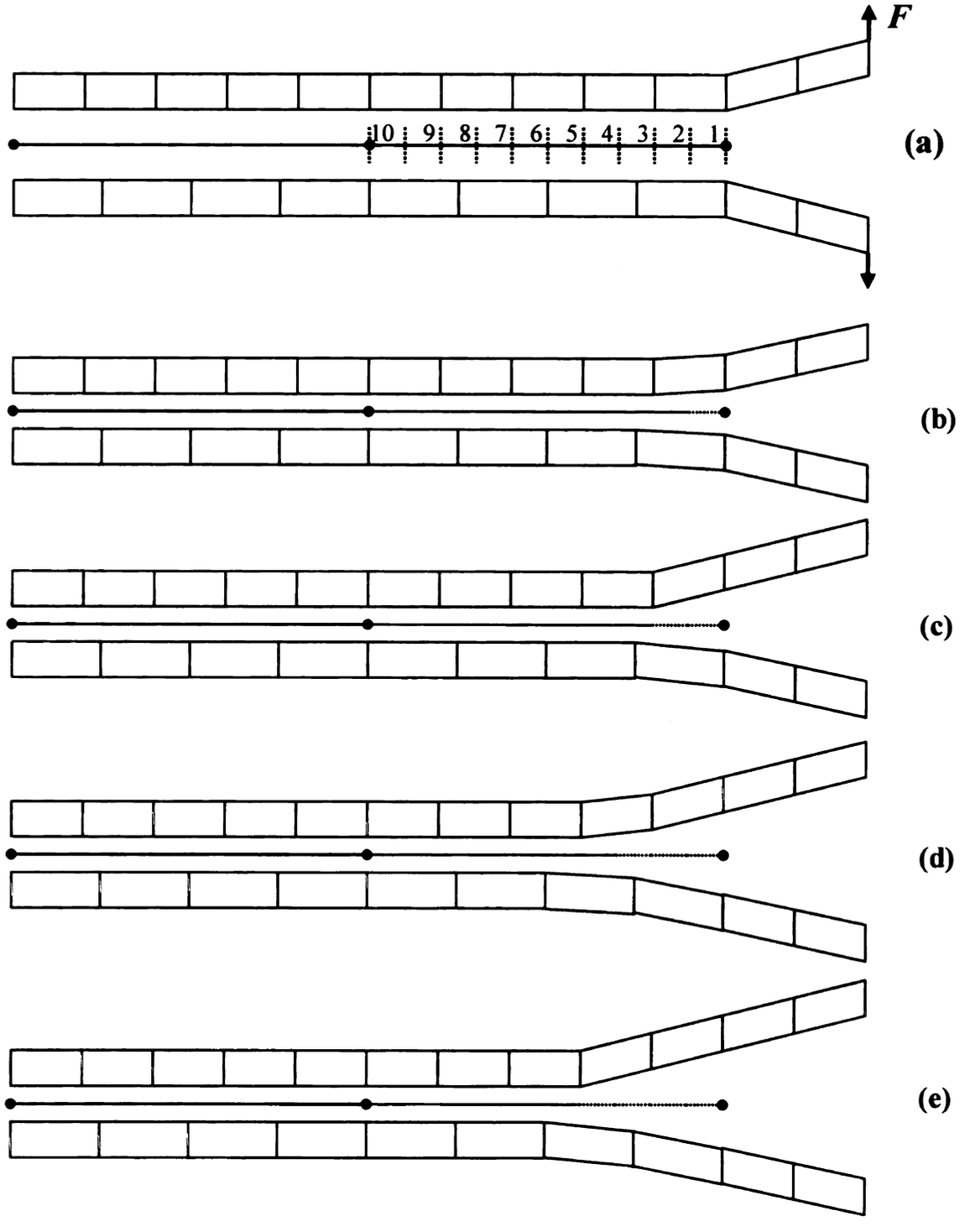

Figure 120. ***Division of the interface element in intervals***

Following the progression in Figure 120, a simulation of the delamination growth is achieved by releasing portions (intervals) of the interface element. In Figure 120(b), the

first interval is failed. The portion of the interface element not released still applies its constraint to the lower and upper element next to the crack tip. In Figure 120(c) the second interval is failed, this determines the complete release of the element on the upper mesh near the crack tip. The element on the lower mesh moves downward too, but being still held in part, the movement is small. The next advance in the crack length, Figure 120(d), frees the lower element and only partially the upper. Figure 120(e) shows the effect of the releasing yet another interval. Similarly, when all the intervals are failed the FE model behaves as though the first interface element is not present. Then, the next interface element starts failing. In this example, intervals whose length is half of the smaller finite element extension have been used. Dividing the interface element into more intervals or reducing its length would obviously improve the accuracy of the model.

8.2 Mixed Mode Approach

A novel approach for correctly simulating the delamination growth in mixed mode I+II conditions has been developed. Due to the peculiar finite element formulation of the penalty interface element, some degree of creativity was required. The damage models for the two modes needed to be linked according the quadratic failure criterion and the quadratic interaction criterion, maintaining at the same time independent damage parameters.

The properties required to define the softening model are the following: the interlaminar tensile and shear strengths T and S, the penalty parameter γ, the critical strain energy release rate G_{Ic}, and G_{IIc}. At a given increment the finite element solution allows the computation of δ_z and δ_x for an interval of the interface element; where δ_z and

δ_x indicate, respectively, the mode I and mode II relative displacements. Using the following relations among stresses and relative displacements:

$$\delta_{z0} = \frac{T}{\gamma_z} \tag{617}$$

$$\delta_{x0} = \frac{S}{\gamma_x} \tag{618}$$

$$\sigma_z = \gamma_z \delta_z \tag{619}$$

$$\tau_{xz} = \gamma_x \delta_x \tag{620}$$

the commonly adopted quadratic failure criterion can be written in the forms:

$$\left(\frac{\sigma_z}{T}\right)^2 + \left(\frac{\tau_{xz}}{S}\right)^2 = 1 \tag{621}$$

$$\left(\frac{\delta_z}{\delta_{z0}}\right)^2 + \left(\frac{\delta_x}{\delta_{x0}}\right)^2 = 1 \tag{622}$$

If the condition in (622) is not satisfied, no action needs to be taken. Otherwise, we assume the following ratio:

$$\frac{\left(\frac{\delta_z}{\delta_{z0}}\right)^{actual}}{\left(\frac{\delta_x}{\delta_{x0}}\right)^{actual}} = C_1 \tag{623}$$

to be the same it was when the failure condition (622) was verified first, the point of damage onset. Figure 121 will help in clarifying the idea. At the increments when the left hand side of equation (622) is bigger than 1, the relative displacements δ_x and δ_z are higher than the minimum values necessary for damage onset. In Figure 121, where δ_x/δ_{x0} and δ_z/δ_{z0} are the main axes, such a configuration could be represented by a generic point

A outside the quarter of circle defined by the quadratic failure criterion.

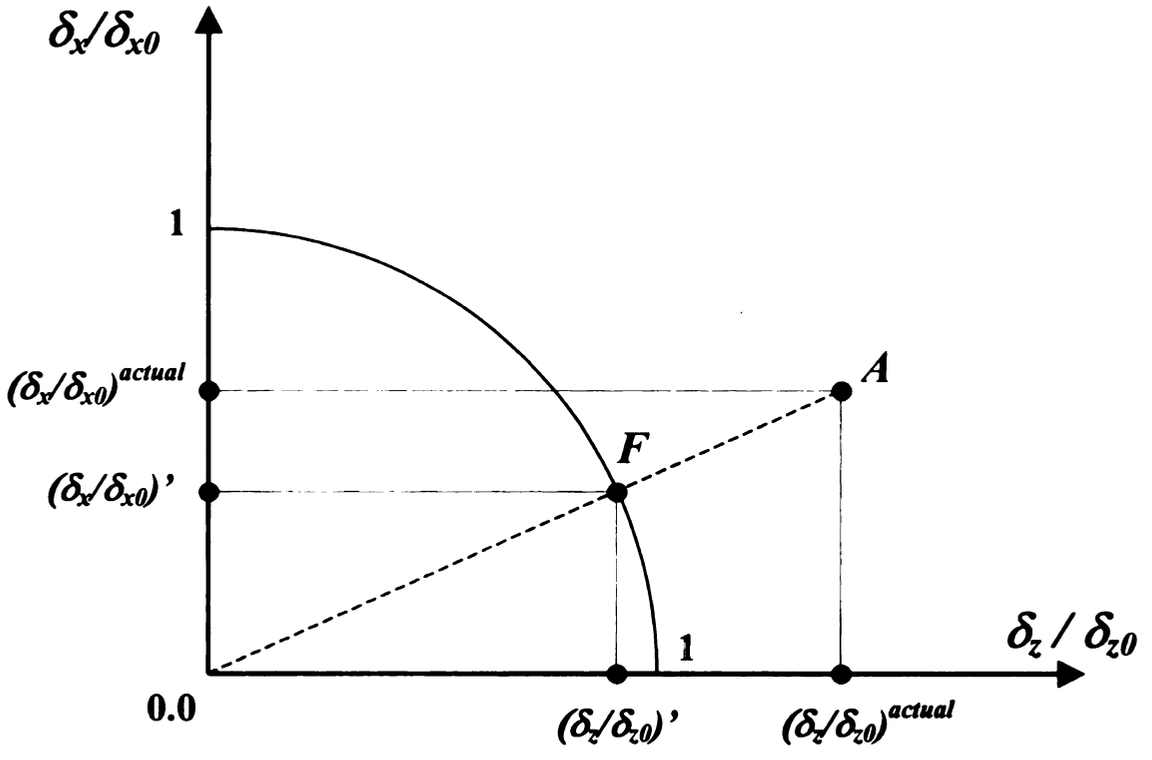

Figure 121. ***Graph δ_x/δ_{x0} versus δ_z/δ_{z0}.***

We assume that when (622) was satisfied first the ratio (623) was the same. If the load steps are small, the assumption holds. Then, from geometry, it is possible to determine the value of the relative displacements δ_x' and δ_z' in F (here the superscript *actual* is omitted).

$$\delta_x' = \delta_{x0} \frac{\left(\frac{\delta_x}{\delta_{x0}}\right)}{\sqrt{\left(\frac{\delta_z}{\delta_{z0}}\right)^2 + \left(\frac{\delta_x}{\delta_{x0}}\right)^2}} \tag{624}$$

$$\delta_z' = \delta_{z0} \frac{\left(\frac{\delta_z}{\delta_{z0}}\right)}{\sqrt{\left(\frac{\delta_z}{\delta_{z0}}\right)^2 + \left(\frac{\delta_x}{\delta_{x0}}\right)^2}} \tag{625}$$

The interfacial constitutive models need to be updated for both delamination modes I and II setting $\delta_{x0}' = \delta_x'$ and $\delta_{z0}' = \delta_z'$, see Figures 122 and 123.

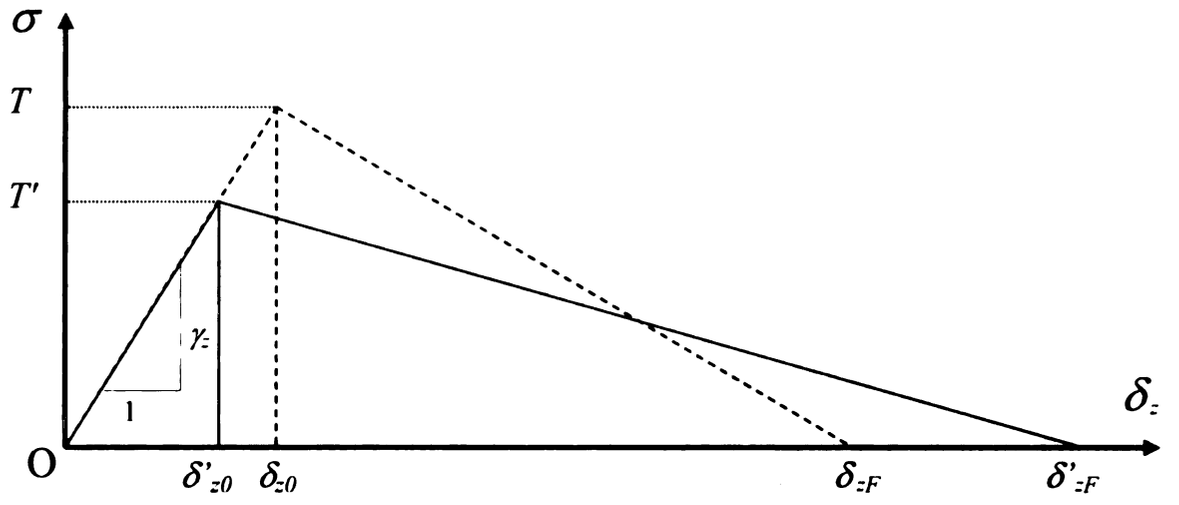

Figure 122. ***Updated interfacial constitutive model for mode I delamination***

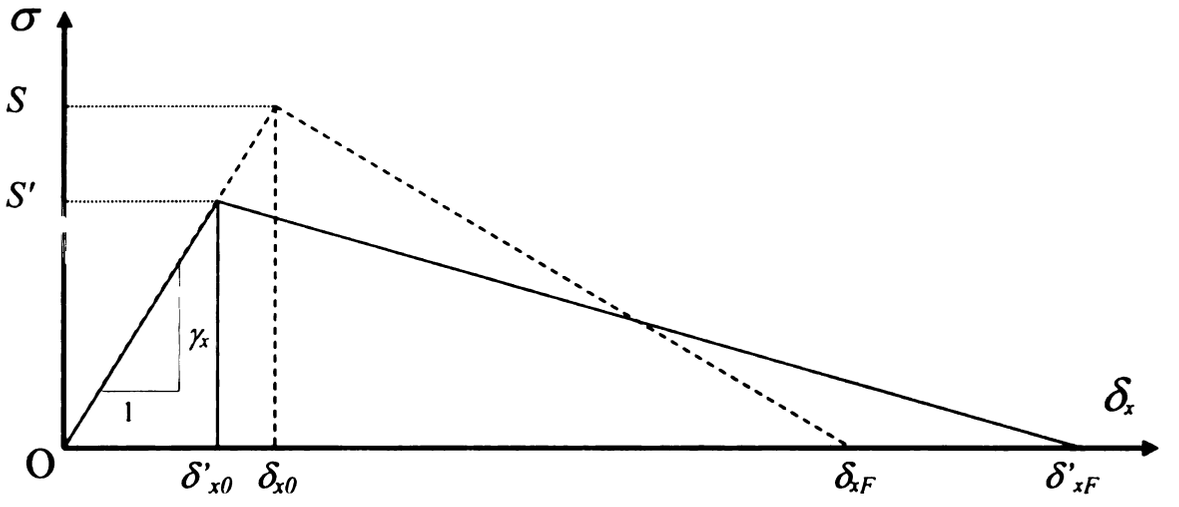

Figure 123. ***Updated interfacial constitutive model for mode II delamination***

The interlayer tensile strengths T and S are updated accordingly:

$$T' = \gamma_z \cdot \delta'_{z0} \tag{626}$$

$$S' = \gamma_x \cdot \delta'_{x0} \tag{627}$$

Note that the following inequalities hold.

$$\delta'_{x0} \le \delta_{x0} \ , \quad \delta'_{z0} \le \delta_{z0} \ , \ \delta_x \ge \delta'_{x0} \ , \quad \delta_z \ge \delta'_{z0} \tag{628}$$

However, the modifications to the interfacial constitutive models do not end with change in the relative displacements at onset of damage. The quadratic interaction criterion predicts final failure to be reached when the following condition is verified:

$$\left(\frac{G_I}{G_{Ic}}\right)^2 + \left(\frac{G_{II}}{G_{IIc}}\right)^2 = 1 \tag{629}$$

In a similar way as we did with the failure criterion, we assume the ratio between $(G_{II}/G_{IIc})^{actual}$ and $(G_I/G_{Ic})^{actual}$ not to vary as the work of separation growth, Figure 124. The point representing the actual situation of the system A, calculated using the strain energy release rate at the current increment, will be inside the domain defined by the quadratic interaction criterion. If not, the interval is totally failed. We assume that when (629) is satisfied the following ratio:

$$\frac{\left(\frac{G_{II}}{G_{IIc}}\right)}{\left(\frac{G_I}{G_{Ic}}\right)} = C_2 \tag{630}$$

will be unchanged. Research on the specimens commonly used for delamination studies shows that for a given configuration (geometry and loads) the ratio between the strain energy release rates for modes I and II, G_I/G_{II}, do not change much during the entire test [56]. This fact provides a valid foundation to our assumption, in particular since the

equation (630) must hold only for the very limited advancement of the crack related to the failure of the portion of the interface element under consideration. Thus, it is possible to determine the value of the strain energy release rate G_I' and G_{II}' in F.

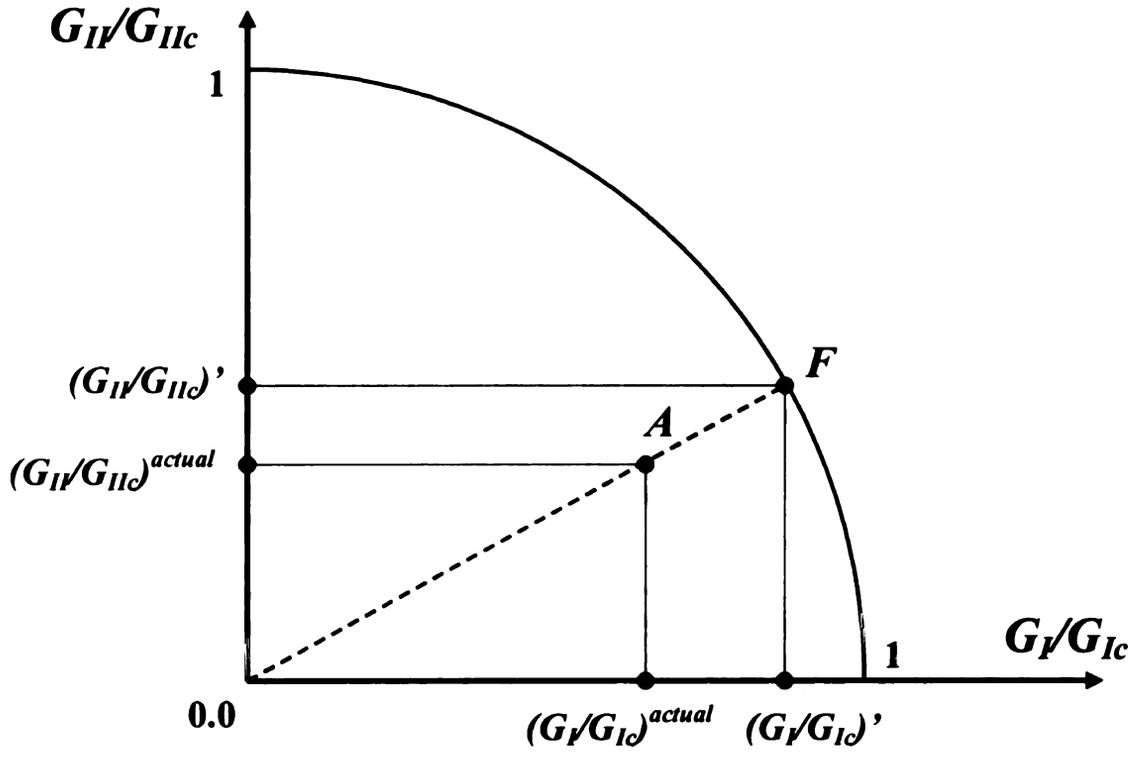

Figure 124. ***Graph G_{II}/G_{IIc} versus G_I/G_{Ic}.***

From geometry it is possible to determine the value of the $(G_I/G_{Ic})'$ in F (here the superscript *actual* is omitted).

$$G_I' = G_{Ic} \frac{\left(\frac{G_I}{G_{Ic}}\right)}{\sqrt{\left(\frac{G_I}{G_{Ic}}\right)^2 + \left(\frac{G_{II}}{G_{IIc}}\right)^2}} \tag{631}$$

In order to evaluate this expression we need to determine (G_I/G_{Ic}), (actual value of G_I divided by G_{Ic}), see Figure 125.

$$G_{Ic} = \frac{T' \cdot \delta'_{zF}}{2} = \frac{\delta'_{z0} \cdot \gamma_z \cdot \delta'_{zF}}{2} \tag{632}$$

$$G_I = G_{Ic} - (\text{Area Triangle } OBK) = \frac{\delta'_{z0} \cdot \gamma_z \cdot \delta'_{zF}}{2} - \frac{[\delta_z(1-D_z)\gamma_z] \cdot \delta'_{zF}}{2} \tag{633}$$

$$\left(\frac{G_I}{G_{Ic}}\right) = \frac{\frac{\delta'_{z0} \cdot \gamma_z \cdot \delta'_{zF}}{2} - \frac{[\delta_z(1-D_z)\gamma_z] \cdot \delta'_{zF}}{2}}{\frac{\delta'_{z0} \cdot \gamma_z \cdot \delta'_{zF}}{2}} = 1 - \frac{\delta_z}{\delta'_{z0}}(1-D_z) \tag{634}$$

With the same methodology, G'_{II} can be computed.

Now, the changes to the interfacial constitutive models can be completed for both delamination modes I and II setting $G'_{Ic} = G'_I$ and $G'_{IIc} = G'_{II}$. Figure 125 and 126 shows the final form of the interfacial constitutive models. As it can be noticed, the models have different penalty and damage parameters. In such a way, the maximum freedom is allowed for modeling modes I and II delamination.

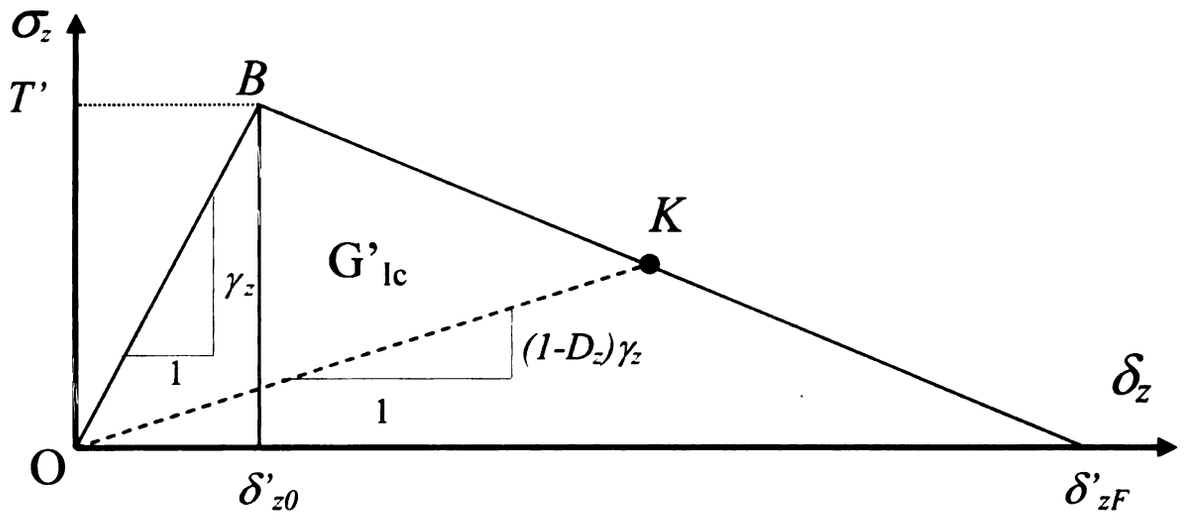

Figure 125. ***Final interfacial constitutive model for mode I delamination***

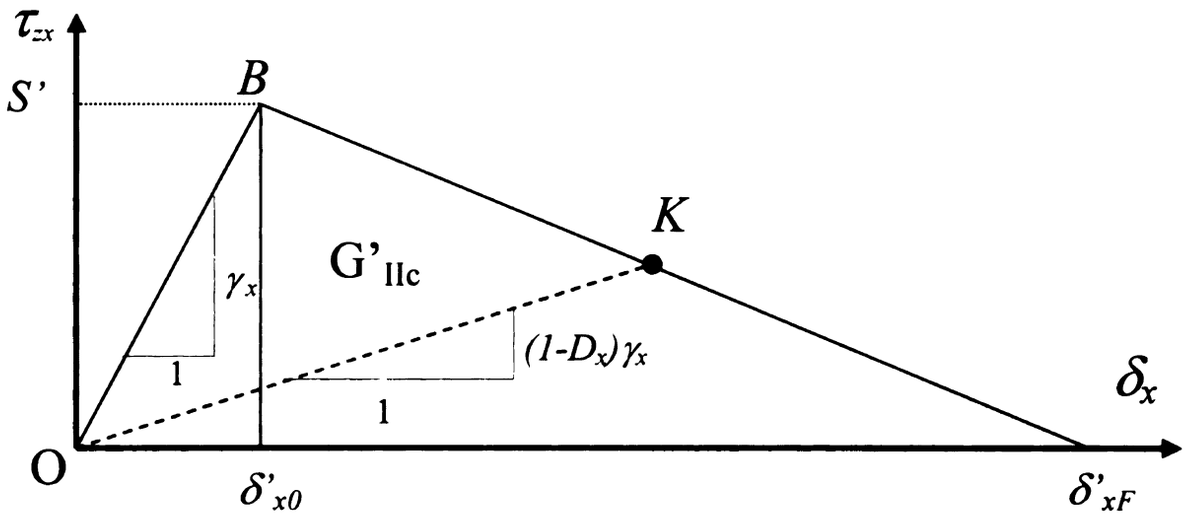

Figure 126. ***Final interfacial constitutive model for mode II delamination***

8.3 Energetic Approach for a Correct Distribution of Stress

Initial numerical testing on the developed damage technique produced very good results for mode II delamination, but prediction of mode I behavior was sometimes inaccurate. In order to identify the causes of the problem, linear elastic fracture mechanics prediction of the stress distribution near the crack tip was compared to the one obtained with the interface model [49, 50, 91, 92].

Geometry and loads for the mode I case are shown in Figure 127(a), while original and deformed meshes of the finite element model are shown in Figure 127(b). The material has Young's modulus 1 MPa and the thickness is 1 mm. Two meshes compose the finite element model; they are joined by one interface elements of 16 nodes along the expected crack growth path. Clearly the two meshes are compatible in this case. Normal stress σ_{yy} is obtained along the interface taking advantage of the peculiar abilities of the interface element in recovering the forces at the interface.

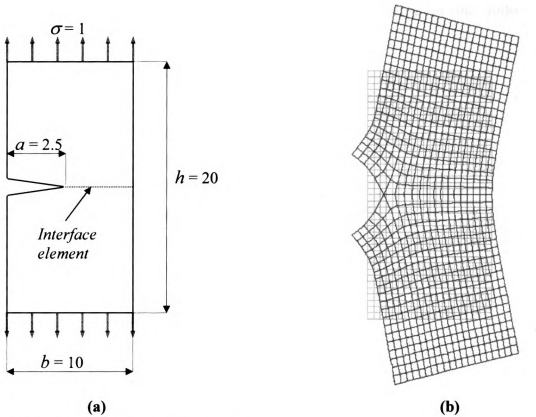

Figure 127. ***Fracture mechanics model.***

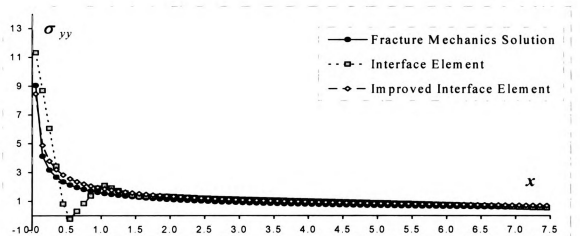

Figure 128. ***Normal stress distribution along the entire interface.***

Figure 128 shows the stress distribution along the entire interface. Stress values in the two graphs are reported in a discrete form, they are averaged at the center of the 75 intervals in which the interface element is divided.

The fracture mechanics solution is computed according to the following equations:

$$\sigma_{yy}(K,\theta,s)=\frac{K}{\sqrt{2\pi s}}\left[1+\sin\left(\frac{\theta}{2}\right)\sin\left(\frac{3\theta}{2}\right)\right]\cos\left(\frac{\theta}{2}\right) \tag{635}$$

$$K=f_1(2.5,10)\cdot\sqrt{(2.5\pi)} \tag{636}$$

$$\begin{aligned} f_1(a,b)=1.122-0.231\left(\frac{a}{b}\right)+10.550\left(\frac{a}{b}\right)^2 \\ -27.710\left(\frac{a}{b}\right)^3+30.382\left(\frac{a}{b}\right)^4 \end{aligned} \tag{637}$$

$$\sigma_i(x_1,x_2)=\frac{\int_{x_1}^{x_2}\sigma_{yy}(K,0,s)dr}{x_2-x_1} \tag{638}$$

Where σ_i is the average value of the stress σ_{yy} inside one interval. If we observe the stress distribution predicted by the Interface Element model, it is easy to notice an abnormal behavior near the crack tip. This behavior can be explained if we remember that in the adopted penalty method the continuity constraint is not enforced exactly. Instead, the integral of the square of the relative displacement must be a very small number. The inaccuracy observed in Figure 128 occurs only when very strong gradient of stresses are present at the interface. Mesh refinement would improve and eventually correct the results, but it is preferred that the model behave correctly for every possible discretization of the domain, especially since the accuracy of the delamination model strongly depends on a precise calculation of the stress and displacement distributions at the crack tip.

The approach for overcoming the problem came from energetic consideration: it is possible to relate the fracture mechanics stress distribution to the interface model

solution by imposing that they must contribute equally to the total potential energy of the system. The energy associated with the continuity constraint imposed by the penalty parameter, can be expressed also in the following form:

$$E(\delta) = \frac{1}{2}\gamma \int_0^L \delta^2 ds \tag{639}$$

where δ is the relative displacement of the connected interfaces and is a function of the position along the interface $\delta = [u_2(s) - u_1(s)] = \delta(s)$. Fracture mechanics predicts, both for Mode I and Mode II opening, the stress to vary near the crack tip according to an expression of the type:

$$\sigma = \sigma(s, K, \theta) \tag{640}$$

For a given geometry and load applied to the system K does not change. Moreover, along the interface $\theta = 0$. It follows:

$$\sigma(s) = \frac{C_1}{\sqrt{s}} \tag{641}$$

For an isotropic material, where s is the distance from the crack tip and C_1 is a constant.

In the penalty interface element approach, the stress at any location is a direct function of the penalty parameter and the relative displacement δ:

$$\sigma(\gamma, \delta) = C_2 \cdot \gamma\delta \tag{642}$$

where C_2 is a constant. Now, we want replace the $\delta(s)$ distribution obtained from the finite element model with a new one, $\delta'(s)$, such that:

$$E(\delta) = E(\delta') \tag{643}$$

If we choose $\delta'(s)$ to be:

$$\delta'(s) = \frac{C_3}{\sqrt{s}} \tag{644}$$

It follows:

$$\sigma(s) = \frac{C_4}{\sqrt{s}} \tag{645}$$

This means that the stress would vary along the interface according to the fracture mechanics predictions. The constant C_3, in the expression for $\delta'(s)$, is computed by imposing the energetic constraint: $E(\delta) = E(\delta')$.

$$E(\delta) = \frac{1}{2}\gamma \int_{s_1}^{s_2} (\delta')^2 \, ds \tag{646}$$

$$E(\delta) = \frac{1}{2}\gamma \int_{s_1}^{s_2} \frac{C_3^2}{s} ds = \frac{1}{2}\gamma C_3^2 \left[\ln s_2 - \ln s_1\right] \tag{647}$$

$E(\delta)$ is a known quantity that is computed once $\delta(s)$ is obtained from the finite element solution. The resulting improved stress distribution is plotted in Figures 128.

This energetic approach for obtaining a correct distribution of stress near the crack tip is used only when the abnormal behavior is present and only for mode I delamination. An algorithm has been implemented in the code able to detect when a wrong stress distribution is present and automatically switch from the normal approach to the modified approach.

In order to identify possible limits of the approach in its applicability to composite materials, the literature on the stress distribution near the crack tip when the materials of the connected meshes are different has been explored [93-97].

It has been found [97] that the change in the stress intensity factor for mode I with a variation of the Young's modulus of the two materials is very limited. Even with a ratio

E_1/E_2=70, where 1 and 2 marks the two different materials, the change in K_I is less than 10%.

In 2001 Alfano and Crisfield [70] have done a parametric study on the influence of the tensile strength σ_t of the interface on the accuracy of the delamination growth prediction. The damage model they implemented in their interface element is the same as the one used by the present approach, the bilinear softening model previously described. They found that as long as the softening behavior is obtained relating the work of separation to the critical value of the energy release rate, moderate changes in σ_t don't affect the results.

Finally, a parametric study on our interface element has been performed. The exponent β of the s, distance from the crack tip, in equations (641), (644) and (645) has been varied. The simulation of delamination growth for a DCB specimen, whose experimental results are in good agreement with our model for β = -1/2, has been done with β = -1/4 and β = -3/4 (according to [94], $0<\beta<-1$). The load-displacement curves obtained with the different values of β, didn't differ from the outcome for β = -1/2.

The limited influence of the ratio E_1/E_2 on the stress intensity factor for mode I, plus the lack of need in getting a completely exact stress distribution, plus the scarce variation of the results with β; lead us to conclude that in the rare cases when the abnormal stress distribution is present and the materials at the interface are different, the proposed energetic approach should still be able to yield correct results.

8.4 Friction Model

8.4.1 Evaluation of the force at the interface

For the 1-D case, Timoshenko beam element, a known relation between the Lagrange multipliers and the penalty parameters can be used to evaluate force at the interface. If the constraint C_1 that has been enforced is:

$$C_1(u_1, u_2, v) = (v - u_1) \tag{648}$$

Defining $u_{1\gamma}, u_{2\gamma}, v_\gamma$ as the solutions derived from the penalty formulation, it is possible to verify that the Lagrange multiplier is related to the penalty parameter in the following way:

$$\lambda_1 = \gamma_1 \cdot C_1(u_{1\gamma}, u_{2\gamma}, v_\gamma) = \gamma_1 \cdot (v_\gamma - u_{1\gamma}) \tag{649}$$

Since the values of the Lagrange multipliers correspond to the force required to hold the two nodes together, the force at the interface can be easily calculated:

$$F_1 = \gamma_1 \cdot C_1(u_{1\gamma}, v_\gamma) = \gamma_1 \cdot (v_\gamma - u_{1\gamma})$$

For 2-dimensional elements, like 2D quadrilaterals and plates, the interface force is still simple to compute, but the relation between Lagrange multipliers and the penalty parameters need to be updated. In this case the term added to the Total Potential Energy of the system is:

$$\frac{1}{2}\gamma \int_s (v - u)^2 \, ds \tag{650}$$

Where u and v are not nodal displacements, but displacements fields functions of s. As a consequence of this difference the Lagrange multiplier is now related to the penalty parameter by:

$$F = \lambda = \gamma \cdot \int_s (v-u)\,ds \tag{651}$$

A very simple verification of this relation is given. A 2D problem, analogous to that of section 3.1, has been analyzed in section 4.4.1. A rectangular plane stress element clamped to a fixed penalty frame along one side is loaded on the other with a uniform axial load F, Figure 17. The interface points V_1, V_2, V_3 are fixed, so their displacements v_1, v_2, v_3 are equal to zero. The solution derived by the finite element analysis for the displacements of the nodes of the element on the interface is:

$$u_9,\ u_{11} = \frac{F}{b\gamma_1} \tag{652}$$

The integration required to compute the desired relation is expressed by:

$$\begin{aligned}
&\int_0^b (v-u)\,dy = \\
&\int_0^{\frac{b}{2}} \left\{ \left[T_1^1(y)v_1 + T_2^1(y)v_2 + T_3^1(y)v_3 \right] - \left[N_1(y)u_9 + N_2(y)u_{11} \right] \right\} dy + \\
&\int_{\frac{b}{2}}^b \left\{ \left[T_1^2(y)v_1 + T_2^2(y)v_2 + T_3^2(y)v_3 \right] - \left[N_1(y)u_9 + N_2(y)u_{11} \right] \right\} dy
\end{aligned} \tag{653}$$

Where T_j^k are the natural cubic spline interpolations functions of section 4.2.2, with the index *k* marking the first and second groups of functions valid, respectively, for the first and second intervals.

The result of this integration is expressed by:

$$\frac{3bv_1}{16} + \frac{5bv_2}{8} + \frac{3bv_3}{16} - \frac{bu_9}{2} - \frac{bu_{11}}{2} \tag{654}$$

Substituting the achieved results in the relation for λ it follows:

$$\lambda = \gamma \cdot \int_s (v-u)\,ds = \gamma \cdot \left(-\frac{b}{2} \cdot \frac{F}{b\gamma} - \frac{b}{2} \cdot \frac{F}{b\gamma} \right) = -F \tag{655}$$

As predicted the correct value of the interface force is obtained.

It is important to notice that we are not restricted to compute the force on the entire interface, but it can be evaluated for a portion of the interface length too. This can be performed by changing the extreme values of the interval of integration.

Finally, computation of the interface force does not depend on the compatibility of the interface meshes. Even if the discretizations of the adjacent layers, or layer and skin-stiffener, are different we are still able to choose liberally the interface length along which to evaluate forces.

8.4.2 Implementation of a Friction Model

The friction model can be applied to interface elements after complete failure or to interface elements whose only purpose is to avoid overlapping and enforce friction.

For each of the intervals in which the interface is divided, the normal force at the interface F_n can be calculated given the normal relative displacement δ_n :

$$F_n = \frac{1}{2}\gamma_n \int_s \delta_n ds \tag{656}$$

The tangential force F_t that the interface element needs to generate to simulate the friction phenomenon is:

$$F_t = \frac{1}{2}\gamma_t (1 - D_t) \int_s \delta_t ds = \mu F_n \tag{657}$$

Where μ is the friction coefficient and δ_t is the tangential relative displacement. The parameter D_t that before failure was used as a damage parameter, is now employed as a scale factor able to reduce the value of the penalty parameter for the tangential DOF.

Assuming the value of D_t that makes the equality (657) to hold true, the right amount of friction will be generated by the interface element.

The required damage parameter D_t^* related to the tangential relative displacement δ_t can be determined from the following relation:

$$D_t^* = 1 - \frac{2\mu F_n}{\gamma_t \int_s \delta_t ds} \tag{658}$$

8.4.3 Numerical Test for the Friction Model

A simple test has been performed to verify the reliability and the accuracy of the friction model implemented into the interface element.

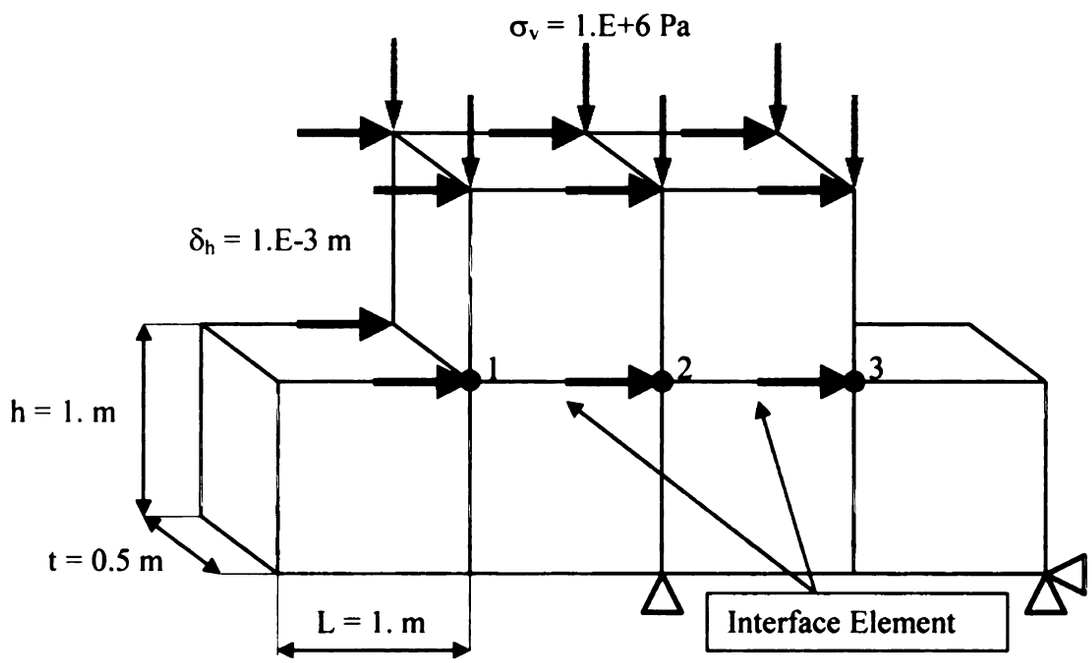

Figure 129. ***Boundary conditions and the geometry of the test for the friction model***

The loading, the boundary conditions and the geometry for the test problem are illustrated in Figure 129. Two finite element meshes are connected along the common boundary using one interface element. All the finite elements are rigid. The drawing is

three-dimensional for clarity, but the FE analysis was performed with a 2D mesh having the indicated thickness.

During a quasi-static analysis of 400 load increments, a 1mm tangential displacement is gradually imposed to the nodes of the upper mesh. At the same time, a pressure load of 1 MPa is applied to the top the upper mesh and is kept constant through the entire analysis. According to the Coulomb law $F_t = \mu \cdot N$, since a coefficient of friction equal to $\mu = 0.1$ is assumed and the contact area is 1 m^2, as outcome is expected a total reaction force at the interface nodes of:

$$F_t = \mu F_n = \mu \sigma A = 0.1 \cdot 1.e6 \frac{N}{m^2} \cdot 1.m^2 = 1.e5N \tag{659}$$

In Figure 130 is reported the reaction forces versus the tangential displacement produced by the FE analysis for the interface nodes 1, 2 and 3.

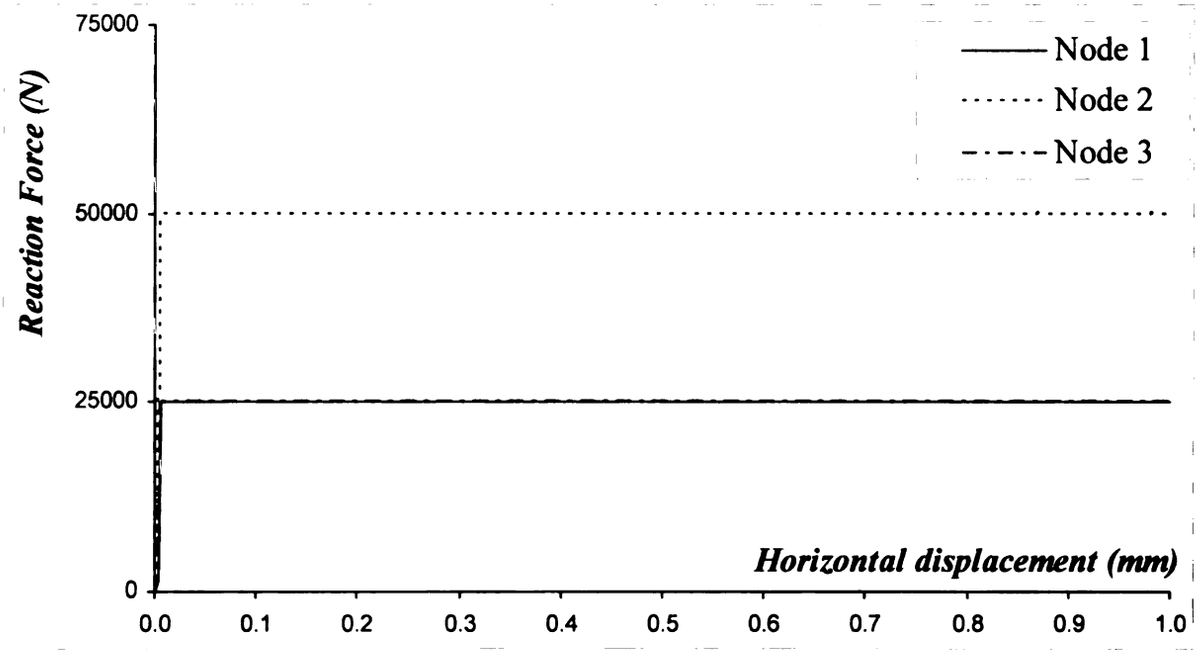

Figure 130. ***Test Friction – Graph Force-Displacements.***

For each of the 400 increments in the displacement value, the reaction force at the central node is recorded to be a constant value of 0.5e5 N while on the other two nodes a

constant value of 0.25e5 N is obtained.

The outcomes of this simple test, being accurate and constant through time, confirm the robustness of the adopted friction model.

8.5 Numerical Results

Results for two different double cantilever beam DCB specimens, one end-loaded split (ELS) specimen and one Fixed-Ratio Mixed Mode (FRMM) specimen are presented. These results are compared to measured data to assess the ability of the present damage model to simulate delamination growth.

8.5.1 Double Cantilever Beam Test #1

The loading, the boundary conditions and the geometry for the double cantilever beam DCB specimen are illustrated in Figure 131. The DCB test is recognized as an accurate pure mode I test. The properties assumed for the beam material are: E_{11}=130 Gpa, E_{22}= E_{33} = 8 Gpa, G_{12} = 6 Gpa, ν= 0.27. The properties of the DCB specimen interface are: G_{Ic} = 257 N/m and σ_t = 48 Mpa.

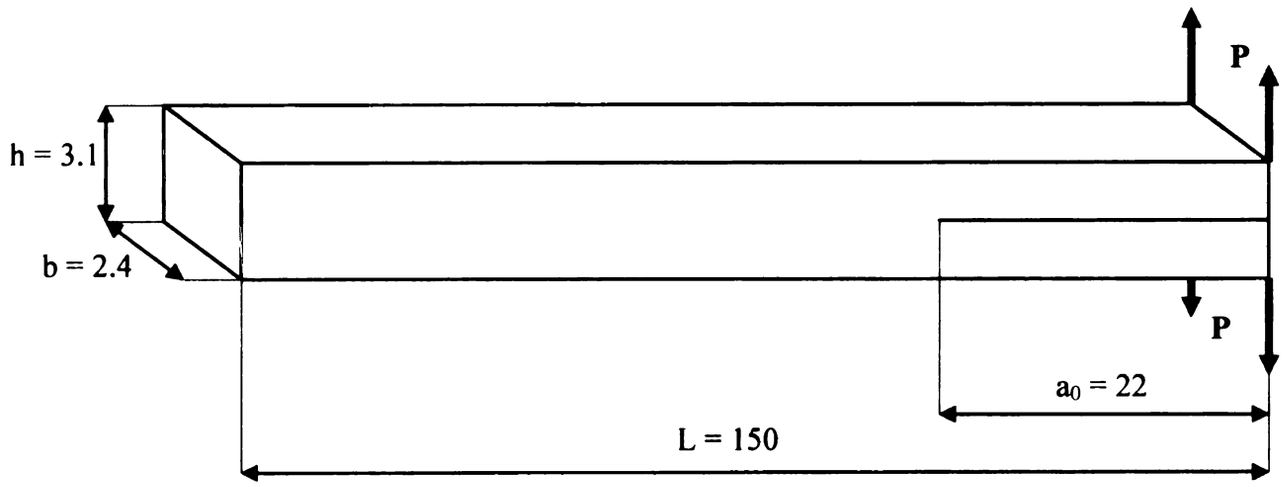

Figure 131. ***Geometry and boundary conditions for the DCB test specimen.***

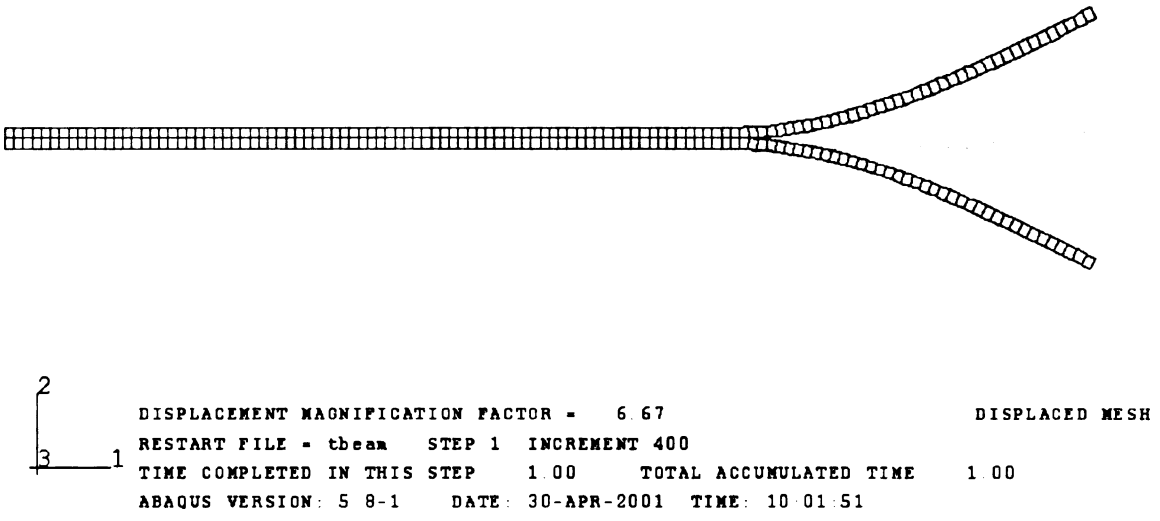

Figure 132. ***Original and deformed (5mm opening) models of the DCB test specimen using a 120x2 mesh.***

Three finite element models of varying mesh refinement have been used to verify the capabilities of the present approach. In Figure 132, original and deformed models of the DCB test specimen are shown for the coarsest mesh. Two independent meshes compose the finite element models of the upper and lower part of the beam; they are joined by several interface elements. Each interface element connects eight finite elements: four on the bottom mesh and four on the top. Experimental results used to validate the present delamination approach have been reported by Chen and colleagues [69]. A plot of the reaction force as a function of the applied end displacement is shown in Figure 133. Results from the experiment are compared to analytical ones for all the finite element models: a) mesh 120x2, b) mesh 300x8, c) mesh 600x8.

Note that the total number of elements in the meshes is indicated, for example two 120x1 meshes joined by interface elements compose the 120x2 mesh. The outcomes from 120x2 mesh present many local "bumps". Mi, Crisfield, Davies and Hellweg [68] have analyzed this phenomenon, concluding that coarse meshes can induce these "false

instabilities". As the mesh is refined, the predicted response agrees very well with that measured experimentally. As discussed previously, the damage technique implemented in our model allows portions of the interface, intervals, much smaller than the finite element length to be released.

In Figure 134 convergence of the solution with the number of intervals is investigated for the 300x8 mesh. It can be noticed that as the number of intervals increases the accuracy of the results raise. Figure 135 illustrates the model behavior as function of the number of increments for the 300x8 mesh. Convergence of the solution to the experimental one increasing number of intervals is achieved.

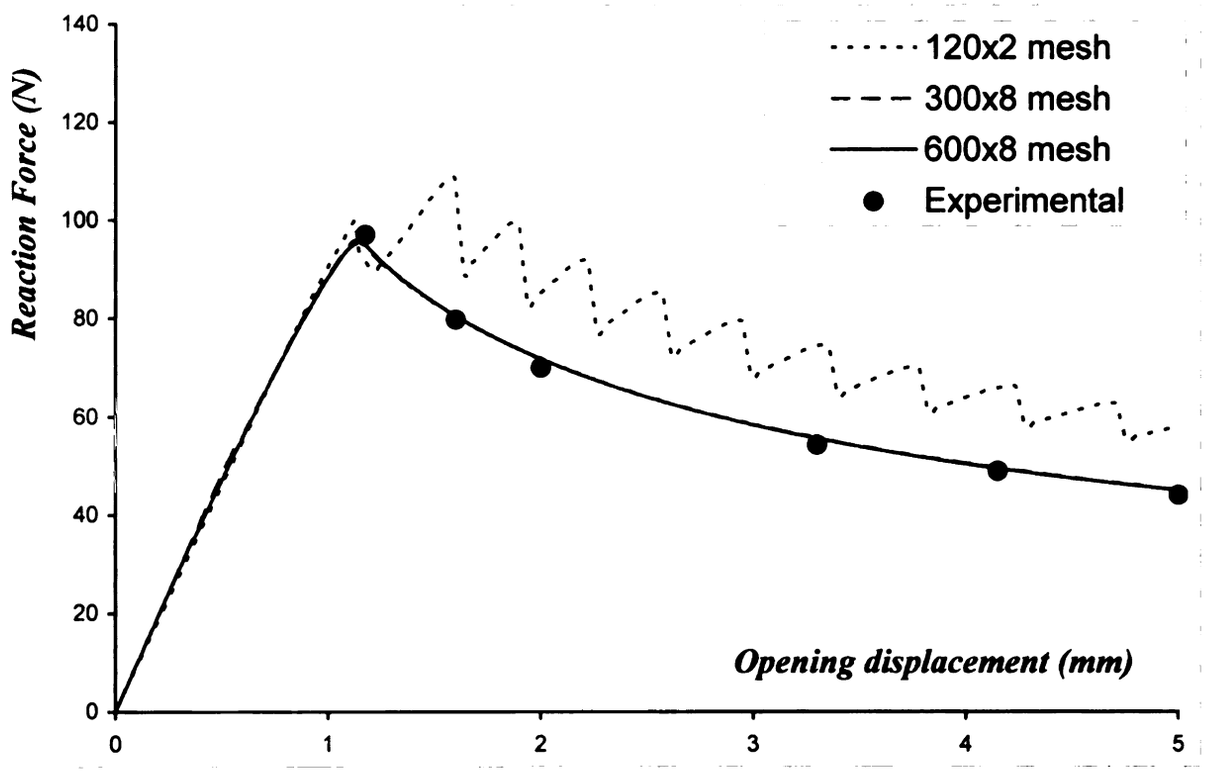

Figure 133. ***Force vs. displacement results of experimental and numerical DCB test***

Reaction Force (N)

Fig

F

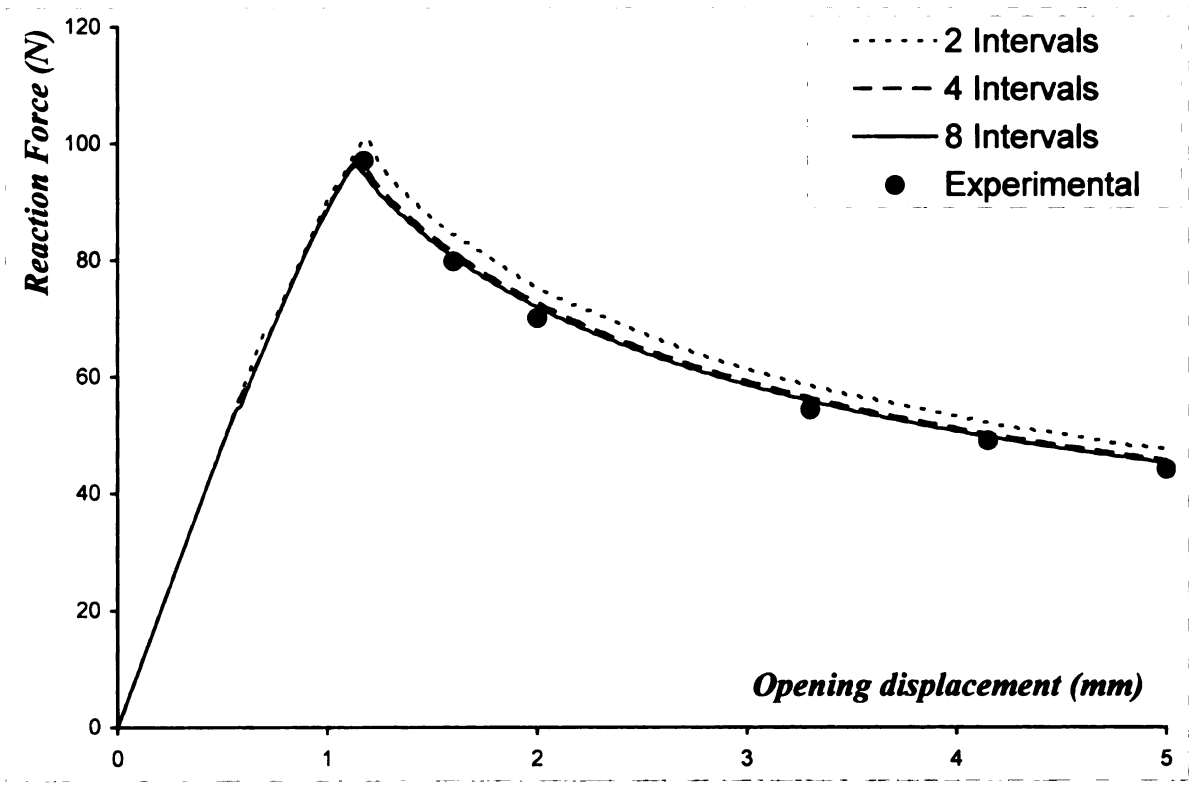

Figure 134. ***Force vs. displacement results of DCB test. Convergence of the solution with intervals number. Mesh 300x8.***

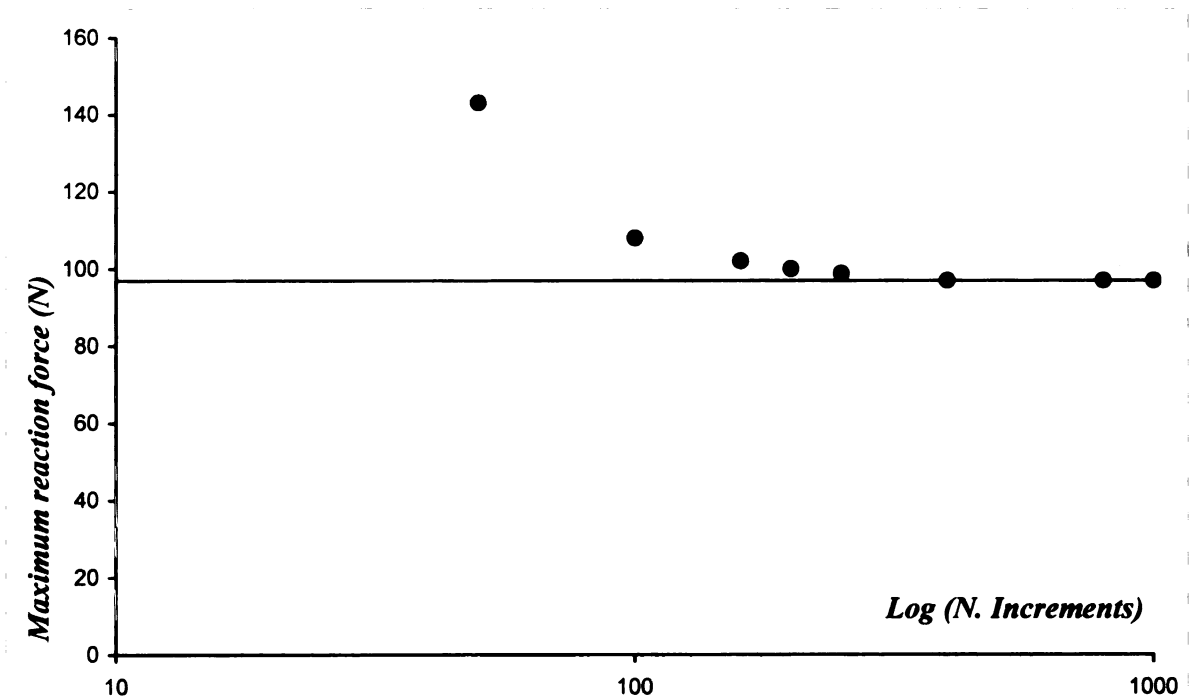

Figure 135. ***Convergence of the solution with the number of increments. Mesh 300x8.***

8.5.

grow

perf

h =

Fig

res

the

as

v =

M

in

el

8.5.2 Double Cantilever Beam Test #2

To further verify the ability of the interface in accurately simulate delamination growth in composite materials, a second double cantilever beam DCB test was performed.

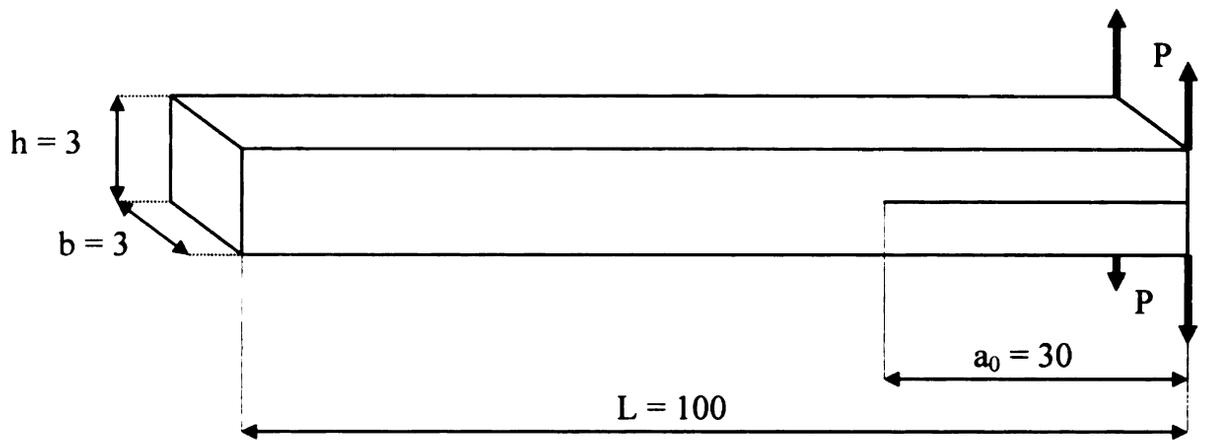

Figure 136. ***Geometry and boundary conditions for the DCB test #2***

Material data and experimental results are taken from a different source [70] with respect to the first DCB test. The loading, the boundary conditions and the geometry for the double cantilever beam DCB specimen are illustrated in Figure 136.

The DCB test is recognized as an accurate pure mode I test. The properties assumed for the beam material are: E_{11}=126 Gpa, E_{22}=E_{33}=7.5 Gpa, G_{12}=4.981 Gpa, ν=0.281. The properties of the DCB specimen interface are: G_{Ic} = 263 N/m and σ_t = 57 Mpa.

A plot of the reaction force as a function of the applied end displacement is shown in Figure 137. A comparison of the experimental results with those from the finite element simulation further asses the robustness of the implemented delamination model.

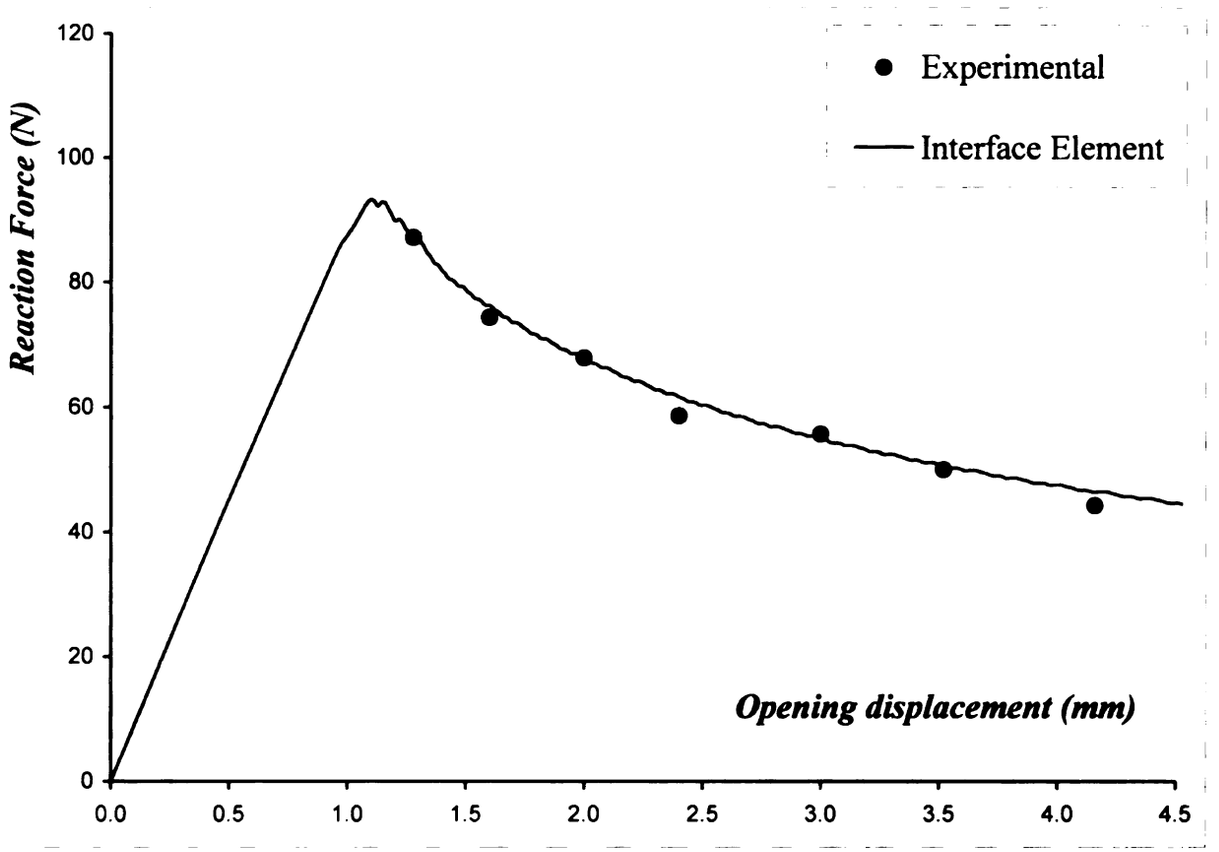

Figure 137. ***Force versus displacement results of experimental and numerical DCB test #2***

8.5.3 End-Loaded Split (ELS) Beam Test

To characterize the mode II delamination, shearing mode, the end-loaded split (ELS) specimen is often used. The loading, the boundary conditions and the geometry for the end-loaded split (ELS) specimen are illustrated in Figure 138.

The properties assumed for the beam material are: E_{11}=130 Gpa, E_{22}= E_{33} = 8 Gpa, G_{12} = 6 Gpa, ν= 0.27. The properties of the ELS specimen interface are: G_{IIc} = 856 N/m and σ_t = 48 Mpa. As in the DCB test specimen models, two meshes compose the finite element models of the ELS specimen; they are joined by several interface elements. For the results shown, a 300x8 finite element mesh has been utilized.

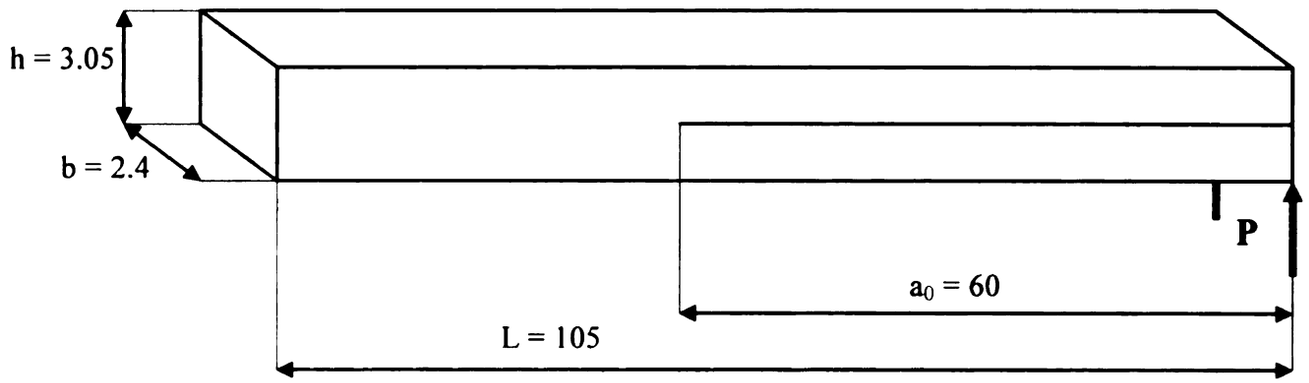

Figure 138. ***Geometry and boundary conditions for the ELS test specimen.***

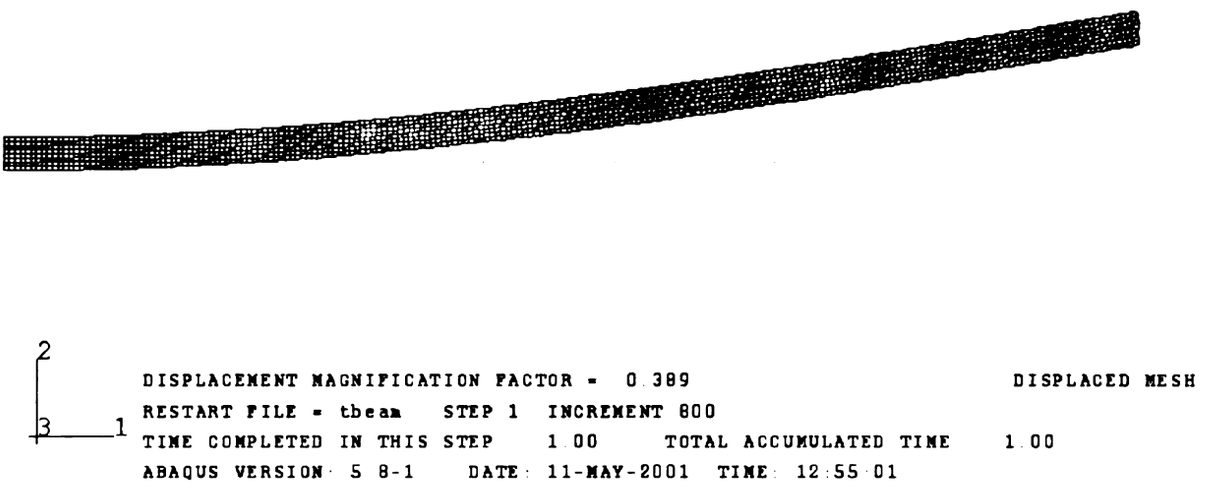

Figure 139. ***Original and deformed (30mm tip displacement) models of the ELS test specimen for a 300x8 mesh.***

In Figure 139, original and deformed models of the ELS test specimen are shown. Experimental results used to validate the present delamination approach have been reported by Chen and colleagues [69]. A plot of the reaction force as function of the applied end displacement is shown in Figure 140. Convergence of the solution as the number of increments increases is demonstrated. These results indicate that the model is reliable and accurate.

Reaction Force (N)

Fig

8.

th

T

fo

sp

c

s

r

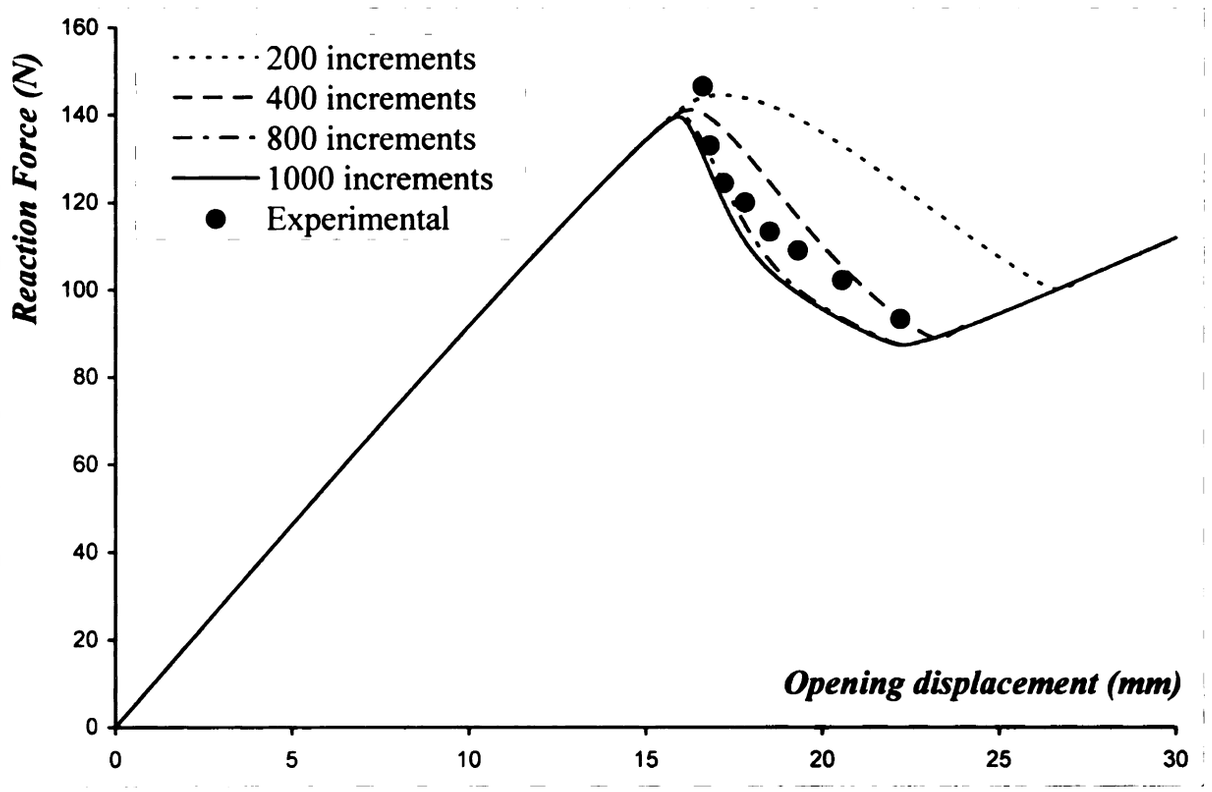

Figure 140. ***Force vs. displacement results of experimental and analytical ELS test for varying number of loading increments.***

8.5.4 End-Loaded Split (ELS) Beam Test – With Friction

Results from the end-loaded split (ELS) specimen test are satisfactory; however the model was not as accurate as in the case of the double cantilever beam DCB tests. This reduction in the quality of the prediction may be related to the absence of friction forces in the simulation. That is the reason why further testing as been done on the ELS specimen test taking into consideration friction forces. The loading, the boundary conditions, the geometry and the material properties are the same as in the previous ELS specimen test, the presence of friction being the only difference.

Initial FE analyses revealed a limited influence of the friction model on the results. A possible reason was identified in the presence of areas of highly concentrated

yet small normal forces at the end of beam where the load is applied and near the crack tip, while in between the normal force was zero. In these conditions the friction model might have been unable to produce the correct amount of friction force. Even if it is hard to say with certainty if the friction forces are really too small in this case to affect the results or if the model couldn't perform well under such conditions, we decided to try to apply a small pressure load on the upper part of the specimen in order to produce a larger contact area. The pressure load is applied approximately in the region indicated in Figure 141, and it is chosen very small, 6 N, so that it shouldn't affect directly the linear portion of the reaction force versus displacement graph.

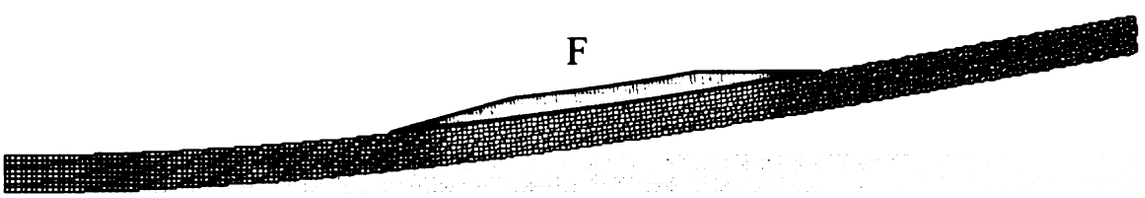

Figure 141. ***Original and deformed (30mm tip displacement) models of the ELS test specimen for a 300x8 mesh.***

Figure 142 shows that in the presence of friction forces, the prediction of the ELS specimen behavior agrees more closely to that observed in the experiments than when friction is ignored.

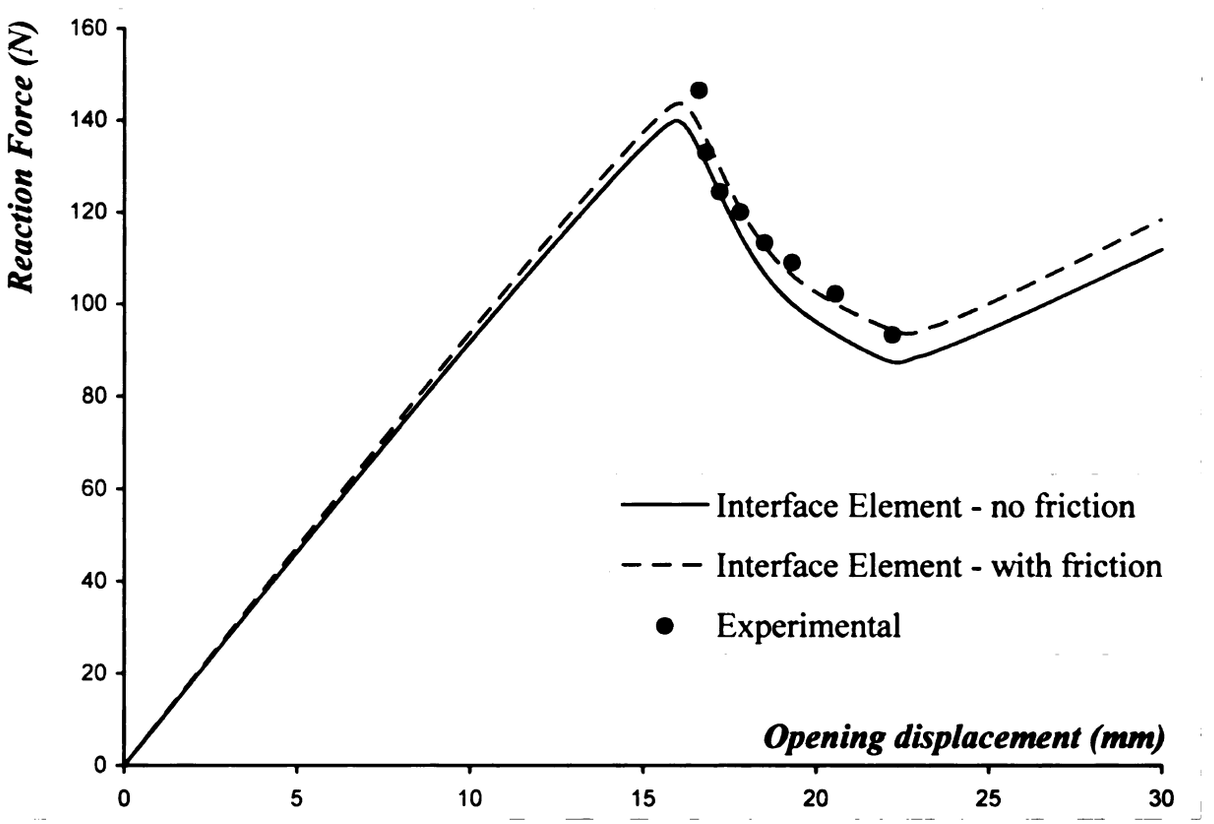

Figure 142. ***Force vs. displacement results of experimental and numerical ELS test in presence of friction.***

8.5.5 Fixed-Ratio Mixed Mode (FRMM) Test

To test the mixed mode I+II delamination capabilities of the interface model, the Fixed-Ratio Mixed Mode (FRMM) specimen has been considered. The loading, the boundary conditions and the geometry for the FRMM specimen are illustrated in Figure 143. The properties assumed for the beam material are: E_{11}=130 Gpa, E_{22}= E_{33} = 8 Gpa, G_{12} = 6 Gpa, ν= 0.27. The properties of the ELS specimen interface are: G_{Ic} = 257N/m, G_{IIc} = 856N/m and σ_t = 48 Mpa. As in the DCB and ELS test specimens models, two meshes compose the finite element models of the ELS specimen; they are joined by several interface elements. For the results shown, a 300x8 finite element mesh has been utilized.

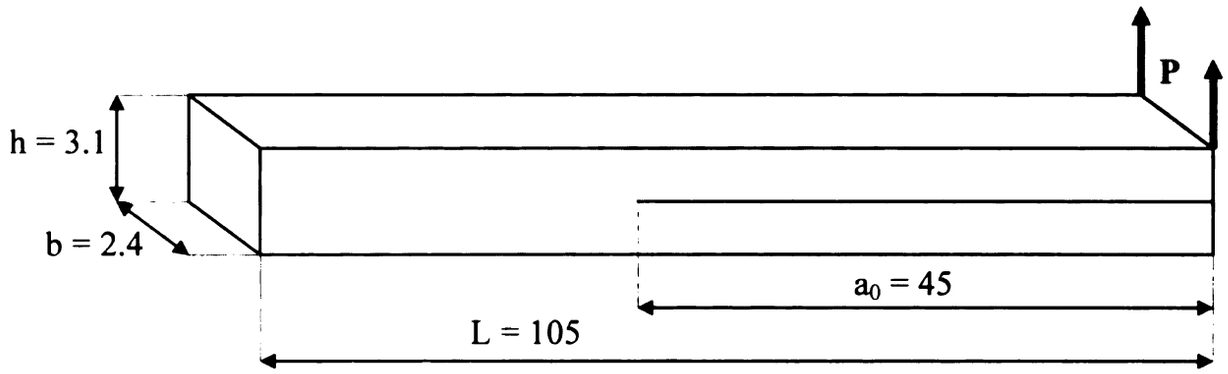

Figure 143. ***Geometry and boundary conditions for the FRMM test***

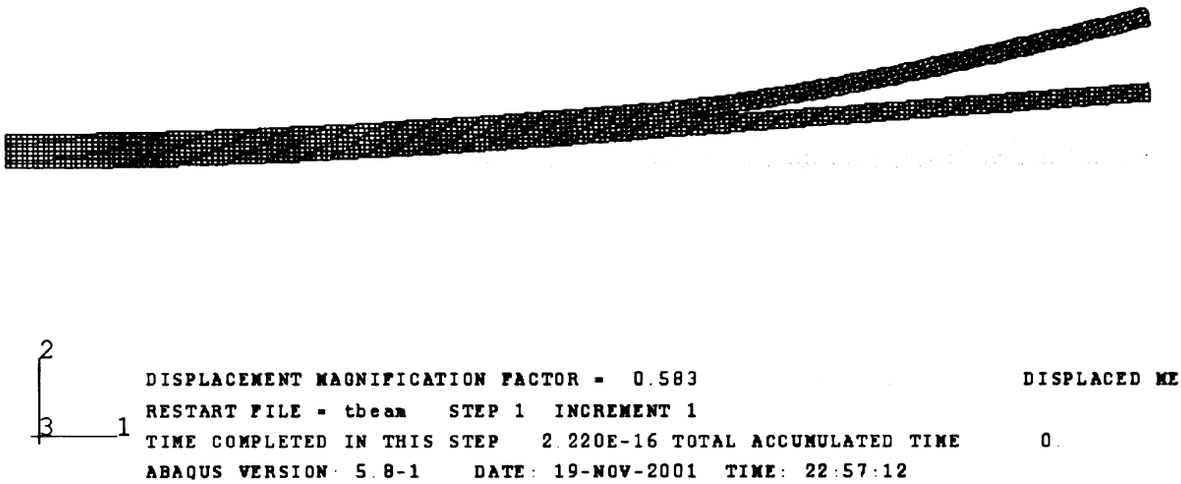

Figure 144. ***Original and deformed (20mm tip displacement in absence of delamination) models of the FRMM test specimen.***

In Figure 144, original and deformed models of the ELS test specimen are shown. Experimental results used to validate the present delamination approach have been reported by Chen and colleagues [69]. A plot of the reaction force as function of the applied end displacement is shown in Figure 145. Though the failure load is underpredicted, the overall results fit well with the experimental results, proving that the novel mixed mode damage model implemented in the interface element is able to correctly predict delamination growth in mixed mode FE simulation.

Reaction Force (N)

Fig

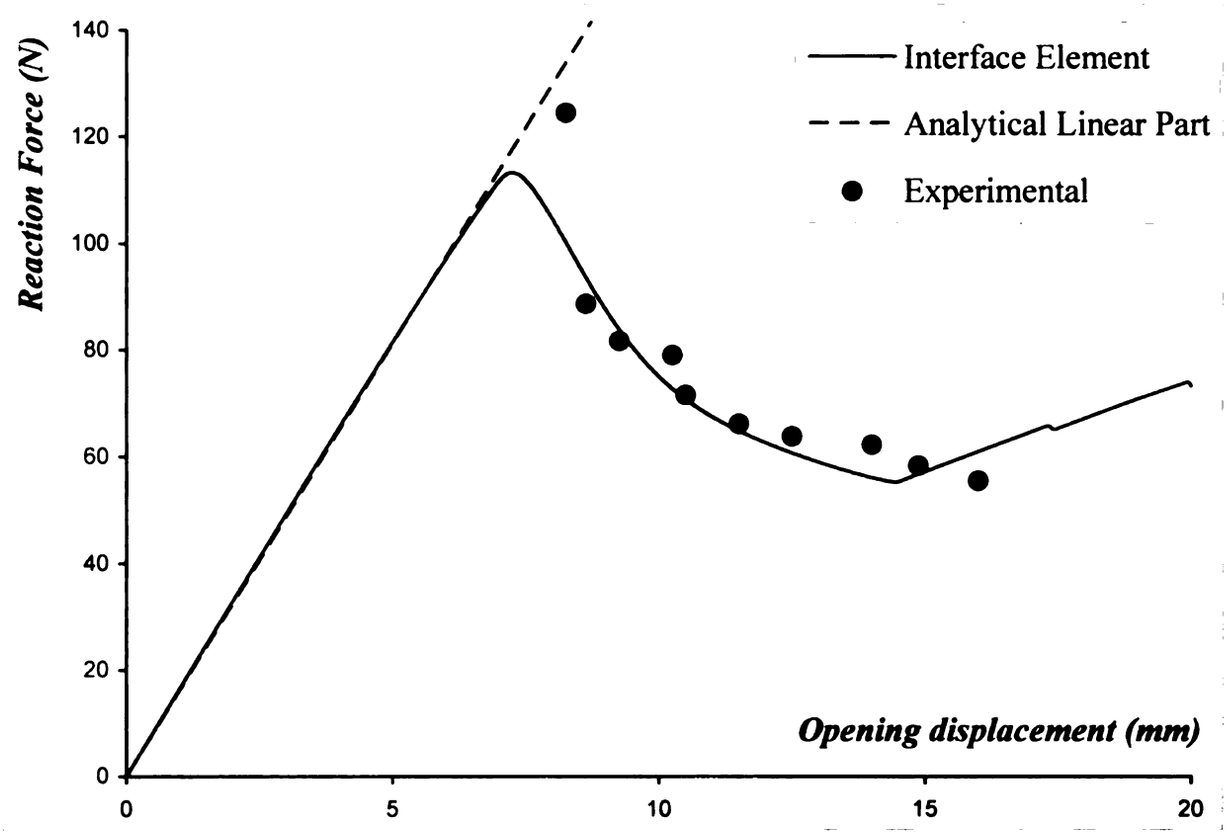

Figure 145. ***Force vs. displacement results of experimental and numerical FRMM test.***

CHAPTER 9 CONCLUSIONS

In the present work, an effective and robust interface element technology has been developed using the penalty method. This approach overcomes the numerical difficulties associated with the existing methods based on Lagrange multipliers. Additionally, the present formulation leads to a computational approach that is very efficient and completely compatible with existing commercial software. Significant effort has been directed toward identifying those model characteristics (element geometric properties, material properties and loads) that most strongly affect the required penalty parameter, and subsequently to developing simple "formulae" for automatically calculating the proper penalty parameter for each interface constraint. A wide variety of problems has been investigated analytically and computationally in order to correctly identify the analytical functional form of the penalty parameter for each constraint within many classes of problems.

The resulting interface element is particularly efficient for finite element modeling of composite structures. When the material properties vary across and/or along the interface, the present method is often much more accurate than adopting a unique value of the penalty parameter.

The present interface element has been implemented in the commercial finite element code ABAQUS as a User Element Subroutine (UEL), making it convenient to test the behavior and accuracy of the interface element for a wide range of problems.

Additional capabilities were implemented in the interface element in order to simulate delamination growth in composite laminates. This entirely new technology is capable of joining and simulating crack growth between independently modeled finite element subdomains (e.g., composite plies). The interface element approach makes it possible to release sub-regions of the interface surface whose length is smaller than that of the finite elements, thereby allowing for a mesh-independent tracking of the crack front. A novel approach for correctly simulating the delamination growth in mixed mode I+II conditions has been developed. It successfully integrates widely used failure criteria in the peculiar penalty-based formulation of the interface element. A mesh-independent friction model has also been created; it can be applied to interface elements after complete failure or to interface elements whose only purpose is to avoid overlapping and enforce friction. Results for double cantilever beam DCB, end-loaded split (ELS) and fixed-ratio mixed mode (FRMM) specimens indicate that the method is capable of accurately predicting delamination growth for Mode I, Mode II and Mixed Mode I+II.

APPENDICES

APPENDIX A USER MANUAL

Uelglue.f for 2-D Quadrilateral Elements

The FORTRAN program uelglue.f is an ABAQUS User Element Subroutine (UEL) that calculates the finite element matrices associated with a penalty-based interface element able to connect incompatible meshes of 2-D quadrilateral linear elements. All of the necessary material and geometric data for the two connected meshes is located in the ABAQUS model input file (.inp). The required parameters are the nodes on the interface and the thickness and Young's modulus of the two domains. Each penalty interface element is composed of a user specified number of equally spaced nodes. A patch test analysis is used to illustrate the basic format of the input file.

Patch Test

A two dimensional rectangular region is assumed to be composed of two domains. The domains are meshed independently and joined by one interface element. The geometrical configuration of the problem is shown in Figure 19. Other properties are: $E_1 = E_2 = 1$ and $thickness = 1$. In discretizing the two subdomains, four-noded bilinear plane stress elements are used. Three different conditions are investigated: uniform axial strain in direction 1, uniform axial strain in direction 2 and uniform shear strain. This problem was intended to serve as a patch test for the interface element. If the continuity constraint along the inclined interface is not correctly imposed by the interface model, then discontinuity of displacements and strains across the interface would result.

The condition of a uniform strain in direction 1 is obtained by assigning a displacement equal to 1.6 mm to all nodes on the right vertical side and constraining the opposite side against movements in the same direction. The node at the bottom left corner

is constrained against vertical motion. The results are in agreement with the exact solution to the number of significant digits available, i.e. axial strain is uniform in direction 1 and equal to 0.1 in all elements of the patch. The displacement distribution in direction 1 is reported in Figure 20.

Similarly, the condition of a uniform strain in direction 2 is obtained by assigning a displacement equal to 1 mm to all nodes on the top horizontal side and constraining the opposite side against movements in direction 2. The node at the bottom left corner is constrained against horizontal motion. The interface element results are in agreement with the exact solution to the number of significant digits available, i.e. axial strain is uniform in direction 2 and equal to 0.1 in all elements of the patch. The displacement distribution in direction 2 is reported in Figure 21.

The condition of a uniform inplane shear strain is obtained by assigning displacements to the nodes on the boundaries such that horizontal sides form an angle with the axis 1 and vertical sides form an angle with the axis 2. The interface element results are in agreement with the exact solution to the number of significant digits available, i.e. shear strain is uniform in all elements of the patch. The displacement distributions in direction 1 and 2 are reported in Figures 22(a) and 22(b).

Creating the input file

The input file for the uniform axial strain loading condition is used to describe the command lines necessary to define the interface model. The complete input file is provided at the end of the section. In the following, all lines in the input file related to the interface element are reported in bold.

For this problem five equally spaced nodes have been used to define the penalty

interface element. The coordinates of each of the five nodes composing the interface frame must be added to the node definition part of the input file. Note that the two subdomains do not have any common nodes. Note that the coordinates of the first and of the last nodes of the three groups of nodes must match. In the present case, the two groups of nodes (2, 101, 20) and (4, 103, 28) must have the same coordinates.

```
*HEADING
Patch Test - Constant strain in direction 1
*NODE
    1,  .00000,     .00000,     .00000
    2,  6.0000,     .00000,     .00000
    3,  3.0000,     .00000,     .00000
    4,  10.000,     10.000,     .00000
    5,  8.0000,     5.0000,     .00000
    6,  .00000,     10.000,     .00000
    7,  5.0000,     10.000,     .00000
    8,  .00000,     5.0000,     .00000
    9,  4.0000,     5.0000,     .00000
   20,  6.0000,     .00000,     .00000
   21,  16.000,     .00000,     .00000
   22,  11.000,     .00000,     .00000
   23,  16.000,     10.000,     .00000
   24,  16.000,     2.0000,     .00000
   25,  16.000,     4.0000,     .00000
   26,  16.000,     6.0000,     .00000
   27,  16.000,     8.0000,     .00000
   28,  10.000,     10.000,     .00000
   29,  13.000,     10.000,     .00000
   30,  9.2000,     8.0000,     .00000
   31,  8.4000,     6.0000,     .00000
   32,  7.6000,     4.0000,     .00000
   33,  6.8000,     2.0000,     .00000
   34,  11.400,     2.0000,     .00000
   35,  11.800,     4.0000,     .00000
   36,  12.200,     6.0000,     .00000
   37,  12.600,     8.0000,     .00000
  101,   6.000,     .00000,     .00000
  102,   7.000,     2.5000,     .00000
  103,   8.000,     5.0000,     .00000
  104,   9.000,     7.5000,     .00000
  105,  10.000,     10.000,     .00000
```

The element connectivity for each of the two subdomains does not require any input concerning the interface element. Note that the two subdomains are not connected.

```
*ELEMENT, TYPE=CPS4, ELSET=BEAM
  1,      1,      3,      9,      8
  2,      3,      2,      5,      9
  3,      8,      9,      7,      6
  4,      9,      5,      4,      7
 20,     20,     22,     34,     33
 21,     22,     21,     24,     34
 22,     33,     34,     35,     32
 23,     34,     24,     25,     35
 24,     32,     35,     36,     31
 25,     35,     25,     26,     36
 26,     31,     36,     37,     30
 27,     36,     26,     27,     37
 28,     30,     37,     29,     28
 29,     37,     27,     23,     29
```

The element section and material properties of the native ABAQUS elements are defined in the usual manner.

```
*SOLID SECTION, ELSET=BEAM, MATERIAL=STEEL
1
*MATERIAL, NAME=STEEL
*ELASTIC
1.E+03, 0.3
```

The group of data related to the interface element begins with the *USER ELEMENT keyword:

```
*USER ELEMENT, NODES=14, TYPE=U1, PROPERTIES=5,
IPROPERTIES=3,
 COORDINATES=2, VARIABLES=4
1, 2
```

These lines should be added to the .inp file exactly as they appear above, with the exception that the parameter NODE must be set equal to the total number of nodes at the interface. The total number of interface nodes is the sum of the number of interface nodes

from each of the two independent subdomains plus the nodes composing the interface element. The user should not change the parameters PROPERTIES, IPROPERTIES, COORDINATES and VARIABLES, since they are the same for every analysis. The numbers in the following line "1, 2" define which degrees of freedom are active for the interface element, and this line must not be changed.

Note that if all of the interface elements in a mesh contain the same total number of nodes at the interface, then the above definition of *USER ELEMENT is used to define all such elements. For each interface element in the mesh that has a different number of total interface nodes, the *USER ELEMENT card should be repeated, with "n" incremented by one within the TYPE=Un parameter. For example, the second interface element definition will use TYPE=U2.

The keyword *ELEMENT defines the element number and connectivity of the interface element:

```
*ELEMENT, TYPE=U1, ELSET=FRAME1
100,    2, 5, 4, 101, 102, 103, 104, 105, 20, 33, 32, 31,
30, 28
```

The parameters TYPE and ELSET are required, where TYPE is set equal to the user element type (Un, where usually n=1) and ELSET identifies the set of interface elements sharing the same properties. The ELSET definition in the *ELEMENT card should match the ELSET definition in the *UEL PROPERTY card described below. The second line is required, as it contains the interface element number (100 in this case) followed by the list of nodes that compose the interface element. The list of nodes must

follow a particular order. Beginning with one of the two subdomain regions being connected, the nodes of this subdomain must be listed in order as they appear along the interface. It does not matter which "end" of this interface region contains the first node in the list, but the same direction chosen for the first subdomain interface region must be used for the subsequent definition of the interface element as well as for the second subdomain region. Next, the five equally spaced nodes of the interface element are defined in order according to the direction defined by the first subdomain interface region. Finally, the nodes of the second mesh are defined in order as they appear and in the same direction as defined in the first subdomain interface region.

The keyword *UEL PROPERTY allows the specification of the main properties of the interface element:

```
*UEL PROPERTY, ELSET=FRAME1
    1.E+5,   1.,   1., 1.E+3, 1.E+3, 3, 6,   5
**   BETA, THK1, THK2,    E1,    E2, N, M, NPS
```

The parameter ELSET is required and must match the definition in *ELEMENT. The second line contains the real and integer data for the interface element. The third line is an optional comment line (indicated by **) that is used as an aid to remember the type of data required in the second line. The parameter BETA is a scaling factor for the penalty parameter. The value 1.E+4 should work well for most analyses. Values of BETA smaller than 1.E+3 often do not enforce compatibility sufficiently and are not recommended. Higher values are allowed thanks to presence of a round-off error control that automatically reduces the value of BETA if it is causing numerical problems. The meaning of the parameter BETA is clearly explained in the technical documentation on

the interface element. The next parameters are the thickness and Young's modulus of the two subdomains, given in the same order as the nodes in *ELEMENT. In case of an orthotropic material, the Young's modulus required is the one in the direction perpendicular to the interface. N and M are the number of nodes at the interface for each of the two subdomain meshes. NPS (Number Points Spline) is the number of equally spaced nodes at the interface used to define the penalty interface element. In the present example, the first interface has three nodes (2, 5, 4), the second interface has six nodes (20, 33, 32, 31, 30, 28) and five nodes (101, 102, 103, 104, 105) have been used to define the penalty interface element, so N=3, M=6 and NPS=5.

Executing the program

The Abaqus command line for performing an analysis with interface elements is the following:

```
abaqus job=job_name user=uelglue interactive
```

The input file (*job_name.inp*), Abaqus include file *aba_param.inc* and the program in its compiled version *uelglue.o* or as source code *uelglue.f* must be present in the directory where the analysis is performed.

Example Input File

```
*HEADING
Patch Test - Constant strain in direction 1
*NODE
    1,  .00000,     .00000,     .00000
    2,  6.0000,     .00000,     .00000
    3,  3.0000,     .00000,     .00000
```

```
     4,   10.000,      10.000,      .00000
     5,   8.0000,      5.0000,      .00000
     6,   .00000,      10.000,      .00000
     7,   5.0000,      10.000,      .00000
     8,   .00000,      5.0000,      .00000
     9,   4.0000,      5.0000,      .00000
    20,   6.0000,      .00000,      .00000
    21,   16.000,      .00000,      .00000
    22,   11.000,      .00000,      .00000
    23,   16.000,      10.000,      .00000
    24,   16.000,      2.0000,      .00000
    25,   16.000,      4.0000,      .00000
    26,   16.000,      6.0000,      .00000
    27,   16.000,      8.0000,      .00000
    28,   10.000,      10.000,      .00000
    29,   13.000,      10.000,      .00000
    30,   9.2000,      8.0000,      .00000
    31,   8.4000,      6.0000,      .00000
    32,   7.6000,      4.0000,      .00000
    33,   6.8000,      2.0000,      .00000
    34,   11.400,      2.0000,      .00000
    35,   11.800,      4.0000,      .00000
    36,   12.200,      6.0000,      .00000
    37,   12.600,      8.0000,      .00000
   101,    6.000,      .00000,      .00000
   102,    7.000,      2.5000,      .00000
   103,    8.000,      5.0000,      .00000
   104,    9.000,      7.5000,      .00000
   105,   10.000,      10.000,      .00000
*ELEMENT, TYPE=CPS4, ELSET=BEAM
  1,      1,      3,      9,      8
  2,      3,      2,      5,      9
  3,      8,      9,      7,      6
  4,      9,      5,      4,      7
 20,     20,     22,     34,     33
 21,     22,     21,     24,     34
 22,     33,     34,     35,     32
 23,     34,     24,     25,     35
 24,     32,     35,     36,     31
 25,     35,     25,     26,     36
 26,     31,     36,     37,     30
 27,     36,     26,     27,     37
 28,     30,     37,     29,     28
 29,     37,     27,     23,     29
*SOLID SECTION, ELSET=BEAM, MATERIAL=STEEL
1
*MATERIAL, NAME=STEEL
```

```
*ELASTIC
1.E+3, 0.3
*USER    ELEMENT,    NODES=14,    TYPE=U1,    PROPERTIES=5,
IPROPERTIES=3,
 COORDINATES=2, VARIABLES=4
1, 2
*ELEMENT, TYPE=U1, ELSET=FRAME1
100,    2, 5, 4, 101, 102, 103, 104, 105, 20, 33, 32, 31,
30, 28
*UEL PROPERTY, ELSET=FRAME1
   1.E+5,   1.,   1., 1.E+3, 1.E+3, 3, 6,   5
**  BETA, THK1, THK2,    E1,    E2, N, M, NPS
*BOUNDARY
1, 1, 2, 0.0
6, 1, 1, 0.0
8, 1, 1, 0.0
*STEP, PERTURBATION
*STATIC
*BOUNDARY
21,  1, 1, 1.6
23,  1, 1, 1.6
24,  1, 1, 1.6
25,  1, 1, 1.6
26,  1, 1, 1.6
27,  1, 1, 1.6
*NODE PRINT
U, RF
*RESTART, WRITE
*END STEP
```

REFERENCES

REFERENCES

[1] Aminpour, M.A. and K. A. Hosapple. "Finite element solutions for propagating interface crack with singularity elements", *Engineering Fracture Mechanics*, Vol. 39, No. 3, 1991, pp. 451-468.

[2] Z. Jinping and A. Huizu. "Stress analysis around holes in orthotropic plates by subregion mixed finite element method", *Computers & Structures*, Vol. 41, No. 1, 1991, pp. 105-108.

[3] Farhat and F. X. Roux. "A method of finite element tearing and interconnecting and its parallel solution algorithm", *Journal for Numerical Methods in Engineering*, Vol. 32, 1991, pp. 1205-1227.

[4] C. Farhat and M. Gerardin. "Using a reduced number of Lagrange multipliers for assembling parallel incomplete field finite element approximations", *Computer Methods in Applied Mechanics and Engineering*, Vol. 97, 1992, pp. 333-354.

[5] Y. Maday, C. Mavriplis and A. Patera. "Non-conforming mortar element methods: Application to spectral discretizations", *NASA CR-181729*, ICASE Report No. 88-59, 1988.

[6] J.B. Ransom, S.L. McCleary and M. A. Aminpour. "A New Interface Element for Connecting Independently Modeled Substructures", *AIAA Paper*, Number 93-1503, 1993.

[7] J.M. Housner, M. A. Aminpour, C.G. Davila, J.E. Schiermeier, W.F. Stroud, J.B. Ransom, and R.E. Gillian. "An Interface Element for Global/Local and Substructuring Analysis", presented at the *MSC World Users' Conference*, Los Angeles, CA, May 8-12, 1995.

[8] M. A. Aminpour, J. B. Ransom, and S. L. McCleary. "A Coupled Analysis Method for Structures with Independently Modeled Finite Element Subdomains",

International Journal for Numerical Methods in Engineering, Vol. 38, 1995, pp. 3695-3718.

[9] J.B. Ransom. "Interface Technology for Geometrically Nonlinear Analysis of Multiple Connected Subdomains", *AIAA* Paper No. 97-1298, 1997.

[10] M. A. Aminpour and T. Krishnamurthy. "A Two-Dimensional Interface Element for Multi-Domain Analysis of Independently Modeled Three-Dimensional Finite Element Meshes", *AIAA* paper no. 97-1297, pp. 1853-1861, 1997.

[11] M. A. Aminpour, T. Krishnamurthy and T. D. Fadale. "Coupling of Independently Modeled Three-Dimensional Finite Element Meshes with Arbitrary Shape Interface Boundaries", *AIAA* paper no. 98-2060, pp. 1853-1861, 1998.

[12] M. A. Aminpour, Stephane Pageau and Youngwon Shin. "An Alternative Method for the Interface Modeling Technology", *AIAA* paper no. 2000-1352, pp. 1-13, 2000.

[13] Maenghyo Cho and Won Bae Kim. "A Coupled Finite Element Analysis of Independently Modeled Substructures by Penalty Frame Method", *AIAA* paper no. 98-2061, pp. 3025-3032, 1998.

[14] Carlos A. Felippa. "Error Analysis of Penalty Function Techniques for Constraint Definition in Linear Algebraic System", *International Journal for Numerical Methods in Engineering*, Vol. 11, pp. 709-728, 1977.

[15] Carlos A. Felippa. "Interactive Procedures for Improving Penalty Function Solutions of Algebraic System", *International Journal for Numerical Methods in Engineering*, Vol. 12, pp. 821-836, 1978.

[16] Carlos A. Felippa. "Penalty-Function Interactive Procedures for Mixed Finite Elements Formulation", *International Journal for Numerical Methods in Engineering*, Vol. 22, pp. 267-279, 1986.

[17] G. Prathap. "Locking, Rank and Singularity of Penalty-Linked Stiffness Matrix and Consistency of Strain-Field", *Computers & Structures*, Vol. 52, No. 1, pp. 35-39, 1994.

[18] Ahmed K. Noor and Jeanne M. Peters. "Penalty Finite Element Models for Nonlinear Dynamic Analysis", *AIAA Journal*, Vol. 24, No. 2, pp. 312-320, 1986.

[19] Ahmed K. Noor, M. Asce and Jeanne M. Peters. "Penalty Finite Element Formulation for Curved Elastica", *Journal of Eng. Mechanics*, Vol. 110, No. 5, pp. 694-712, 1984.

[20] E. Haugeneder. "A New Penalty Function Element for Thin Shell Analysis", *International Journal for Numerical Methods in Engineering*, Vol. 18, pp. 845-861, 1982.

[21] Ted Belytschko and Mark O. Neal. "Contact-Impact by the Pinball Algorithm with Penalty and Lagrangian Methods", *International Journal for Numerical Methods in Engineering*, Vol. 31, pp. 547-572, 1991.

[22] G. F. Carey and R. Krishnan. "Convergence of Iterative Methods In Penalty Finite Element Approximation Of The Navier-Stokes Equations", *Computer Methods In Applied Mechanics And Engineering*, Vol. 60, pp. 1-29, 1991.

[23] J. N. Reddy. "On The Accuracy and Existence of Solutions to Primitive Variable Models of Viscous Incompressible Fluids", *Int. J. Engineering Sci.*, Vol. 16, pp. 921-929, 1978.

[24] Henry Bertin and Hiroyuki Ozoe. "Technique for Rapid Convergence of the Penalty Finite-Element Method with a Modified Galerkin Scheme and Its Application to Natural Convection", *Numerical Heat Transfer*, vol. 10, pp. 311-325, 1986.

[25] E-M. Salonen. "An Iterative Penalty Function Method in Structural Analysis", *International Journal for Numerical Methods in Engineering*, Vol. 10, pp. 413-421, 1976.

[26] R. Codina, M. Cervera And E. Orate. "A Penalty Finite Element Method for Non-Newtonian Creeping Flows", *International Journal for Numerical Methods in Engineering*, Vol. 36, pp. 1395-1412, 1993.

[27] A. W. Al-Khafaji and J. R. Tooley. "Numerical Methods in Engineering Practice", *HRW Series in Mechanical Engineering*, 1986.

[28] M. L. James, G.M. Smith and J. C. Wolford. "Applied Numerical Methods for Digital Computation", *Harper & Row*, 1985.

[29] Arthur Sard and Sol Weintraub. "A Book of Splines", *Wiley*, 1971.

[30] Larry L. Schumaker, "Spline functions: basic theory". New York: *Wiley*, c1981.

[31] P. M. Prenter. "Splines and variational methods", New York: *Wiley*, 1975.

[32] Elaine Cohen, Richard F. Riesenfeld and Gershon Elber. "Geometric modeling with splines: an introduction". Natick, Mass.: *AK Peters*, c2001.

[33] C. de Boor, K. Höllig, S. Riemenschneider. "Box splines". New York: *Springer-Verlag*, c1993.

[34] Pierre-Jean Laurent, Alain Le Méhauté, Larry L. Schumaker. "Curves and surfaces". Boston: *Academic Press*, c1991.

[35] J. H. Ahlberg, E. N. Nilson. "The theory of splines and their applications". New York, *Academic Press*, 1967.

[36] Gerald E. Farin. "Curves and surfaces for computer aided geometric design: a practical guide", Boston: *Academic Press*, 1993.

[37] Paul Dierckx. "Curves and surfaces fitting with splines". New York: *Clarendon Press*, 1993.

[38] H Spath. "Two dimensional spline interpolation algorithms", Wellesley, Mass.: *AK Peters*, 1995.

[39] Abaqus Manuals, Hibbit, Karlsson & Sorensen Inc., 1999.

[40] Jonathan B. Ransom. "On Multifunctional Collaborative Methods in Engineering Science", Langley Research Center, Hampton, Virginia, *NASA*/TM-2001-211046, 2001.

[41] J. N. Reddy. "An introduction to the finite element method". Highstown, NJ, *McGraw-Hill*, 1993.

[42] R. D. Cook, D. S. Malkus, M. E. Plesha. "Concepts and applications of finite element analysis". New York: *Wiley*, 1989.

[43] K-J Bathe. "Finite element procedures". Englewood Cliffs, NJ, *Prentice Hall*, 1996.

[44] W.Chen and S. Yang. "Multilayered Hybrid-Stress Finite Element Analysis of Composite Laminates with Delamination Crack Originating from Transverse Cracking", *Engineering Fracture Mechanics*, Vol. 54, No. 5, pp. 713-729, 1996.

[45] A. A. Griffith. "The Phenomena of Rupture and Flow in Solids", *Phil. Trans.*, A221, 1921, pp. 163-198.

[46] G. R. Irwin. "Analysis of stresses and strains near the end of a crack traversing a plate", *J. of Applied Mechanics, Transaction of ASME*, pp. 361-364, 1957.

[47] H. Tada, P. C. Paris and G. R. Irwin. "The stress analysis of cracks handbook", *ASME Press – Third Edition*, New York, NY, USA, 2000.

[48] T. Ireman, J.C. Thesken, E. Greenhalgh, R. Sharp, M. Gadke, S. Maison, Y. Ousset, F. Roudolff, A. La Barbera. "Damage propagation in composite structural elements - coupon experiments and analyses", *Composite Structures*, v 36, n 3-4, Nov-Dec, p 209-220, 1996.

[49] D. Broek. "The practical use of Fracture Mechanics", *Kluwer Academic Publishers*, Boston, MA, USA, 1989.

[50] A. R. Luxmoore and D. R. Owen. "Numerical Methods in Fracture Mechanics", *Proceedings of the First International Conference* – Swansea, U.K, 1978.

[51] F. Ozdil and L. A. Carlsson. "Characterization of mode I delamination growth in glass/epoxy composite cylinders", *J. of Composite Materials*, Vol. 34, No. 5, pp. 398-419, 2000.

[52] N. S. Choi, A. J. Kinloch and J. G. Williams. "Delamination fracture of multidirectional carbon-fiber/epoxy composites under mode I, mode II and mixed-mode I/II loading", *J. of Composite Materials*, Vol. 33, No. 1, pp. 73-100, 1999.

[53] M. Kenane, M.L. Benzeggagh. "Mixed-mode delamination fracture toughness of unidirectional glass/epoxy composites under fatigue loading", *Composites Science and Technology*, v 57, n 5, May, p 597-605, 1997.

[54] F. Ducept, P. Davies, D. Gamby. "An experimental study to validate tests used to determine mixed mode failure criteria of glass/epoxy composites", *Composites - Part A: Applied Science and Manufacturing*, v 28A, n 8, p 719-729, 1997.

[55] Chyanbin Hwu, C.J. Kao, L.E. Chang. "Delamination fracture criteria for composite laminates", *Journal of Composite Materials*, v29, n15, p 1962-1987, 1995.

[56] A.J. Kinloch, Y. Wang, J.G. Williams, P. Yayla. "Mixed-mode delamination of fiber composite materials", *Composites Science and Technology*, v 47, n 3, p 225-237, 1993.

[57] N. J. Pagano. "Interlaminar response of composite materials", *Composite Materials Series, Elsevier, Editor: N. J. Pagano*, Vol. 5, 1989.

[58] A. C. Garg. "Delamination – A Damage Mode in Composite Structures", *Engineering Fracture Mechanics*, Vol. 29, No. 5, pp. 557-584, 1988.

[59] S.C. Pradhan and T. E. Tay. "Three-Dimensional Finite Element Modelling of Delamination Growth in Notched Composite Laminates Under Compressive Loading", *Engineering Fracture Mechanics*, Vol. 60, No. 2, pp. 157-171, 1998.

[60] Chyanbin Hwu, C.J. Kao, L.E. Chang. "Delamination fracture criteria for composite laminates", *Journal of Composite Materials*, v29, n15, p 1962-1987, 1995.

[61] K. Kaczmarek, M.R. Wisnom, M.I. Jones. "Edge delamination in curved (0/±45)s glass-fibre/epoxy beams loaded in bending", *Composites Science and Technology*, v 58, n 1, Jan, p 155-161, 1998.

[62] E.D. Jr. Reedy, F.J. Mello, T.R. Guess. "Modeling the initiation and growth of delaminations in composite structures", *Journal of Composite Materials*, v 31, n 8, p 812-831, 1997.

[63] S. Rinderknecht, B. Kroplin. "A computational method for the analysis of delamination growth in composite plates", *Computers and Structures*, v 64, n 1-4, Jul-Aug, p 359-374, 1997.

[64] J. T. Wang and I. S. Raju. "Strain Energy Release Rate Formulae for Skin-Stiffener Debond Modeled with Plate Elements", *Engineering Fracture Mechanics*, Vol. 54, No. 2, pp. 221-228, 1996.

[65] I.S. Raju, R. Sistla and T. Krishnamurthy. "Fracture Mechanics Analyses for Skin-Stiffener Debonding", *Engineering Fracture Mechanics*, Vol. 54, No. 3, pp. 371-385, 1996.

[66] D. Hitchings, P. Robinson and F. Javidrad. "Finite Element Model for Delamination Propagation Composites", *Computers & Structures*, Vol. 60, No. 6, pp. 1093-1104, 1996.

[67] C. Davila, P. P. Camanho and M. F. de Moura. "Mixed-Mode Decohesion Elements for Analyses of Progressive Delamination", *42nd AIAA/ASME/ASCE/AHS/ASC Structural Dynamics and Materials Conference*, Seattle, Washington, paper AIAA-01-1486, 2001.

[68] Y. Mi, A. Crisfield, A. O. Davies and H. B. Hellweg. "Progressive Delamination Using Interface Elements", *J. of Composite Materials*, Vol. 32, No. 14, pp. 1246-1272, 1998.

[69] J. Chen, M. Crisfield, A. J. Kinloch, E. P. Busso, F. L. Mattehws and Y. Qiu. "Predicting Progressive Delamination of Composite Materials Specimens via Interface Elements", *Mechanics of Composite Materials and Structures*, Vol. 6, pp. 301-317, 1999.

[70] G. Alfano and M. A. Crisfield. "Finite element interface models for the delamination analysis of laminated composites: mechanical and computational issies", *International Journal for Numerical Methods in Engineering*, Vol. 50, pp. 1701-1736, 2001.

[71] L. Lammerant, I. Verpoest. "Modelling of the interaction between matrix cracks and delaminations during impact of composite plates", *Composites Science and Technology*, v 56, n 10, Oct, p 1171-1178, 1996.

[72] J. C. J. Schellekens and R. DE Boerst. "A Non-Linear Finite Element Approach for the Analysis of Mode-I Free Edge Delamination in Composites", *Int. J. of Solids Structures*, Vol. 30, No. 9, pp. 1939-1953, 1993.

[73] J. H. A. Schipperen and F.J. Lingen. "Validation of two-dimensional calculation of free-edge dalamination in laminated composites", *Composite Structures*, Vol. 45, pp. 233-240, 1999.

[74] C. M. Dakshima Moorthy and J. N. Reddy. "Recovery of Interlaminar Stresses and Strain Energy Release Rates in Composite Laminates", *Finite Elements in Analysis and Design*, Vol. 33, pp. 1-27, 1999.

[75] O. Allix and A. Corigliano. "Geometrical and interfacial non-linearities in the analysis of delamination in composites", *I. J. of Solids and Structures*, Vol. 36, pp. 2189-2216, 1999.

[76] N. Point and E. Sacco. "A Delamination Model for Laminated Composites", *Int. J. of Solids Structures*, Vol. 33, No. 4, pp. 483-509, 1996.

[77] P. Ladevèze. "A Damage Computational Method for Composite Structures", *Computers & Structures*, Vol. 44, No. 1/2, pp. 78-87, 1992.

[78] W. J. Bottega. "A growth law for propagation of arbitrary shaped delaminations in layered plates", *Int. J. of Solids Structures*, Vol. 19, No. 11, pp. 1009-1017, 1983.

[79] Z. Petrossian, Michael R. Wisnom. "Prediction of delamination initiation and growth from discontinuous plies using interface elements", *Composites - Part A: Applied Science and Manufacturing*, v 29, n 5-6, p 503-515, 1998.

[80] D. Chakraborty and B. Pradhan. "Effect of ply thickness and fibre orientation on delamination initiation in broken ply composite laminate", *J. of Reinforced Plastic and Composites*, Vol. 18, No. 8, pp. 735-758, 1999.

[81] J. W. Joo and C. T. Sun. "Failure criterion for laminates governed by free edge interlaminar shear stress", *Journal of Composite Materials*, v. 26, n. 10, pp 573-586, 1994.

[82] Chu-Cheng Ko, Chien-Chang Lin, Hsiang Chin. "Prediction for delamination initiation around holes in symmetric laminates", *Composite Structures*, v 22, n 4, p 187-191, 1992.

[83] S. Mohammadi, D. R. J. Owen and D. Peric. "A Combined Finite/Discrete Element Algorithm for Delamination Analysis of Composites", *Finite Elements in Analysis and Design*, Vol. 28, pp. 321-336, 1998.

[84] J. Zhao, S. V. Hoa, X. R. Xiao and I. Hanna. "Global/Local Approach Using Partial Hybrid Finite Element Analysis of Stress Fields in Laminated Composites with Delamination Under Bending", *J. of Reinforced Plastic and Composites*, Vol. 18, No. 9, pp. 827-843, 1999.

[85] F. Chang and G. S. Springer. "Strength of fiber reinforced composite bends", *Journal of Composite Materials*, v. 20, pp 30-45, 1986.

[86] M Ortiz and A. Pandolfi. "Finite-deformation irreversible cohesive element for three-dimensional crack-propagation analysis". *International Journal for Numerical Methods in Engineering*, Vol. 44, pp. 1267-1282, 1999.

[87] A. Pandolfi, P. Krysl and M Ortiz and. "Finite element simulation of ring expansion and fragmentation: The capturing of length and time scale through cohesive models of fracture". *International Journal of Fracture*, Vol. 95, pp. 279-297, 1999.

[88] N. Moes, J. Dolbow and T. Belytschko. "A finite element method for crack growth without remeshing", *Int. J. Numer. Meth. Engng.*, Vol. 46, pp. 131-150, 1999.

[89] M.A. Aminpour and K. A. Hosapple. "Finite element solutions for propagating interface crack with singularity elements", *Engineering Fracture Mechanics*, Vol. 39, No. 3, 1991, pp. 451-468.

[90] Jin Lee and Huajian Gao. "A hybrid finite element analysis of interface cracks". *International Journal for Numerical Methods in Engineering*, Vol. 38, pp. 2465-2482, 1995.

[91] A.S. Krausz and K. Krausz. "Fracture kinetics and crack growth", *Kluwer Academic Publishers*, Boston, MA, USA, 1988.

[92] M. H. Aliabadi and D. P. Rooke. "Numerical Fracture Mechanics", *Kluwer Academic Publisher*, 1991.

[93] R. El Abdi. "A special finite element for analysis of the singularity in a bimaterial containing a crack perpendicular to the interface". *Engineering Fracture Mechanics*, Vol. 39, No. 6, pp. 1061-1065, 1991.

[94] S. H. Staab and T. C. Chang. "A finite element analysis of the finite width interface mixed mode bimaterial fracture problem", *Computers & Structures*, Vol. 19, No. 5/6, pp. 879-884, 1984.

[95] K. Saito, S. Araki, T. Kawakami and I. Moriwaky. "Global-local finite element analysis of stress intensity factor for a crack along the interface of a two phase material", *Proceedings of the ICCM-10*, Whistler, B.C., Canada, Vol. I, August, 1995.

[96] Q. Yang and Q. Qin. "Numerical simulation of cracking process in dissimilar media", *Composite Structures*, Vol. 53, pp. 403-407, 2001.

[97] K. Machida. "Stress intensity factor of three-dimensional interface crack under mixed-mode loading by finite element analysis". *Key Engineering Materials*, Vol. 145-149, pp. 589-594, 1998.

[98] F. Ozdil and L. A. Carlsson. "Characterization of mode II delamination growth in glass/epoxy composite cylinders", *J. of Composite Materials*, Vol. 34, No. 4, pp. 274-298, 2000.

[99] F. Ozdil and L. A. Carlsson. "Characterization of mixed mode delamination in glass/epoxy composite cylinders", *J. of Composite Materials*, Vol. 34, No. 5, pp. 420-441, 2000.

[100] Aditi Chattopadhyay, Changho Nam and Dan Dragomir-Daescu. "Delamination modeling and detection in smart composite plates", *J. of Reinforced Plastic and Composites*, Vol. 18, No. 17, pp. 1557-1572, 1999.

[101] R. M. Jones. "Mechanics of composite materials", *Taylor & Francis Inc.*, Philadelphia, PA, USA, 1999.

[102] A. S. D. Wang. "Free-edge delamination in layered composites- A historical review of the past 30 years", *ASME1998*, MD-Vol. 84, pp. 223-226, 1998.

[103] S. H. Narayan and J. L. Beuth. "Designation of mode mix in orthotropic composite delamination problems", *Int. J. of Fracture*, Vol. 90, pp. 383-400, 1998.

[104] Narendra V. Bhat, Paul A. Lagace. "Analytical method for the evaluation of interlaminar stresses due to material discontinuities", *Journal of Composite Materials*, v 28, n 3, p 190-210, 1994.

[105] Wan-Lee Yin. "Simple solution of the free-edge stresses in composite laminates under thermal and mechanical loads", *Journal of Composite Materials*, v. 28, n. 6, pp 573-586, 1994.

[106] Jerry Zhiqi Wang, Darrell F. Socie. "Failure strength and damage mechanisms of e-glass/epoxy laminates under in-plane biaxial compressive deformation", *Journal of Composite Materials*, v 27, n 1, pp 40-58, 1993.

[107] S. F. Muller de Almeida and G. M. Candido. "Effect of the free edge finishing on the tensile strength of carbon/epoxy laminates", *Composite Structures*, v 25, pp 287-293, 1993.

[108] W. Becher. "Closed-form solution for the free-edge effect in cross-ply laminates", *Composites Structures*, v 26, pp 39-45, 1993.

[109] D. Bruno and A. Grimaldi. "Delamination Failure of Layered Composite Plates Loaded in Compression", *Int. J. of Solids Structures*, Vol. 26, No. 3, pp. 313-330, 1990.

[110] W. J. Bottega. "A growth law for propagation of arbitrary shaped delaminations in layered plates", *Int. J. of Solids Structures*, Vol. 19, No. 11, pp. 1009-1017, 1983.

[111] W. J. Bottega and A. Maewal. "Delaminations buckling and growth in laminates", *J. of Applied Mechanics*, Vol. 50, pp. 184-189, 1983.

[112] J. D. Whitcomb and I. S. Raju. "Superposition Method for Analysis of Free-Edge Stresses", *J. of Composite Materials*, Vol. 17, pp. 492-507, 1983.

[113] S. S. Wang and I. Choi. "Boundary-layer effects in composite laminates: Part 1 – Free-edge singularities", *J. of Applied Mechanics*, Vol. 49, pp. 541-548, 1982.

[114] S. S. Wang and I. Choi. "Boundary-layer effects in composite laminates: Part 2 – Free-edge stress solution and basic characteristics", *J. of Applied Mechanics*, Vol. 49, pp. 549-560, 1982.

[115] E. Altus, A. Rotem and M. Shmueli. "Free-Edge Effect in Angle Ply Laminates – A New Three Dimensional Finite Difference Solution", *J. of Composite Materials*, Vol. 14, pp. 21-30, 1980.

[116] R. L. Spliker and S. C. Chou. "Edge Effects in symmetric composite Laminates: importance of satisfying the traction-free-edge condition", *J. of Composite Materials*, Vol. 14, pp. 2-20, 1980.

[117] N. J. Pagano and E. F. Rybicki. "On the significance of effective modulus solutions for fibrous composites", *J. of Composite Materials*, Vol. 8, pp. 214-228, 1974.

[118] R. Byron Pipes and N. J. Pagano. "The influence of stacking sequence on laminate strength ", *J. of Composite Materials*, Vol. 5, pp. 50-57, 1971.

[119] R. Byron Pipes and N. J. Pagano. "Interlaminar stresses in composite laminates under uniform axial extension", *J. of Composite Materials*, Vol. 4, pp. 538-548, 1970.

[120] H. S. Kim, M. Cho and G. Kim. "Free-edge strength analysis in composite laminates by the extended Kantorovic method", *Composite Structures*, Vol. 49, pp. 229-235, 2000.

[121] M. Schulze and W. D. Nix. "Finite Element Analysis of the Wedge Delamination Test ", *Int. J. of Solids and Structures*, Vol. 37, pp. 1045-1063, 2000.

[122] Y. Ousset. "Numerical simulation of delamination growth in layered composite plates", *I. J. of Mechanics and Solids*, Vol. 18, pp. 291-312, 1999.

[123] J. Macklerle. "Delamination of Composites - Finite Element and Boundary Element Analyses – A bibliography (1995-1997)", *Finite Elements in Analysis and Design*, Vol. 30, pp. 243-252, 1998.

[124] H. T. J. Yang and C. C. He. "Three-Dimensional Finite Element Analysis of Free Edge Stresses and Delamination Composite Laminates", *J. of Composite Materials*, Vol. 28, No. 15, pp. 1394-1412, 1994.

[125] K. N. Shivakumar and I. S. Raju. "An Equivalent Domain Integral Method for Three-Dimensional Mixed-Mode Fracture Problems", *Engineering Fracture Mechanics*, Vol. 42, No. 6, pp. 935-959, 1992.

[126] X. Lu and D. Liu. "Finite Element Analysis of Strain Energy Release Rate at Delamination Front", *J. of Reinforced Plastic and Composites*, Vol. 10, pp. 279-292, 1991.

[127] E. J. Barbero and J. N. Reddy. "Modelling of Delamination in Composite Laminates Using a Layer-Wise Plate Theory", *Int. J. of Solids Structures*, Vol. 28, No. 3, pp. 373-388, 1991.

[128] S. El-Sayed and S. Sridharan. "Predicting and tracking interlaminar crack growth in composites using a cohesive layer model". *Composites Part B: engineering*, Vol. 32, pp. 545-553, 2001.

[129] N. E. Jansson and R. Larsson. "A damage model for simulation of mixed mode delamination growth". *Composites Structures*, Vol. 53, pp. 409-417, 2001.